Development of novel linear drive machines

Cox, Thomas

Award date:
2008

Awarding institution:
University of Bath

Development of Novel Linear Drive Machines

Thomas Daniel Cox

A thesis submitted for the degree of Doctor of Philosophy

University of Bath

Department of Electronic & Electrical Engineering

August 2008

Contents

Contents 2
Figures & Tables 4
Acknowledgements 7
Abstract 8
1. Introduction 10
2. Applications of Linear Induction Motors 17
2.1. Amusement Rides 17
2.2. Urban Transport 19
2.3. Materials and Baggage Handling 20
2.4. Industrial Applications 21
2.5. Aircraft and UAV Launch 23
3. Development Methods 24
3.1. Equivalent Circuit Theory 24
3.2. Layer Theory 25
3.3. Finite Element Modelling 26
3.4. Custom Designed Tools 29
3.5. Experimental Results 31
4. Concentrated Windings 34
4.1 Introduction 34
4.2. End Turn Leakage Reactance 37
4.2.1. Equations 38
4.2.2. Air Cored 3D FE Modelling 39
4.2.3. Full 3D Finite Element Multiple Core Modelling 44
4.2.4. Experimental Prototype Machine Multiple Core Modelling 51
4.2.5. Air Cored Prototype Machine Modelling 54
4.2.6. Results Comparison 56
4.2.7. Simple Method of End Turn Leakage Inductance Calculation 58
4.2.8. Parameterised Equation Modelling Method 62
4.2.9. Conductive shielding 69
4.3. Slot Packing Factor 69
4.4. Dual Concentric Coil Concentrated Winding Stators 72
4.5. Plate Rotor Performance of Machines 75
4.6. Motor Harmonics 79
4.6.1. Winding Analysis of a General Three Phase Winding 81
4.6.2. Winding Analysis of Concentrated Windings 82
4.6.3. Winding Factor 89
4.6.4. Standard Winding Factor Equation 90
4.6.5. Machine Winding Factor Spectra 92
5. Wound Rotors 96
5.1. Introduction 96
5.2. Wound Rotor Action 98
5.3. Development of a Four Pole Wound Rotor 98
5.3.1 Time Stepped Four Pole Wound Rotor FE Results 99
5.3.2. Four Pole Experimental Rig Results 100
5.3.3. Four Pole Wound Rotor Concentrated Winding Results 102
5.4. Eight Pole Wound Rotor Design 102
5.4.1 Eight Pole Wound Rotor FE Results 104
5.4.2. Eight Pole Wound Rotor Experimental Results 106
5.5. Further FE Comparisons of Conventional and Concentrated Machines 107
5.5.1. Thrust Speed Curves 109
5.5.2. Variable Frequency 111
5.5.3. Normal Forces 112
5.5.4. Variable Resistance 113
5.5.5. Thrust per Kilo 114
5.6. Simple Modelling Techniques 116
5.7. Conclusions and Advantages 119
6. Short Rotors 121
6.1. Introduction 121

6.2. Double-Sided Geometry 121
6.3. Analytical Modelling Method 122
6.4. Flux Conditions 124
6.5. Short Rotor Current Behaviour 125
6.6. Results 129
6.7. Examples Using Layer Theory 132
6.8. Conclusions 134
7. Offset Stator Harmonic Cancellation 136
7.1. Principle of Harmonic Cancellation 136
7.1.1. Harmonic Analysis 143
7.2. Concentrated Offset Machine Slot to Tooth Ratio 145
7.3. Four Pole Machine Finite Element Analysis 151
7.3.1. Four Pole Machine Experimental Results 157
7.4. 8 Pole Launcher Finite Element Analysis 158
7.5. 2D & 3D FE Comparisons 165
7.6. Dynamic Test Rig Design for Offset Machines 166
7.6.1. Stators 169
7.6.2. Rotors 171
7.6.3. Stator Cradle Structure 173
7.6.4. Load Motor and Drive 174
7.6.5. Motor Power and Control 175
7.6.6. Instrumentation 176
7.7. Dynamic Test Rig FE Modelling for Offset Machines 178
7.8. Dynamic Test Rig Results for Offset Machines 179
7.9. Offset Machine Conclusions 181
8. Overall Conclusions 184
9. Further Work 186
References 187
Appendix 1 - A Spreadsheet Winding Factor Calculation Method 191
Appendix 2 - Two Coil Concentric Concentrated Winding Factor Calculator 195
Appendix 3 - Four-layer fractional-slot windings 197

Figures & Tables

Fig. 1. The concept of a linear induction motor 11
Fig. 2. Components of a linear stator 12
Fig. 3. Conductive plate rotor current regions 13
Fig. 4. Flux paths in a double-sided linear induction motor 14
Fig. 5. Single-sided short stator linear induction motor 15
Fig. 6. Double-sided short rotor linear induction motor 15
Fig. 7. Linear induction motor launched roller coaster 18
Fig. 8. An example of a PRT system using LIMs 20
Fig. 9. An example of a baggage handling system vehicle 21
Fig. 10. An aluminium extrusion puller using linear induction motors 22
Fig. 11. A UAV Launcher Test Facility [5] 23
Fig. 12. The LIM equivalent circuit 24
Fig. 14. The impedance network for a linear induction motor in layer theory 26
Fig. 15. A finite element model mesh 28
Fig. 16. A program used to find harmonic content of flux waveforms 30
Fig. 17. Full dynamic test rig for concentrated winding induction machines 31
Fig. 18. LIM equivalent circuit at slip s (a) and at standstill (b) 32
Fig. 19. A 6 coil 4-8 pole concentrated winding 34
Fig. 20. A 9 coil 8-10 pole concentrated winding 35
Fig. 21. A 12 coil 10-14 pole concentrated winding 35
Fig. 22. A 6 coil 5-7 pole concentrated winding 35
Fig. 23. A standard 2 layer winding 36
Fig. 24. Simplification of concentrated coil to a circular or oval coil made up of the end sections 38
Fig. 25. Coil dimensions used in model 39
Fig. 26. 3D coils generated in Finite Element 40
Table 1: Induced emf's in air cored coils 41
Fig. 27. A 3D FE model of a concentrated winding stator (A – Core, B - Core & Coils) 45
Fig. 28. 3D FE model generated in Mega 46
Table 2: Applied voltages for various core width 3DFE models 47
Table 3: Phase currents calculated from 3DFE modelling 48
Table 4: Reactance per phase values for stators of various core widths 48
Fig. 29. 3D FE Reactance against core width with and without a periodic boundary 49
Fig. 30. Geometry of the Xe problem 49
Fig. 31. Experimental concentrated winding linear machines of varying core width 51
Table 5: Experimental results for stators of various core width 52
Fig. 32. Reactance and core width plots for each test current 53
Fig. 33. Expanded plot, showing a drop in X at 20 & 27A for the 10mm core 53
Table 6: Experimentally derived end turn leakage reactance values 54
Table 7: Experimental results for air cored coils of various core width 55
Fig. 34. Air cored coil reactances 55
Fig. 35. Inductance calculations from the various methods 56
Fig. 36. Force Speed curve showing experimental and 2D finite element results 57
Table 8: Table of impedances for 2D & 3D FE models 60
Fig. 37. Reactances for 3 core width models plotted back to zero 60
Table 9: Normalised inductance for machines using 3 core & 2D-3D method 61
Fig. 38. Relevant coil dimensions for determining end turn inductance of a concentrated coil machine 62
Fig. 39. Normalised inductance variation according to coil pitch 63
Table 10: Normalised inductance variation with coil width 64
Fig. 40. Value of the variable a_n in equation (27) for a 30mm coil depth 64
Fig. 41. The value of coefficient f in equation (37) according to coil depth and its equation 66
Table 11: Full set of constants for normalised inductance equation 67
Fig. 42. Dual coil concentric winding 3D FE model 72
Fig. 43. Coil dimensions for determining end turn inductance of a 2 coil concentric machine 73
Fig. 44. The finite element mesh for a conventional machine 77
Fig. 45. The finite element mesh for a concentrated winding machine 77
Fig. 46. Thrust speed curve for conventional & concentrated stators with plate rotors 78
Fig. 47. Conventional winding slot current waveform plots 79
Fig. 48. Concentrated winding slot current waveform plots 80

Table 12: The relative magnitude of harmonic waves in the 2-pole and 4-pole cases 84
Fig. 49. Addition of forwards and backwards going harmonics at t = 0 85
Fig. 50. Addition of forwards and backwards going harmonics at t = T/4 85
Fig. 51. 6 coil 4 – 8 pole resultant flux and principal harmonic components at 0° 86
Fig. 52. 6 coil 4 – 8 pole resultant flux and principal harmonic components at 120° 87
Fig. 53. 9 coil 8 – 10 pole resultant flux and principal harmonic components at 0° 87
Fig. 54. 9 coil 8 – 10 pole resultant flux and principal harmonic components at 120° 88
Fig. 55. 12 coil 10 – 14 pole resultant flux and principal harmonic components at 0° 88
Fig. 56. 12 coil 10–14pole resultant flux and principal harmonic components at 120° 89
Table 13: Distribution and Pitch factor variation with coil pitch, pole pitch and S/p/p 90
Fig. 57. Plot of winding factor variation with coil pitch, pole pitch and Spppp 91
Fig. 58. 2 layer 5/6ths chorded 2S/p/p stator winding diagram 92
Fig. 59. Winding factors from spreadsheet of 2S/p/p 5/6ths chorded 4 pole winding 93
Fig. 60. Winding factor per harmonic for a 6 coil 4-8 pole concentrated winding 93
Fig. 61. Winding factor per harmonic for a 9 coil 8-10 pole concentrated winding 94
Fig. 62. Winding factor per harmonic for a 12 coil 10-14 pole concentrated winding 94
Fig. 63. A single-sided short rotor wound secondary machine 97
Fig. 64. A double-sided short rotor wound secondary machine 98
Fig. 65. Fractional slot 4 layer wound rotor winding diagram 99
Fig. 66. 4 pole comparison between plate and wound rotors used with concentrated windings 100
Fig. 67. 4 pole wound rotor static thrust test rig 100
Fig. 68. Wound rotor concentrated stator thrusts from FE analysis and experiment 101
Table 14: Table of slot contents for wound rotor 103
Fig. 69. Winding factors of the wound rotor 103
Fig. 70. Thrusts for wound rotor with modular stator, plate rotor with conventional & modular stator .. 104
Fig. 71. Wound rotor experimental and FE results 107
Fig. 72. Thrust speed curves for wound & plate rotor FE element models 110
Fig. 73. Calculated thrust speed curves for wound and plate rotors at 50 and 25 Hz 111
Fig. 74. Stator to rotor normal forces 112
Fig. 75. Thrust speed curves for various values of rotor resistance in Ohms/phase 113
Fig. 76. Thrust per Kg motor weight against speed 115
Fig. 77. The LIM equivalent circuit 116
Fig. 78. 2 layer stator with a wound rotor FE, experimental & equivalent circuit thrusts 117
Fig. 79. Concentrated stator with a wound rotor FE, experimental & equivalent circuit thrusts 118
Fig. 80. Double-sided short rotor linear induction motor 121
Fig. 81. Geometry assumed to develop the analytical force expression 122
Fig. 82. Flux distribution in an 8-pole rotor short rotor machine at stall (a) & at peak force 18 m/s (b) . 124
Fig. 83. Current density in the rotor for continuous and 8 pole short rotors at stall 125
Fig. 84. Current density in the rotor for continuous and 8 pole short rotors at peak thrust 125
Fig. 85. 2 pole short & continuous rotor current density at 0 Deg 126
Fig. 86. 2 pole short & continuous rotor current density at 90 Deg 127
Fig. 87. 2 pole short & continuous rotor current density at 180 Deg 127
Fig. 88. 2 pole short & continuous rotor current density at 270 Deg 128
Fig. 89. Variation of plate current density by phase for conventional & short rotor machines at stall 128
Fig. 90. Plate current density variation by phase for conventional & short rotor machines at 18m/s 129
Fig. 91. Force per metre plate against speed results using FE for different short rotor lengths 130
Fig. 92. Calculated and FE model thrusts for 4 6 & 8 pole short rotors & conventional machine 131
Fig. 93. Calculated and FE model thrusts for 1/2, 1 & 2 pole short rotors & conventional machine 132
Fig. 94. 8 pole high speed launcher short rotor & conventional machine modelling 133
Fig. 95. 4 pole low-medium speed short rotor & conventional machine modelling 133
Fig. 96. 4 pole low speed short rotor & conventional machine modelling 134
Fig. 97. 2 & 4 pole flux components from double-sided concentrated winding 136
Fig. 98. Flux components from offset double-sided concentrated winding, 2 pole cancellation 137
Fig. 99. Flux components from offset double-sided concentrated winding, 4 pole cancellation 137
Fig. 100. Spreadsheet to find % positive and negative harmonic present in an offset configuration 139
Fig. 101. 6 coil positive 4 pole & negative 8 pole % of harmonic for various offset angles 140
Fig. 102. 6 coil reversed positive 4 pole & negative 8 pole % of harmonic for various offset angles 140
Fig. 103. 9 coil positive 8 pole & negative 10 pole % of harmonic for various offset angles 141
Fig. 104. 9 coil reversed positive 8 pole & negative 10 pole % of harmonic for various offset angles ... 141
Fig. 105. 12 coil positive 10 pole & negative 14 pole % of harmonic for various offset angles 142

Fig. 106. 12 coil reversed positive 10 pole & negative 14 pole % harmonic for various offset angles.... 142
Fig. 107. 3 coil 2-4 pole reversed airgap flux analysis 143
Fig. 108. 9 coil 8-10 pole airgap flux analysis 144
Fig. 109. 12 coil 10-14 pole airgap flux analysis 145
Fig. 110. Offset machines showing various slot to tooth ratios 145
Fig. 111. Single tooth FE model showing various slot openings used 146
Fig. 112. Force for various % slot widths 147
Fig. 113. Current for various % slot widths 147
Fig. 114. VA/N for various % slot widths 148
Fig. 115. Force per Amp for various % slot widths 148
Fig. 116. FE model with semi closed slots 149
Fig. 117. C clip type tooth tip 150
Fig. 118. 2D FE model of double-sided conventional machine 151
Fig. 119. 2D FE model of double-sided concentrated offset machine 152
Table 15: Performance of short stator double-sided offset machines 155
Fig. 120. Offset pair experimental thrust speed comparisons 157
Table 16: Basic parameters of offset concentrated concentric launcher 158
Table 17: 3D modelling results for offset concentrated concentric launcher reactances 159
Fig. 121. 3 core width end turn reactances for 2 coil concentric offset launcher 159
Fig. 122. Force developed on the vehicle by time 160
Fig. 123. Velocity developed on the vehicle by time 161
Fig. 124. Velocity of the vehicle by distance travelled 161
Fig. 125. Force developed on the vehicle by velocity 162
Fig. 126. Total current draw by vehicle velocity (Sum of magnitudes of current per phase) 162
Fig. 127. VA/N by velocity (sum of magnitudes of volts times amps per phase over force 163
Fig. 128. Copper Watts per Newton of the system by Velocity (8 * I2R loss per stator / Force) 163
Fig. 129. Watts per Newton of the system by Velocity (CuW/N + Vel*Force/Force) 164
Fig. 130. Cos Phi of the system (W/VA) 164
Fig. 131. Efficiency of the system (100 * Vel / W/N) 165
Fig. 132. A schematic of the dynamic test Rig (front view) 167
Fig. 133. A schematic of the dynamic test Rig (side view) 168
Fig. 134. Lamination details for dynamic test rig stators 170
Fig. 135. Dynamic test rig stator 171
Fig. 136. Test rig short rotor sections 172
Fig. 137. Dynamic test rig short rotor sections 173
Fig. 138. Dynamic test rig cradle 174
Fig. 139. Dynamic rig load motor and pulley 175
Fig. 140. Dynamic test rig for offset machines 177
Fig. 141. 3D FE of the dynamic test rig 178
Table 18: 3D FE modelling results 179
Table 19: Test Rig experimental results 179
Fig. 142. Test rig output force compared with 3D FE 180
Fig. 143. . Test rig current draw compared with 3D FE 180
Fig. 144. Test rig VA/N compared with 3D FE 181
Fig. 145. Disk type rotary concentrated offset induction motor 182
Fig. 146. Cage or drag cup type rotary concentrated offset induction motor 183
Fig. 147. Harmonics equal to multiples of the fundamental pole pairs 191
Fig. 148. Component vectors of slot angle θ with Content M for one phase 192
Fig. 149. Spreadsheet top stator slot angles per phase including number of conductors 192
Fig. 150. Bottom stator slot angles per phase including number of conductors 193
Fig. 151. Overall components of magnitude per phase 193
Fig. 152. Concentrated winding factor calculator inputs and outputs 195
Fig. 153. Stator and rotor with a common phase pattern 197
Fig. 154. Electrical/MMF angles 199
Fig. 155. Illustration of a two-layer winding 200

Acknowledgements

I wish to express my deepest gratitude and appreciation to Professor Fred Eastham for all the help and support he has provided throughout this project. His abilities as a teacher, thinker, and expert in electrical machines are truly unparalleled.

I would like to thank both Dr Hong Lai and Dr Paul Leonard for their excellent work as supervisors over the course of this project.

I also wish to thank Mr Alan Foster and Mr Jeff Proverbs for all their valuable input to the project, and for providing me with this marvellous opportunity. My gratitude is also extended to all of those at Force Engineering who have aided greatly in the development of this project.

I would like to thank my family, particularly my wife, whose love and support is the rock upon which all of my successes are built.

Finally, I would like to thank all those involved in managing the KTP project.

This thesis is based on work undertaken through a Technology Strategy Board Knowledge Transfer Partnership between the University of Bath and Force Engineering.

Abstract

Linear induction machines currently play a relatively minor role in the industrial world. This is partly due to relatively high production costs, complexity of construction and the inability to apply standard mass production techniques. The aim of this thesis is to investigate the design of linear machines that are cheaper and faster to produce, and that may easily be mass-produced.

This thesis principally concerns the use of concentrated winding linear stators. These are cheap and easy to manufacture and can be easily mass-produced. However, high levels of negative harmonics make them unsuitable for use with simple sheet rotors.

To allow the use of concentrated winding linear stators, a wound rotor may be used to filter out the negative harmonics, and so produce good performance from a simple, inexpensive stator. Computational results of plate and wound rotor systems are compared and contrasted, as well as results from experimental systems. These show that not only do wound rotors provide good performance from concentrated stators, they also have various other benefits and increase design freedom. Computational methods are developed in order to efficiently design wound rotor systems.

Another method to mitigate the effect of negative harmonics in double-sided concentrated windings is the use of mechanical and electrical offsetting. Certain combinations of mechanical and electrical offset can be used to eliminate the negative harmonics from concentrated windings, whilst reinforcing the positive harmonics. Various forms of this system are studied and the offset behaviour of various winding configurations is investigated.

Further topics include methods for the prediction and reduction of end turn leakage reactance in concentrated windings. A method has been developed to simply predict end turn leakage reactance that accounts for the presence of stator iron.

A study of general performance and end effects in short rotor linear machines has also been undertaken, and some of the advantageous behaviours of short rotor systems have been highlighted.

In order to further study technologies described within this thesis, a high speed dynamic test rig was developed to prove the performance of the offset machines.

1. Introduction

An electric motor is a device that converts electrical energy into mechanical energy. These motors principally use the electromagnetic phenomenon whereby a mechanical force is generated on a current carrying wire in a magnetic field. Various designs and topologies of electrical motor use this fundamental principle to provide mechanical force and motion from electricity.

Conventional or rotary machines typically have two parts, a rotating centre section (rotor) and a stationary outer section (stator). In a first form permanent magnets or electromagnets on one section generate a magnetic field. Current carrying wires on the other section generate a second magnetic field, and the two interact to provide rotary motion.

Alternatively, alternating current carrying wires on one section create a magnetic field which induces a current in conductive materials on the other section. These induced currents produce a counter magnetic field, again producing rotary motion. This is commonly known as an induction motor. The rotary induction motor was invented by Nikola Tesla in 1888 [1], and has become an extremely common and capable form of rotary machine. A widely used rotor design consists of a cage made up of conductive bars shorted together at both ends, in which currents are induced. This is generally known as a squirrel cage induction motor.

The current focus of this development project is Linear Induction Motors (LIMs). These are essentially a conventional 3-phase rotary induction motor opened out flat as in Fig. 1.

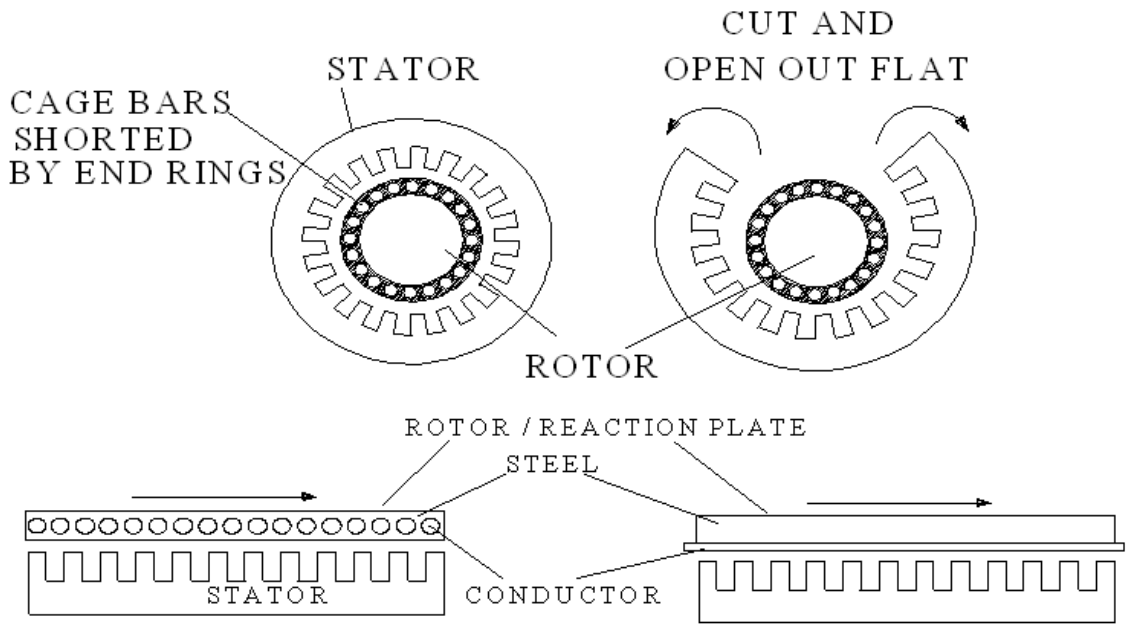

Fig. 1. The concept of a linear induction motor

The Linear motor was first developed in the 1840's by Sir Charles Wheatstone [2], however their application has been limited until recent times. In the 1940's, a linear motor based aircraft launcher [3] was developed by Westinghouse, but the project never produced a viable alternative to contemporary technology. Since the 1960's, Linear motors have been developed for various fields of application and with various degrees of success [4].

In 1996 Linear induction motors were successfully applied to produce a relatively high speed vehicle launch system for roller coasters. This has since become an established technology in the amusement industry, with launch systems in the USA, China, the Middle East and Canada where vehicles weighing up to 8 tonnes are accelerated to around 70mph in under 4 seconds.

The amusement ride work has helped to demonstrate LIM launch as an established technology for high speed applications. Design work has been ongoing into LIMs for even higher speed and acceleration applications, including the development and successful testing of a high speed UAV (Unmanned Aerial Vehicle) launcher, propelling a vehicle from 0-50m/s in 0.7s

[5]. Further development is ongoing in high speed launch fields including UAV and aircraft launchers.

When connected to a 3-phase AC supply a linear motor produces a travelling magnetic field that generates straight-line force in the rotor, rather than torque as in the case of a rotating machine.

The motor consists of two parts. The stator or primary, which is very similar to that of a conventional machine, and the rotor or secondary, which is rather different.

The stator's stack or core is made from ferrous material, chosen to provide a good path for flux, and is generally made up of a group of laminations. These can be welded or bolted together to form a core, into which pre-wound conductive coils are inserted as in Fig. 2.

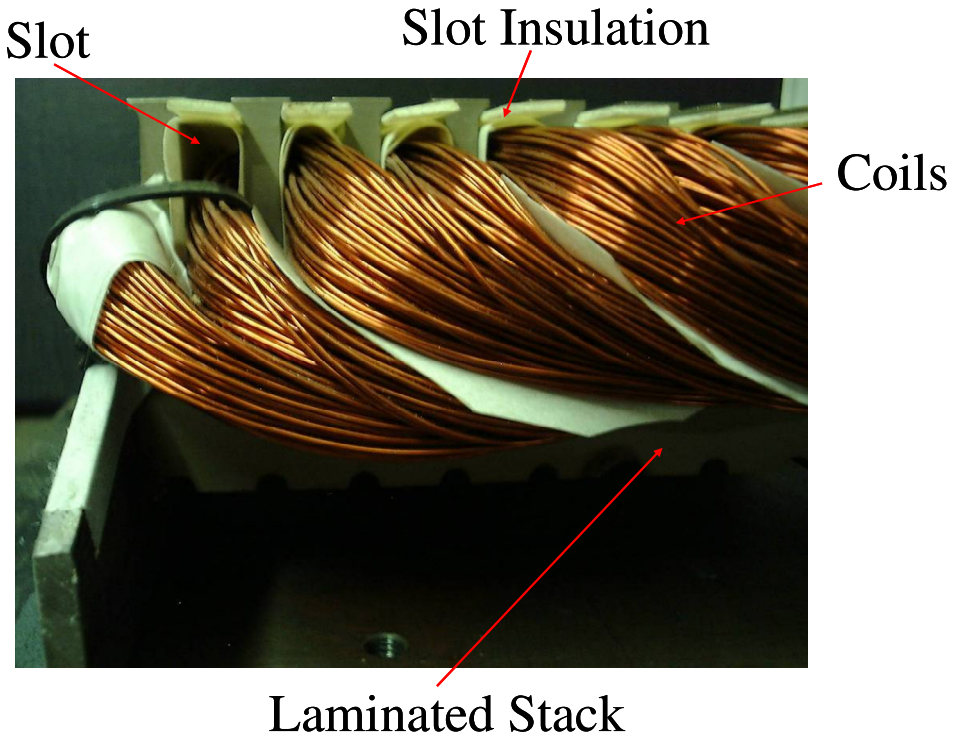

Fig. 2. Components of a linear stator

The simple induction rotor, commonly called the reaction plate in linear motors, has both its iron sections and conductor bars 'smoothed out' into the form of

flat sheets. This means that the conventional 'squirrel cage' is replaced by a flat conductive sheet backed by a sheet of steel, as shown in Fig. 1. This is commonly known as a single-sided linear induction motor. The rotor must still have the same electrical characteristics as before. It must provide a low reluctance path for the stator's magnetic flux and a low resistance path for the induced electric currents. An illustration of the eddy current patterns and important regions in a plate rotor is shown in Fig. 3. The width of the reaction plate should be chosen to give an acceptable end ring. If the end ring section in shown in Fig. 3 is too narrow, the eddy current path in the end ring is constrained and the secondary resistance is consequently increased.

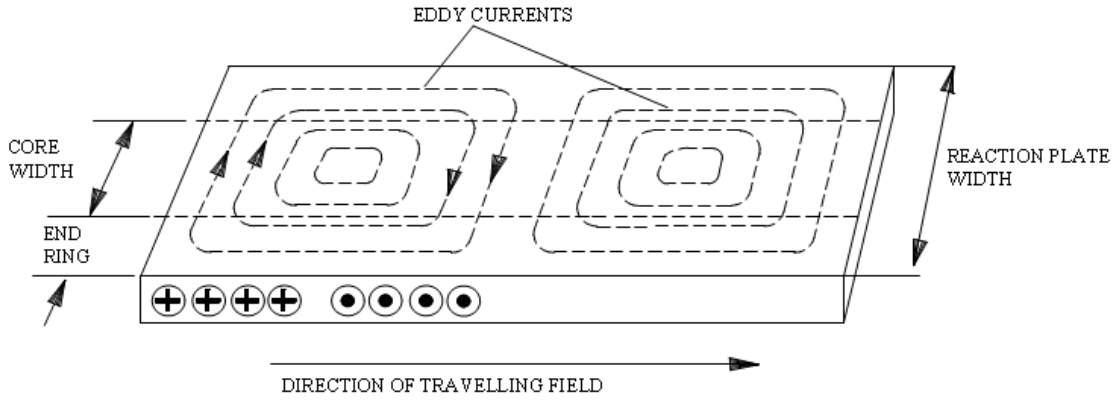

Fig. 3. Conductive plate rotor current regions

If two LIMs are mounted face to face either side of a sheet conductor Fig. 4, the need for steel in the reaction plate is eliminated. Each linear stator now completes the other's magnetic circuit. This method is often used to reduce the moving mass, eliminate any normal force on the plate and to generate increased thrusts. This is generally known as a double-sided linear induction motor.

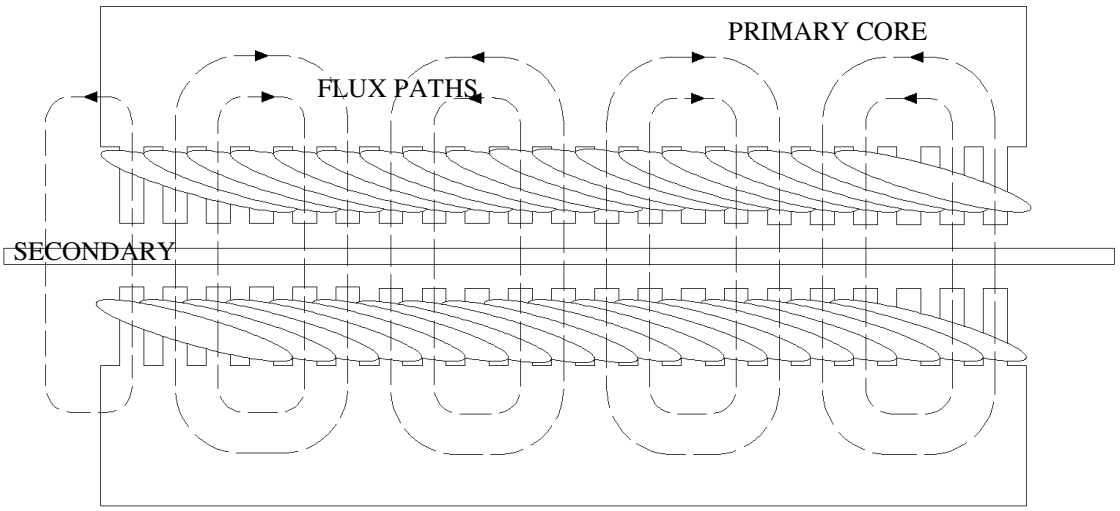

Fig. 4. Flux paths in a double-sided linear induction motor

There are several important changes introduced with the move to linear motion. The air gaps involved are generally increased by a significant amount. This is due partly to tolerances. In a rotary machine, rotary tolerances can be established very accurately, and so machines can work at very small air gaps in the single millimetre range. With linear machines, particularly transportation projects and launch systems, much larger mechanical tolerances and so stator to rotor clearances are involved, generally between 3 and 10 mm. Added to this is the fact that the steel to steel path also now includes the thickness of the sheet conductor, which adds a further several millimetres to the high reluctance section of the flux path.

A further issue in the single-sided case is stator to rotor attraction or repulsion forces, generally referred to as normal force. In a rotary machine, the stator to rotor normal force is largely cancelled out due to it acting to an equal degree around the entire periphery of the airgap. In a linear machine, this force is entirely acting in a single direction and so must be accounted for.

Another significant difference occurs at the ends of the machine. For continuous action either the secondary or the primary member of the linear machine has to be shorter than the other member. This introduces end effects which occur at

the ends of both the stator and rotor and can have a significant effect on machine performance.

The short stator or short primary LIM is a machine in which the rotor is longer than the stator Fig. 5. The short rotor, sometimes called a short secondary is a machine in which the rotor is shorter than the stator Fig. 6. Short stator and short rotor machines may be either single-sided or double-sided depending on requirements.

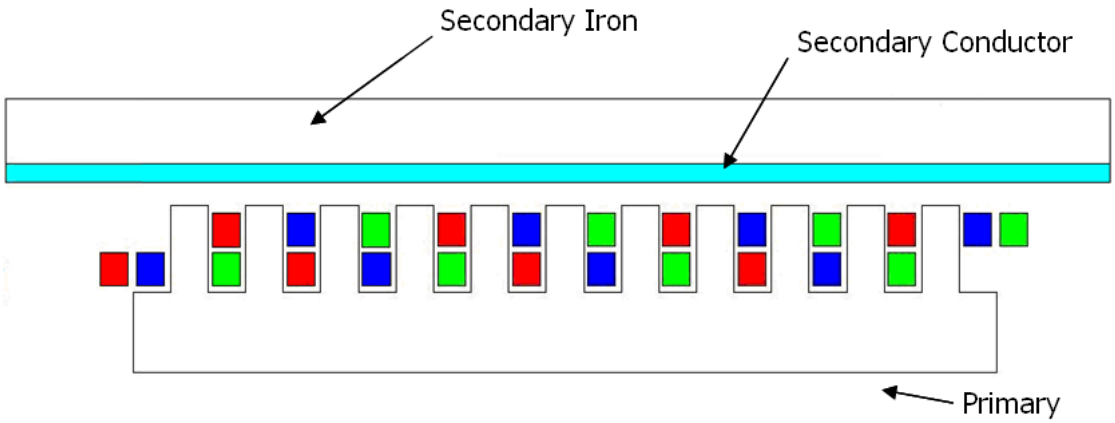

Fig. 5. Single-sided short stator linear induction motor

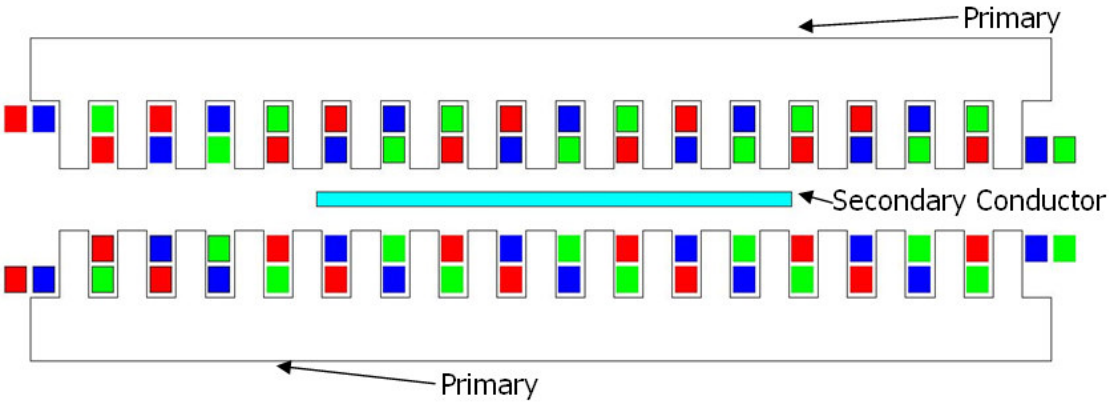

Fig. 6. Double-sided short rotor linear induction motor

Linear machines have a relatively minor role in the industrial world, with the majority of linear motion tasks still performed by the conversion of rotary motion to linear.

One problem associated with linear machines is a relatively high production cost. This cost is partly due to the complexity of construction of the linear machine. A further problem is that low production volumes and diverse requirements often prevent the use of mass production methods..

One of the principal areas explored is the design of linear machines that are cheaper and faster to produce, with the capability to be easily mass- produced.

In order to meet the many diverse applications found within the linear machine market, new systems must be able to adapt to meet a wide range of design criteria. Increasing the design flexibility of linear motor systems gives the designer freedom to create motors that are better suited to their particular role.

Another area of development is to provide improved performance from conventional linear motor systems. Performance improvements may make existing systems more economical and powerful, and may broaden the use of linear motors into applications that previous systems were unsuited to. Improved motor performance can also reduce the significant cost and complexity of linear motor power and control equipment.

2. Applications of Linear Induction Motors

Linear induction motors can potentially fulfil any application that requires linear motion. However many markets are already saturated with various other solutions that would make market entry for LIMs extremely difficult. LIMs do however fulfil some significant roles. Examples include:

- Amusement rides
- Urban Transport
- Materials handling
- Industrial applications
- Aircraft/UAV launch

The characteristics that suit LIMs to each of these roles will now be identified, in order to determine areas where new technological development would be of most benefit.

2.1. Amusement Rides

LIMs are mainly used on roller coasters as a catapult launch system Fig. 7. This means that the vehicle is given a large initial velocity (typically a large acceleration along a straight section of track) and this kinetic energy carries the vehicle through the rest of the track. This system is in contrast to the conventional roller coaster where the vehicle is mechanically lifted to the top of the first "hill" from where it coasts around the rest of the track using its potential energy.

Fig. 7. Linear induction motor launched roller coaster

The main feature of LIMs that makes them suitable for this application is their ability to exert a linear thrust force on a moving conductor. If this moving conductor is attached to a roller coaster vehicle, and the motors are attached to the track, the vehicle will be accelerated in relation to the track. This sudden acceleration itself is an attraction for a roller coaster.

Motors can also be mounted at any point on the vehicle track in order to give the vehicle a further boost. LIM technology has been successfully applied to vehicles in order to maintain a steady velocity while climbing the uphill sections of a gravity-powered ride.

Another feature of LIMs is that they do not usually need complex positioning control systems. This is an important feature when compared to linear synchronous machines where position must be known at all times. In synchronous machines required positional accuracy is dependant on machine type and control method. In sinusoidal permanent magnet synchronous motors

7-8 bit position resolution estimation is required [6], equating to an accuracy of 1.4-2.8 degrees. This increases to 60 electrical degrees for trapezoidal permanent magnet synchronous motors [6]. LIMs are by nature non-contact, and so have none of the mechanical wear and friction problems usually associated with conventional drive systems.

LIM stators have no moving parts, and the stator is generally encapsulated, meaning that these motors require very little to no regular maintenance and have a high level of environmental protection.

LIMs can be arranged in a double-sided configuration, in order to increase thrust on the reaction plate and reduce vehicle weight, as the rotor may now consist of a simple conductive sheet as in Fig. 6.

2.2. Urban Transport

LIMs are commonly used in urban transportation systems, which move people from place to place using vehicles travelling on tracks. This includes applications ranging from small scale transit systems travelling short distances to large train systems travelling long distances. LIM's may be mounted either on the vehicle or at regular intervals along the track. These systems are generally designed to provide a much lower thrust than launchers, but the vehicle spends a relatively longer time under power.

Many of the same advantages listed above apply equally in the field of people movers. Linear thrust, no need for positioning control for optimum thrust, no mechanical motor wear, low maintenance and lower vehicle weight are all important factors in transportation, as these all aid in reducing costs and so making systems more economically sound.

LIMs can be specifically tailored to this type of application, with a lower output thrust but a much longer rating (this represents the time they can operate for before overheating).

There are many different types of linear motor people movers. A common type is PRT or personal rapid transport Fig. 8.

Fig. 8. An example of a PRT system using LIMs

One of the key problems in this area is the relatively high unit cost of LIMs and their associated control equipment. When it is considered that many thousands of motors may go into a single people mover project, it is clear that small cost savings per motor system would translate to huge savings over a whole system.

2.3. Materials and Baggage Handling

LIMs are a very useful tool in the materials handling industry. The application of LIMs to this industry can bear many similarities to people moving applications, especially in the field of baggage handling. Small vehicles containing the material to be transported are moved along a track by LIMs, as in Fig. 9. These systems benefit from all the same features as previous transportation applications.

Fig. 9. An example of a baggage handling system vehicle

An alternative use in materials handling is when LIMs are used to move a low speed large object, e.g. a baggage carousel, usually using attached rotors. LIMs can be distributed all around the carousel and the simple contact-less linear motion once again gives significant advantages over more conventional mechanical drives.

A significant alternative is in the use of the object itself as a rotor. This can occur, particularly in industry when LIMs are required to move ferrous or conductive items, e.g. cans, tubes, sheet metal and even some liquids. This can be a huge saving in transportation costs, and can lead to much less complex transport systems.

2.4. Industrial Applications

Linear induction motors have found many industrial applications, and are often able to provide a unique solution that would be very difficult to implement with conventional machines.

LIMs can be used for metal separation. Due to the nature of its operation, the LIM will act on conductive and ferrous materials, but not on non-conductive or

non-ferrous ones. This means that it may be used as a method to sort the one from the other. This can be a significant task, for instance in scrap sorting or metals recycling, and is a very efficient and cheap method of sorting.

Mould heating is an important task in the injection moulding industry, as a mould must be brought up to the correct temperature before it can be used. With conventional contact heating this can take a very long time, and can give uneven heat distribution throughout the mold.

A stationary linear motor can be mounted with a conductive mould held stationary in relation to it. The motor will induce eddy currents in the mould, causing it to quickly heat up to the required temperature. This exploits the effect of induced currents in the rotor of a LIM.

Extrusion pullers are a good example of a highly specialised industrial application, shown in Fig. 10.

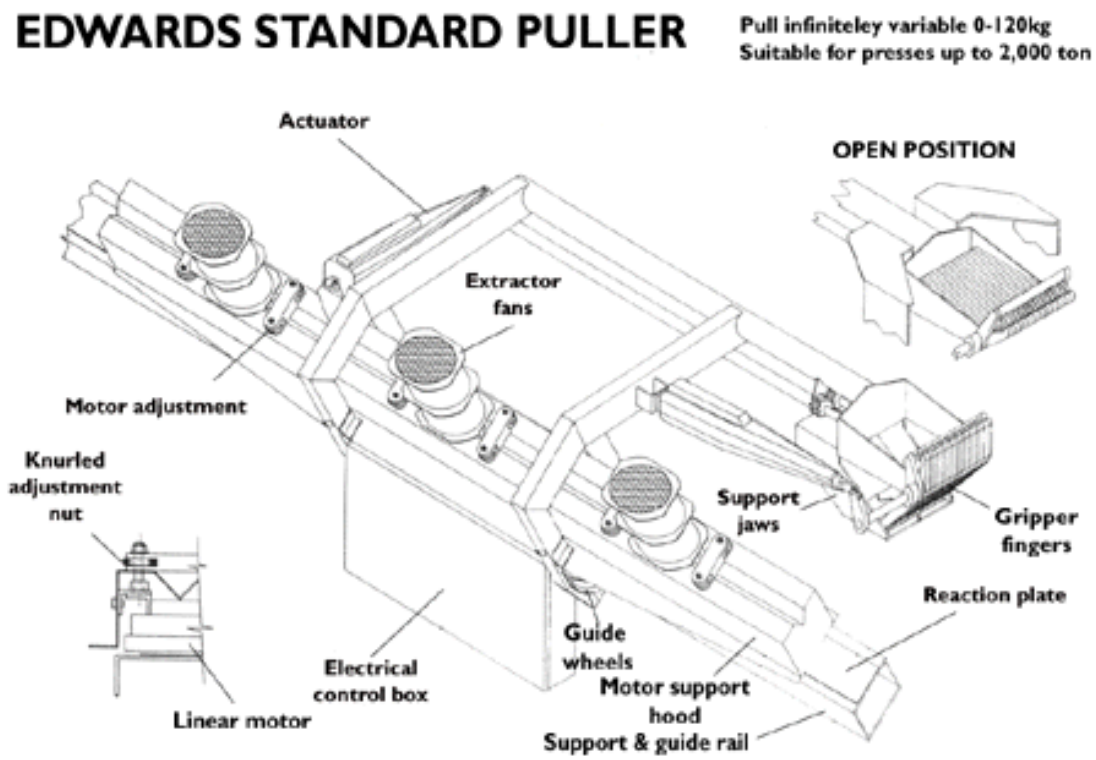

Fig. 10. An aluminium extrusion puller using linear induction motors

The LIM provides a low speed high force linear pulling force for the extrusion process, and then a high-speed low force return to repeat the process. Again, the contactless non-mechanical LIM operation proves to be an advantage, as does the simple control and robustness of LIMs.

2.5. Aircraft and UAV Launch

The same high thrust, short duration linear motor systems that are used on roller coasters can also be applied in areas such as aircraft or Unmanned Aerial Vehicle launch Fig. 11.

Fig. 11. A UAV Launcher Test Facility [5]

These systems typically require higher velocities, greater thrust and acceleration than on roller coasters. This is particularly the case with UAV launch, where G Forces applied to the vehicle may be many times greater than the safe level for manned vehicles. There are several other challenges in the area of UAV and aircraft launch including a wide variation in launch vehicle mass and shape, power supply limitations and extreme working environments.

3. Development Methods

Several methods have been used to develop and study electrical machines within this project. These can be roughly broken down into the following categories.

- Programs based on equivalent circuit theory
- Programs based on layer theory
- Finite element based methods
- Custom designed tools
- Experimental test rigs

These methods vary significantly in terms of speed, accuracy, cost, development time and solution time. Some of the key features of the various methods will be outlined below.

3.1. Equivalent Circuit Theory

In equivalent circuit theory, the machine performance is modelled as an electrical circuit, with various components representing aspects of the machine. The equivalent circuit model for one phase of a LIM is shown in Fig. 12.

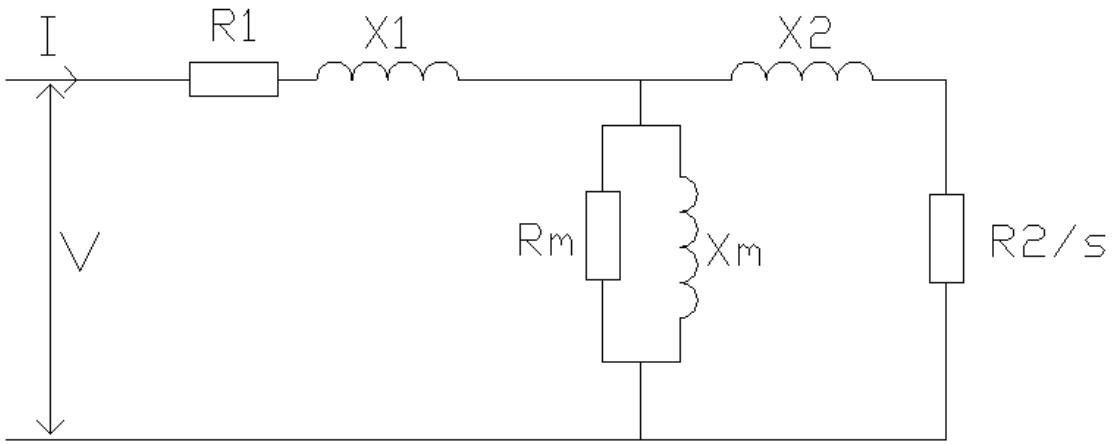

Fig. 12. The LIM equivalent circuit

R_1 represents the resistance of the stator winding. X_1 represents the leakage reactance of the stator and can be further broken down into its main components, end turn leakage reactance X_e and slot leakage reactance X_s. This component represents non useful flux. R_2 represents the resistance of the current path developed in the rotor, referred to the stator. s represents the slip of the rotor and R_2/s represents the power transferred to the rotor. X_2 represents the leakage (non useful) inductance of the rotor, referred to the stator. Finally, X_m represents the flux path linking together stator and rotor and R_m represents the magnetising losses developed in the machine. In practice, the R_m component is negligible for the range of applications outlined in the previous chapter, and so can generally be neglected.

If all of these components can be calculated, then the performance of the machine ignoring end effects can be calculated very quickly and with a degree of accuracy, typically within 15% of machine performance.

3.2. Layer Theory

Layer theory [7] is a more complex method than equivalent circuit theory, which represents a linear machine as a series of layers as in Fig. 13.

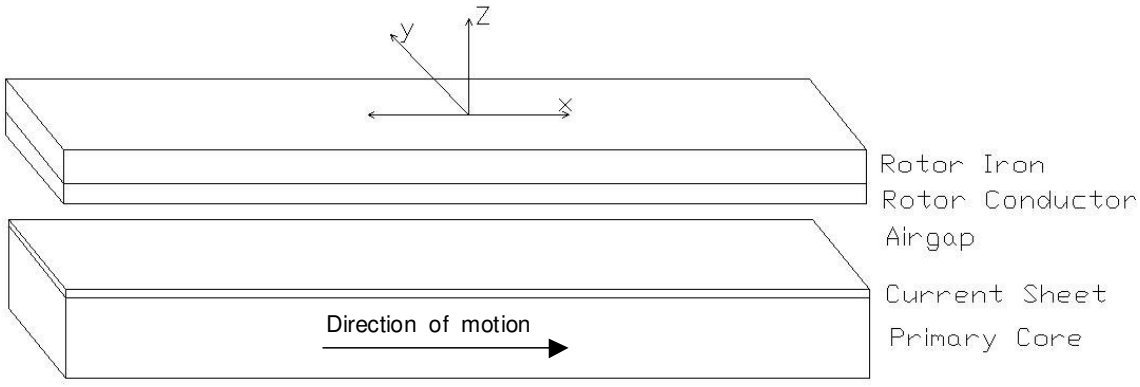

Fig. 13. Layer Theory model of a linear induction motor

The primary is represented as a current sheet on the surface of smooth iron. Correction factors based on more detailed calculations are applied, in order to bring the results from these assumptions closer to those of actual machines.

The motor is then modelled electrically as an impedance network Fig. 14, taking the impedances of each layer into account. In this model the Jx represents the current sheet, whilst the various Z components represent the transmission line impedances for each layer of the model.

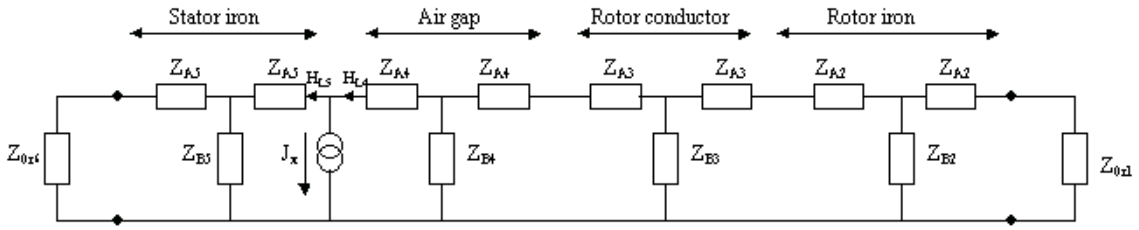

Fig. 14. The impedance network for a linear induction motor in layer theory

This method can produce more accurate results than the equivalent circuit, typically within 10%, although it also requires more processing time. With modern PC technology however, both circuit and layer theory give effectively instant answers.

3.3. Finite Element Modelling

Finite element or FE modelling uses a computer model consisting of regions, each of which is made up of many small elements, in order to model a full machine.

Each region is assigned material properties including resistivity and conductivity, in order to accurately model the materials (conductor, iron, air etc) present within the machine. The software is able to model the electromagnetic interactions between elements in order to predict the behaviour of the overall machine.

Finite Element models are often 2D, modelling a single slice through a stator and adapting the results according to the actual stator dimensions. In 2D, electromagnetic fields can be modelled using the magnetic vector potential, **A**, the governing equation is:

$$\nabla \times \frac{1}{\mu} \nabla \times \mathbf{A} + \sigma \frac{\partial \mathbf{A}}{\partial t} = \mathbf{J} \qquad (1)$$

Where:

μ is the permeability in henries/metre

A is the magnetic vector potential in webers/metre

σ is the conductivity in siemens/metre

This can be transformed into a system of equations by using the finite element method together with the Galerkin weighted residual procedure.

In order that the dynamic behaviour of the motor is simulated a time-stepping scheme is used, which takes into account the transient nature of the supply to the motor and the dynamic motion of the rotor.

The movement of the rotor is handled by a special sliding surface FE scheme [8]. In this scheme, the stator and rotor of the motor are represented by separate FE meshes, which touch each other at a common interface. In our case, this common interface is located at the middle of the air-gap. The stator and rotor mesh are allowed to freely slide relative to each other along the interface and in so doing enable the dynamic motion of the rotor to be handled without needing any re-meshing. Fig. 15 shows a magnified view of the stator and rotor mesh touching each other at the middle of the air gap.

Fig. 15. A finite element model mesh

To couple the meshes electromagnetically, the Lagrange Multipliers technique is used. The method essentially enforces the following constraint (2) at the interface of the stator and rotor mesh.

$$A_s - A_r = 0 \tag{2}$$

Where A_s and A_r are the vector potential unknowns at the stator and rotor interface nodes respectively.

The 2D methods do not account for some effects such as the primary resistance, primary end turn reactance and secondary resistance end ring effect. To compensate for this, external circuits can be coupled to the model [9] including separately calculated values for primary resistance and end turn reactance. The conductivity of the secondary conductor material may also be modified by a factor based on the work of Russell and Norsworthy [10] in order to account for end ring behaviour.

Alternatively, a full 3D FE model is able to represent all aspects of a linear induction motor.

If the rotor has a constant cross section at right angles to the direction of motion e.g. a sheet rotor, motion modelling can be performed using a Minkowski transform [11]. This allows a single, fast solution to be found for a constant velocity problem. Otherwise, full motion must be represented by analysing the machine over a series of time steps, with the rotor motion taken into account by the model.

FE is a very accurate modelling tool, however its chief drawback is processing power and time required. Not only do FE models take longer to set up than their circuit or layer theory counterparts, they also take a lot longer to solve, particularly when the model contains a large number of elements or is three dimensional.

3.4. Custom Designed Tools

For some tasks within this project, tools and equations have been developed and adapted in order to meet specific goals. A common tool used for this is Microsoft Excel, which allows mathematical models to be produced of various machine characteristics. For example, Fig. 16 shows a spreadsheet used to calculate flux harmonic content in concentrated windings of various configuration.

Degrees Offset 180			Reversed? (Y or N) Y	-1
Positive Poles 4		Negative Poles 8	Teeth 6	

Peak % of Max	Positive	Negative	Tooth	Cover
	100	0	0	0

Password: Edit

	Bottom Stator		Top Stator		Resultant		Tooth offset	
Angle	Positive	Negative	Positive	Negative	Positive	Negative	Bottom	Top
0	0.00	0.00	0.00	0.00	0.0	0.0	-1.00	1.00
5	0.09	0.17	0.09	-0.17	8.7	0.0	-0.97	0.97
10	0.17	0.34	0.17	-0.34	17.4	0.0	-0.87	0.87
15	0.26	0.50	0.26	-0.50	25.9	0.0	-0.71	0.71
20	0.34	0.64	0.34	-0.64	34.2	0.0	-0.50	0.50
25	0.42	0.77	0.42	-0.77	42.3	0.0	-0.26	0.26
30	0.50	0.87	0.50	-0.87	50.0	0.0	0.00	0.00
35	0.57	0.94	0.57	-0.94	57.4	0.0	0.26	-0.26
40	0.64	0.98	0.64	-0.98	64.3	0.0	0.50	-0.50
45	0.71	1.00	0.71	-1.00	70.7	0.0	0.71	-0.71
50	0.77	0.98	0.77	-0.98	76.6	0.0	0.87	-0.87
55	0.82	0.94	0.82	-0.94	81.9	0.0	0.97	-0.97
60	0.87	0.87	0.87	-0.87	86.6	0.0	1.00	-1.00
65	0.91	0.77	0.91	-0.77	90.6	0.0	0.97	-0.97
70	0.94	0.64	0.94	-0.64	94.0	0.0	0.87	-0.87
75	0.97	0.50	0.97	-0.50	96.6	0.0	0.71	-0.71
80	0.98	0.34	0.98	-0.34	98.5	0.0	0.50	-0.50
85	1.00	0.17	1.00	-0.17	99.6	0.0	0.26	-0.26
90	1.00	0.00	1.00	0.00	100.0	0.0	0.00	0.00
95	1.00	-0.17	1.00	0.17	99.6	0.0	-0.26	0.26
100	0.98	-0.34	0.98	0.34	98.5	0.0	-0.50	0.50
105	0.97	-0.50	0.97	0.50	96.6	0.0	-0.71	0.71
110	0.94	-0.64	0.94	0.64	94.0	0.0	-0.87	0.87
115	0.91	-0.77	0.91	0.77	90.6	0.0	-0.97	0.97

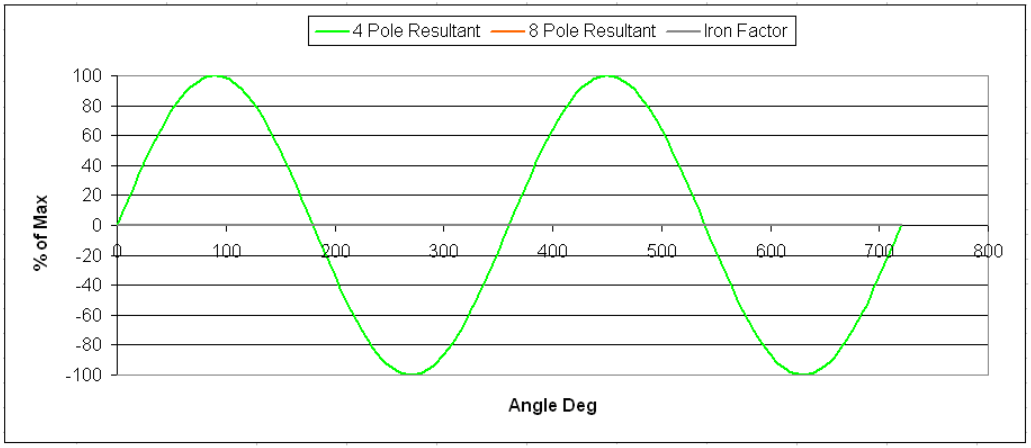

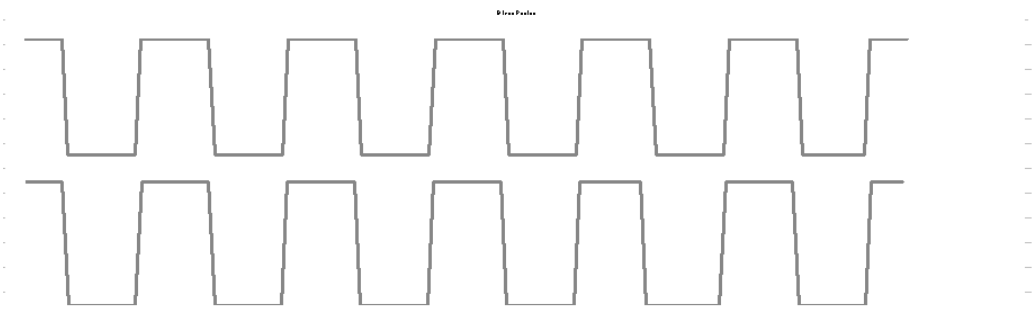

Fig. 16. A program used to find harmonic content of flux waveforms

3.5. Experimental Results

Wherever possible, results have been verified by experimental methods. Various experimental rigs have been produced, ranging from simple static test rigs to the full dynamic rig shown in Fig. 17.

Fig. 17. Full dynamic test rig for concentrated winding induction machines

The test rigs gave conclusive proof of the performance of various machine types and allowed the validation of other methods of performance prediction.

When static test rigs are considered it is necessary to use a technique called variable frequency testing [12] in order to gain results for various velocity points. This test allows the prediction of dynamic performance from static test conditions.

The process can be explained with the aid of Fig. 18.

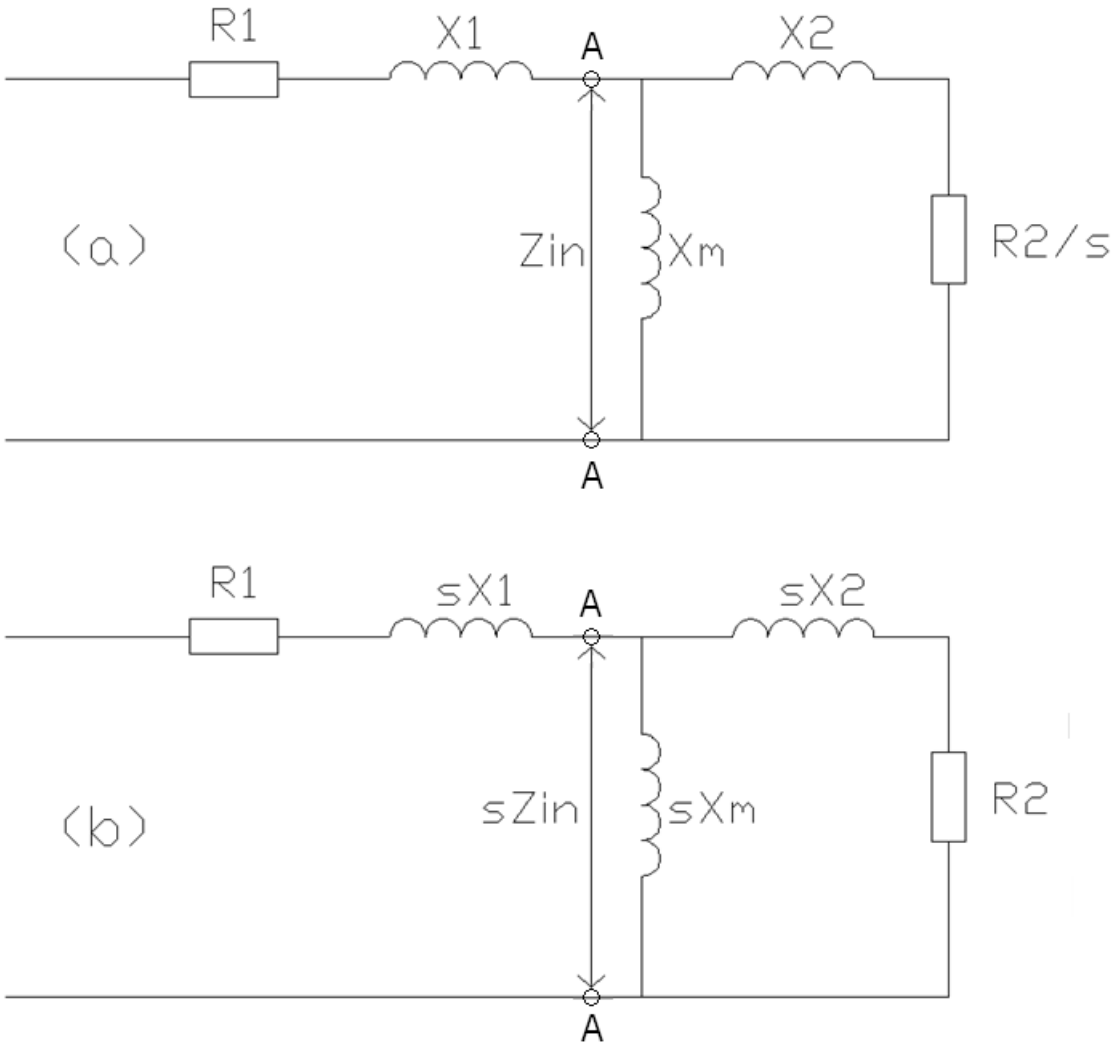

Fig. 18. (a) LIM equivalent circuit at slip s and (b) at standstill with supply frequency sf

Fig. 18 (a) shows the equivalent circuit of the machine at slip s when fed with the normal supply frequency. A standstill version of this equivalent circuit, Fig. 18 (b), is fed by the same magnitude of current as at standstill but at a frequency sf rather than f.

The power input to the secondary (at terminals A-A) of the circuit in Fig. 18 (a) per phase is:

Power input = $\mathrm{Re}(Z_{in})I^2$ Watts (3)

and the force produced per phase is then

Force = Power / Field speed = $\mathrm{Re}(Z_{in})I^2 / V_s$ Newtons (4)

The power input to the secondary of the standstill variable frequency circuit Fig. 18 (b) per phase is:

$$\text{Power input} = \mathrm{Re}(s\overline{Z}_{in})I^2 \quad \text{Watts} \tag{5}$$

and the force produced per phase is then

$$\text{Force} = \mathrm{Re}(s\overline{Z}_{in})I^2 / sV_s \tag{6}$$

$$= \mathrm{Re}(\overline{Z}_{in})I^2 / V_s \quad \text{Newtons} \tag{7}$$

Where:

I is the input current to the equivalent circuit in amperes

$\mathrm{Re}(Z_{in})$ is the real part of the secondary impedance calculated from the equivalent circuit at slip s and frequency f, in Ohms

$\mathrm{Re}(sZ_{in})$ is the real part of the secondary impedance calculated from the standstill equivalent circuit fed with a frequency sf, in Ohms

It can be deduced from equations (4) & (7) that taking results from standstill tests at frequency sf gives the same force as those produced by the same machine at a slip s.

One limitation on this method is that it does not take into account end effects. Care must be taken to ensure that this is accounted for when using the method at high frequencies and small slips.

4. Concentrated Windings

4.1 Introduction

The main focus of development in the thesis is into the use of planar concentrated windings with induction machines, particularly linear induction machines. These types of windings are commonly used only with permanent magnet rotor type machines.

The planar concentrated winding has only a single layer of coils, which can be connected together in a variety of ways. As will be developed later, concentrated windings have two principal flux harmonics travelling in opposite directions relative to one another. Note that harmonics may be referred to as positive and negative. This is no reference to their effects on the system, but rather to their direction of travel relative to one another. The method used to describe the winding pattern of concentrated windings within this document therefore refers firstly to the number of coils in the basic winding, then to the number of poles for the two principal harmonics. For example, shown below Fig. 19 is a 6 coil 4-8 pole, so named as its 6 coil configuration produces both 4 and 8 pole flux harmonic waves. It may be observed that the winding pattern repeats after 3 coils, and in fact the basic unit of this winding is 3 coil 2-4 pole.

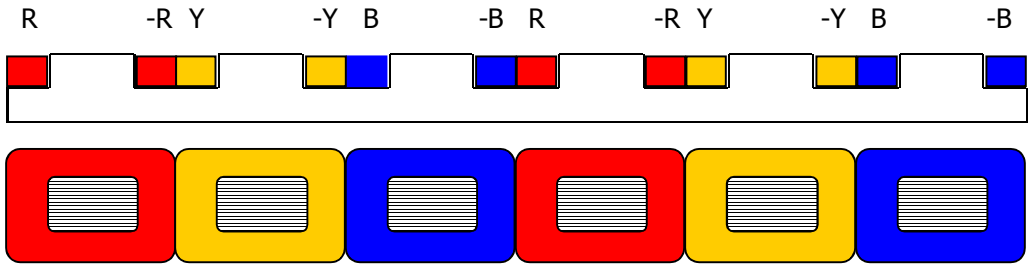

Fig. 19. A 6 coil 4-8 pole concentrated winding

Many other forms of connection are known [13][14][15]. Three basic winding configurations were chosen for development in this project, chosen principally due to their low pole numbers (4-14 pole) and their relatively high winding

factors. The first is the 3 coil 2-4 pole type described above. The next is the 9 coil 8-10 pole type shown in Fig. 20.

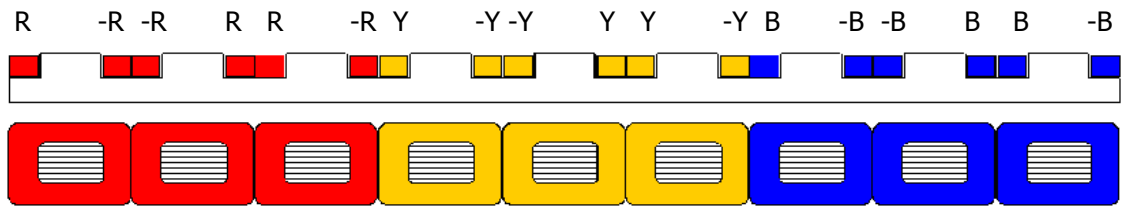

Fig. 20. A 9 coil 8-10 pole concentrated winding

The third winding under consideration is the 12 coil 10-14 pole winding shown in Fig. 21. An important feature of this winding is that while rotary machines operate with an even number of poles, short stator linear machines are not required to produce an even number of poles as the opposite ends of the winding are not adjacent. Therefore, the first half of this winding can be used alone in order to produce a 6 coil 5-7 pole machine for short stator operation as in Fig. 22.

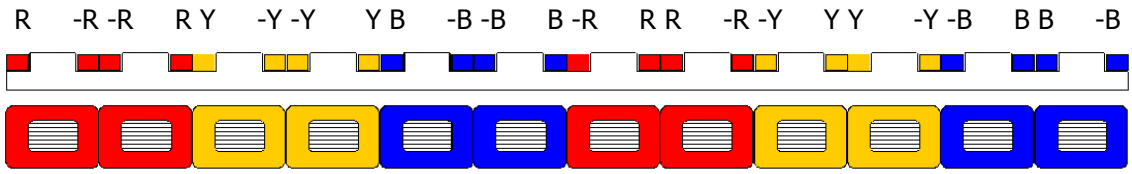

Fig. 21. A 12 coil 10-14 pole concentrated winding

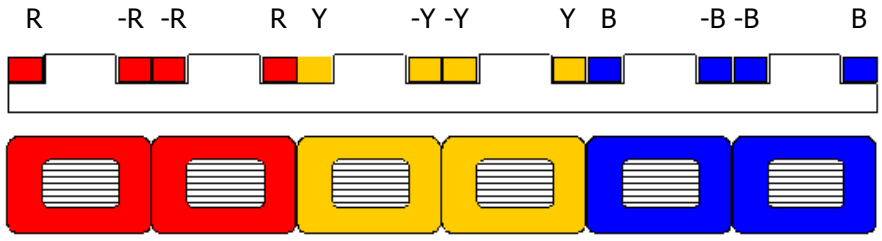

Fig. 22. A 6 coil 5-7 pole concentrated winding

A standard two layer winding is shown for reference in Fig. 23. This configuration is commonly used in linear induction machines.

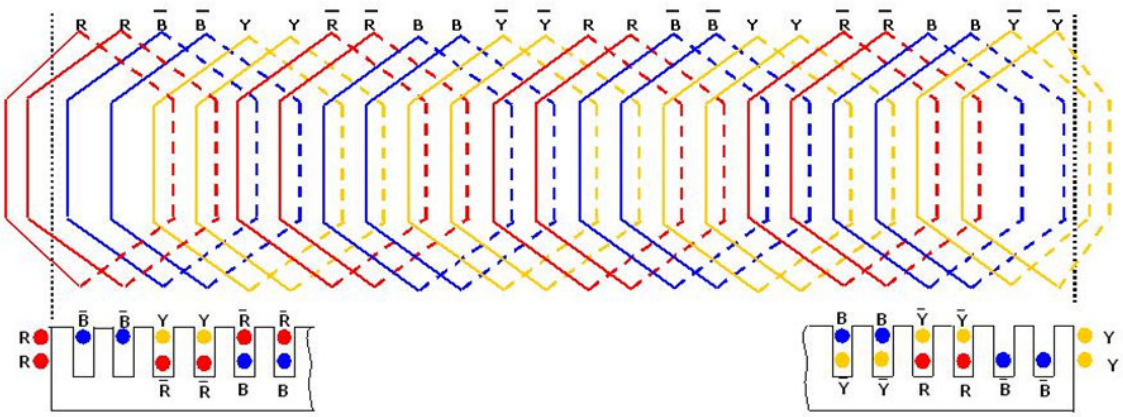

Fig. 23. A standard 2 layer winding

There are several key advantages that may be gained through the use of concentrated windings.

- No coil overlap is present at the sides of the machine which allows a larger active pole width for a given total machine width.
- If open slots are used the coils can be totally pre-formed into simple shapes and easily inserted in the slots, simplifying construction. Double-layer windings may also be pre-formed, however this adds significantly to the complexity of construction as the pre-formed double layer coils must be bent into a specific shape in order to interlock.
- The winding produces no difficulties at the ends of the machine as every slot is filled and there are no coil sides protruding beyond the end of the core. This is very significant, as if a long-stator assembly is required, this can be created by simply butting up several concentrated winding linear motors to give a truly continuous stator. This type of layout is advantageous for launcher systems.
- Because of the regular shape of the coils and their ability to be pre-formed, concentrated winding linear motors can be created with packing factors much higher than available in conventional linear motors. This means that more copper can be packed into a slot to produce higher thrusts, or thrust levels can be produced with a better thermal rating.

- The end turn of a concentrated winding can be significantly reduced, as pre-formed coils can be built to smaller tolerances and tighter bend angles than are possible with current production methods. Preformed two layer coils will generally have a much larger end turn than concentrated coils.
- The simplest component, an individual coil around a tooth has the potential to be mass produced and connected together to form a variety of different stator types.

4.2. End Turn Leakage Reactance

To investigate the performance of the concentrated windings, 2D Finite Element modelling will be used. In order to successfully model the electrical characteristics of a stator in 2D FE, several extra factors need to be used to compensate for winding resistance, end turn leakage reactance and rotor current paths.

The winding resistance is simple to calculate using the number of turns per coil, number of coils per phase, copper resistivity, coil dimensions and copper cross sectional area.

The rotor current paths can still be modelled by applying the Russell and Norsworthy factor [10] to the rotor resistivity. This factor compensates for the full rotor current path length including current loops in the end regions of the plate as shown in Fig. 3.

The factor that presented significant issues was the end winding leakage reactance, as the established equations for two layer windings will be unable to model the planar concentrated cases accurately. A study was made of the end turn leakage reactance of concentrated winding linear motors.

4.2.1. Equations

First, the current equations for the modelling of end turn reactance were studied. Various methods were investigated, including those of Hendershot & Miller [16], Grover [17] and Liwschitz-Garik [18]. The common method employed in developing these equations neglects the presence of core iron and simplifies the racetrack shaped coil structure to that of an oval or circle composed purely of the end windings as in Fig. 24. This circular end winding section is then solved using conventional inductance formulae.

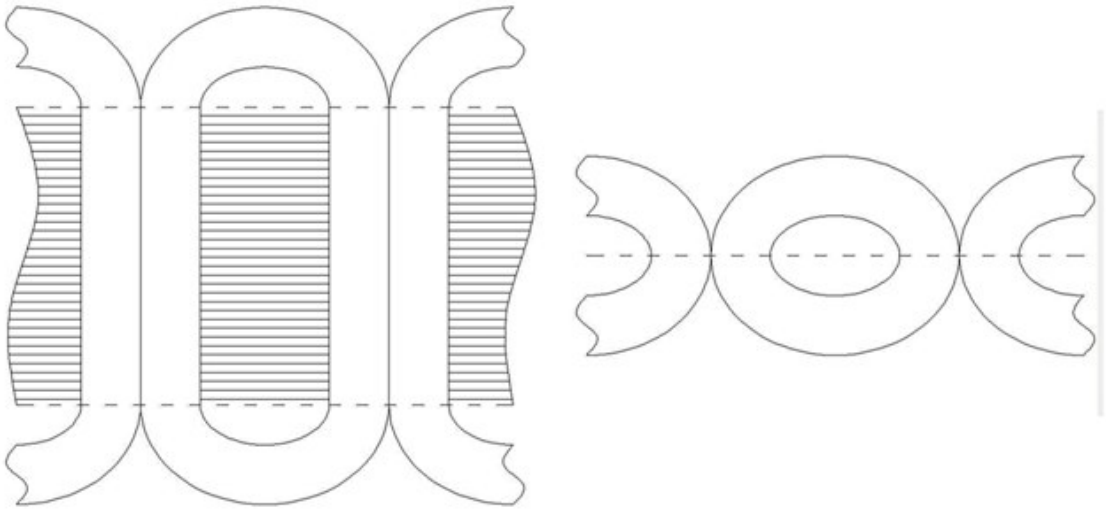

Fig. 24. Simplification of concentrated coil to a circular or oval coil made up of the end sections

Application of the equation methods to concentrated coil machines showed significant differences between methods. A critical issue is that many of the equation based methods do not take into account the presence and effects of core iron, where it is known [19][20] that the presence of core iron does make a significant difference to the accuracy of end turn leakage reactance modelling.

4.2.2. Air Cored 3D FE Modelling

To further investigate the performance of the conventional methods, the end turn leakage reactance of a concentrated winding track was modelled using an air-cored 3-coil set in 3D Mega FE, with dimensions based on a model developed for testing.

The modelling process was relatively straightforward. First, a 3D cube of air was created, and meshed with a relatively coarse mesh. Next, the coils were created using the 3D coil making tools available in Mega FE. These coils were designed to the same dimensions as were used in an experimental model Fig. 25.

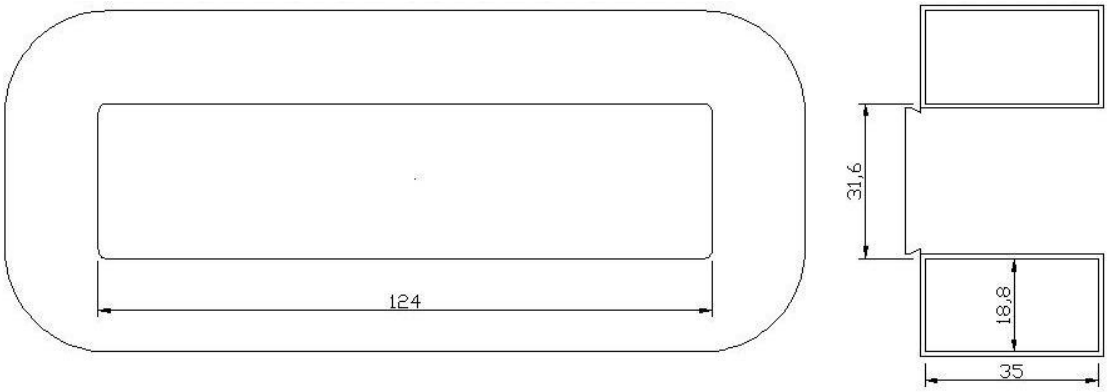

Fig. 25. Coil dimensions used in model

The coils were modelled with the end winding of one end projecting into and merged with the 3D cube of air. This was to discount any effects in the system other than those of the end winding. This model can be seen in Fig. 26. The red bars indicate the extents of the air region. The top and bottom faces of the cube of air were given a zero flux condition. The front of the air cube was a normal flux boundary while the back (cut by the coils) was a tangential flux boundary.

Two versions of the model were set up. Firstly, a periodic boundary version of the model was set up in order to model the continuous nature of a track of concentrated windings. This boundary was set on either end of the three-coil

segment shown in Fig. 26. In an alternative model, the air section was expanded at either end of the 3 coil set and the end boundaries were set to zero flux condition (without a periodic boundary) in order to represent a single 3 coil stator.

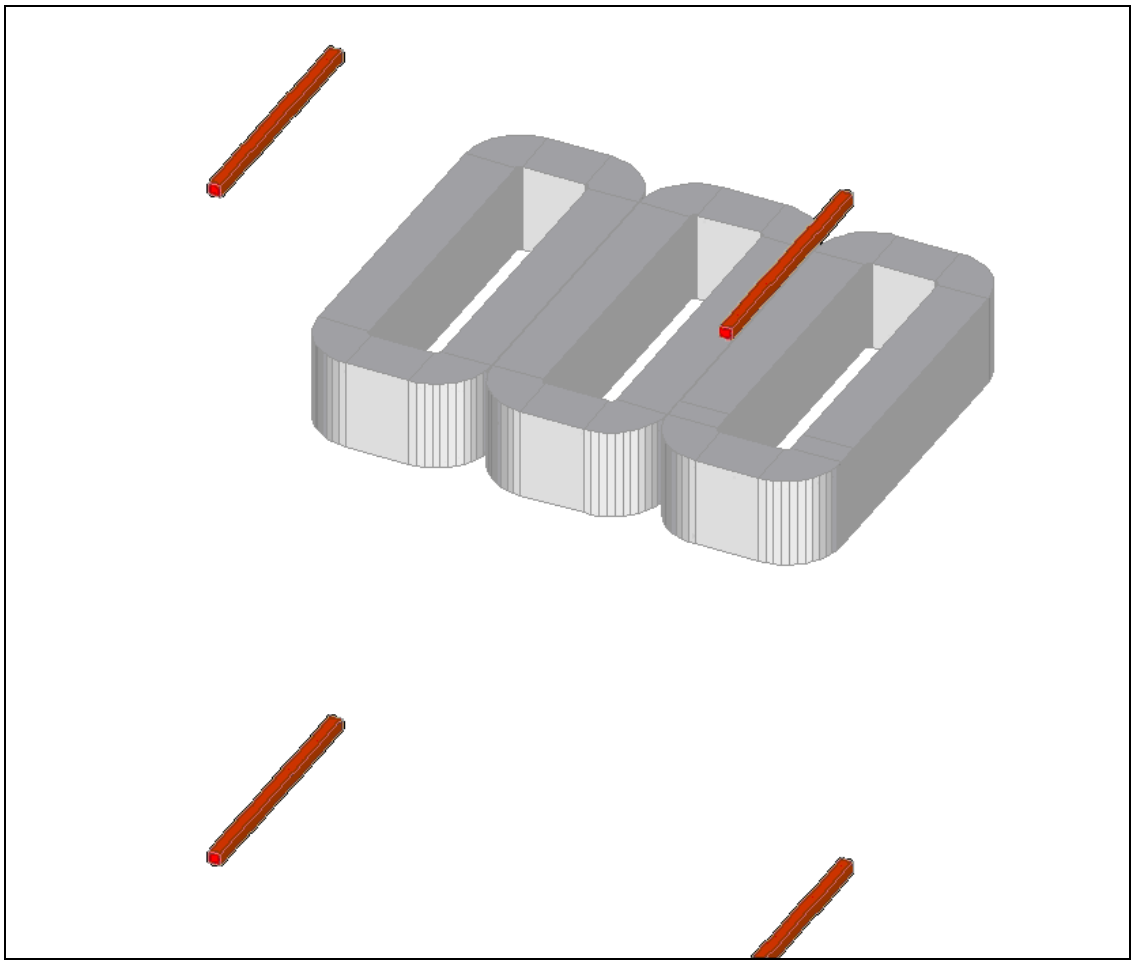

Fig. 26. 3D coils generated in Finite Element

The system was current fed with a 3-phase supply, 120° between phases. The current value was 1A per phase, and the phase resistance was zero. The induced emf across each coil was calculated, with and without a periodic boundary. The results are shown in Table 1 (E_1 is the center coil, E_2 & E_3 are the two outer coils).

Table 1: Induced emf's in air cored coils

With Periodic Boundary			Without Periodic Boundary		
E_1	E_2	E_3	E_1	E_2	E_3
.245	.250	.250	.245	.229	.229

In the model with periodic boundaries (continuous track), the induced emf's of the three coils were very close to one another, as would be expected in a continuous track of identical coils. The slight differences between the three results are due to meshing artefacts within the model.

In the model without periodic boundaries, the center coil emf is the same as in the continuous track, but the end coils are significantly different due to the non continuous nature of the track.

If we were representing this specific set up, with a single 3 coil 2-pole motor, the model without a periodic boundary would be the best to use. The model with the periodic boundary corresponds to an infinitely long machine taking balanced currents. This is the best model to use in order to represent a continuous track of coils, which is a layout advantageous for transport or launch machines.

The following algebraic method was developed to find the apparent inductance including the effects of mutual inductance of the end turn from the results above. The coils in the model were taken to be zero resistance.

$$E_1 = j\omega I_1 M_{11} + j\omega I_2 M_{12} + j\omega I_3 M_{13}$$
$$E_2 = j\omega I_1 M_{21} + j\omega I_2 M_{22} + j\omega I_3 M_{23}$$
$$E_3 = j\omega I_1 M_{31} + j\omega I_2 M_{32} + j\omega I_3 M_{33} \quad (8)$$

Where:

E_X is the induced emf in coil x, I_X is the applied current in coil x, M_{XX} is the self-inductance of coil x and M_{XY} is the mutual inductance of coils x and y.

For the infinite track condition, the three coils are identical, and so the problem may be simplified.

$$M_{11} = M_{22} = M_{33} = S$$
$$M_{12} = M_{13} = M_{21} = M_{23} = M_{31} = M_{32} = M \quad (9)$$

The self-inductances of the three coils are all equal, and are all replaced with S. The mutual inductances are also equal and are replaced with M.

$$I_2 = I_1 \angle 120$$
$$I_3 = I_1 \angle 240$$
$$E_2 = E_1 \angle 120$$
$$E_3 = E_1 \angle 240 \quad (10)$$

The currents and emf's in the three coils are equal but at 120° from each other. This gives

$$E_1 = j\omega I_1 S + j\omega I_1 \angle 120\, M + j\omega I_1 \angle 240\, M$$
$$E_2 = E_1 \angle 120 = j\omega I_1 M + j\omega I_1 \angle 120\, S + j\omega I_1 \angle 240\, M$$
$$E_3 = E_1 \angle 240 = j\omega I_1 M + j\omega I_1 \angle 120\, M + j\omega I_1 \angle 240\, S \quad (11)$$

$$E_1 = j\omega I_1 S + j\omega I_1 M\, e^{-j\frac{2\pi}{3}} + j\omega I_1 M\, e^{-j\frac{4\pi}{3}} \quad (12)$$

$$E_1 = j\omega I_1 \left(S + M\, e^{-j\frac{2\pi}{3}} + M\, e^{-j\frac{4\pi}{3}} \right) \quad (13)$$

Using $e^{-j\theta} = \cos\theta - j\sin\theta$

$$E_1 = j\omega I_1\left(S + M\left(\cos\frac{2\pi}{3} - j\sin\frac{2\pi}{3} + \cos\frac{4\pi}{3} - j\sin\frac{4\pi}{3}\right)\right) \quad (14)$$

$$E_1 = j\omega I_1\left(S + M\left(-0.5 - j0.866 - 0.5 + j0.866\right)\right) \quad (15)$$

$$E_1 = j\omega I_1\left(S - M\right) \quad (16)$$

$$L = \left(S - M\right) = \frac{E_1}{j\omega I_1} \quad (17)$$

Where:

(S-M) is equal to L, the total apparent inductance of the end turns including the mutual inductances. This is often referred to as 'the end winding inductance' in the literature. ω is the angular frequency of the supply.

The values recorded in Table 1 may now be used with (17) to calculate the end turn leakage reactance X_E.

$$X_E = j\omega L = \frac{E_1}{I_1} \quad (18)$$

As I_1 = 1A

$$X_E = \frac{E_1}{I_1} = \frac{E_1}{1} = E_1 \quad (19)$$

The basic 4-pole concentrated winding motor contains two coils in series per phase, and so the value must be doubled.

For the repeating track representation using a periodic boundary

V = (.245190 + .249676 + .249709) / 3 = 0.248V (average V)

X_E = 2*0.248 = 0.496Ω

For the single motor representation without a periodic boundary, the equation for infinite coils is still used as the influence of the ends of the machine is reduced by the use of a full 6 coil machine, rather than a 3 coil set.

V = (.245192 + .228605 + .228657) / 3 = 0.234V (average V)

$X_E = 2*0.234 = 0.468\Omega$

The value of end turn reactance can be critical to the accurate prediction of linear machine performance. Therefore, a further method was sought to provide another value of end turn leakage reactance.

The values of end turn leakage reactance calculated in this section are compared to those from other methods in section 4.2.6, results comparison.

4.2.3. Full 3D Finite Element Multiple Core Modelling

3D Finite element modelling using the MEGA package was performed to accurately model the end turn inductance of the concentrated coils. A method of calculating end turn inductance was employed using several full 3D stator models of varying core widths [21][22][23] Fig. 27. For convenience these were linear in form.

The difference between this modelling and the modelling in 4.2.2. is the presence of core iron in the model. In the previous section, the air cored modelling method removed the core iron altogether, as shown in Fig. 24.

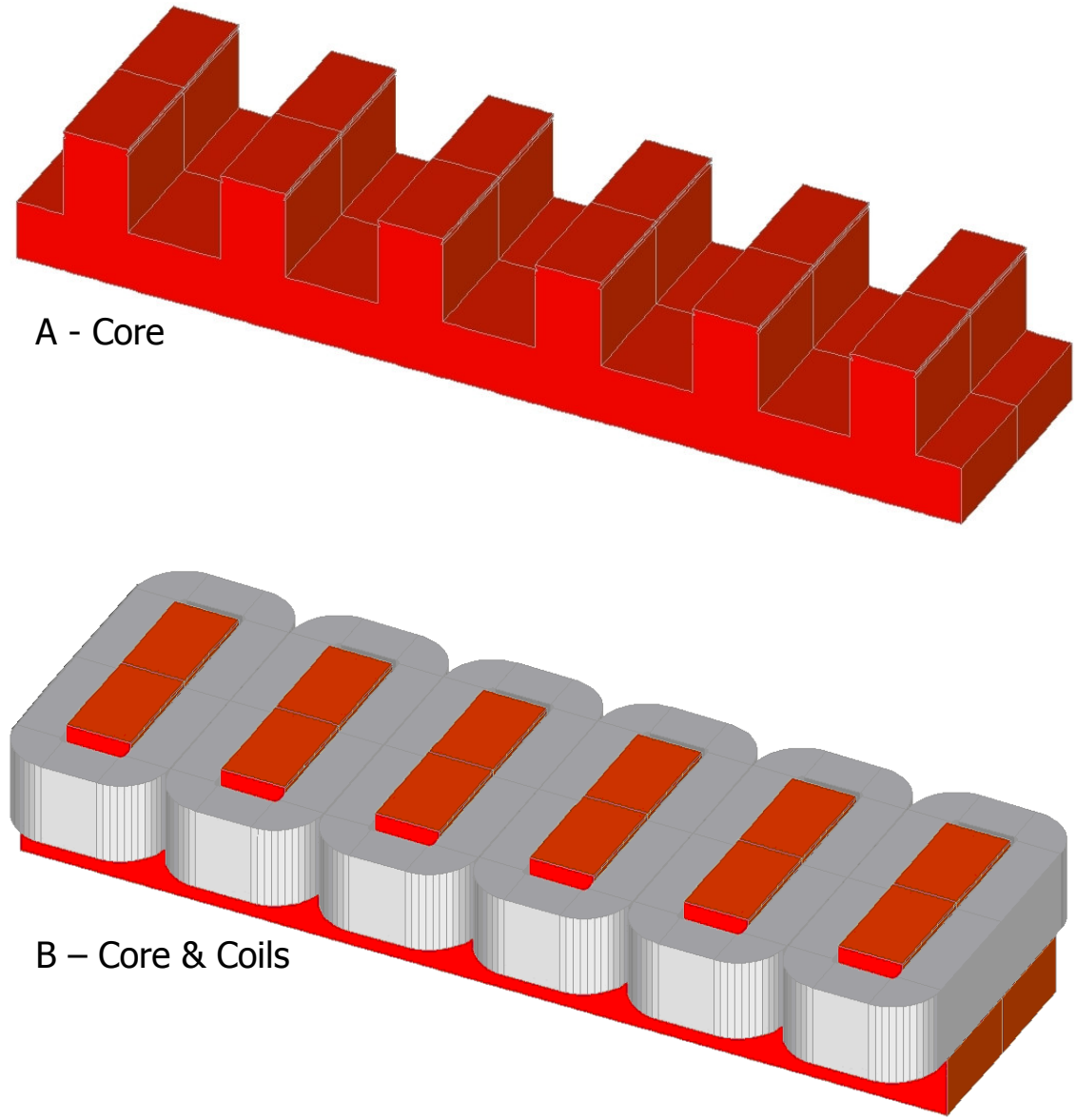

Fig. 27. A 3D FE model of a concentrated winding stator (A – Core, B - Core & Coils)

The modelling process was relatively straightforward. First, the dimensions from the original model were adapted to suit the requirements of 3D modelling. A 2D base plane was created, and then extended to make the core. More air was added onto the sides of the core to represent the air around the end windings. Next the coils were created, using the same dimensions as in the simple air cored coil case and the initial model.

In this case, Mega was instructed to model the whole motor from only one symmetrical half. This is because there is a plane of symmetry along the middle

of the active face of the motor core. This model can be seen below in Fig. 28. Blue bars indicate the extents of the air region, the red region is the core (non linear iron with a BH curve based on mild steel) and the grey regions represent the coils.

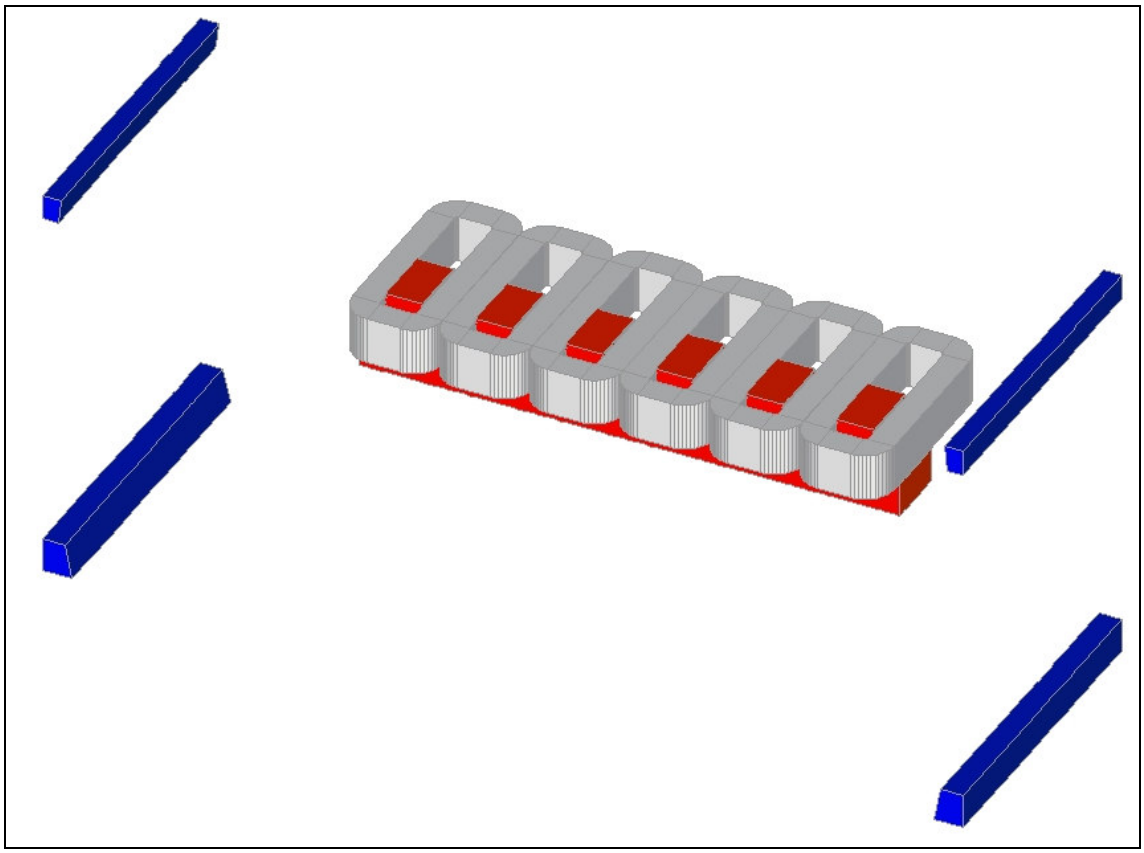

Fig. 28. 3D FE model generated in Mega

The top and bottom faces of the cube of air were given a zero flux condition. The front of the air cube was a normal flux boundary while the back (the plane of symmetry) was a tangential flux boundary. A periodic boundary version of the model was set up in order to model a continuous track of these motor types. This boundary was set on either end of the six-coil segment. A further model was set up with air regions at either end of the model to represent a 6 coil stator working in isolation.

The stator inductance calculated from the terminals comprises several parts including end turn leakage, slot leakage and magnetising inductance

components. It can be shown that whereas all other inductance components are directly proportional to core width, end turn leakage inductance is constant [21]. Therefore, if the terminal inductances of several otherwise identical machines of varying core width are plotted, referring this plot to zero core width will yield a value for end turn leakage inductance per coil.

The system was voltage fed with a 3 phase 50Hz supply, 120° between phases, with current levels such as to avoid saturation of the iron regions. This allowed the model to take into account mutual inductance effects between the end turns of the coils, as well as self inductance effects.

The voltage values were varied between motors. The phase resistances also varied between motors, these were based on previous calculation Table 2.

Table 2: Applied voltages for various core width 3DFE models

Core width mm	Phase resistance	Applied peak voltage
10	0.492Ω	90V
50	0.673Ω	120V
100	0.902Ω	225V

The currents generated in each phase were within 0.2% of each other in the periodic case and within 4% in the non-periodic case, allowing only one phase value to be used. The current generated across the red phase of each motor was calculated, with and without the periodic boundary. The results of this are shown in Table 3.

Table 3: Phase currents calculated from 3DFE modelling

Core width mm	Red phase rms current with Periodic Boundary	Red phase rms current without Periodic Boundary
10	68.54A	70.00A
50	48.62A	32.80A
100	58.43A	47.50A

These models are aimed to represent a real set of motors being built, and the non-periodic boundary results may be closer to this. However, for the general case of a track consisting of many of these motors, the periodic boundary case will be the more accurate.

From the results for Voltage V and Current I above, overall impedance Z can be calculated.

$$Z = V / I \tag{20}$$

As impedance and resistance R are now known, reactance X can be calculated.

$$X = \sqrt{(Z^2 - R^2)} \tag{21}$$

Using formulas (20) & (21) with the values for current, voltage and resistance the reactances per phase can now be calculated, and are shown in Table 4 and plotted in Fig. 29.

Table 4: Reactance per phase values for stators of various core widths

Core width mm	Reactance per phase with periodic boundary	Reactance per phase without periodic boundary
10	1.22Ω	1.18Ω
50	2.37Ω	2.28Ω
100	3.74Ω	3.57Ω

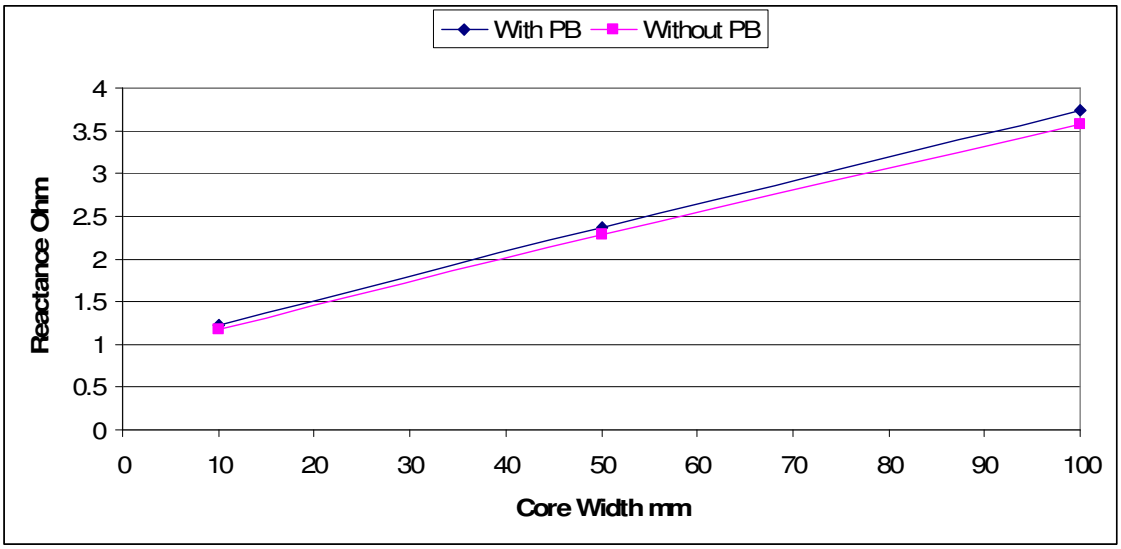

Fig. 29. 3D FE Reactance against core width with and without a periodic boundary

It can be seen that this plot is reasonably linear, and will give a non-zero value of reactance at zero core width. This further confirms the method of referring back to zero core width. Using this linearity, we can use the following trigonometry in Fig. 30 to find the value of X at zero core width.

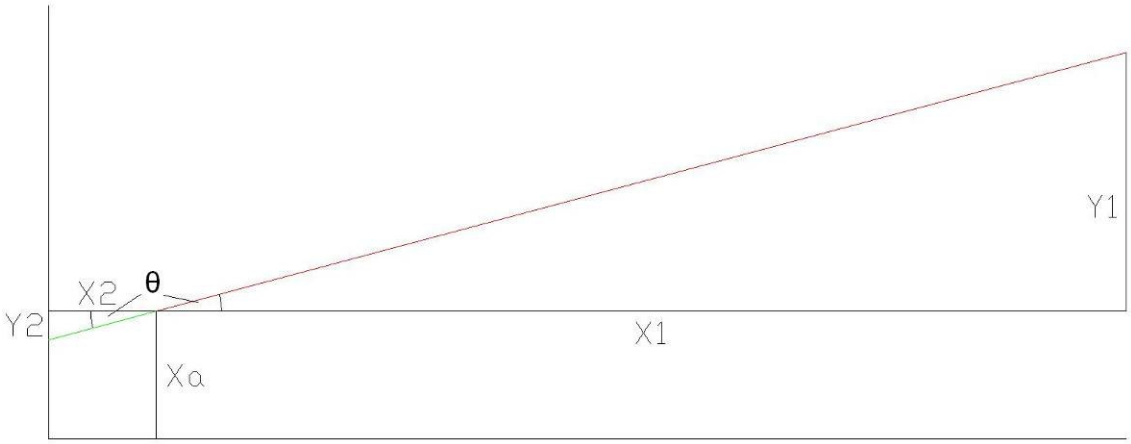

Fig. 30. Geometry of the Xe problem

If the red line represents our straight line, it can be seen that X1 and Y1 can be easily found, by taking the lowest values of reactance and core width from the highest. With these values, we can calculate theta

$$\theta = \tan^{-1}(Y1/X1) \qquad (22)$$

And X2 is equal to the lowest value of core width. Therefore

$$X2 \tan \theta = Y2 \quad (23)$$

And reactance at zero core width = Xa-Y2 where Xa is the reactance of the narrowest core.

Now, taking Xs and Ws as reactance and core width of the narrowest motor, and X_L and W_L as the reactance and core width of the widest motor. X_E is the reactance of the zero width motor, and is also the end turn leakage reactance.

$$X_E = Xs - (Ws \tan \theta) \quad (24)$$

$$X_E = Xs - (Ws ((X_L - X_S) / (W_L - W_S))) \quad (25)$$

And so we can calculate values for the end turn leakage reactance per phase of both cases.

As shown earlier, only half of the motor was modelled along a plane of symmetry. Therefore, the values above must be doubled in order to give values for the full motor.

For the continuous stator case, with a periodic boundary
$X_E = 0.940 \times 2 = 1.880\Omega$

For the single stator case, without a periodic boundary
$X_E = 0.914 \times 2 = 1.828\Omega$

The values of end turn leakage reactance calculated in this section are compared to those from other methods in section 4.2.6, results comparison.

4.2.4. Experimental Prototype Machine Multiple Core Modelling

The 3 core method and its results have been validated experimentally, by constructing 3 otherwise identical machines of reducing core width with identical end turn dimensions Fig. 31 and referring to zero core width [21][22][23].

Fig. 31. Experimental concentrated winding linear machines of varying core width

The motors were constructed with 10mm, 50mm and 100mm core widths. The cores were built from mild steel laminations laser cut to the correct dimensions and clamped together with aluminium angles. The 100mm core width stator was also tested with wooden clamps in place of aluminium angles, in order to confirm that the presence of the aluminium had no significant effect on stator behaviour. The coils were inserted and connected into a 3 phase, two-coil per phase arrangement with the phases connected together in a star point at one end.

The motors were powered using a 50Hz variable voltage power supply feeding the motor through a three-phase power analyser. The motors were tested without secondary plate or iron at various supply currents and the current, voltage and power in each phase was recorded. The phase resistance was measured using a resistance bridge.

The measured values were converted to per phase values where necessary. Reactance was calculated using (20) & (21).

The results of the testing and the values derived from these results are shown in Table 5 with measured results highlighted.

Table 5: Experimental results for stators of various core width

Current	Core Width	Voltage	V/phase	I/phase	Input power	P/phase	R	Z	X
A	mm	V	V	A	W	W	Ohm	Ohm	Ohm
1	100	12.973	7.490	1.011	3.246	1.082	0.802	7.410	7.366
1	50	9.010	5.202	1.027	2.757	0.919	0.603	5.066	5.030
1	10	4.663	2.692	1.018	1.958	0.653	0.420	2.645	2.612
5	100	65.390	37.753	5.027	77.800	25.933	0.802	7.510	7.467
5	50	42.910	24.774	4.978	59.060	19.687	0.603	4.977	4.940
5	10	22.340	12.898	5.019	46.890	15.630	0.420	2.570	2.535
8	100	103.850	59.958	7.986	194.820	64.940	0.802	7.508	7.465
8	50	69.090	39.889	8.039	152.030	50.677	0.603	4.962	4.925
8	10	35.390	20.432	7.953	115.590	38.530	0.420	2.569	2.535
10	100	130.040	75.079	10.020	306.600	102.200	0.802	7.493	7.450
10	50	84.420	48.740	10.007	232.600	77.533	0.603	4.871	4.833
10	10	45.800	26.443	9.996	173.720	57.907	0.420	2.645	2.612
12	100	156.560	90.390	12.061	441.900	147.300	0.802	7.494	7.451
12	50	102.930	59.427	12.005	338.800	112.933	0.603	4.950	4.913
12	10	53.230	30.732	12.055	265.800	88.600	0.420	2.549	2.515
15	100	194.360	112.214	14.989	687.700	229.233	0.802	7.486	7.443
15	50	128.660	74.282	14.995	535.000	178.333	0.603	4.954	4.917
15	10	64.540	37.262	15.044	415.000	138.333	0.420	2.477	2.441
20	100	259.600	149.880	20.040	1246.500	415.500	0.802	7.479	7.436
20	50	172.370	99.518	20.040	990.200	330.067	0.603	4.966	4.929
20	10	79.730	46.032	20.020	728.500	242.833	0.420	2.299	2.261
27	100	343.000	198.031	27.010	2294.000	764.667	0.802	7.332	7.288
27	50	227.000	131.059	27.090	1803.000	601.000	0.603	4.838	4.800
27	10	96.470	55.697	26.820	1335.700	445.233	0.420	2.077	2.034

The values of X against core width were then plotted against width of motor for each supply current in Fig. 32.

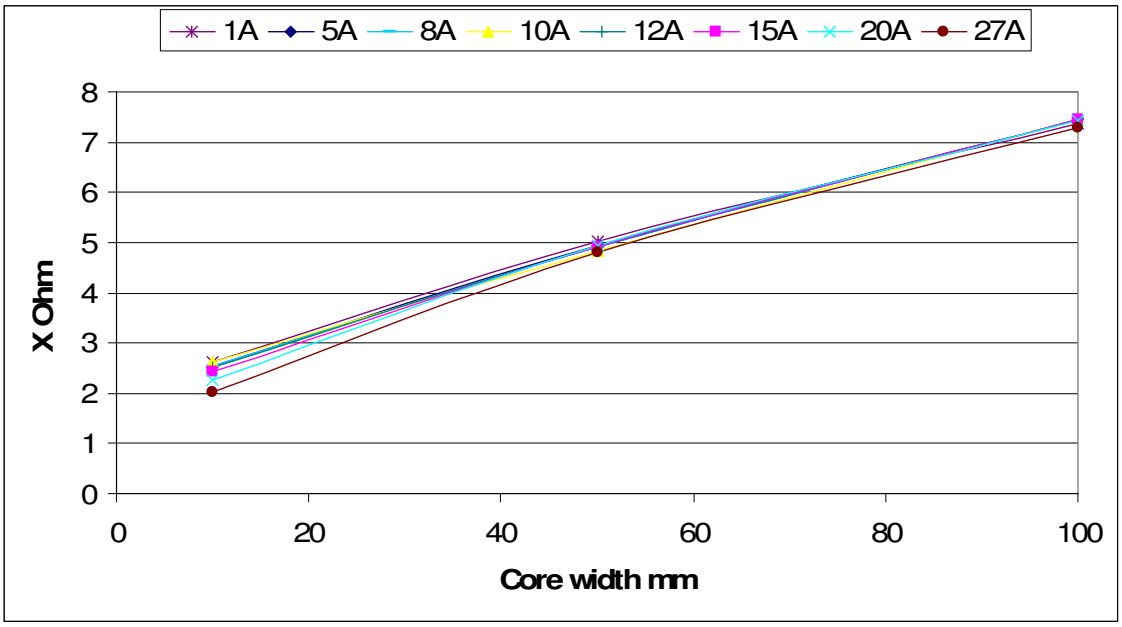

Fig. 32. Reactance and core width plots for each test current

It can be seen that the line profile changes quite significantly at higher currents. Investigation of the core flux using search coils and finite element study revealed that saturation of the core was occurring in the 10mm motor, causing a drop in X.

This effect can be seen more clearly in the 20&27A cases in Fig. 33.

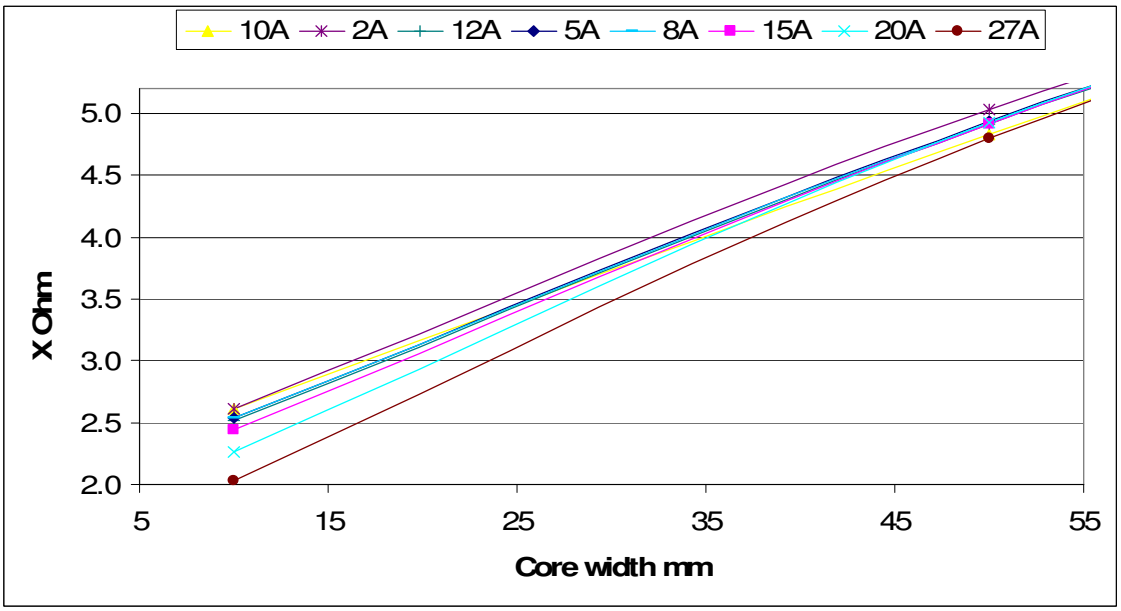

Fig. 33. Expanded plot, showing a drop in X at 20 & 27A for the 10mm core

For a normal motor, X is made up of a combination of reactances from slot leakage, air gap leakage, end turn leakage and magnetising reactance.
Slot leakage, air gap leakage and magnetising reactance are all dependant on core width. This means that the reactance value at zero core width will ignore these components and simply give the end turn leakage reactance of the concentrated winding.

From Fig. 32 trend lines were fitted to find the intercept value when the core width equals zero. This value of X will represent the end turn leakage reactance of the motor. These values of end turn leakage reactance are shown in Table 6.

Table 6: Experimentally derived end turn leakage reactance values

Current A	1	5	8	10	12	15
XE Ω	2.198	2.068	2.062	2.101	2.043	1.981

As can be seen, the end turn leakage reactance of the prototype motor remained relatively stable over a range of applied current levels, as long as saturation did not occur. The average end turn leakage reactance value was 2.076Ω. These results are again compared to other methods in 4.2.6.

4.2.5. Air Cored Prototype Machine Modelling

To confirm the results of the air cored modelling method, further experiments were undertaken. A variant of the 3 core method used above was employed, as the method remains valid regardless of the presence or absence of a physical core. The core width represents the width of the coil not including the end turns, and can still be referred to zero.

The preformed coils were carefully removed from the 3 core width prototype machines and secured together in the same 6 coil 3 phase configuration. The coils were supplied with 50Hz 3 phase voltages, and the currents in the sets were then measured in order to obtain values of reactance for each core width.

The air cored coil value at zero core width was then obtained. The results of the tests can be seen in Table 7 and are plotted in Fig. 34.

Table 7: Experimental results for air cored coils of various core width

Core Width	Current	Voltage	Resistance	Impedance	Reactance	Avg Reactance
mm	Amps	Volts	Ohm	Ohm	Ohm	Ohm
100	5.386	4.869	0.413	0.90	0.80	0.80
100	9.869	8.773	0.413	0.89	0.79	
50	5.336	3.467	0.31	0.65	0.57	0.57
50	10.146	6.654	0.31	0.66	0.58	
10	4.943	1.9945	0.221	0.40	0.34	0.34
10	10.312	4.157	0.221	0.40	0.34	

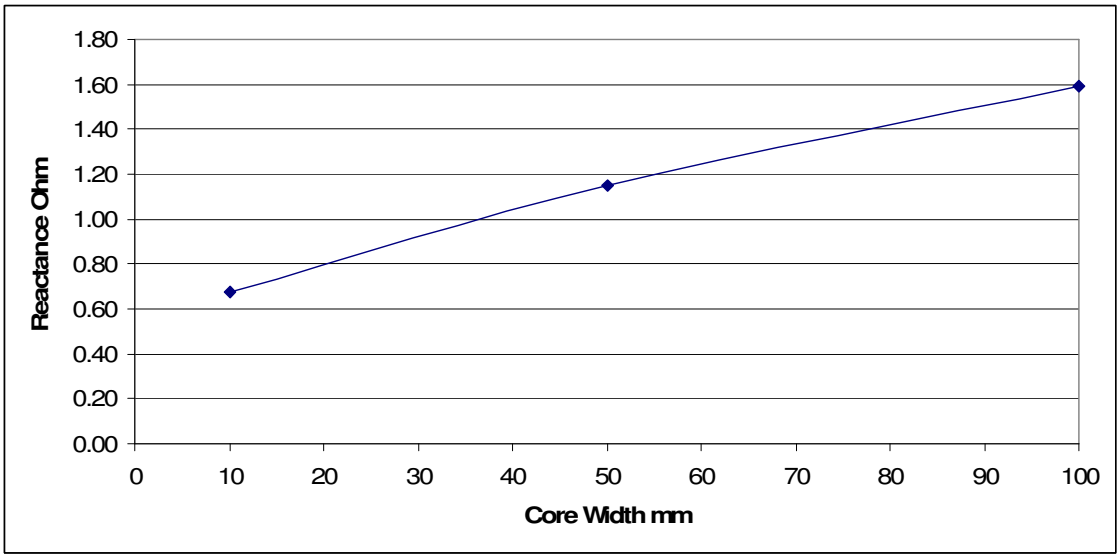

Fig. 34. Air cored coil reactances

Curve fitting gave an end turn leakage reactance value of 0.540 Ohm for this method.

4.2.6. Results Comparison

The results of all four methods for calculating end turn leakage inductance have been plotted below in Fig. 35.

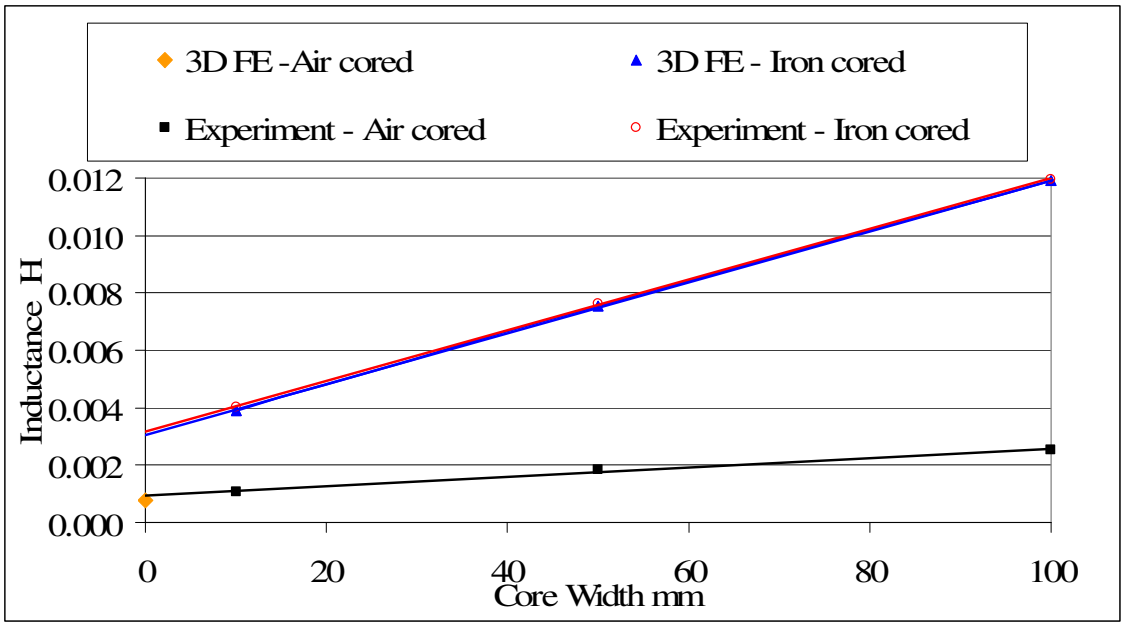

Fig. 35. Inductance calculations from the various methods

From the above results, it can be seen that the iron cored stator model 3D FE and the iron cored stator experimental results tie up very closely with one another. The inductances for each core width model are very close, within 3% and the calculated values of end turn leakage reactance vary by 4% between FE and experiment.

Further, the air cored coil experimental results tie up with the 3D FE end turn modelling, with FE calculated values of end turn leakage reactance within 17% of experimental results.

Looking at the results above, it is obvious that there is a significant difference in end turn leakage reactance predictions, dependant on the use of air or iron cored modelling methods [19][20]. Methods based on air cored coil modelling such as the simple analytical method described in 4.2.1. make insufficient allowances for the presence of core iron, where this has been shown

experimentally to have a significant effect on the calculated end turn inductance.

A further confirmation of the need for an end turn inductance model that takes iron into account is shown in Fig. 36. This shows the performance curve of a voltage fed machine modelled in 2D finite elements firstly using iron cored models to predict end turn inductance, then using a value of end turn inductance based on the simple air cored coil method. Finally, both methods are compared to experimental results taken using a standstill variable frequency method [12].

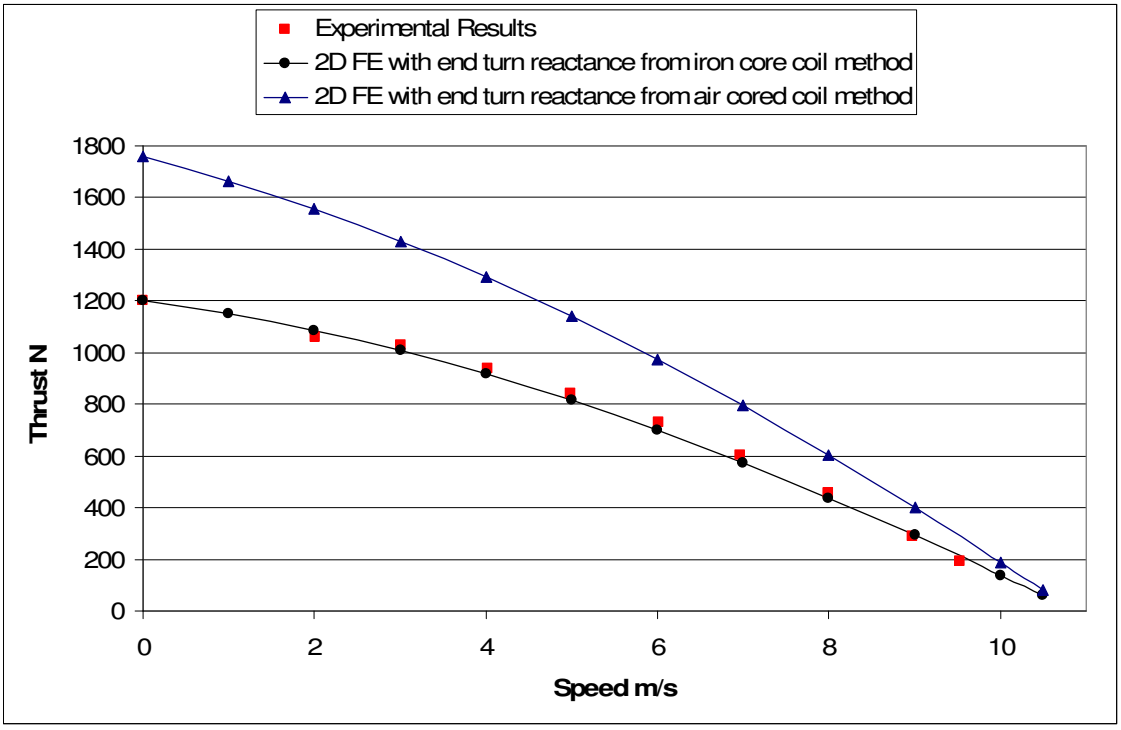

Fig. 36. Force Speed curve showing experimental and 2D finite element results

It is apparent that the iron cored inductance method based model is predicting very accurately, while the method based on air cored models has caused a significant error in machine performance calculations.

It must be noted that although in this case the end turn inductance makes a significant difference to the overall results, the end turn inductance in terms of

overall inductance is relatively large in this type of linear machine, due to the relatively narrow (100mm) core width. In machines of greater core width, other inductances become dominant and the effect of errors in end turn inductance is much less apparent.

For example, for the machine of Fig. 36 with a 100mm core width the error in stall thrust due to an incorrect end turn inductance value is 46%. With a 500mm core width the stall thrust error in the same machine due to incorrect end turn inductance is now only 10%.

4.2.7. Simple Method of End Turn Leakage Inductance Calculation

The work above has established the need for prediction methods that account for the presence of the iron core. However these methods currently require the construction of several full 3D FE models, which take a significant amount of time both to construct and solve. With a static 3D FE problem using a non-linear iron representation, FE model programming time is approximately 2 hours, whilst solve time is around 1 day. This is largely due to the high number of elements required in a 3D model, as a 3D model typically uses 20 or more times the elements required in a 2D model.

A simpler method has been developed that markedly reduces the time taken to work out end turn inductance of a machine [24].

3D Finite Element models and prototype models are able to accurately model the full concentrated winding stator performance, including coil end turn leakage reactance.

A 2D FE model can accurately model per metre depth all stator characteristics whose parameters can be described in two dimensions. These are essentially a slice through the motor, taking the X axis as the direction of motion and the Y axis as a plane taken from behind the stator through the stator and rotor. A 2D

FE model is able to account for all stator inductance effects, with the exception of end turn leakage inductance, which is totally neglected by this method unless added as an external circuit component.

Therefore, if a 2D FE model is produced based on the characteristics of a 3D FE model or experimental machine, the difference in inductance between the 2D and 3D or experimental results must be due largely due to end turn leakage reactance. This can be calculated simply by working out the difference in calculated stator inductance between the 2D and 3D FE models.

To prove the effectiveness of this modelling method several test cases over a wide range of configurations were modelled firstly using multiple 3D models, and then using the 2D-3D method described above. This will allow the determination of the accuracy of the 2D-3D method compared to the full 3D method. The cases were:

Case A: Coil pitch 80mm, coil width 20mm & coil depth 40mm
Case B: Coil pitch 160mm, coil width 60mm & coil depth 30mm
Case C: Coil pitch 240mm, coil width 105mm & coil depth 50mm

All cases were 3 coil 2 pole windings voltage sourced at 10Vrms 50Hz, with 100 turns per coil and 2 coils per phase. All three cases used a 100mm wide core. The output current for each stator was calculated, and used to obtain input impedance Z. The reactance of the model X can be found simply using (21). The results for the 2D and 3D models are shown in Table 8.

Table 8: Table of impedances for 2D & 3D FE models

Case	Dimensions			2D 100mm				3D 100mm			
	Pitch mm	Width mm	Depth mm	R1 Ohm	I A	Z Ohm	X Ohm	R1 Ohm	I A	Z Ohm	X Ohm
A	80	20	40	0.337	4.095	2.442	2.419	0.337	2.857	3.500	3.484
B	160	60	30	0.211	7.432	1.346	1.329	0.211	4.213	2.374	2.364
C	240	105	50	0.093	8.829	1.133	1.129	0.093	4.152	2.409	2.407

Case	Dimensions			3D 50mm				3D 10mm			
	Pitch mm	Width mm	Depth mm	R1 Ohm	I A	Z Ohm	X Ohm	R1 Ohm	I A	Z Ohm	X Ohm
A	80	20	40	0.251	4.422	2.261	2.247	0.182	8.145	1.228	1.214
B	160	60	30	0.173	5.977	1.673	1.664	0.142	9.471	1.056	1.046
C	240	105	50	0.080	5.592	1.788	1.786	0.070	8.176	1.223	1.221

Fig. 37 shows the 3 core width reactances plotted back to zero to give the values for end turn leakage reactance.

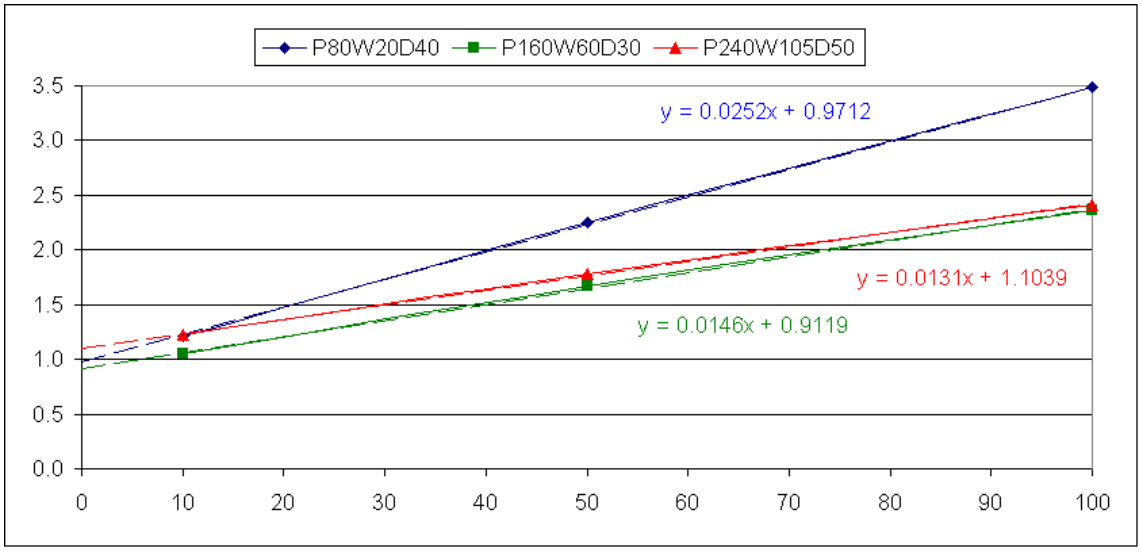

Fig. 37. Reactances for 3 core width models plotted back to zero

The results of the multiple 3D model method are compared to the 2D-3D model method in Table 9 in terms of normalised inductance, worked out as in (26)

$$L_N = \frac{X}{2\pi f N_c N_t^2} \tag{26}$$

Where:

L_N is the normalised end turn leakage inductance per coil H

X is end turn leakage reactance per phase of the model Ohms

f is the supply frequency Hz

N_C is the number of coils per phase of the model

N_t is the number of turns per coil of the model

Table 9: Normalised inductance for machines using 3 core & 2D-3D method

	Model Dimensions			3 Core Method	2D-3D Method	Difference
Case	Pitch mm	Width mm	Depth mm	L_N H	L_N H	%
A	80	20	40	1.546E-07	1.695E-07	9.7
B	160	60	30	1.451E-07	1.648E-07	13.5
C	240	105	50	1.757E-07	2.034E-07	15.8

As can be seen from the results above, this method loses some accuracy at greater coil pitches and widths. However, it still gives values within 16% of the experimental and full 3D results with significant saving in computation. This is a great improvement on prediction methods based on air cored coils. For example, in 4.2.6. it is shown that air cored coil methods can give values of end turn leakage reactance 75% lower than those found by experiment.

The method used will likely depend on the level of accuracy required, with the 2D-3D method used for initial specification and the full 3D method used for final production designs.

The errors in this method are in part due to three dimensional fringing of the flux due to the open rotor conditions, as this is also not taken into account by a 2D machine. A simple solution to this problem has been attempted by including a laminated iron secondary close enough to the primary to reduce the fringing, while not so close as to adversely effect the end turn inductance of the machine. However, the results from this method show no significant improvement in accuracy.

4.2.8. Parameterised Equation Modelling Method

The new simple method developed reduces the computation time, but generating a solution for the end turn inductance of a given machine still requires significant amounts of FE programming and solving time. Therefore, a simple parameterised equation based method was sought to give quick and easy results for normalised end turn leakage inductance [25].

The physical dimensions of the machine that affected end turn inductance were first defined as shown in Fig. 38.

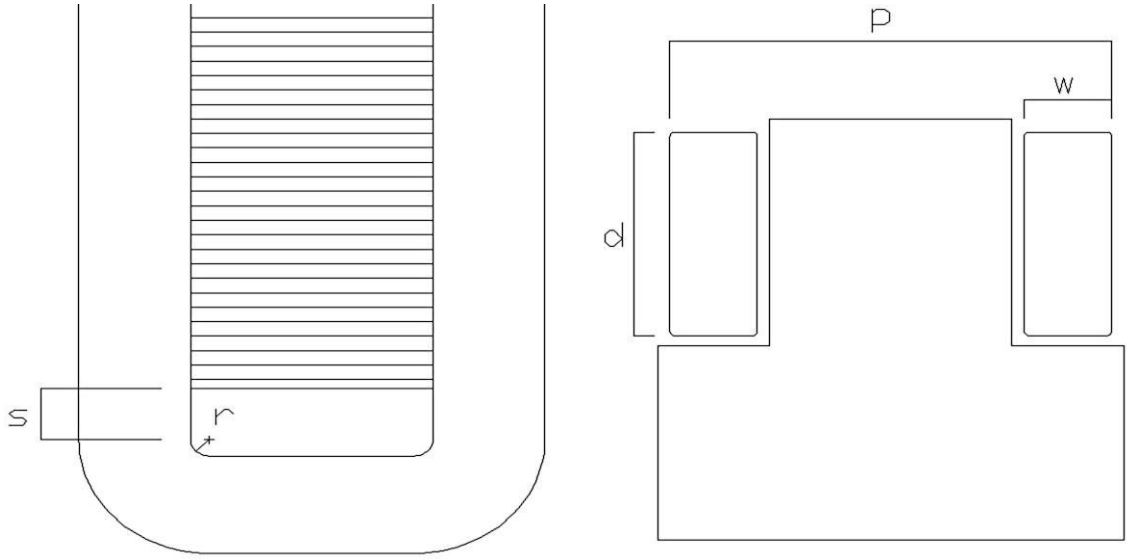

Fig. 38. Relevant coil dimensions for determining end turn inductance of a concentrated coil machine

The distance between the stack and the inner edge of the coil was fixed, based on the minimum likely clearance from the stack side *s* (5mm) and the minimum inner bend radius *r* (2mm). The principal parameters that affect end turn inductance are coil width *w*, coil depth *d* and coil pitch *p*.

A useful range of parameters was then defined, suitable for a range of machines usually encountered in practice. Coil width *w* was modelled between 10-120mm, coil depth *d* between 30-50mm and coil pitch *p* between 40-280mm.

The 2D and 3D comparison method described above was used to find values of end turn inductance for approximately 100 cases throughout the range of parameters.

For each value of coil depth *d*, normalised inductance variation according to coil pitch *p* was plotted for coils with the same coil width *w*. Further plots were created for a range of coil width *w* values. Fig. 39 represents the plot for 10mm wide coils, with the three plots representing three different coil depths.

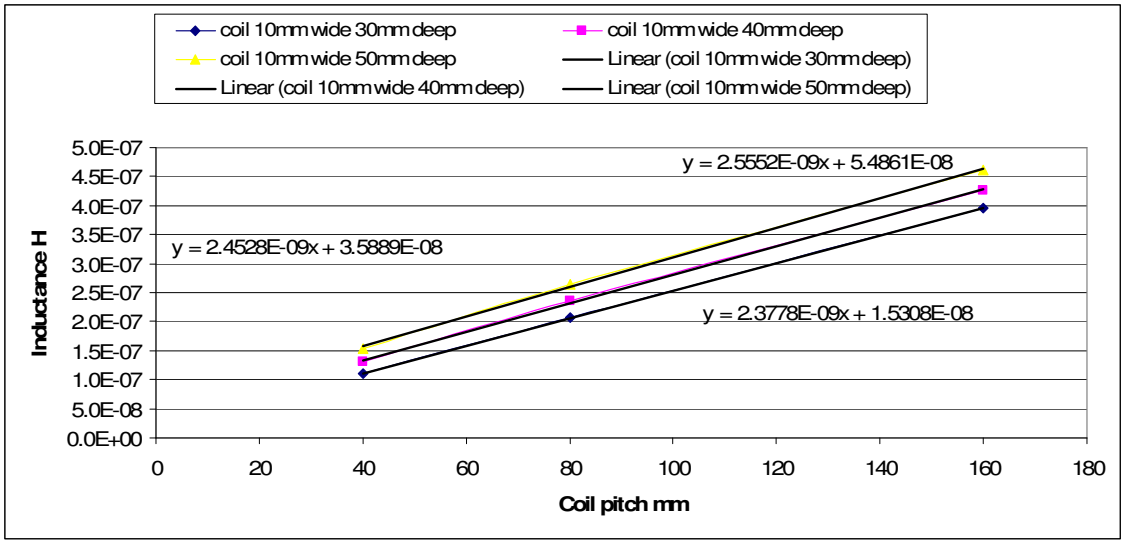

Fig. 39. Normalised inductance variation according to coil pitch

This yielded a function for each coil width present in more than one model.

$$L_N = a_n * p + b_n \quad (27)$$

For a constant 30mm coil depth

$$L_N = a_{30} * p + b_{30} \quad (28)$$

Normalised inductance variation with coil width is shown in Table 10.

Table 10: Normalised inductance variation with coil width

Coil width	a_{30}	b_{30}
10	2.4028×10^{-9}	1.3908×10^{-8}
15	2.2360×10^{-9}	-8.1610×10^{-9}
20	2.0600×10^{-9}	-1.5190×10^{-8}
30	1.9350×10^{-9}	-4.4760×10^{-8}
60	1.7850×10^{-9}	-1.2090×10^{-7}

These functions were then plotted against coil width to find a function to represent values a_{30} and b_{30} over a range of coil widths Fig. 40.

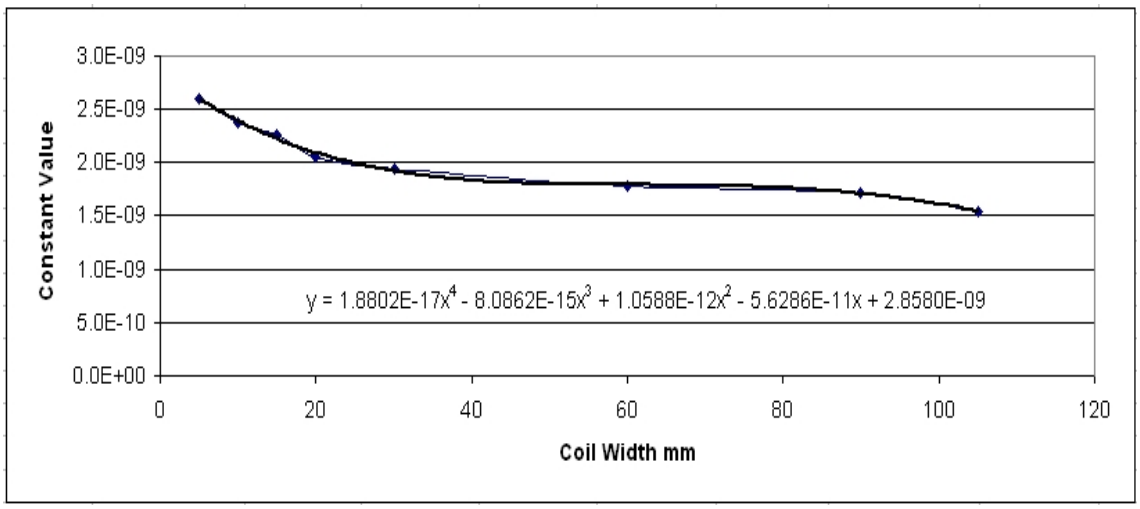

Fig. 40. Value of the variable a_n in equation (27) for a 30mm coil depth

This was found to have some limitations modelling the largest and smallest coil widths, so more data was added to the basic set at the extremes. This gave fourth order polynomial equations that can predict normalised inductance for their own coil width 30mm.

The equations for a_{40} b_{40} a_{50} b_{50} were found to have further variations, so extra points at 280mm coil pitch, 90 and 75 mm coil width were added at the three coil depths.

For 30mm coils, the coefficients of (27) are

$$a_{30} = 1.8802\text{x}10^{-17} * w^4 - 8.0862\text{x}10^{-15} * w^3 + 1.0588\text{x}10^{-12} * w^2 - 5.6286\text{x}10^{-11} * w + 2.858\text{x}10^{-9} \quad (29)$$

$$b_{30} = 1.1805\text{x}10^{-14} * w^4 - 2.5212\text{x}10^{-12} * w^3 + 1.8822\text{x}10^{-10} * w^2 - 8.1600\text{x}10^{-9} * w + 8.5552\text{x}10^{-8} \quad (30)$$

Similarly for 40mm coils, the coefficients of (27) are

$$a_{40} = 3.7050\text{x}10^{-17} * w^4 - 1.2335\text{x}10^{-14} * w^3 + 1.4030\text{x}10^{-12} * w^2 - 6.7418\text{x}10^{-11} * w + 3.0321\text{x}10^{-9} \quad (31)$$

$$b_{40} = 1.2709\text{x}10^{-14} * w^4 - 2.8498\text{x}10^{-12} * w^3 + 2.2367\text{x}10^{-10} * w^2 - 9.8125\text{x}10^{-09} * w + 1.2095\text{x}10^{-7} \quad (32)$$

And for 50mm coils, the coefficients of (27) are

$$a_{50} = 5.6936\text{x}10^{-17} * w^4 - 1.6991\text{x}10^{-14} * w^3 + 1.7825\text{x}10^{-12} * w^2 - 8.0125\text{x}10^{-11} * w + 3.2471\text{x}10^{-9} \quad (33)$$

$$b_{50} = 1.3177\text{x}10^{-14} * w^4 - 3.0901\text{x}10^{-12} * w^3 + 2.5413\text{x}10^{-10} * w^2 - 1.1353\text{x}10^{-08} * w + 1.5419\text{x}10^{-7} \quad (34)$$

The three fourth order polynomial equations above will predict normalised inductance to within 10% for their own coil depth. The generalised equation for these is

$$L_N = a_n * p + b_n \quad (35)$$

$$a_n = a * w^4 + b * w^3 + c * w^2 + d * w + e \quad (36)$$

$$b_n = f * w^4 + g * w^3 + h * w^2 + i * w + j \quad (37)$$

The next stage is to model the variation of constants a-j in the 4th order polynomials (36) and (37) according to coil depth Fig. 41. The equation of these lines will represent generalised coefficients of a-j for the 4th order polynomials that are related to coil depth and can then be added into the fourth order polynomial equations above to give a single overall equation for XE dependant on coil pitch, width and depth.

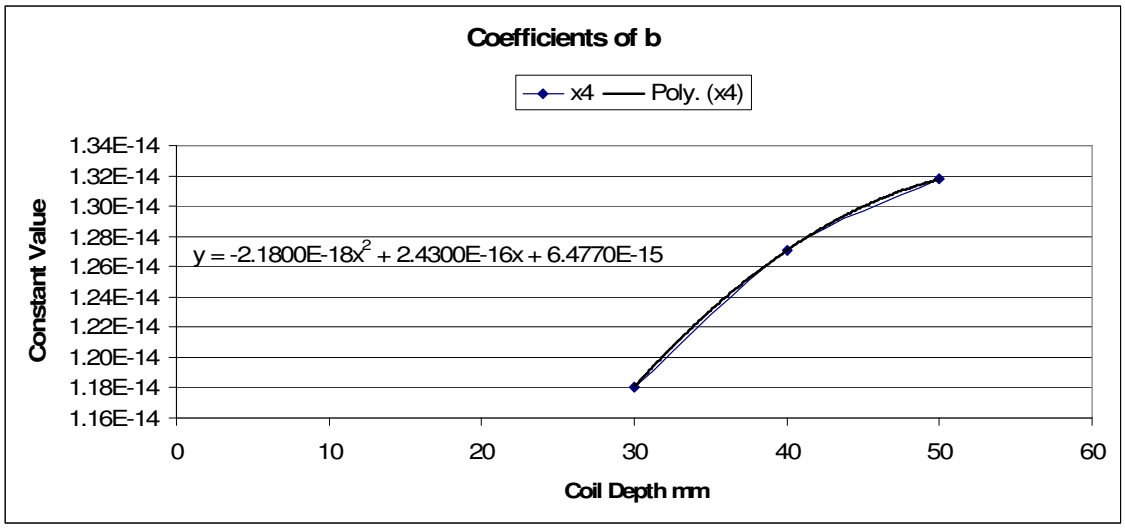

Fig. 41. The value of coefficient f in equation (37) according to coil depth and its equation

These lines were modelled with second order polynomials. So,

$a = ax*d^2 + ay*d + az$

to

$j = jx*d^2 + jy*d + jz$

And for a general case n

$$n = nx*d^2 + ny*d + nz \quad (38)$$

The full range of constants for equation (38) is shown in Table 11.

Table 11: Full set of constants for normalised inductance equation

	a	b	c	d
x	8.1900×10^{-21}	-2.0360×10^{-18}	1.7650×10^{-16}	-7.8750×10^{-15}
y	1.2515×10^{-18}	-2.8236×10^{-16}	2.2065×10^{-14}	-5.6195×10^{-13}
z	-2.6114×10^{-17}	2.2170×10^{-15}	2.3800×10^{-13}	-3.2340×10^{-11}
	e	f	g	h
x	2.0450×10^{-13}	-2.1800×10^{-18}	4.4150×10^{-16}	-2.4950×10^{-14}
y	3.0950x10-^{12}	2.4300×10^{-16}	-6.3765×10^{-14}	5.2915×10^{-12}
z	2.5811×10^{-09}	6.4770×10^{-15}	-1.0056×10^{-12}	5.1930×10^{-11}
	i	j		
x	5.6000×10^{-13}	-1.0790×10^{-11}		
y	-2.0445×10^{-10}	4.2951×10^{-09}		
z	-2.5305×10^{-09}	-3.3590×10^{-08}		

The overall equation for inductance related to all 3 coil dimensions is

$$L_N = ((ax*d^2 + ay*d + az)*w^4 + (bx*d^2 + by*d + bz)*w^3 + (cx*d^2 + cy*d + cz)*w^2 + (dx*d^2 + dy*d + dz)*w + (ex*d^2 + ey*d + ez))*p + ((fx*d^2 + fy*d + fz)*w^4 + (gx*d^2 + gy*d + gz)*w^3 + (hx*d^2 + hy*d + hz)*w^2 + (ix*d^2 + iy*d + iz)*w + (jx*d^2 + jy*d + jz)) \quad (39)$$

Or, adding all the coefficients

$$L_N = \left(\begin{array}{l} \left(+8.190\times10^{-21}\times d^2 + 1.252\times10^{-18}\times d - 2.611\times10^{-17}\right)\times w^4 + \\ \left(-2.036\times10^{-18}\times d^2 - 2.824\times10^{-16}\times d + 2.217\times10^{-15}\right)\times w^3 + \\ \left(+1.765\times10^{-16}\times d^2 + 2.207\times10^{-14}\times d + 2.380\times10^{-13}\right)\times w^2 + \\ \left(-7.875\times10^{-15}\times d^2 - 5.620\times10^{-13}\times d - 3.234\times10^{-11}\right)\times w + \\ \left(+2.045\times10^{-13}\times d^2 + 3.095\times10^{-12}\times d + 2.581\times10^{-09}\right) \end{array} \right) \times p$$
$$+ \left(\begin{array}{l} \left(-2.180\times10^{-18}\times d^2 + 2.430\times10^{-16}\times d + 6.477\times10^{-15}\right)\times w^4 + \\ \left(+4.415\times10^{-16}\times d^2 - 6.377\times10^{-14}\times d - 1.006\times10^{-12}\right)\times w^3 + \\ \left(-2.495\times10^{-14}\times d^2 + 5.292\times10^{-12}\times d + 5.193\times10^{-11}\right)\times w^2 + \\ \left(+5.600\times10^{-13}\times d^2 - 2.045\times10^{-10}\times d - 2.531\times10^{-09}\right)\times w + \\ \left(-1.079\times10^{-11}\times d^2 + 4.295\times10^{-09}\times d - 3.359\times10^{-08}\right) \end{array} \right) \quad (40)$$

The equation (40) predicts all values of normalised inductance within its limits to within 10% of FE model answers, with 95% of calculated values within 5% of the FE modelled answers. Including the range of accuracy found in 4.2.7. between 2D-3D methods and full 3D prediction, the equation gives answers within 20% of 3D and experimental results for 95% of cases, and within 24% of 3D & experiment for all cases. Once again, this level of accuracy is acceptable for initial designs, but the full 3D method would likely need to be applied for final designs.

The accuracy of the developed equation has not been tested outside the specified limits, and further verification of the normalised inductance value should be undertaken if working beyond them.

A method to further improve the accuracy of the equation would be to model additional coil widths, as some coil pitch equations were based on only 2 values of coil width. We can then represent L using

$$L_N = a_n * p^2 + b_n * p + c_n \quad (41)$$

However the present model seems accurate enough, so this method will not currently be required.

Despite being relatively large, this equation also gives results in a fraction of the time taken by even the fastest FE solutions. For other machine types, the above method may be applied to find a new parameterised equation for the type in question.

4.2.9. Conductive shielding

An investigation was undertaken into the use of conductive shielding to reduce end turn leakage reactance. In a first form, a concentrated coil was separated into 2 coils in the same slot, with conductive barriers placed between the end turns of the two coils. A second form used conductive sides on the core in an attempt to mitigate the effects of the presence of core iron on end turn leakage reactance.

Both of these methods showed small improvements to end turn leakage reactance in some cases. However, these improvements were small compared to the significant performance disadvantages caused by the extra conductive material and these methods were not pursued further.

4.3. Slot Packing Factor

A significant difference between the concentrated planar winding and the two layer winding is in the slot packing factor, which represents the amount of copper that can be packed into a slot of a given size. For example, a slot packing factor of 0.5 means that only 50% of a slot's area contains active copper. The rest consists of insulation and space required by mechanical considerations. For a typical mush type 2 layer wound linear induction motor, slot packing factors are less than 0.5.

For concentrated windings, machine wound coils have been suggested to ease construction of a concentrated winding. Another advantage to these coils is that machine produced layer wound coils can be produced with a slot packing factor of 0.7 using strip wound coils. If foil wound coils were used, the packing factors could rise to 0.8-0.9. A typical case starting with mush wound coils is explored below.

If the number of turns remains constant, increasing the packing factor will affect phase resistance, as the area of copper in the slot and area per turn will increase.

$$R = \rho l / A = \rho l /(A * (0.7/0.434)) = \rho l / A * 1.613 \quad (42)$$

Where:
R is resistance, ρ is resistivity of coil material, l is length of coil and A is area of coil

So resistance will be factored by 1/1.613 = 0.62
A typical motor (with a .434 packing factor) has an I^2R loss of
$I^2R = 27^2*.802 = 584.66W$

I^2R loss is the main component of stator heating and heavily influences motor rating (how long a motor can operate for without overheating). Using a higher packing factor machine, we can draw a higher current while producing the same I^2R loss (heating) as the original.

$$P = I^2R \rightarrow I = \sqrt{\frac{P}{R * 0.62}} = \sqrt{\frac{584.6}{0.802 * 0.62}} = 34.29A$$

So slot current can be increased by 34.29/27 = 1.27 whilst keeping the same I^2R losses in the primary. Increasing the current by 1.27 will increase the force by $1.27^2 = 1.62$.

So to generalise, slot current can be increased by a factor equal to the root of the ratio of the two packing factors.

$$\sqrt{\frac{0.7}{0.434}} = 1.273$$

And force is simply increased by a factor equal to the ratio of the two packing factors

.7/.434 = 1.613

This means that not only will using machine wound coils simplify construction, it will allow higher slot currents and up to 61% higher thrusts to be produced by increasing the amount of copper in the slot. Alternatively, the same amount of copper could be used to produce a much better rated machine. Potentially, a cheaper material such as aluminium could be used for windings, using the extra material allowed by higher packing factor to produce an equivalent resistance coil in the same area.

It should be noted that this is a simplistic analysis, as I^2R loss based thermal rating is only one aspect of a machines performance. For example, if current in the above example is increased by 27% this will cause an increase in flux density which may cause saturation of the iron regions and reduce performance. This example only serves to illustrate the potential for motor improvement through higher packing factors.

4.4. Dual Concentric Coil Concentrated Winding Stators

A method has also been investigated to reduce the effects of end turn leakage inductance by moving from single concentrated coils as in Fig. 27 to two or more concentrically wound distributed coils as in Fig. 42.

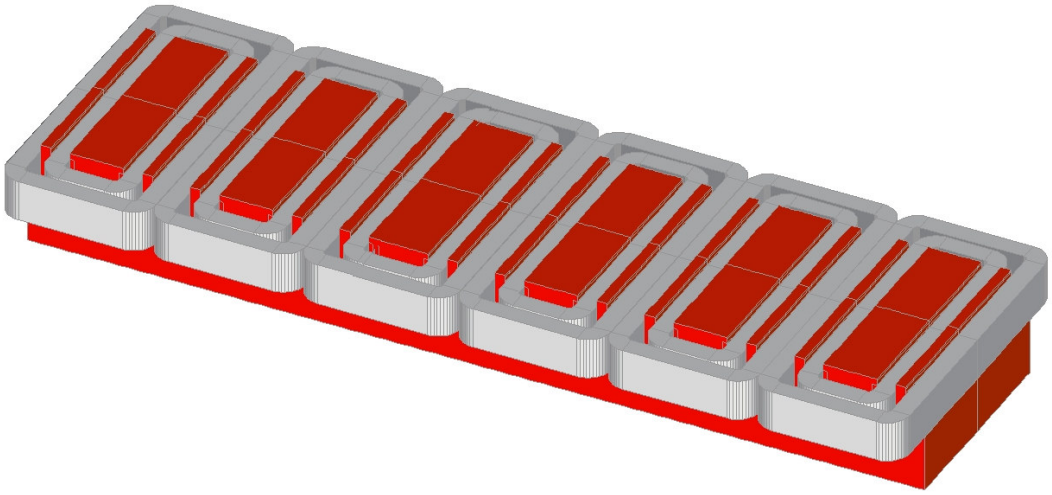

Fig. 42. Dual coil concentric winding 3D FE model

This has the effect of dramatically reducing the self inductance of each coil, whilst including some mutual coupling between the two coils, based on the separation and dimensions of the pair. With careful design, a configuration such as this can significantly reduce the overall end turn inductance of a stator.

The end turn inductance of these concentric groups can be modelled using the 2D-3D method described above, and may be parameterised using the methods previously described.

Starting from the original concentrated coil machine, each coil is divided into two concentric coils as shown in Fig. 43. The coil depth of the new coils is still *d*, the offset from stack for the inner coil is still *s* and the bend radius is still *r*. The coil width for each concentric is now ½*w*. The tooth width between the coils *t* can take any value. The coil pitch of the outer coil is still *p* and the coil pitch of the inner coil *p2* is:

$$P2 = p - w - 2t \tag{43}$$

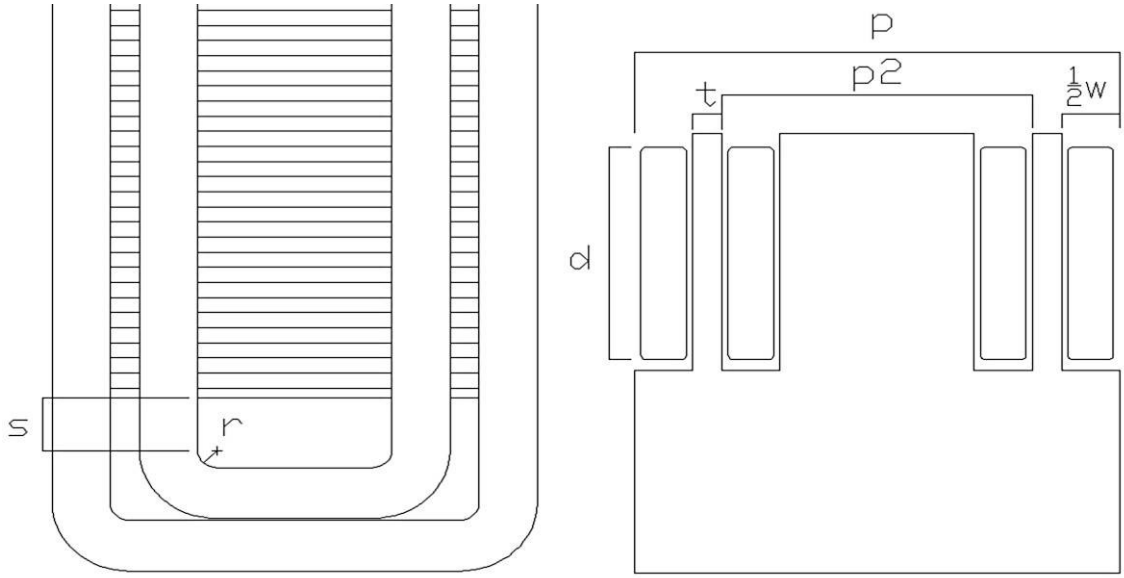

Fig. 43. Coil dimensions for determining end turn inductance of a 2 coil concentric machine

A significant variable in the 2 coil concentric method is inter-coil tooth width *t*. The greater this value is the less mutual inductance there will be between the two concentric coils and the lower the end turn leakage inductance will be. However, splitting the coil into two concentrics also reduces performance by adding a distribution factor to the overall winding factor, hence reducing it. This distribution factor is related to concentric coil separation and hence inter-coil tooth width *t*. An example case is detailed below.

The original coil had the following characteristics: Coil pitch *p* 71.2mm, coil width *w* 20.8 mm, coil depth *d* 37mm, offset from stack *s* 5mm and bend radius *r* 2mm. The winding used a 6 coil 4-8 pole layout.

The end turn inductance per coil of this machine found from both 3 core full 3D FE and experiment was 0.0032H.

The above method was used to develop a 2 coil concentric version of the machine. The characteristics of this were: Outer coil pitch *p* 71.2mm, inner coil pitch *p2* 40.4mm, inter-coil tooth width *t* 5mm, coil width ½*w* 10.4 mm, coil depth *d* 37mm, offset from stack *s* 5mm and bend radius *r* 2mm.

The end turn inductance per coil of this machine, using 3 core results for full 3D FE was 0.00195H, a reduction in end turn inductance of 40%. The new winding factor for the 4 pole harmonic due to phase coil distribution is reduced to 0.647 from 0.866, a reduction of 25% from that of the original machine.

For the 2 coil concentric example given above, winding factor was considerably reduced, however this need not always be the case. A second example of concentrated and concentric machines using a 9 coil 8-10 pole winding has been studied.

The original coil had the following characteristics: Coil pitch *p* 139.6mm, coil width *w* 34.8 mm, coil depth *d* 22mm, offset from stack *s* 5mm and bend radius *r* 2mm.

The characteristics of the 2 coil concentric equivalent machine were: Outer coil pitch *p* 139.6mm, inner coil pitch *p2* 95.4mm, inter-coil tooth width *t* 4.7mm, coil width ½*w* 17.4 mm, coil depth *d* 22mm, offset from stack *s* 5mm and bend radius *r* 2mm.

The end turn inductance for the concentric machine was reduced from 0.0331H to 0.0128H, a reduction of 61%. The winding factor of the 8 pole harmonic was reduced from 0.945 to 0.810, a reduction of only 14%.

There is also an increase in complexity of construction with the 2 concentric coil machines, when compared to the single coil counterpart. These designs however are still far less complex in construction than conventional 2 layer windings.

In practice, there is a delicate balance to be found between reducing end turn inductance and limiting the reduction of winding factor in order to produce an overall improvement using this method.

4.5. Plate Rotor Performance of Machines

Now that the end turn leakage inductance can be quickly and accurately calculated, finite Element modelling was used to investigate the performance of the concentrated winding linear stator with a plate rotor. The design of the concentrated winding was based on a standard linear motor type, and this motor was also modelled in order to show the relative performance of concentrated and standard linear motor systems. The two systems were modelled as:

- A regular, repeating track of conventional linear stators with a short reaction plate rotor.
- A continuous track consisting of concentrated winding stators with a short reaction plate rotor.

It should be noted that in the conventional linear stator case, this is an idealised version of systems currently used. In reality a track consists of a row of individual motors with some half-filled slots and clearance gap at each end, rather than a continuous track. This layout was used in order to give a good benchmark to measure other systems against, without creating end effects. As previously discussed, concentrated windings can but up into a continuous track. A concentrated winding machine was developed based on a typical two layer wound linear stator.

The conventional motor was based on a typical linear motor used for low speed applications. The parameters of this motor are as follows:

Winding: 3 phase, 4 pole, 2 Slots per pole and phase, 5/6 corded, 40 turns per coil, pole pitch 0.1068m

Steel Core: Length 0.4272m, Width 0.1m, Height .0748m, 24 slots, slot pitch .0178m, core back 0.027m.

The concentrated winding motor was designed as closely as possible to be equivalent to the standard linear motor.

Steel core: Length 0.4272m, Width 0.1m, Height .067m, 5 slots and 2 half-width end slots, slot pitch .0712m, core back 0.027m.

Winding: 3 phase, 4 pole, ½ a slot per pole and phase, 160 turns per coil, pole pitch 0.1068m

The plate rotor used was a 4-pole length plate 0.4272m long and 0.1m wide. The aluminium conductive section is .0035m thick, with 0.014m depth of steel backing. Rotor resistivity was 4.3×10^{-8} Ohm m.

The stators were connected in star, and initially were current driven at 27Arms. Current sourcing the model allows the current flowing in the stator winding to be set directly in order to study the interaction of the stator with the rotor without having to model the exact electrical characteristics of the stator.

The models were time stepped, with a time step being taken every 0.0005 seconds. As a continuous track was being modelled, each finite element solution was run until a stable thrust pattern had been established, in order to give results without any transient effects.

The initial modelling was performed using Mega 2D Finite Element Analysis. The finite element mesh for the two motors can be seen in Fig. 44 & Fig. 45.

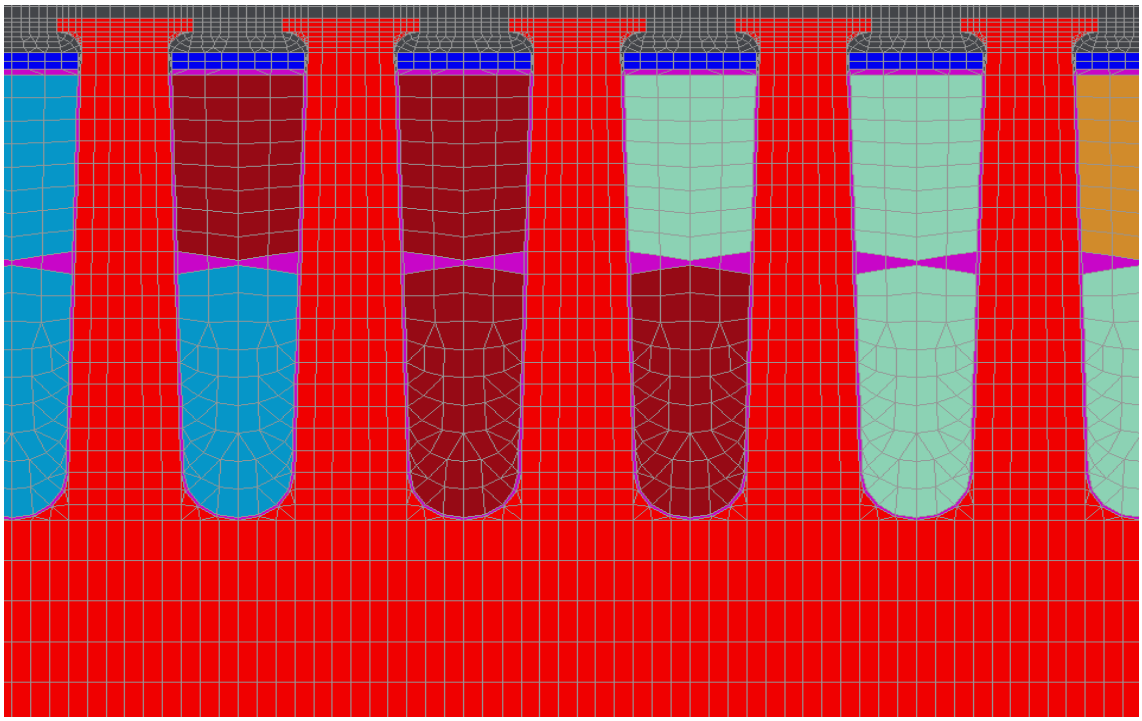

Fig. 44. The finite element mesh for a conventional machine

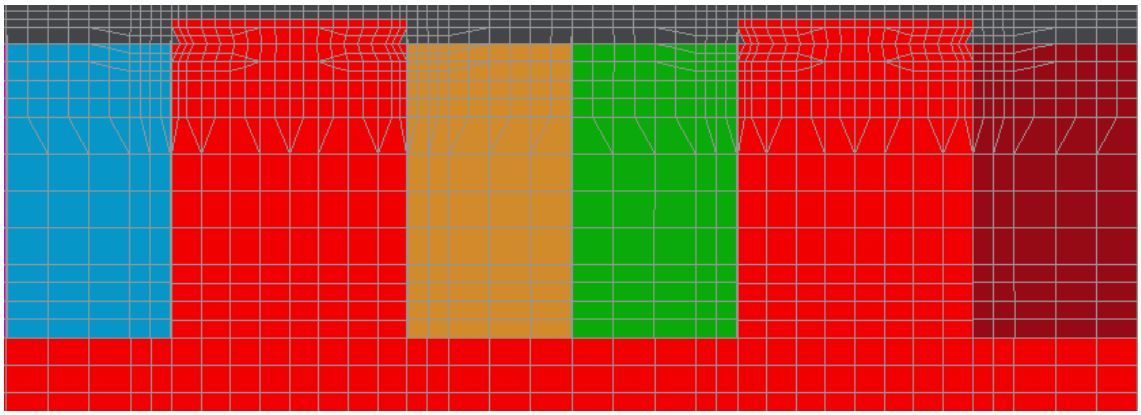

Fig. 45. The finite element mesh for a concentrated winding machine

Modelling was also undertaken of the concentrated winding under voltage fed conditions using the end turn leakage inductance methods found previously.

The thrust speed curve for the concentrated and conventional LIMs with a plate rotor can be seen below Fig. 46.

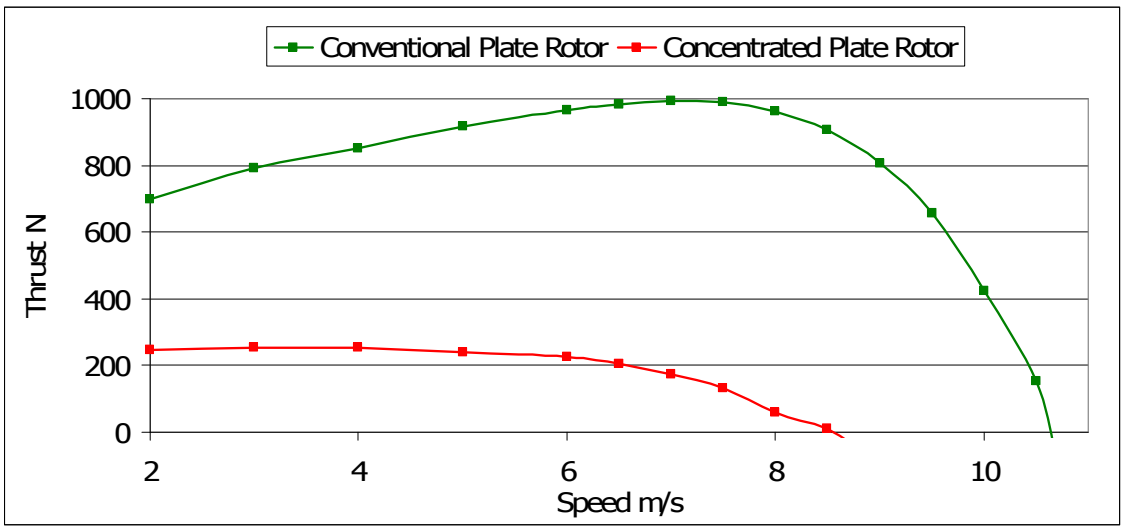

Fig. 46. Thrust speed curve for conventional & concentrated stators with plate rotors

As is obvious from the thrust speed curves, the concentrated stator with a plate rotor has critical disadvantages. Not only is the force significantly reduced compared to the conventional LIM, the force profile becomes negative at a speed much less than the designed synchronous speed of the machine. Therefore it was determined to identify the root causes of this poor performance and find methods to improve it.

4.6. Motor Harmonics

A standard double layer linear induction motor produces an approximately sinusoidal slot current and mmf waveform Fig. 47 that can be seen to be symmetrical about the zero line.

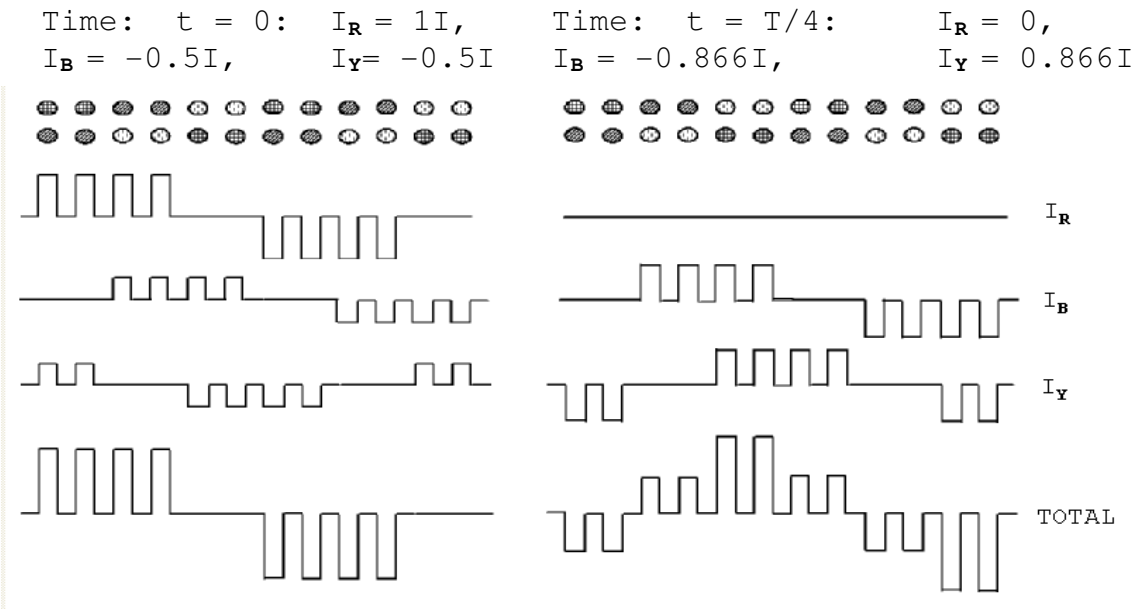

Fig. 47. Conventional winding slot current waveform plots

This symmetry demonstrates that only odd harmonic fields are present in the slot current profile of a standard LIM.

When the slot currents from each phase are summed with the correct phase relationships, a travelling wave is produced. The progression of this wave can be illustrated by working out the total slot current and resultant mmf pattern at several instants over a full cycle. Fig. 47 also shows the same double layer conductor arrangement progressed by T/4 of a cycle in time. It can be seen that the mmf field pattern has progressed by ¼ of wavelength in space. The differences in the shape of the field between the two instants in time indicate that harmonic travelling fields are present.

The sinusoidal travelling mmf produced by the standard double layer winding LIM is known to produce good performance with a conductive plate secondary.

The behaviour of the concentrated winding waveform is different and it is evident that much larger harmonic fields are present. Fig. 48 represents the slot currents and resultant mmf of a two-pole section of a concentrated winding.

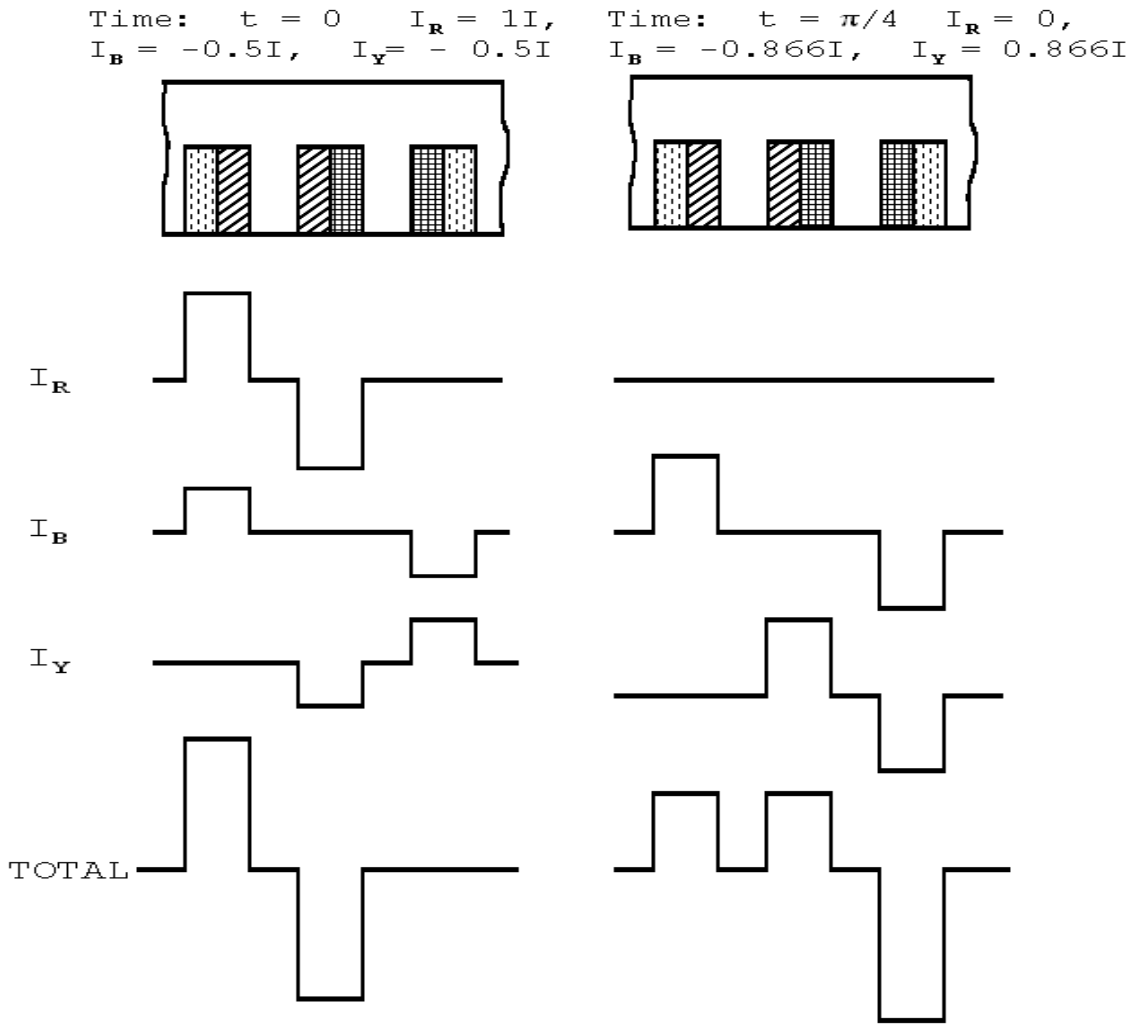

Fig. 48. Concentrated winding slot current waveform plots

The slot current patterns produced are not symmetrical about the zero line, which means it can be deduced algebraically that both odd and even harmonics are present in the waveform. Plotting the mmf pattern at two instants in time shows the travelling wave performance. The considerable change in shape between the two instants indicates that large travelling harmonic fields are present.

4.6.1. Winding Analysis of a General Three Phase Winding

A winding composed of a group of coils connected in series is equivalent to a set of windings where each winding is represented by a sinusoidal distribution of conductors, with these distributions being harmonically related in space. The conductor distribution can then be expressed as a Fourier expansion with a zero average term.

A machine consisting of conductors placed in slots can be modelled using patches of infinitely thin conductors positioned on a plane iron surface. The patches of conductors are of the same width and placed in the same positions as the slot openings.

If a slot at θ_s contains N_s conductors and has a slot opening of 2δ, the conductor distribution produced by the slot is given by

$$N_p = \frac{1}{\pi}\int_{\theta s-\delta}^{\theta s+\delta} \frac{N_s}{2\delta}\exp\left(-jp\,\theta_s\right)d\theta$$

$$N_p = \frac{1}{\pi}\frac{\sin\, p\delta}{p\delta} N_s \exp\left(-jp\,\theta_s\right) \qquad (44)$$

Where p is an integer, the harmonic number.

The winding distribution for say the 'a' phase of the winding is then given by

$$N_{pa} = \frac{1}{\pi}\frac{\sin\, p\delta}{p\delta}\sum_{s=1}^{s=S} N_{sa}\exp\left(-jp\,\theta_{sa}\right) \qquad (45)$$

Where there are N_{sa} conductors from the 'a' phase in the general s th slot at θ_{sa}.

The corresponding winding distributions for the b and c windings are similarly N_{pb} and N_{pc}

The phase conductor distributions may be resolved into equivalent space sequence sets where n_f, n_b, and n_z are the forward, backward and zero components respectively.

$$n_f = \frac{1}{3}\left[N_{pa} + N_{pb}\exp j\frac{2\pi}{3} + N_{pc}\exp j\frac{4\pi}{3} \right] \quad (46)$$

$$n_b = \frac{1}{3}\left[N_{pa} + N_{pb}\exp j\frac{4\pi}{3} + N_{pc}\exp j\frac{2\pi}{3} \right] \quad (47)$$

$$n_Z = \frac{1}{3}\left[N_{pa} + N_{pb} + N_{pc} \right] \quad (48)$$

4.6.2. Winding Analysis of Concentrated Windings

For a 3 coil 2-4 pole concentrated winding, if each of the coils has N turns the 'a' phase distribution is

$$N_{pa} = \frac{N}{\pi}\frac{\sin p\delta}{p\delta}\left(\exp j0 - \exp\frac{j2\pi p}{3} \right) \quad (49)$$

$$N_{pa} = \frac{2N}{\pi}\frac{\sin p\delta}{p\delta}\exp(-j\pi p/3)\exp(j\pi/2)\sin \pi p/3 \quad (50)$$

This means that N_{pa} is zero for p=3m where m is an integer.

The equivalent expressions for the other two phases 'b' and 'c' may be found by an origin shift hence

$$N_{pa} = N_p \quad (51)$$

$$N_{pb} = N_p \exp(-2\pi p/3)$$
$$N_{pc} = N_p \exp(-4\pi p/3)$$

The phase conductor distributions may be resolved into equivalent space sequence sets where n_f, n_b, and n_z are the forward backward and zero components respectively

$$n_f = N_p/3\{\exp(j0) + \exp(-j2\pi p/3 + j2\pi/3) + \exp(-j4\pi p/3 + j4\pi/3)\} \quad (52)$$

and it follows that $n_f = N_p$ for p=1,4,7 etc and is zero for all other p

$$n_b = N_p/3\{\exp(j0) + \exp(-j2\pi p/3 + j4\pi/3) + \exp(-j4\pi p/3 + j2\pi/3)\} \quad (53)$$

and it follows that $n_b = N_p$ for p=2,5,8 etc and is zero for all other p

$$n_z = N_p/3\{\exp(j0) + \exp(-j2\pi p/3) + \exp(-j4\pi p/3)\} \quad (54)$$

The sum of the term in the brackets is zero unless p=3m where m is a positive integer. Therefore since it was deduced earlier that N_p is zero when p=3m the zero sequence winding distribution is zero for all values of p.

When a positive sequence set of windings is fed with positive sequence currents a positive going field is produced, conversely when a negative sequence set of windings is fed with positive sequence currents a negative going field is produced. It follows that positive going waves are produced at p=1,4,7 and negative going waves are produced when p= 2,5,8

The relative amplitudes of the waves are given by the factor

$$\frac{\sin\ p\delta}{p\delta}\sin\ \pi p\ /\ 3 \tag{55}$$

The mark to space ratio of the slots and teeth is commonly 60:40, which means that

$$\delta = 0.8\pi / 3 \tag{56}$$

Algebraic analysis shows that two major travelling fields are present. The first is the two-pole field that the winding is designed to produce and the second is a four-pole field travelling in the negative direction.

The two-pole section studied uses 3 coils and produces a forward-going 2 pole wave and a backward-going 4 pole wave. The four pole machine studied is produced simply by repeating the 3 coils of the 2 pole machine and therefore produces a forward-going 4 pole wave and a backward-going 8 pole wave.
The relative magnitudes of the various forward and backward going harmonic waves can be seen in Table 12.

Table 12: The relative magnitude of harmonic waves in the 2-pole and 4-pole cases

P	1	2	3	4	5	6	7	8	9
Direction	F	B		F	B		F	B	
Harmonic wave poles	4	8	12	16	20	24	28	32	36
Relative Magnitude	1	0.669	0	0.07	0.233	0	0.078	0.0684	0

It can be seen that the negative going 8 pole harmonic is 2/3 the magnitude of the fundamental 4 pole harmonic. As an illustration of the concentrated windings' action the addition of a two-pole positively going wave (dashed line)

and a four-pole negatively going wave (dotted line) is plotted. Two instants of time are shown t=0 at Fig. 49, and t =T/4 at Fig. 50. The total patterns (solid line) approximate in shape to the total slot currents in Fig. 48.

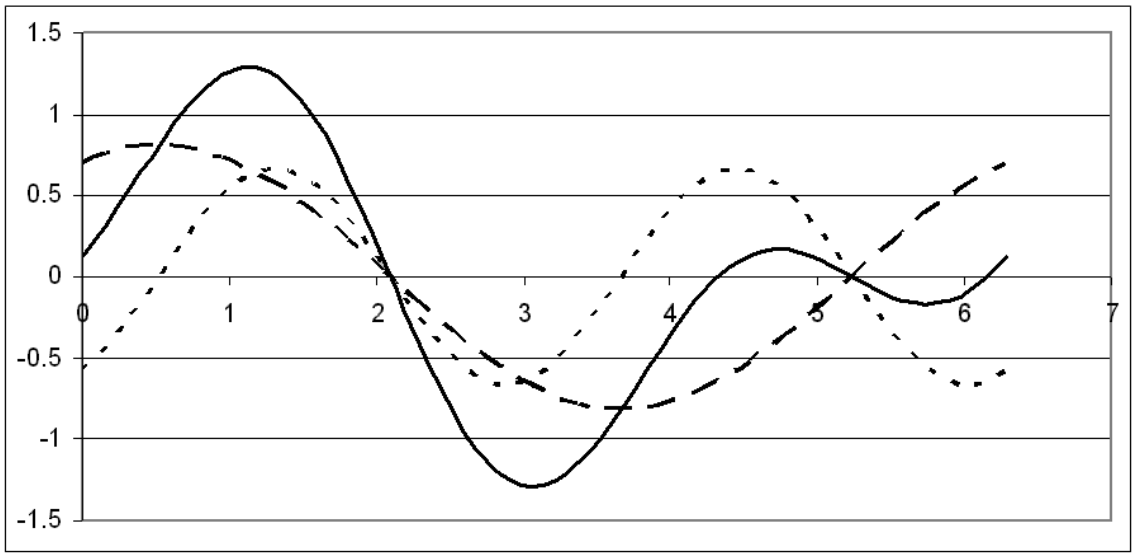

Fig. 49. Addition of forwards and backwards going harmonics at t = 0

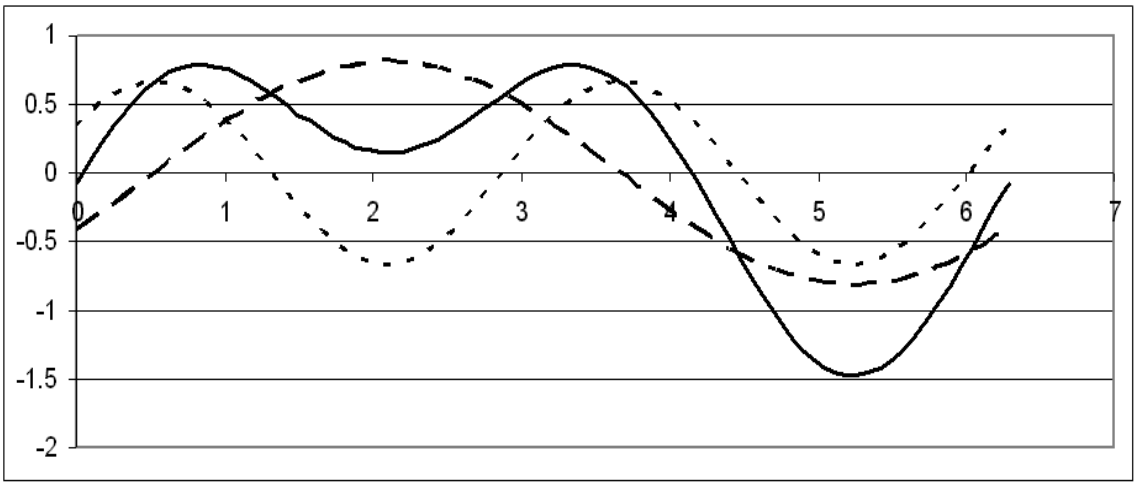

Fig. 50. Addition of forwards and backwards going harmonics at t = T/4

It will be observed that the general shapes produced by the two harmonics are similar to the wave shapes given in Fig. 48, providing further conformation that the concentrated winding produces 2 and 4 pole fields travelling in opposite directions.

It would be possible to produce a similar analysis to that above for the 9 coil 8 pole and the 12 coil 10 pole windings but it is just as convenient to use numerical summation and this appears in section 4.6.5., Machine winding factor spectra.

As a further exercise to verify the presence and scale of the mmf harmonics, 2D FE models were produced of all three winding layouts, 3 coil 2 pole Fig. 51 & Fig. 52, 9 coil 8 pole Fig. 53 & Fig. 54 and 12 coil 10 pole Fig. 55 & Fig. 56. The airgap mmf of each machine was plotted at first at zero then advanced by 120° in order to determine what harmonic components were present and the direction of travel of each component.

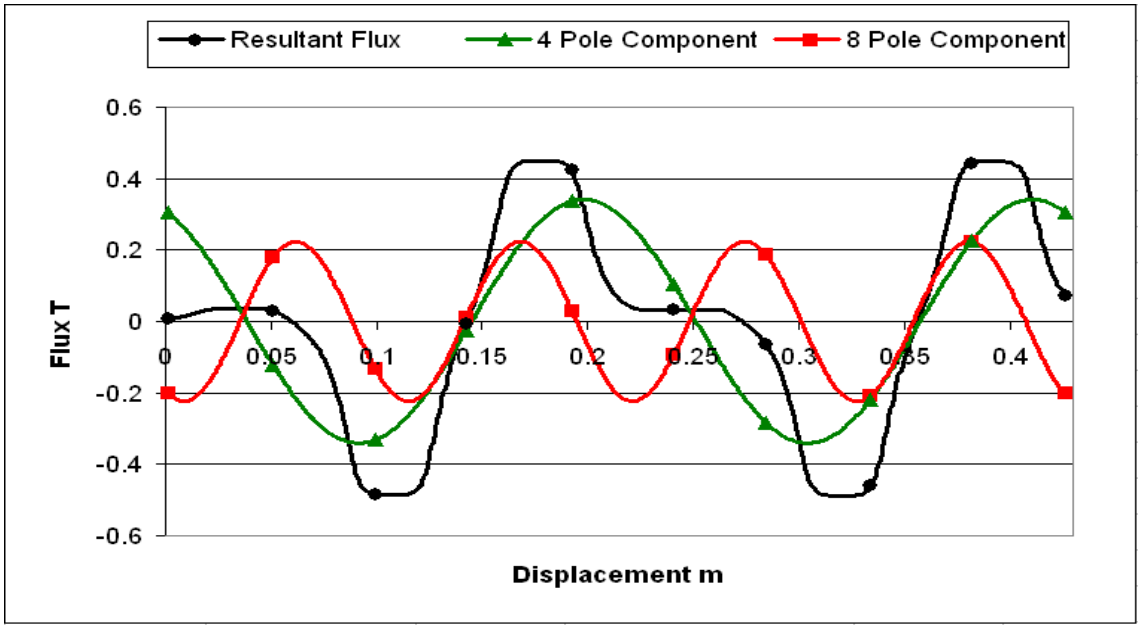

Fig. 51. 6 coil 4 – 8 pole resultant flux and principal harmonic components at 0°

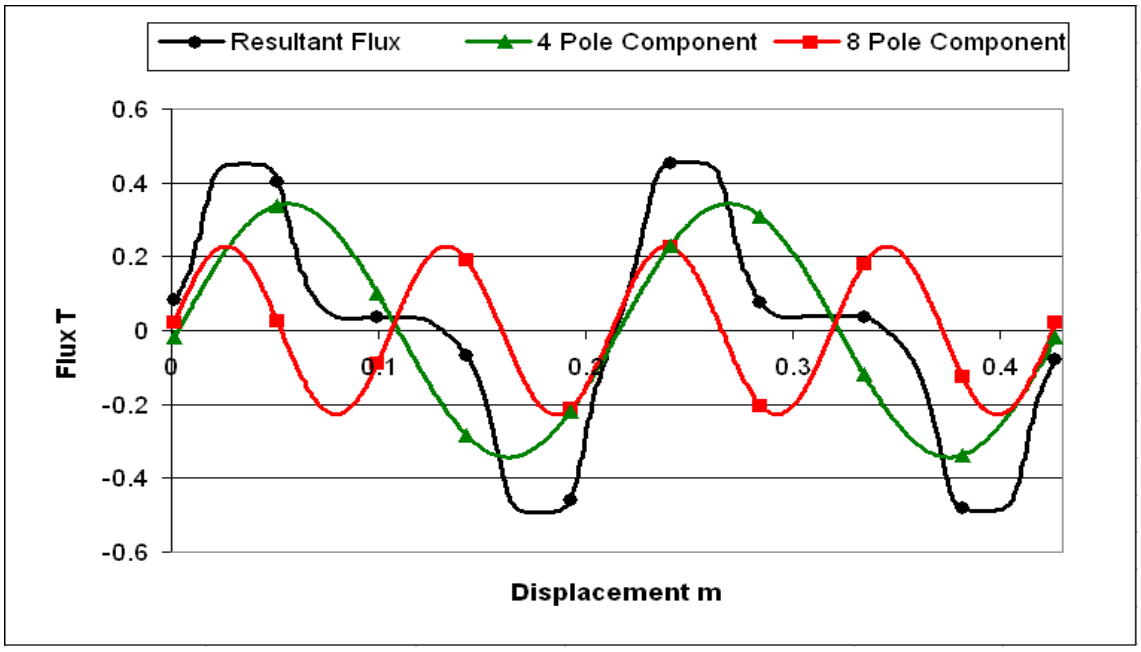

Fig. 52. 6 coil 4 – 8 pole resultant flux and principal harmonic components at 120°

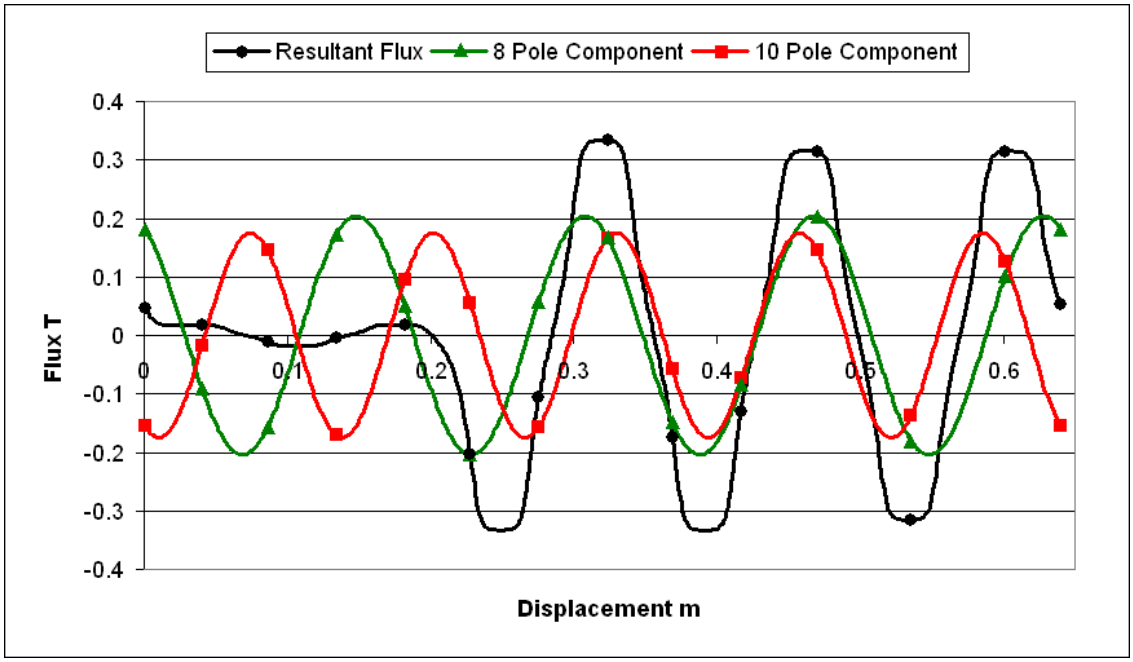

Fig. 53. 9 coil 8 – 10 pole resultant flux and principal harmonic components at 0°

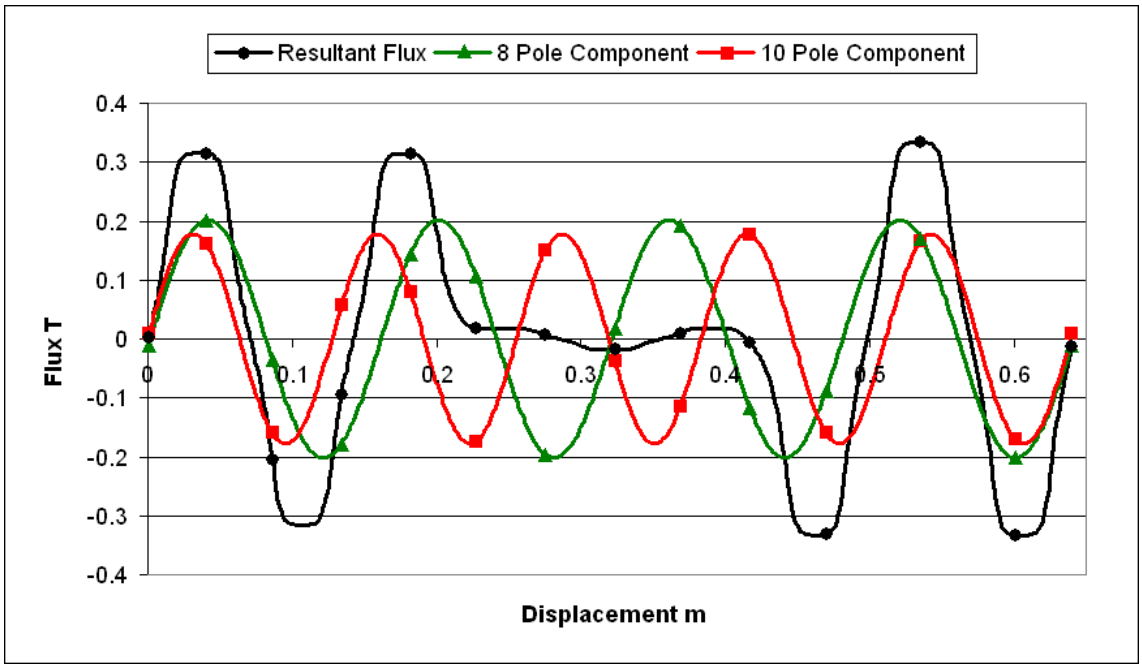

Fig. 54. 9 coil 8 – 10 pole resultant flux and principal harmonic components at 120°

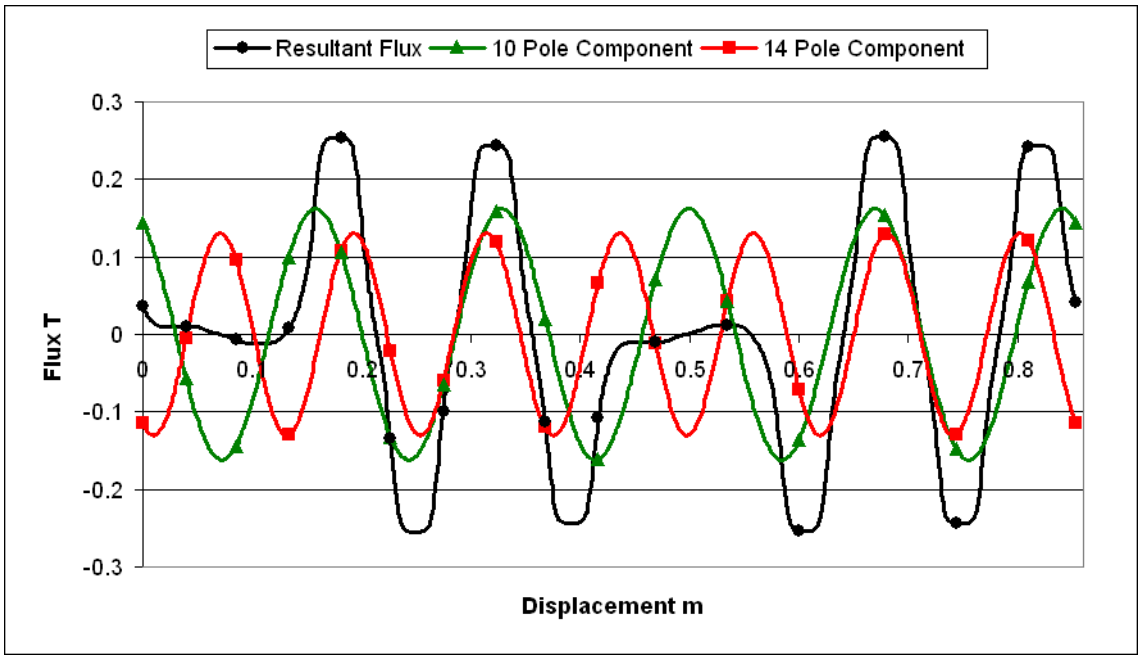

Fig. 55. 12 coil 10 – 14 pole resultant flux and principal harmonic components at 0°

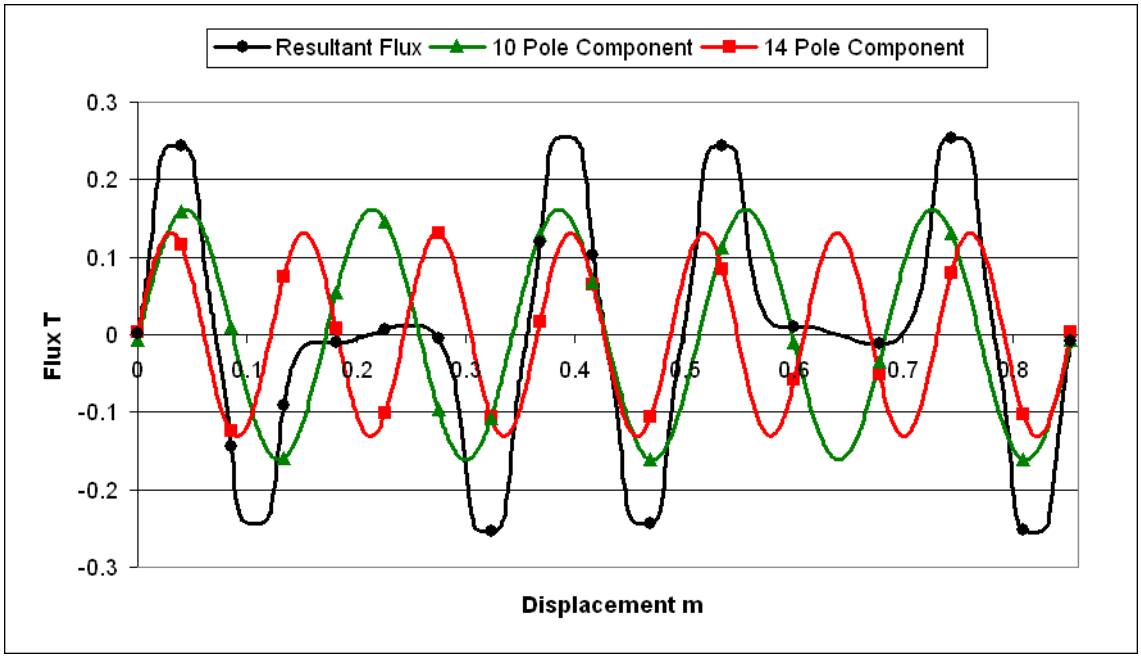

Fig. 56. 12 coil 10–14pole resultant flux and principal harmonic components at 120°

4.6.3. Winding Factor

In an ideal winding equation N_{pac} (57) is equal to the number of conductors per phase N_c.

$$N_{pac} = \pi \frac{\sin p\delta}{p\delta} \sum_{s=1}^{s=S} N_{sa} \exp\left(-jp\theta_{sa}\right) \tag{57}$$

Therefore in a non ideal winding a 'winding factor' which expresses the quality of the winding in using the conductors can be expressed as

$$\text{Winding Factor} = N_{pac} / N_c \tag{58}$$

An important point to consider is that each harmonic has its own winding factor and so will have a distinct effect on the output waveform. The winding factors of each harmonic must therefore be modelled in order to assess their true impact on the machine performance.

4.6.4. Standard Winding Factor Equation

A standard equation [26] is often used to calculate the winding factors of 2 layer windings. The standard equation uses a combination of distribution and pitch factor to develop a winding factor Kw using the method below.

Winding Factor = Pitch factor * Distribution factor

$$\text{Winding Factor} = \left[\sin\left(\frac{\pi \times \text{coil pitch}}{2 \times \text{pole pitch}}\right)\right] \times \left[\frac{\sin\left(\frac{\pi}{6}\right)}{\text{Spppp} \times \sin(\pi \times (6 \times \text{Spppp}))}\right] \quad (59)$$

Pitch factor is dependant only on the ratio between coil pitch and pole pitch, more familiarly known in fraction form as the chording. This represents the effects on emf of short pitching the coils to improve the waveform.

Distribution factor is dependant only on slots per pole and phase. This represents the ratio of emfs in a distributed winding to that if the windings were concentrated. The variation of the two factors according to their dependants is shown in Table 13.

Table 13: Distribution and Pitch factor variation with coil pitch, pole pitch and S/p/p

cp	pp	Ratio	Chording	Pitch Factor
1	1	1.000	1/1	1.000
1	1.1	0.909	10/11	0.990
1	1.2	0.833	5/6	0.966
1	1.3	0.769	10/13	0.935
1	1.4	0.714	5/7	0.901
1	1.5	0.667	2/3	0.866
1	1.6	0.625	5/8	0.831
1	1.7	0.588	10/17	0.798
1	1.8	0.556	5/9	0.766
1	1.9	0.526	10/19	0.736
1	2	0.500	1/2	0.707

S/p/p	Distribution Factor
1	1.000
1.5	0.975
2	0.966
2.5	0.962
3	0.960
3.5	0.959
4	0.958
4.5	0.957
5	0.957
7.5	0.956
10	0.955

Graphically, this produces an overall winding factor as seen below Fig. 57.

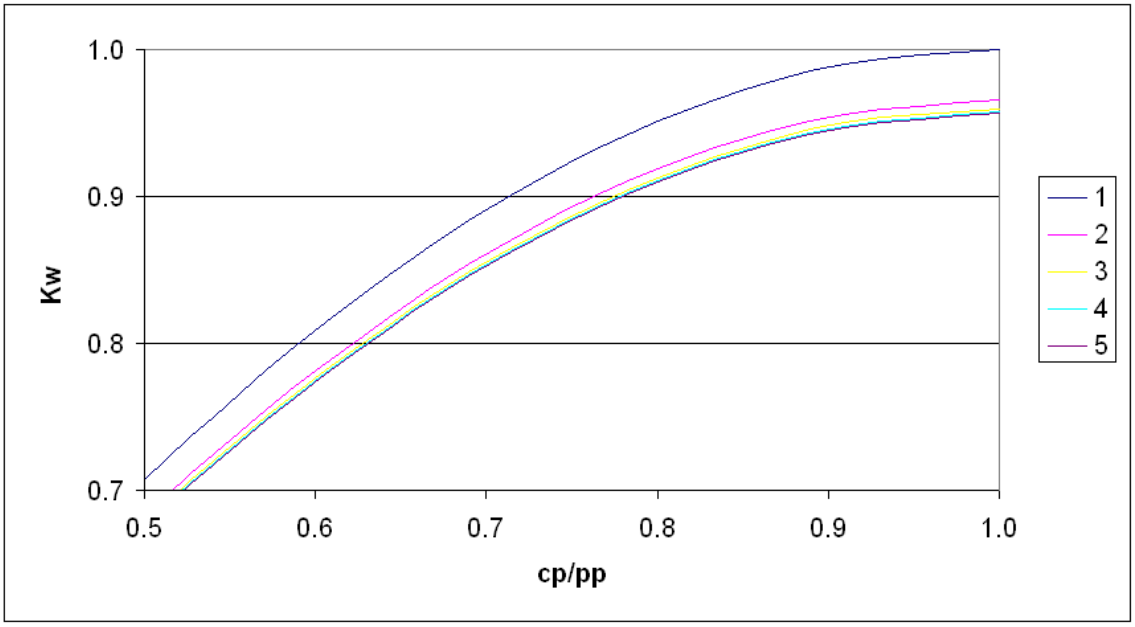

Fig. 57. Plot of winding factor variation with coil pitch, pole pitch and Spppp

The plot shows winding factors over a range of coil pitch/pole pitch ratios, with each plot line representing a different number of slots per pole and phase. The difference between this equation and the more complex spreadsheet method developed later is that the simple equation uses only simple data inputs. It works from overall coil pitch, pole pitch and S/p/p only.

This approach is very accurate when windings are completely regular and symmetrically disposed but does not take into account any of the unusual end conditions that may be present in linear motors. For instance short pitched coils or reduced S/p/p may be present in the ends of the machine, and this simple equation will totally ignore these differences.

This may not be particularly significant. For example, modelling a 5/6ths chorded 2S/p/p winding with half filled slots at the ends as in Fig. 58 with the simple equation gives a winding factor of 0.933. More advanced modelling of the full LIM winding with ends gives a winding factor of 0.927. This is a small difference. However more extreme end conditions may produce larger discrepancies.

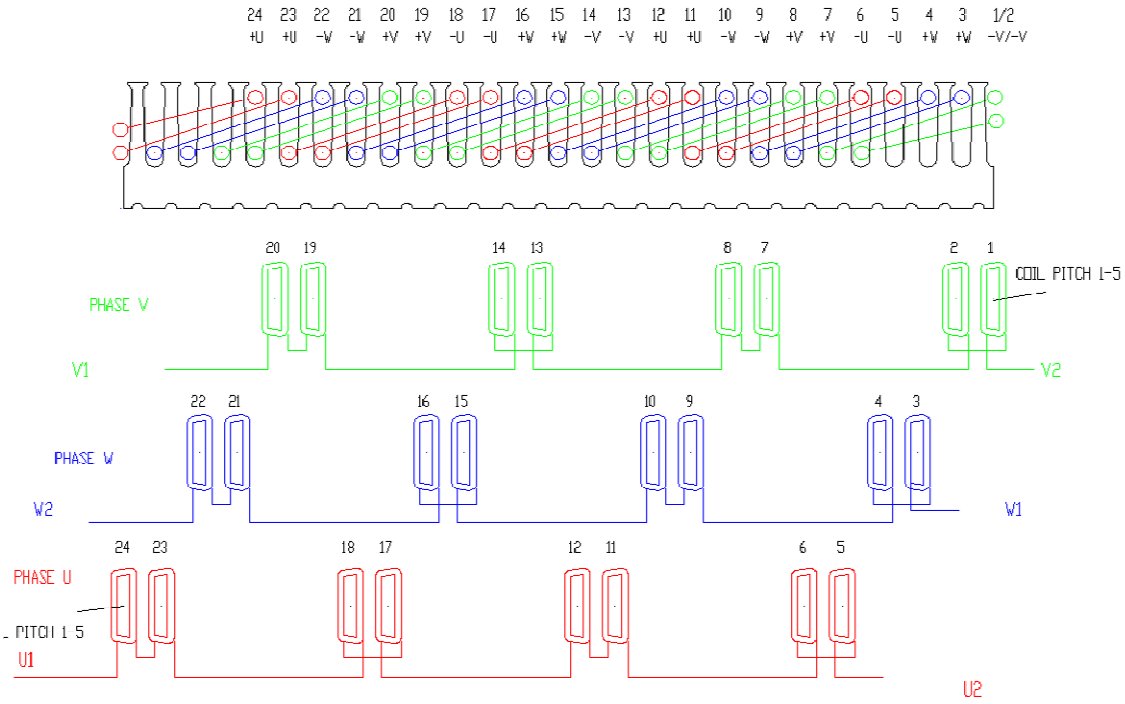

Fig. 58. 2 layer 5/6ths chorded 2S/p/p stator winding diagram

Also, single layer machines such as planar concentrated windings have no distribution factor, and any attempt to use the simple winding factor equation will result in a nonsense distribution factor greater than 1 due to the S/p/p being less than 1.

4.6.5. Machine Winding Factor Spectra

For each on the concentrated machines studied, full winding factor spectra have been produced using the methods described in the previous sections and in Appendices 1 & 2. Firstly, the winding factor spectrum of a 2 layer 2s/p/p 5/6ths chorded 4 pole linear induction motor winding as Fig. 59 above has been modelled to give a comparison.

Harmonic Poles	NPS	PPS
2	-0.011	0.007
4	-0.021	0.927
6	-0.025	0.004
8	-0.021	0.021
10	-0.007	0.040
12	-0.015	0.057
14	-0.040	0.066
16	-0.062	0.062
18	-0.076	0.047
20	-0.011	0.021
22	-0.066	0.011
24	-0.042	0.042

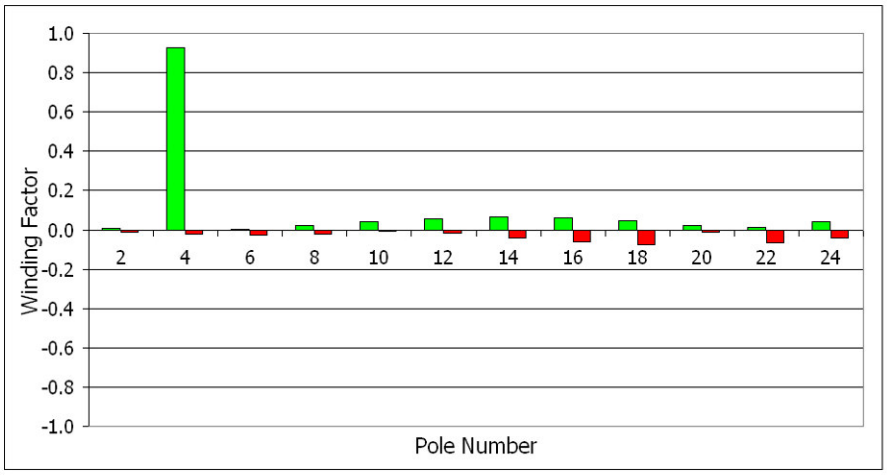

Fig. 59. Winding factors from spreadsheet of 2S/p/p 5/6ths chorded 4 pole winding

As would be expected, the winding contains a 4 pole harmonic of magnitude .927 and several extremely small positive and negative components. This is slightly less than the .933 predicted by simple winding factor calculations, this variation being due to the inclusion of half filled end slots.

The winding factor per harmonic is shown in Fig. 60 for a 6 coil 4-8 pole variant of the 3 coil 2-4 pole type concentrated winding.

Harmonic Poles	NPS	PPS
2	0.000	0.000
4	0.000	0.866
6	0.000	0.000
8	-0.866	0.000
10	0.000	0.000
12	0.000	0.000
14	0.000	0.000
16	0.000	0.866
18	0.000	0.000
20	-0.866	0.000
22	0.000	0.000
24	0.000	0.000

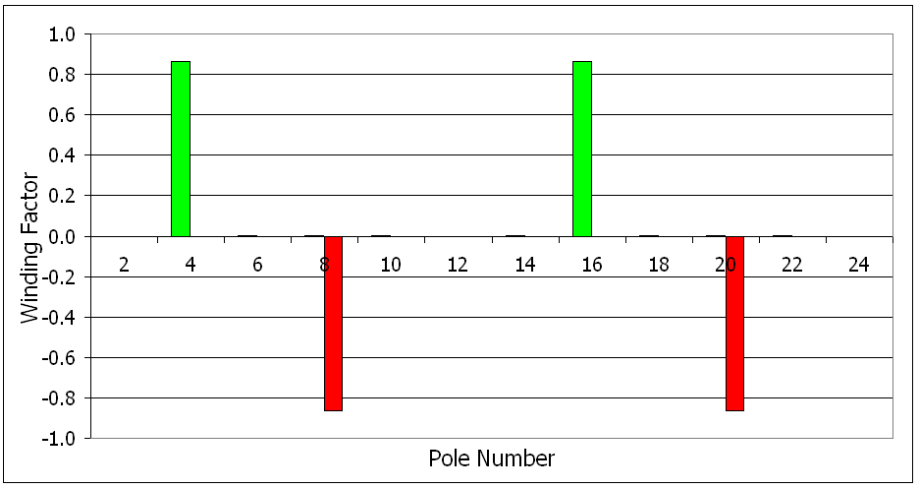

Fig. 60. Winding factor per harmonic for a 6 coil 4-8 pole concentrated winding

Next the winding factor per harmonic is shown in Fig. 61 for a 9 coil 8-10 pole concentrated winding.

Harmonic Poles	NPS	PPS
2	0.000	0.061
4	-0.140	0.000
6	0.000	0.000
8	0.000	0.945
10	-0.945	0.000
12	0.000	0.000
14	0.000	0.140
16	-0.061	0.000
18	0.000	0.000
20	0.000	0.061
22	-0.140	0.000
24	0.000	0.000

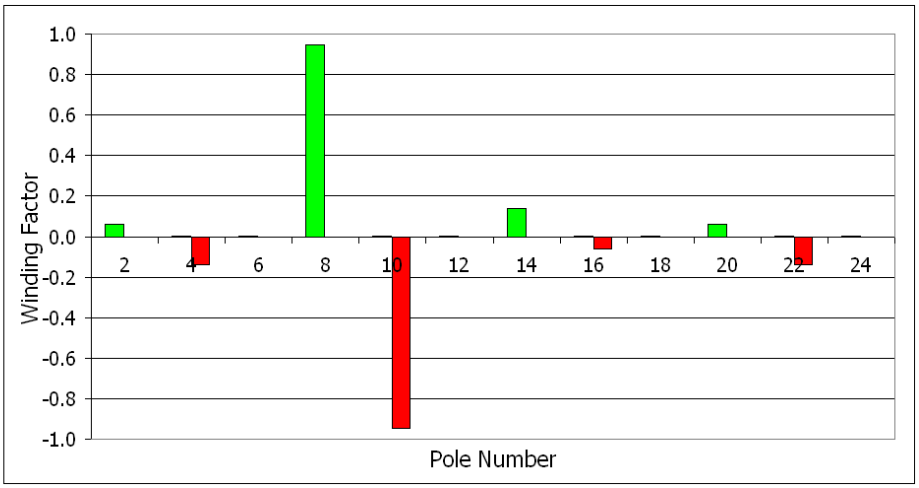

Fig. 61. Winding factor per harmonic for a 9 coil 8-10 pole concentrated winding

Finally the winding factor per harmonic is shown in Fig. 62 for a 12 coil 10-14 pole concentrated winding.

Harmonic Poles	NPS	PPS
2	-0.067	0.000
4	0.000	0.000
6	0.000	0.000
8	0.000	0.000
10	0.000	0.933
12	0.000	0.000
14	-0.933	0.000
16	0.000	0.000
18	0.000	0.000
20	0.000	0.000
22	0.000	0.067
24	0.000	0.000

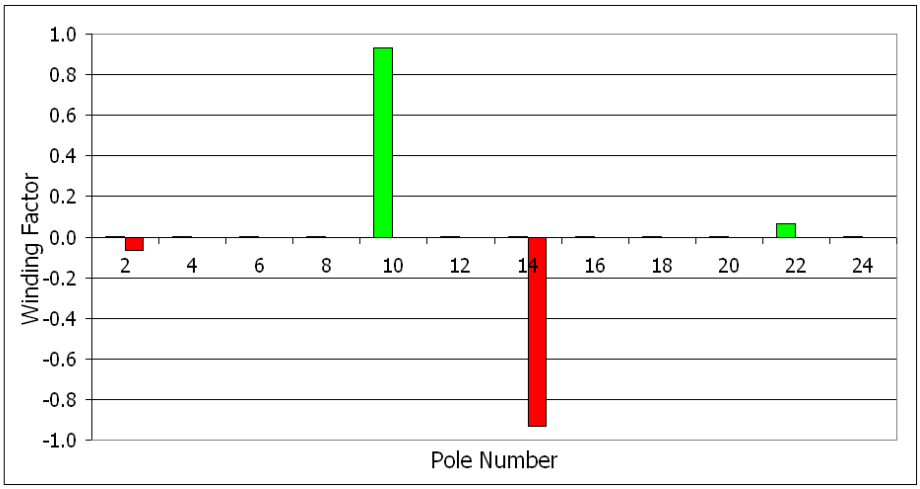

Fig. 62. Winding factor per harmonic for a 12 coil 10-14 pole concentrated winding

Good windings will generally have a single pole number with a high winding factor and very low or zero winding factors on any other harmonics. Positive and negative harmonics travel in opposite directions, so a motor will work well with a single dominant positive **or** negative harmonic.

As can be seen each concentrated winding stator produces two principal harmonics travelling in opposite directions. Each of these harmonics will be

present in the output of the stator, and can be observed by Fourier analysis of the flux waveform and by the effect on the rotor.

Because the sheet conductor used in a conventional LIM will respond to and produce force from every harmonic of the stator field the similar magnitude positive & negative harmonics produced from the concentrated winding will result in poor performance due to oppositional forces and extra losses in the plate rotor.

Concentrated winding stators have previously only been used successfully with permanent-magnet rotors. This works, as the permanent magnet rotor will only produce force from a mmf that has the same pole number. This means that the rotor works as a harmonic filter, accepting only the harmonic matching its own fixed pole number. This also allows a single concentrated winding stator to use various rotors with different pole numbers. For the concentrated winding stator studied, a permanent magnet rotor of either four or eight poles could be used.

In order to use a concentrated winding stator in an induction motor, a method must be developed to reduce the effect of negative harmonics to a point where the concentrated winding will provide an output comparable to that of conventional LIM designs.

5. Wound Rotors

5.1. Introduction

It has been determined that the poor performance of a concentrated winding with a sheet rotor is due to the detrimental effects of multiple stator harmonics. These harmonics increase rotor losses and will also decrease thrust in the required direction by generating opposing forces on the plate.

In rotary induction machines wound rotors are sometimes used, leading to some advantages in starting and speed control by rotor resistance insertion. Wound secondary linear machines are known [27][28][29]. Yamamura suggested a 'wound plate' for use with a double-sided machine and with the objective of reducing the entry and exit effects in a short stator machine.

A proposal of this project is to investigate the use of a wound rotor with a concentrated stator linear machine. As well as effects on harmonics, the benefits of wound rotors to other areas of linear motor performance will also be investigated.

Conventional stator windings are designed to have a high winding factor on the fundamental and low winding factors on harmonics. The detrimental effects of harmonics are suppressed, giving a better output transmitted from the stator to the rotor.

A double layer wound secondary will behave in a similar fashion to a permanent magnet secondary in that it will respond substantially only to the pole number for which it is wound. This is due to the winding factor controlling the induced emf being small except for the fundamental.

If a wound rotor is used with a concentrated winding stator the wound rotor may be designed to pick up on only the required fundamental. The wound rotor will ignore all other harmonics that would be accepted by a simple sheet rotor, in theory giving excellent performance from a simple, cheap stator winding.

In order to avoid force perturbations due to magnetic locking the secondary slots can be skewed. Alternatively a solution which is simpler mechanically can be adopted, using a fractional slot winding so that the mutual slotting pattern repeats only in the secondary length, as developed in Appendix 3.

The new principle of using a wound secondary so that simple modular primary windings may be used is described in the patent of [30] and papers [31][32][33].

Wound rotors are also possible for short stator machines and single and double-sided versions are shown in Fig. 63 and Fig. 64 respectively. Fig. 63 shows a single-sided short-secondary wound rotor linear motor where both the primary and secondary windings are contained in slotted cores. The primary has a long double layer winding provided with excitation currents and the secondary carries a winding which is short-circuited so that currents can be induced in it by the long stator.

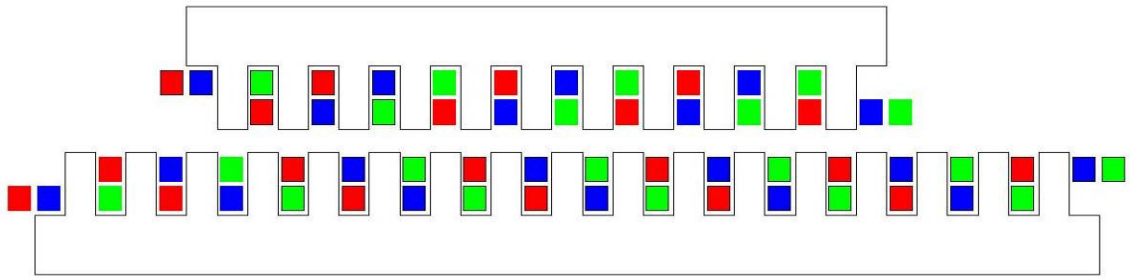

Fig. 63. A single-sided short rotor wound secondary machine

In the secondary shown in Fig. 64 the flux travels through the secondary so that the links between each of the rotor teeth are sized solely from mechanical considerations.

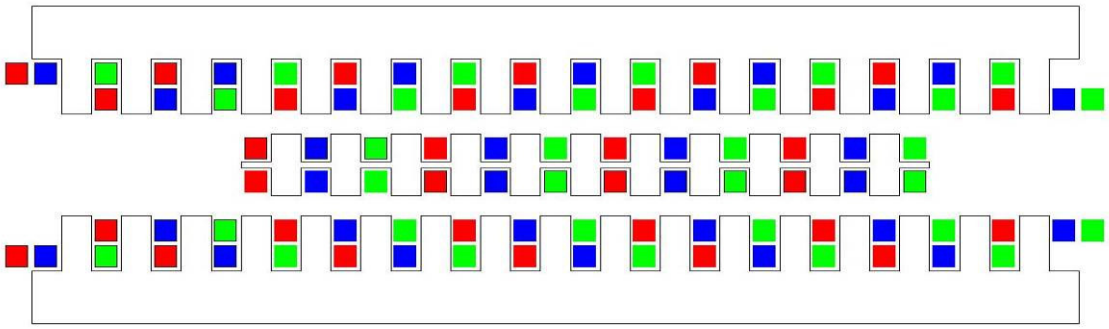

Fig. 64. A double-sided short rotor wound secondary machine

5.2. Wound Rotor Action

The wound rotor in the machine described above is used as a selector so that only one harmonic is effective. However wound rotors can improve the behaviour of linear motors apart from this effect [27].

The action of the wound rotor machine is different to that of the plate rotor machine because of edge effects. In a long stator arrangement the stator current is forced to be virtually constant by the impedance of the winding outside the active region. The flux density is therefore smaller inside the plate region where plate currents oppose the stator current than it is outside. As the edge of the plate moves between the flux densities in the two regions currents are induced at the plate edges that try to prevent the flux density change. These currents detract from the performance. Conversely in the wound rotor case since a series 3 phase set of coils take up position along the length of the secondary the winding current is the same along its length and there are no space transient effects [27].

5.3. Development of a Four Pole Wound Rotor

The first test cases used the 6 coil 4-8 pole concentrated winding stator (as used previously with a plate rotor) matched with a wound rotor using a special 4 pole winding designed to accept the 4 pole component and reject the 8 pole component of the field, designed in Appendix 3.

The winding used Fig. 65 was a special fractional slot 4 layer type with variable turns per coil in order to avoid locking with the stator.

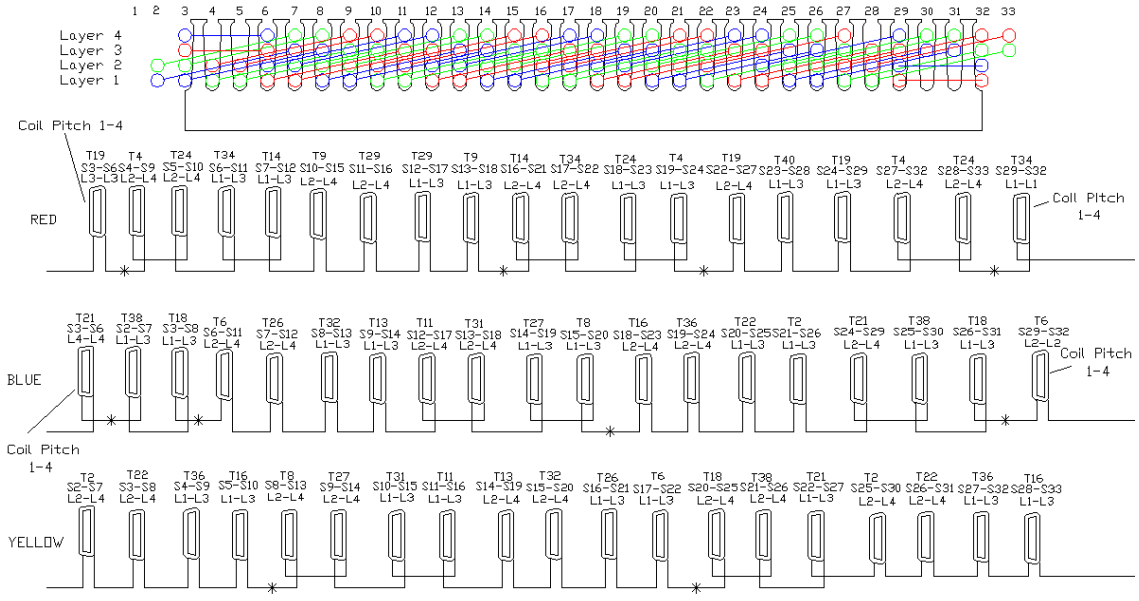

Fig. 65. Fractional slot 4 layer wound rotor winding diagram

5.3.1 Time Stepped Four Pole Wound Rotor FE Results

Fig. 66 shows the results of the Finite Element Analysis of force using a single-sided long stator machine carrying a planar concentrated LIM primary winding as described previously. This is modelled with two different secondary members, a plate conductor rotor 4 pole–pitches in length backed with an iron core and a slotted secondary carrying a multi-layer winding. Also shown are the results for a conventional stator of the same winding factor with a plate rotor.

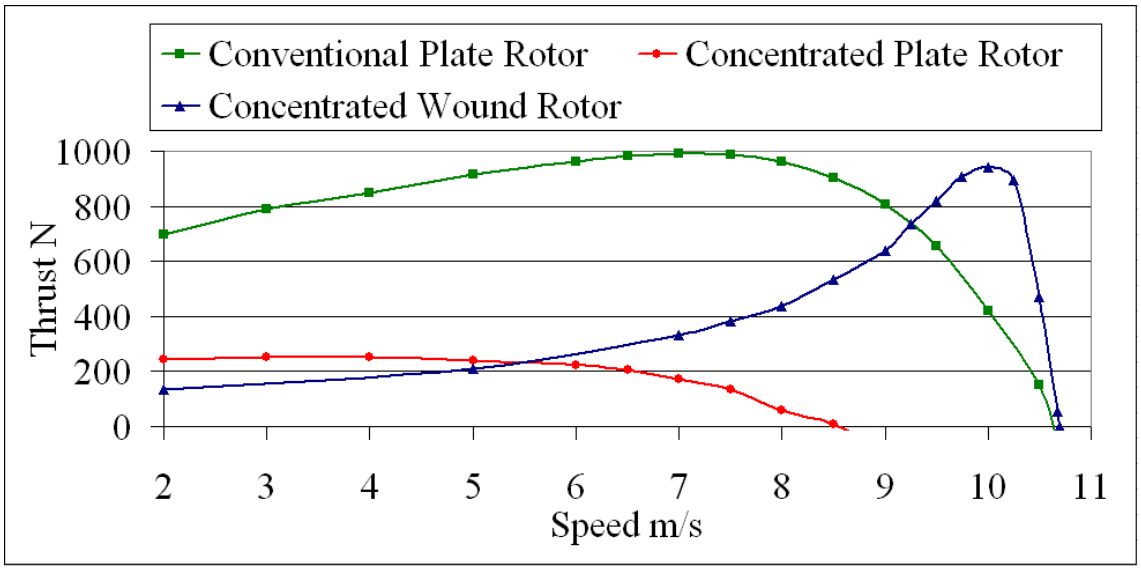

Fig. 66. 4 pole comparison between plate and wound rotors used with concentrated windings

5.3.2. Four Pole Experimental Rig Results

To verify the results of the finite element work, a practical wound rotor model has been made. A planar concentrated winding stator was constructed to use as the primary together with a wound secondary of identical pole pitch. This used a special winding in order to minimise locking forces. The secondary phases were connected in star at both ends to give the required rotor current paths. The rig used is shown in Fig. 67.

Fig. 67. 4 pole wound rotor static thrust test rig

The stator was mounted to a test bed, and the wound rotor was mounted above the stator, on a rig instrumented to record static thrust. The stator was fed through an inverter and the feed was instrumented to display the relevant inputs to the stator.

In order to gain results for various velocity points, variable frequency testing was used [12]. This test allows the prediction of dynamic performance from static test conditions.

The results of the testing are shown in Fig. 68, along with the results of finite element analysis. It will be observed that the agreement between the finite element and experimental results is excellent.

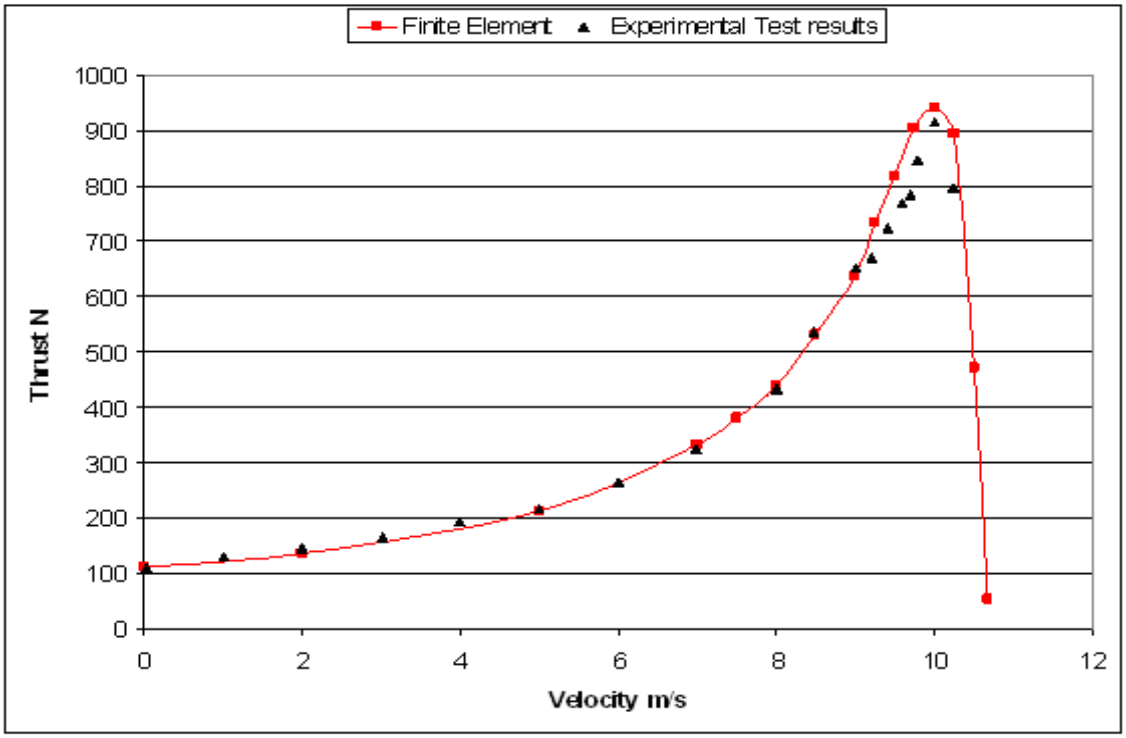

Fig. 68. Wound rotor concentrated stator thrusts from FE analysis and experiment

5.3.3. Four Pole Wound Rotor Concentrated Winding Results

The force speed characteristic of the concentrated stator using a wound rotor Fig. 66 is excellent with a good peak force and a high rotor efficiency of 92%. The good performance of the machine is due to the action of the secondary winding which has a high winding factor only on the pole number for which it is designed and therefore has induced emf, current and force only corresponding to that wanted pole number. The wound rotor machine therefore has an action that is analogous to that of a permanent magnet rotor and selects the four-pole fundamental field.

The experimental method neglects end effects, whilst the FE method takes them into account. As the experimental results and FE predictions are in close agreement, this indicates that the end effects are negligible for the configuration analyzed.

5.4. Eight Pole Wound Rotor Design

A further wound rotor design was developed in order to evaluate the wound rotor performance with a higher pole number winding more apt for launcher and high speed transport use. This design used a 9 coil 8 pole type concentrated planar winding stator. A fractional slot 8 pole wound rotor was developed using 4 slots per pole and coils with a pitch of 3 slots Table 14.

Table 14: Table of slot contents for wound rotor

8-pole 32 slot fractional slot rotor winding

Coil Number	1	2	3	4	5	6	7	8
Coil phase & connection	R	R	-B	Y	-R	B	B	-Y
Coil Number	9	10	11	12	13	14	15	16
Coil phase & connection	R	-B	Y	Y	-R	-R	B	-Y
Coil Number	17	18	19	20	21	22	23	24
Coil phase & connection	R	-B	-B	Y	-R	B	-Y	-Y
Coil Number	25	26	27	28	29	30	31	32
Coil phase & connection	R	R	-B	Y	-R	B	B	-Y

The winding factors of each pole number for the rotor winding are shown in Fig. 69. The sign of the winding factor indicates direction of travel for each harmonic.

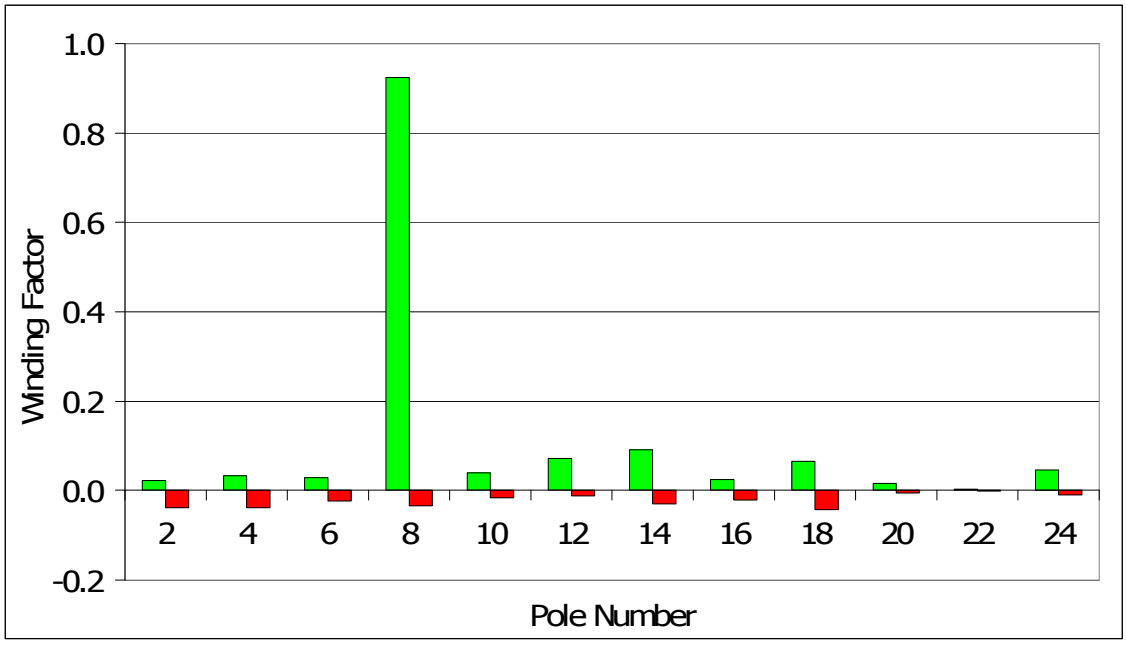

Fig. 69. Winding factors of the wound rotor

It can be seen that this rotor has a large 8 pole winding factor, with only very small winding factors for harmonics of other pole number, particularly the 10 pole harmonic, as this is the significant negative harmonic of the stator.

5.4.1 Eight Pole Wound Rotor FE Results

Fig. 70 compares the response of an 8 pole short plate rotor first to a double layer winding with small harmonic content and secondly to the 9 coil modular winding described previously. The results for a wound secondary are also shown in Fig. 70. These results were obtained by time stepped FEA modelling using the MEGA package.

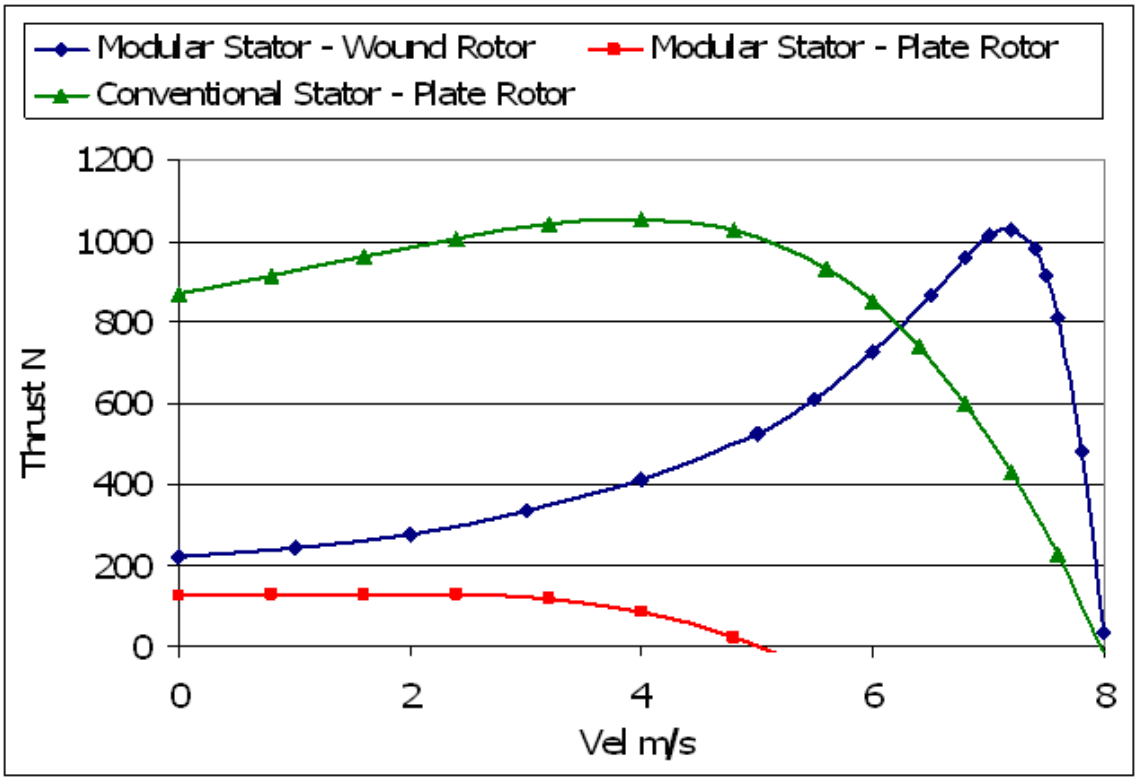

Fig. 70. Thrusts for wound rotor with modular stator, plate rotor with conventional & modular stator

The response of the winding is again excellent; the peak force is closely the same as when a double layer stator and plate rotor is used but the peak is closer to the synchronous speed and since secondary efficiency is given by

1/slip this indicates a much better secondary efficiency (92% compared to 52%).

Further comparisons can be drawn from Fig. 70 with regard to the performance of wound and plate rotor machines with short rotors. As argued previously the stator current is approximately constant in a short rotor induction motor. In this circumstance the peak of the force speed curve occurs at a slip of approximately $R_2/(X_m+X_2)$ [34] where R_2 is the referred secondary resistance, X_m is the magnetising reactance and X_2 is the referred secondary leakage reactance.

The force speed curve for the wound rotor has a high force low slip characteristic with a peak that implies that the ratio of $R_2/(X_m+X_2)$ is low. In contrast, the plate rotor shows a drooping characteristic, indicating that the ratio of $R_2/(X_m+X_2)$ is higher in the plate rotor case than in the wound rotor case. Based on machine parameters, both magnetising reactance and referred secondary leakage reactance are likely to be higher in a wound rotor machine, while rotor resistance is likely to be lower in the wound rotor case. The difference in the characteristic of course follows from the physical arrangement.

The magnetising reactance is governed by the inverse of the magnetic gap. This is small in the wound rotor case since it is set by the clearance. In contrast the magnetic gap is larger in the plate rotor machine since it is governed by the clearance plus the plate thickness. It follows that the magnetising reactance tends to be larger in wound rotor machines.

The referred secondary leakage reactance is likely to be greater in wound rotor machines. A. In plate rotors, secondary leakage reactance is generally small in comparison to primary leakage reactance and is often neglected. A wound rotor generally uses multiple turns per coil, and inductance is proportional to turns squared. This means that the secondary leakage reactance of the wound rotor

is generally of the same order of magnitude as the primary leakage reactance and must be included.

The secondary resistance in the wound rotor case is set by such factors as the slot dimensions and can be arranged independently of the magnetising reactance and designed to be small. However in the plate rotor machine the secondary resistance and magnetising reactance are closely linked. For example if the plate thickness is increased to produce a lower resistance the magnetic gap is also increased reducing the magnetising reactance. This tends to keep the ratio of R to X_m the same and it is difficult to change the shape of the force speed curve. It follows that the wound rotor machine will always have a design advantage and be more easily arranged to have a low peak slip high peak efficiency characteristic.

5.4.2. Eight Pole Wound Rotor Experimental Results

A test rig has been constructed to prove this principle using 9 slot 8/10 pole stator winding sections. This cooperates with a short wound rotor carrying the fractional slot double layer 8 pole winding described above. Tests were performed using the standstill variable frequency principle [12] to estimate the dynamic response of the system and the results are plotted on Fig. 71 at 10A constant current for comparison with FE standstill variable frequency results. It will be observed that the correlation is excellent. This shows that end effects are again negligible for the wound rotor configuration analysed.

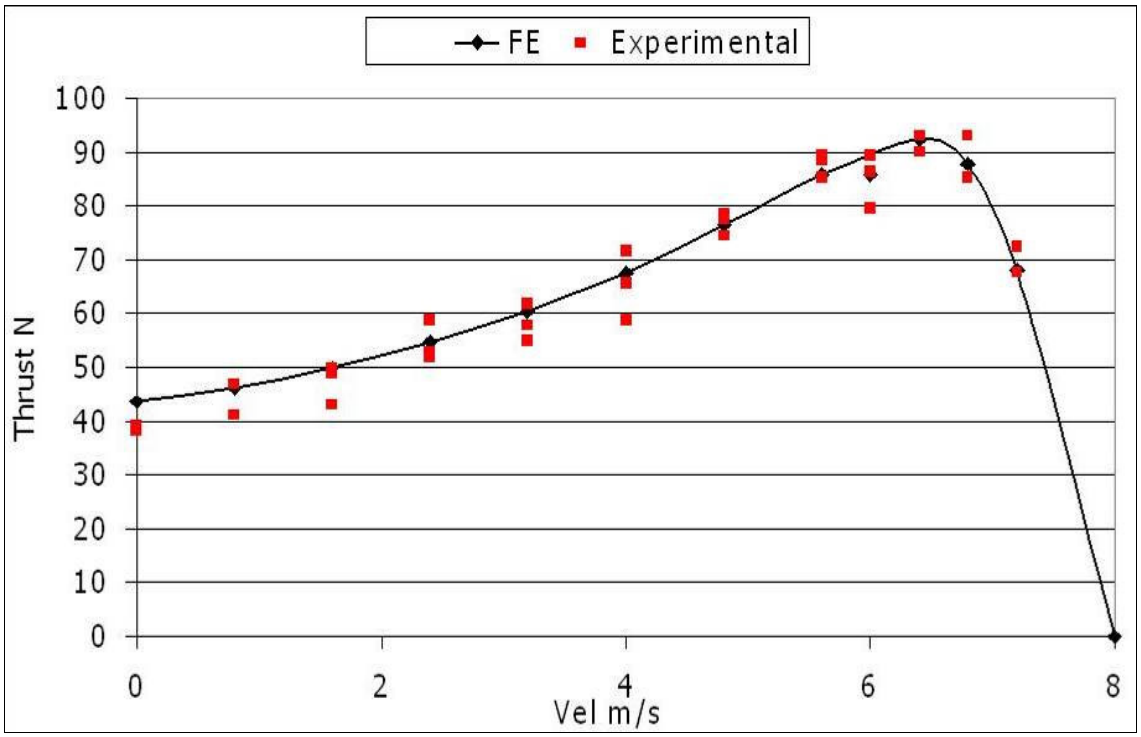

Fig. 71. Wound rotor experimental and FE results

The work has shown by time-stepped finite element modelling validated by experimental results that 9 coil 8 pole type modular windings in which the coils do not overlap can be used for linear induction motor stators when wound rotors are employed. The new arrangement enables inexpensive stator modules to be used in EM launch and urban transport systems. These systems will display a good peak force and efficiency.

5.5. Further FE Comparisons of Conventional and Concentrated Machines

Further finite element analysis was performed in order to get a better idea of wound rotor performance. Extra FE models were produced to represent concentrated and conventional winding stator tracks using both wound and plate short rotors. These motors have been modelled over a range of rotor speeds.

The four motors represent the following cases:

A regular, repeating track of conventional stators with a reaction plate rotor, as a standard to judge against. This is the system currently used in LIM systems, although this is an idealised case. In reality a track consists of a row of individual motors with some half-filled slots, rather than a continuous track. This was used as it would give a good benchmark to measure other systems against, as exceeding the performance of the idealised system must also exceed the performance of the non idealised real world system.

A track consisting of concentrated winding stators with a reaction plate rotor. This will allow the judgement of the performance of a concentrated winding without any compensation for the detrimental motor harmonics.

A track consisting of concentrated winding stators with a wound rotor. This will allow the judgement of the performance of a concentrated winding stator track when a wound rotor is used to filter out unwanted harmonics.

A track consisting of conventional stators with a wound rotor. This will allow us to investigate the differences in performance of the wound rotor with two different stators.

The conventional motor was based on a typical low speed LIM design. This motor was redesigned to give a continuous stator track. The characteristics of this motor are as follows
Winding: 3 phase, 4 pole, 2 Slots per pole and phase, 5/6 corded, 40 turns per coil, pole pitch 0.1068m
Stack: Length 0.4272m, Width 0.1m, Height .0748m, 24 slots, slot pitch .0178m

The concentrated winding motor was a 3 coil 2-4 pole track designed to have a matching pole pitch to the conventional stator. This allowed the same wound and sheet rotors to be used on both stators, and easier comparisons to be drawn between the two systems.
Stack: Length 0.4272m, Width 0.1m, Height .067m, 5 slots, slot pitch .0712m

Winding: 3 phase, 4 pole, 0.5spppp, 160 turns per coil, pole pitch 0.1068m

The plate rotor is a 4-pole length plate (.4272m). Its width is 0.1m. The aluminium conductive section is .0035m thick, with 0.014m depth of steel backing. The resistivity of the conductive material in the rotor was taken as $4.3x10^{-8}$ Ohm m, which represents a grade of aluminium commonly used in low speed LIM systems.

The wound rotor uses a special 4 layer 23 slot 4 pole non locking winding as defined previously Fig. 65. The winding is 3 phase, connected in star at both ends. The rotor length is .4272 and the pole pitch is 0.1068m. The resistance across one phase of the wound rotor was taken as 1 Ohm, as this is approximately equivalent to the stator resistance.

The stators were connected in star, and current driven at 27A rms. Current sourcing the model essentially simplifies the model by allowing the current flowing in the stator winding to be set directly, without setting up a whole electrical system. This situation would usually occur only if the motor input were controlled. Because they were current driven, the stators were modelled without resistance.

The models were time stepped, with a time step being taken every 0.0005 seconds. As a continuous track was used, the finite element models were run until a stable thrust pattern had been established. This was in order to give results without any transient effects.

5.5.1. Thrust Speed Curves

Thrust speed curves were calculated for the motor set ups that are detailed above. The thrust speed curves for all 4 motors can be seen below in Fig. 72.

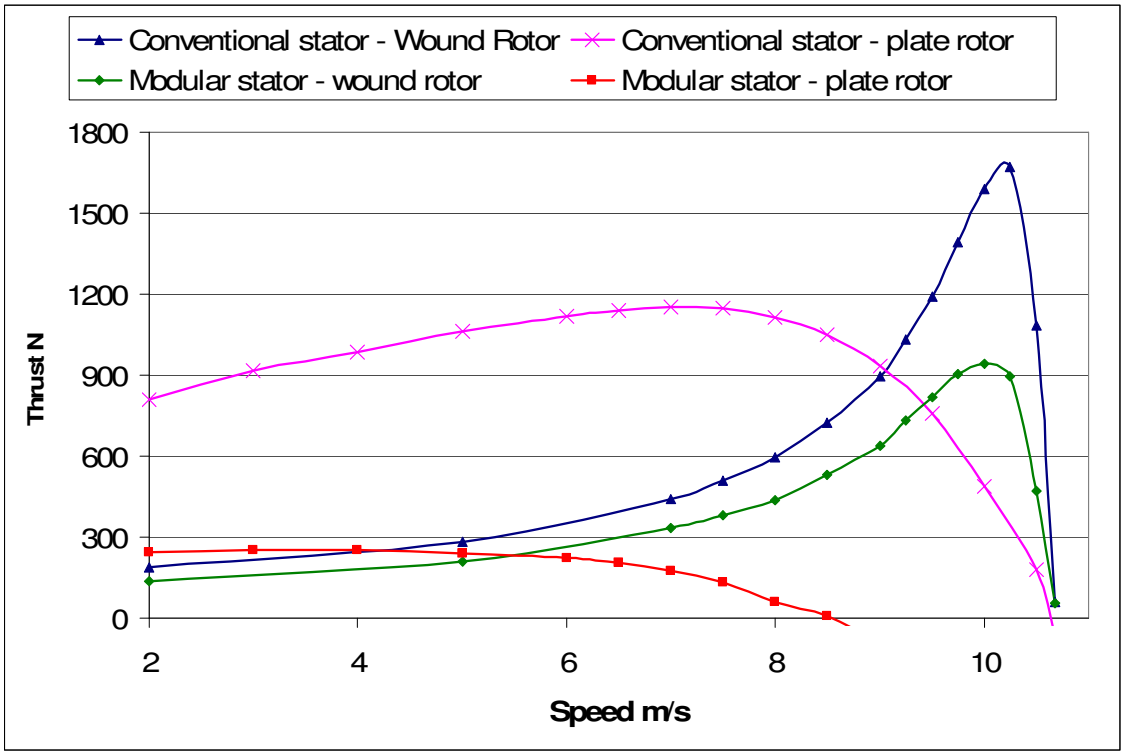

Fig. 72. Thrust speed curves for wound & plate rotor FE element models

As can be seen from Fig. 72, the plain concentrated winding with a plate gave very poor performance, with a low level of thrust that went negative well before synchronous speed.

When a wound rotor was used with this winding however, the thrust profile was vastly improved, giving a thrust profile only around 20% less than a fully optimised conventional type stator with a plate rotor.

Further optimisation of the concentrated winding, specifically improving the packing factor to a level easily possible with concentrated windings will improve the force output by 1.61 times. This will give a value of force for the concentrated stator with a wound rotor that is comparable to that of the conventional stator with a wound rotor, and much greater than that of the conventional stator with a plate rotor.

The other case, the conventional type stator with a wound rotor performed extremely well, giving an excellent peak thrust output. The peak thrust developed was 30% higher than with a plate rotor.

The rotor efficiency at peak force in both wound rotor cases was around 90% whilst the efficiency where substantial force was produced (7 m/s) in the plate rotor case was 62%

5.5.2. Variable Frequency

The Mega models for the conventional LIM stator with both rotors were now re run with a supply frequency of 25Hz. This test was used in order to gain an understanding of wound rotor motor performance with variable frequency. The results of this can be seen in Fig. 73.

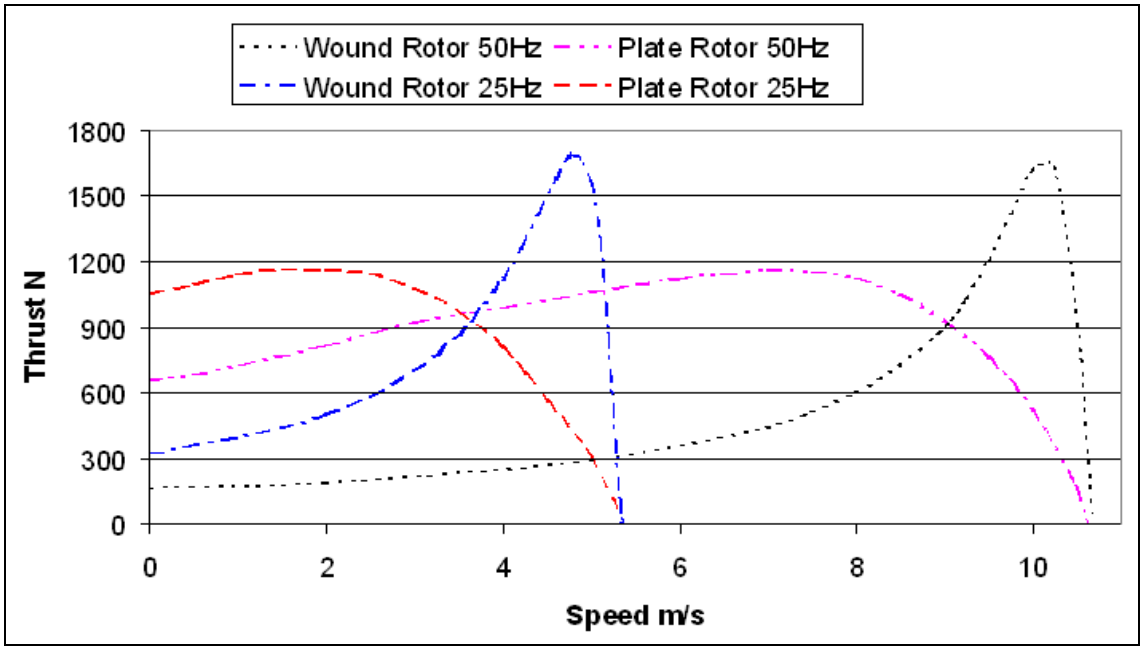

Fig. 73. Calculated thrust speed curves for wound and plate rotors at 50 and 25 Hz

Launcher machines are generally supplied at variable frequency from an inverter. Fig. 73 shows that the peak force available from the wound rotor remains as high at 50% frequency.

It was found from the frequency runs that the peak thrusts and shape of the thrust speed curve remained unchanged. The velocity values at which these thrust points occurred were effectively halved. The significance of this result is that if a wound rotor system is frequency controlled, the peak thrust can be altered to occur at any required velocity.

5.5.3. Normal Forces

Normal forces occur between stator and rotor for all four models. These represent stator to rotor normal force for a single-sided case, or stator to stator normal force for a double-sided case. These can be seen in Fig. 74.

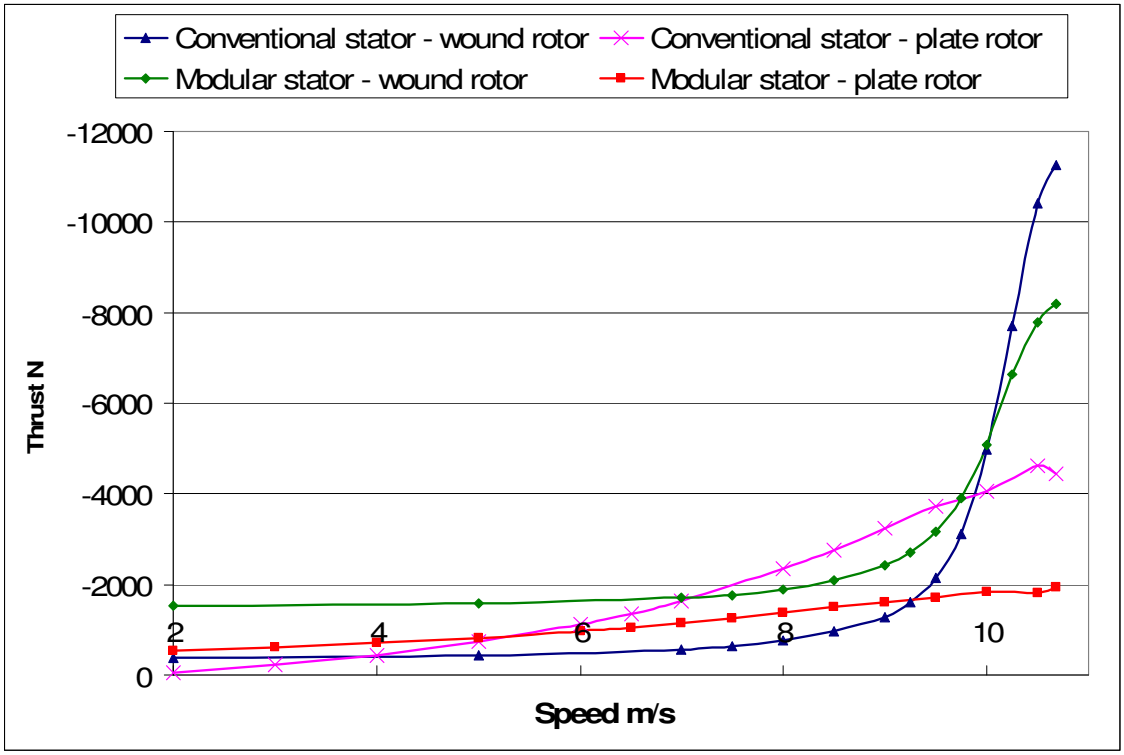

Fig. 74. Stator to rotor normal forces

As can be seen from Fig. 74, while normal force for both plate rotor systems remains linear, both wound rotor systems develop a large peak attraction force near to peak thrust. For the conventional stator, peak wound rotor force is 2½ times peak plate rotor force.

This extra force is mainly due to the significantly reduced steel-steel gap. This has the potential to cause problems, as 8-12kN attraction forces would require additional rigidity in the support structure to compensate.

Single-sided machines of both plate and wound rotor types suffer from normal forces between the primary and the secondary and problems of secondary weight. The single–sided wound machine is more apt for urban transport systems (where a horizontal gap is of advantage) rather than EM catapult launch systems. Double-sided machines are usually favoured for EM launch and double-sided iron-cored arrangements are possible. These largely deal with the normal force problem but the weight penalty remains. For some applications an air-gap type wound rotor construction as in [27] could be advantageous.

5.5.4. Variable Resistance

To find the behaviour of the wound rotor when its resistance is modified, the phase winding resistance was varied between 1 and 8 Ohms, and the thrust speed curve was produced for each rotor resistance Fig. 75.

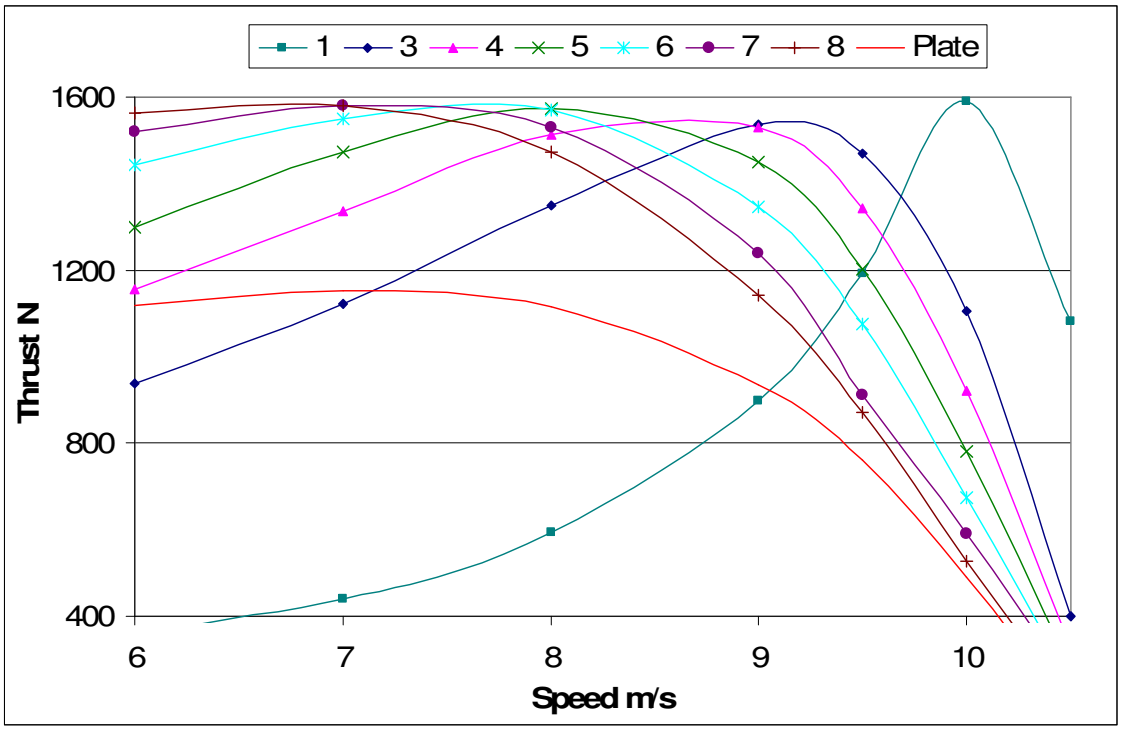

Fig. 75. Thrust speed curves for various values of rotor resistance in Ohms/phase

As can be seen, the variation of rotor resistance causes the peak thrust to occur at a lower rotor velocity. This is a very important characteristic, as it indicates that the secondary resistance can be varied in order to improve the performance of the motor at various rotor velocities. The conventional LIM with a plate rotor has been included for comparison. Its resistivity is optimised for 6-7m/s. As can be seen From Fig. 75, the output thrust is still much less than that of a wound rotor optimised to 6-7m/s.

The resistance may be chosen to optimise performance at a particular point. An alternative available with the wound rotor is to use variable extra rotor resistance to give peak thrust at any current velocity, giving a method of speed control.

5.5.5. Thrust per Kilo

Thrust per Kg represents the thrust on the rotor per kilo of total motor weight. This is an important factor in fields such as aerospace, where machine weight can be much more critical than production cost or efficiency. The weight of the two motors has been worked out according to simple calculations of mass of copper and iron in the stator and rotor. These were 25.8Kg for the conventional LIM, 21.8Kg for the concentrated winding, 10.9Kg for the plate rotor and 29.5Kg for the wound rotor. From this, the thrust per Kg motor weight was worked out, and is shown below in Fig. 76.

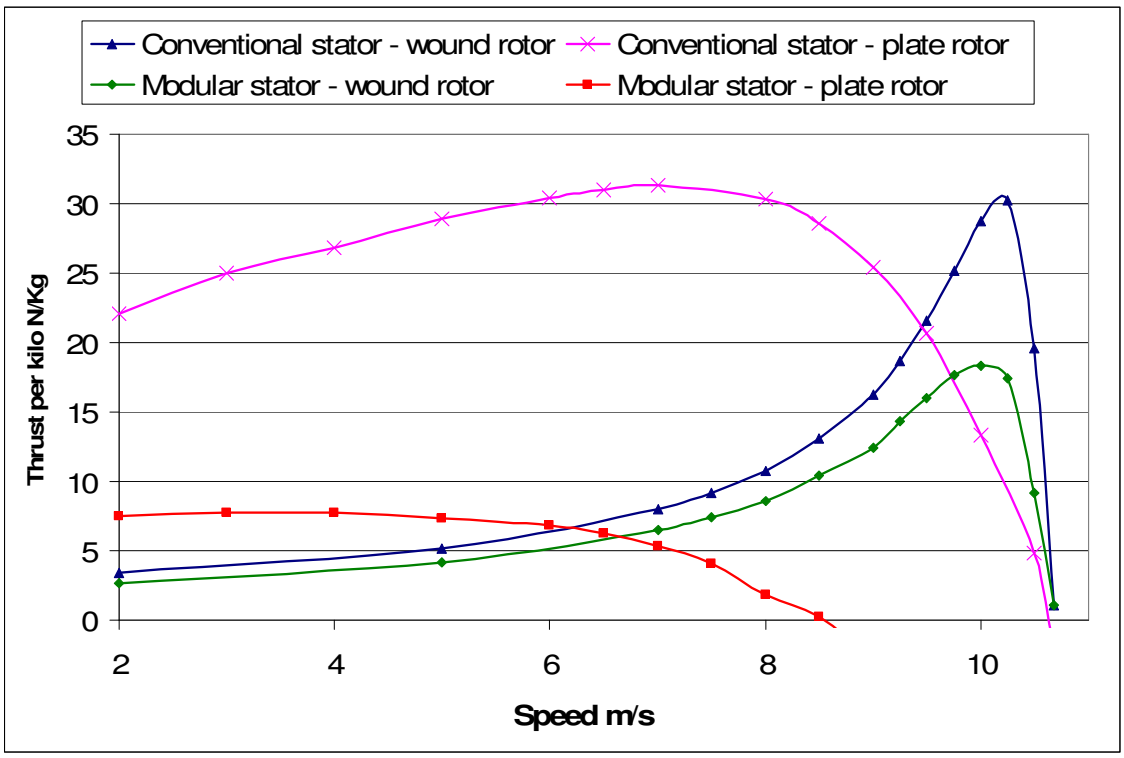

Fig. 76. Thrust per Kg motor weight against speed

This measure is useful, as the extra weight of the wound rotor will be a detrimental factor when compared with a plate rotor. Fig. 76 shows that the thrust output per kilogram is almost identical for the conventional single-sided LIM stator with a plate and with a wound rotor, indicating that improvements in thrust will often be balanced out by gains in rotor weight. However, for a double-sided wound rotor, the weight of the rotor would not be much greater than that of an equivalent plate rotor.

It must also be noted that this calculation only accounts for the immediate weight of the motor. The increased normal forces shown in 5.5.3. may require additional structural support which will add further weight to the overall wound rotor systems and reduce thrust per kilo further.

5.6. Simple Modelling Techniques

A simple technique has been developed to model the performance of the wound rotor machine. The LIM equivalent circuit is shown in Fig. 77.

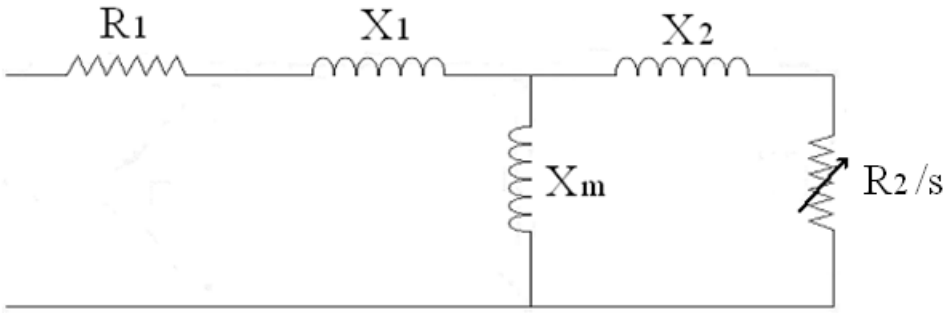

Fig. 77. The LIM equivalent circuit

For a stator with a plate rotor, R_1 represents stator resistance, X_1 represents stator leakage reactance (made up principally of slot and end turn leakage reactances), X_m represents magnetising reactance, R_2/s represents referred rotor resistance modified by slip for velocity conditions, and X_2 represents referred rotor leakage reactance.

To represent a wound rotor, X_2 is replaced with the slot and end turn leakage reactances of the rotor and R_2 is replaced with rotor resistivity modified by slip for velocity conditions. Wound rotor end turn and slot leakage reactance and rotor resistance can all be calculated very simply using the same equations as for the stator. Magnetising reactance stays the same, except that a second Carter's coefficient must be applied due to the slotting in the rotor surface.

Modelling of wound rotors with concentrated stators is slightly more difficult as non standard equations must be used to develop some of the stator characteristics. An equation for end turn leakage reactance has been developed previously and can be used. Several other formulas must be adapted such as primary resistance, winding factor and Carter's coefficient.

The performance of the 4 pole wound rotor is shown in Fig. 78 with a 2 layer stator winding and in Fig. 79 with a concentrated stator winding using the same packing factor as the 2 layer winding. The agreement between the three methods in both cases is good.

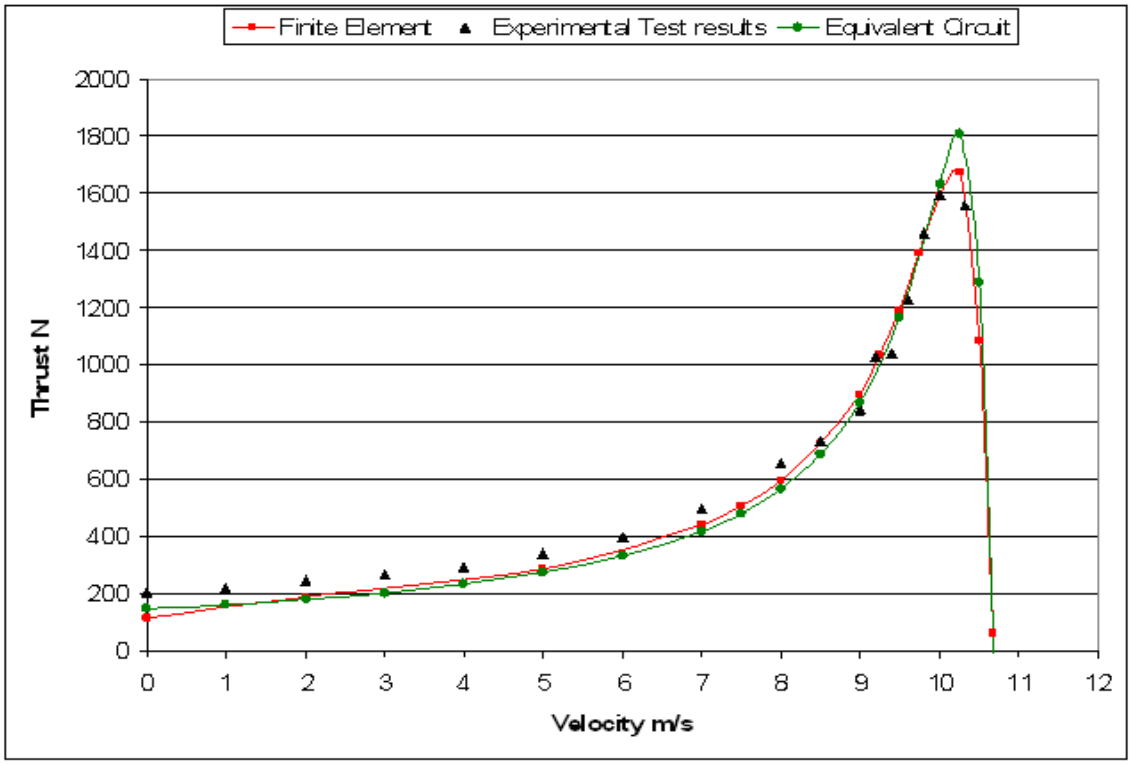

Fig. 78. 2 layer stator with a wound rotor FE, experimental & equivalent circuit thrusts

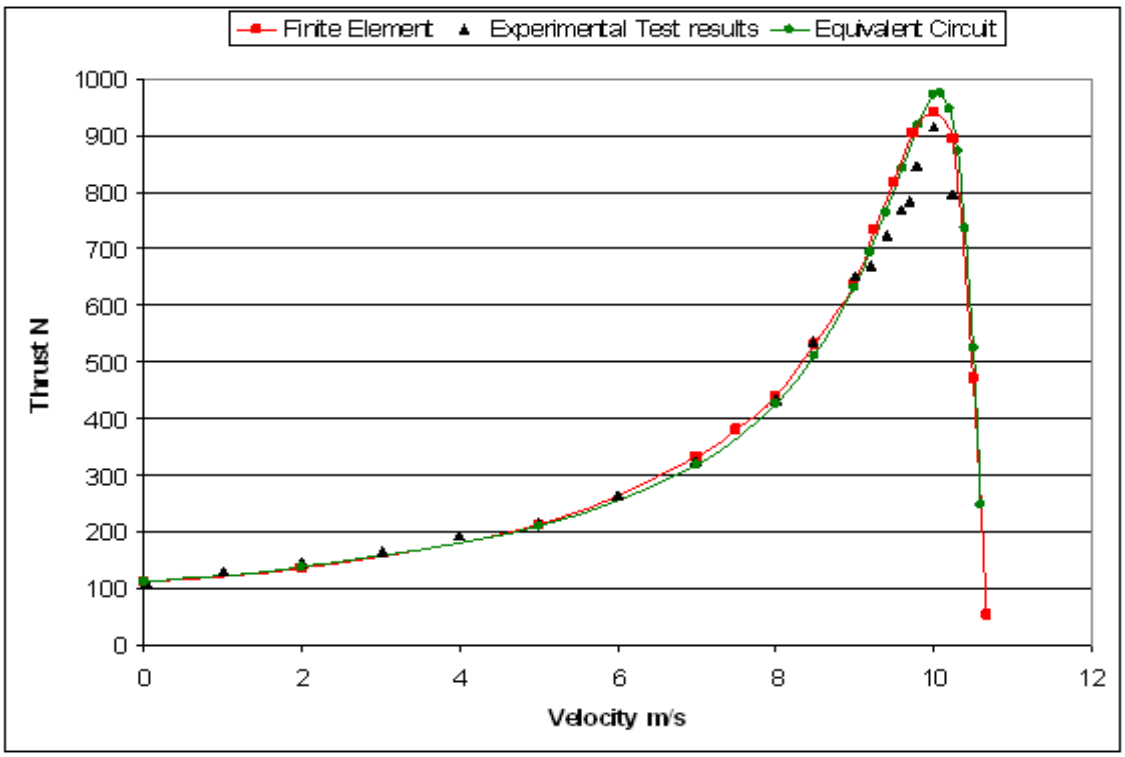

Fig. 79. Concentrated stator with a wound rotor FE, experimental & equivalent circuit thrusts

Time stepped finite element analysis takes into account the edge effects from a short rotor machine. The equivalent circuit analysis uses only one harmonic field and therefore does not. Since the force results from the finite element work and the equivalent circuit analysis are in close agreement it can be deduced that the edge effects in a wound rotor linear machine are negligible for the geometry analysed. The time taken to compute the equivalent circuit analysis is only a few seconds whereas the time step solution can take several hours.

5.7. Conclusions and Advantages

The wound rotor used with a planar concentrated stator winding provides an excellent novel arrangement [30][31][32][33] and can be applied to both low speed and high speed applications. For example it would enable an inexpensive concentrated winding track arrangement for use with an urban transport system.

The use of wound rotors also enables design freedom. This means that higher forces and efficiencies become available, with the ability to generate high thrusts at lower slips and a reduced size and cost of the overall system, including a reduction in the size and cost of power conditioning equipment.

Wound rotors allow the designer to tune R_2 and X_2 to give any desired performance characteristic, and these could even be altered dynamically to give peak thrust at any current speed. Another possible use is power pickup, using power in the rotor that would otherwise be wasted as heat to supply onboard systems.

The force output from FE modelling and equivalent circuit analysis is similar, indicating that edge effects in a wound rotor linear motor are negligible. This will result in enhanced performance, particularly at higher speeds where end effects become very significant.

The use of a wound rotor also allows the working airgap to be significantly decreased, as the steel to steel gap no longer includes the thickness of the reaction plate.

The thrust speed characteristic of a wound rotor system can be designed to closely resemble that of a conventional (rotating) machine. This indicates that known control methods such as flux vector control can be used, simplifying control expertise and equipment needed.

The use of a rotor winding also opens up the possibility of control by modifying the shape of the thrust speed curve through the addition of variable resistance in the rotor.

If we apply all of these ideas in an example, the advantages of this system become apparent. An urban transport system could be developed using concentrated stators and wound rotors. A wound rotor would be used on the vehicle with thyristors to modify the rotor resistance and hence provide speed control. Potentially, an inverter could be used to draw off useful power from the rotor for onboard systems.

The track would be made up of cheap, mains voltage and frequency supplied concentrated windings, with simple proximity activated on off switching. No inverters or complex control equipment would be needed for the stators. (Power factor improvement may still be required).

Not only would the stator cost be less than with regular LIMs, but there would be a huge saving due to removing or greatly reducing the need for power conditioning equipment on the stators (which often costs more than the stators themselves).

The efficiency of the system would be high due to the reduced airgap & secondary resistance and the increased secondary leakage reactance. There would be virtually no edge effects at speed, as shown by the experimental work within this section and in [27].

6. Short Rotors

6.1. Introduction

Linear induction machines are in use for leisure ride launching and have been proposed for use in aircraft launchers. A typical launcher topology consists of a double-sided long stator arrangement with a short conductive plate secondary. In this configuration rotor end effects are present which detract from machine performance. This topology also requires a relatively large magnetic gap. The configuration has been considered for conveyor application [35]. Mathematical modelling and FE will be used to compare the performance of short rotor machines having various plate lengths with conventional machines of the same air gap geometry [36].

6.2. Double-Sided Geometry

A double-sided short rotor linear induction motor is illustrated in Fig. 80.

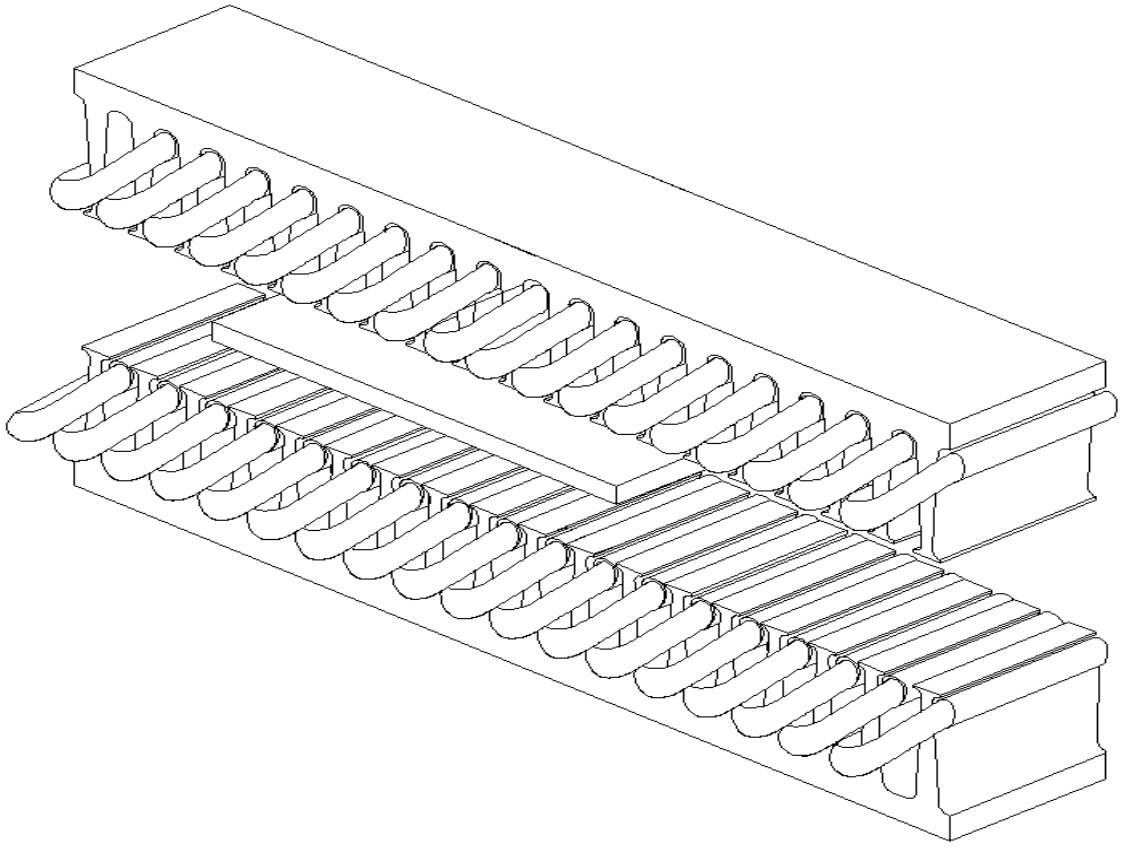

Fig. 80. Double-sided short rotor linear induction motor

The stators may be constructed of separate sections arranged with a minimum of longitudinal gap between a motor and its neighbour, or as continuous blocks. The analysis assumes that these gaps are small and that the stators are long so that the input current may be considered to be constant due to dominant impedance of the stators outside the plate region.

6.3. Analytical Modelling Method

An analytical method [35] was evaluated. This gives a method of modelling short rotor behaviour without the need for complex and lengthy FE solutions. This method uses the idealised geometry shown in Fig. 81.

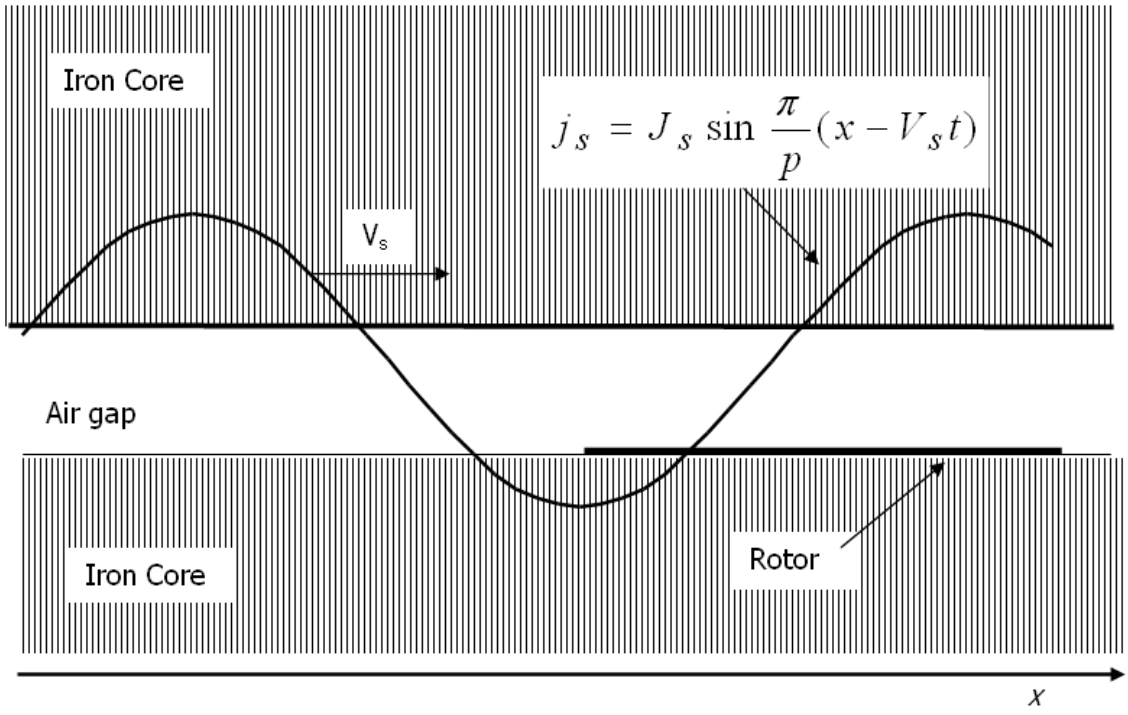

Fig. 81. Geometry assumed to develop the analytical force expression

This, as in the FE case needs to represent only one half of the problem. Here the stator and rotor core iron are both considered to be infinitely long, to have zero conductivity, and to have infinite permeability. The rotor and stator currents are assumed to be concentrated in infinitely thin sheets that lie on the surfaces of the cores, the stator sheet is infinite in length whilst the rotor current is confined to the length of the short rotor. The air-gap flux is assumed

to have no component in the direction of motion so that the flux crosses the gap normally. The equation for the force per metre of stack length, F, developed in the reference for these conditions is given below:

$$F = \frac{1}{2} J_s^2 a \frac{\rho_r}{v_s} . \frac{\sigma}{\sigma^2 + 1/G^2} [1 + Y(Z_1 + Z_2)] \tag{60}$$

Where

$$Y = \frac{1}{k[\cosh 2mk - \cos 2mk]} \tag{61}$$

And

$$Z_1, Z_2 = \frac{1}{m^2 + (m \pm 1)^2} \left[\begin{array}{l} [(m \pm 1)\sin 2mk - m \sinh 2mk \\ -2(m \pm 1)\sin mk.\cos k.\cosh mk \\ +2m \cos mk.\cos k.\sinh mk] \\ +\sigma G[m \sin 2mk + (m \pm 1)\sinh 2mk \\ -2m \sin mk.\cos k \cosh mk \\ -2(m \pm 1)\cos mk.\cos k.\sinh mk] \end{array} \right] \tag{62}$$

With Z1 taking the upper and Z2 the lower signs and:

$$G = 2p^2 \mu_0 f / \pi \rho_r g \tag{63}$$

$$k = \pi a / p \tag{64}$$

$$m = \sqrt{\sigma G / 2} \tag{65}$$

Where:

σ = slip

a = plate length, m

Js = Current density A / m

Vs = 2pf = field velocity in m/s

f = supply frequency in Hz

p = pole pitch, m

x = Instantaneous position along x axis at which to find point value of current sheet, m

ρ_r = surface resistivity in Ohms including factor taken from [10] to include plate end ring effects

g = magnetic air-gap including Carter's coefficient to allow for the effects of stator slotting, m

6.4. Flux Conditions

There are two distinct air-gap flux regions in a series connected short rotor machine. First the plate region where the rotor currents oppose the stator currents and give a lower flux and secondly the rest of the machine, where the stator currents are unopposed and so produce a larger gap flux.

This flux distribution pattern can be seen clearly in Fig. 82, which shows finite element modelling of the flux distribution for the 8 pole machine at stall and at peak thrust, 18 m/s.

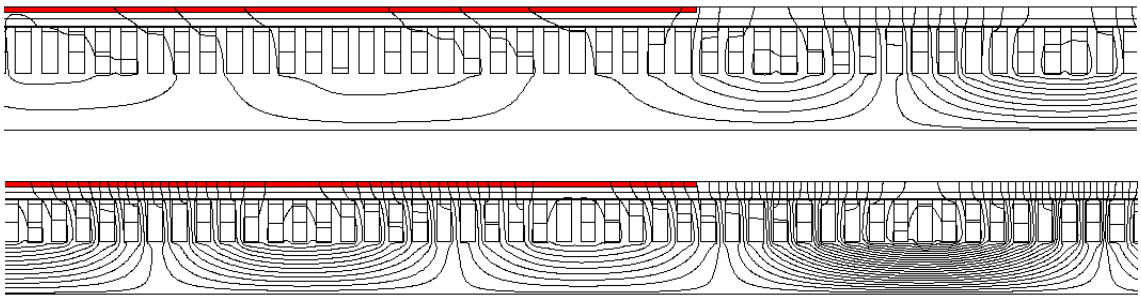

Fig. 82. Flux distribution in an 8-pole rotor short rotor machine at stall (a) & at peak force 18 m/s (b)

6.5. Short Rotor Current Behaviour

The unusual behaviour of short rotor machines is due to regions of abnormal plate current density found at the ends of the short rotor, which are not present in the continuous rotor of a conventional machine. Rotor current density is plotted for 8 Pole continuous and short rotor machines at stall Fig. 83 and at peak thrust Fig. 84.

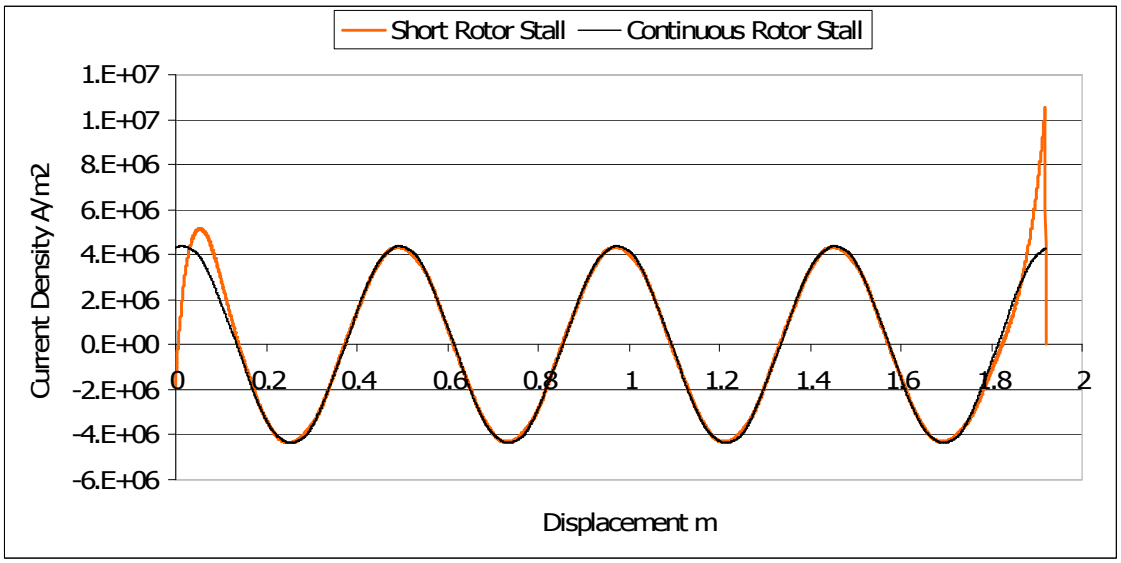

Fig. 83. Current density in the rotor for continuous and 8 pole short rotors at stall

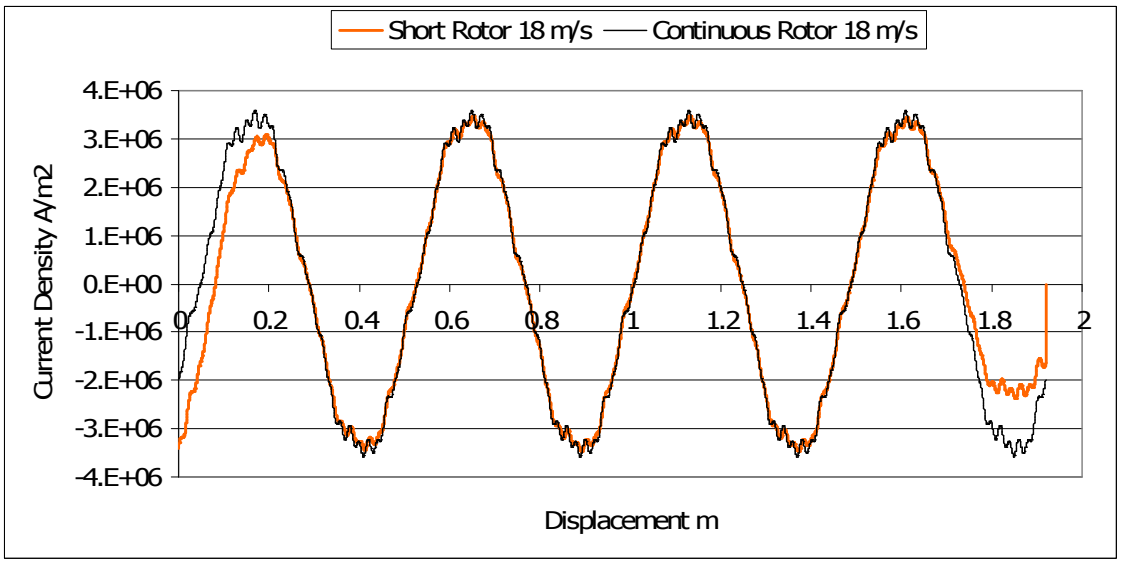

Fig. 84. Current density in the rotor for continuous and 8 pole short rotors at peak thrust

At stall, the high current regions are caused by the changes in the flux linking the edges of the plate. As the field moves relative to the plate, plate current increases to oppose this change of flux. At peak force, the difference between plate speed and field speed is much smaller, so the change of flux linking the ends of the plate is lessened, as is its effect on plate current.

The current density in the plate Jz has been studied in more detail in a shorter plate. A two pole short rotor FE model was constructed and the current density Jz along the X axis of the reaction plate was plotted at stall for various instants throughout a cycle. The plots for this can be seen below.

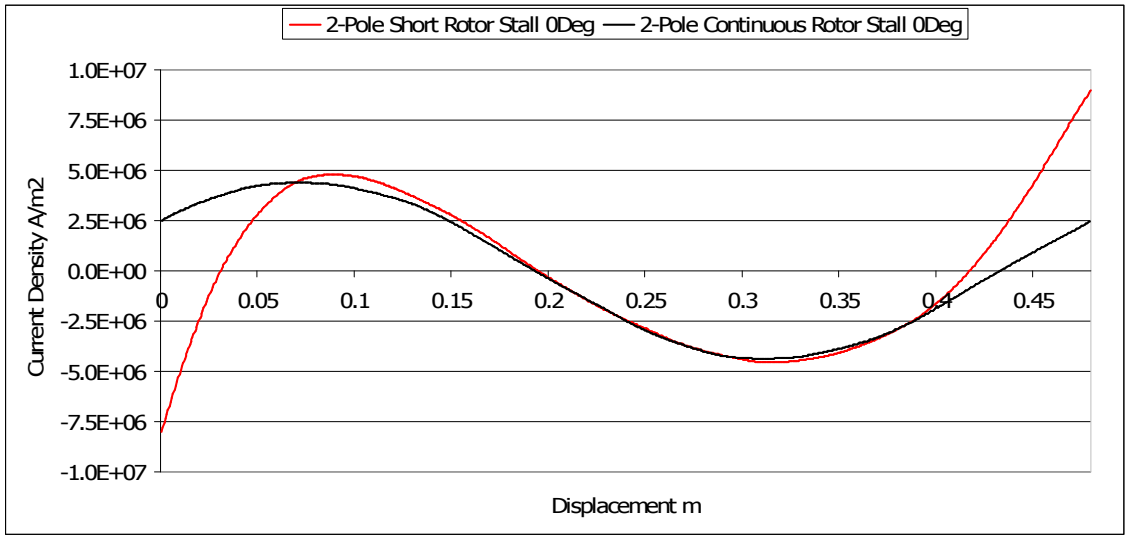

Fig. 85. 2 pole short & continuous rotor current density at 0 Deg

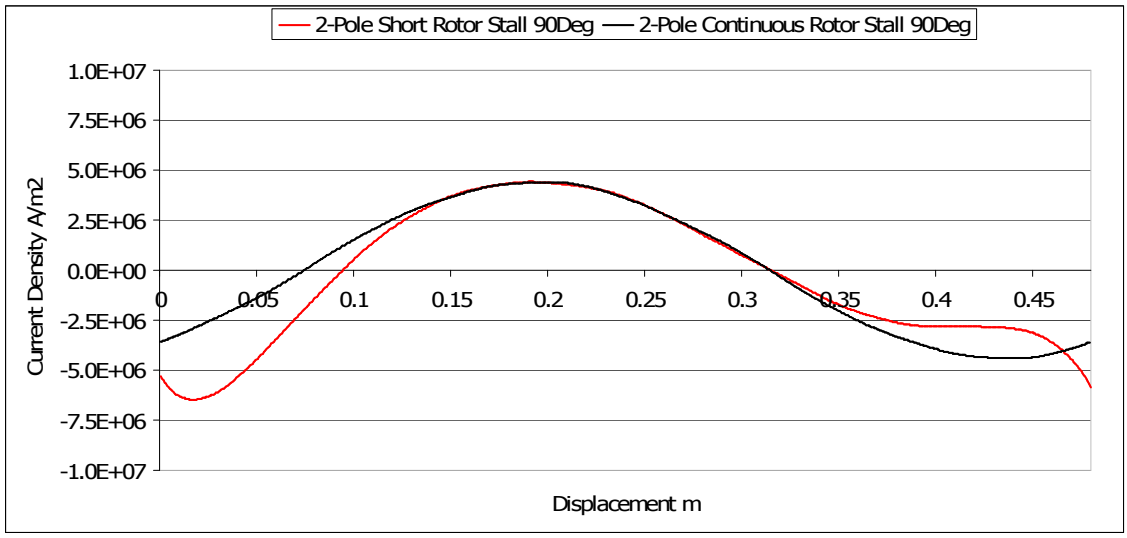

Fig. 86. 2 pole short & continuous rotor current density at 90 Deg

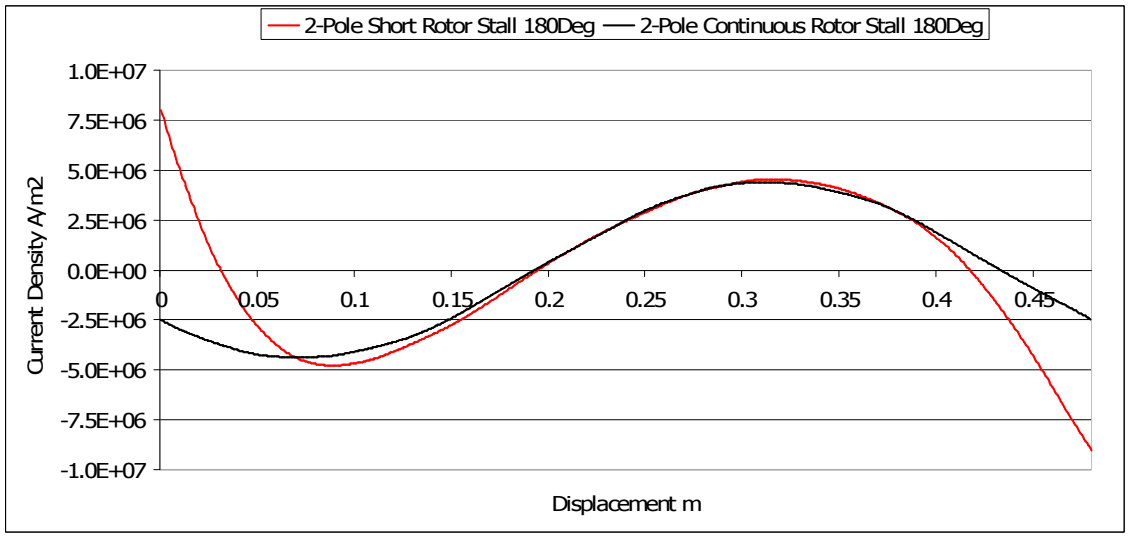

Fig. 87. 2 pole short & continuous rotor current density at 180 Deg

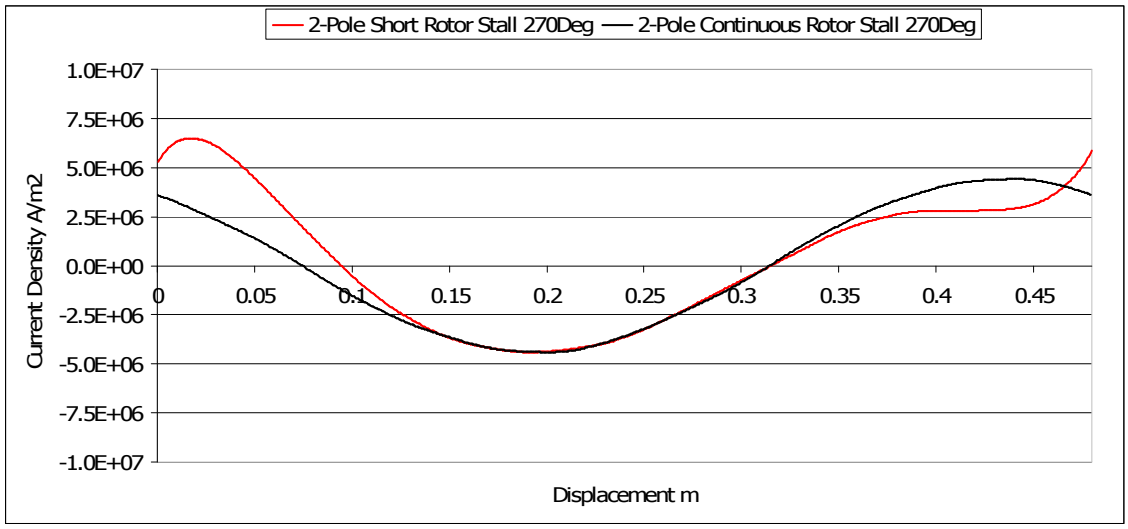

Fig. 88. 2 pole short & continuous rotor current density at 270 Deg

The current density at the ends of the short rotor plate is increased. This can be seen more clearly in the figure below, a plot of the RMS value of Jz by phase angle for both a conventional and a short rotor 2 pole machine at stall Fig. 89.

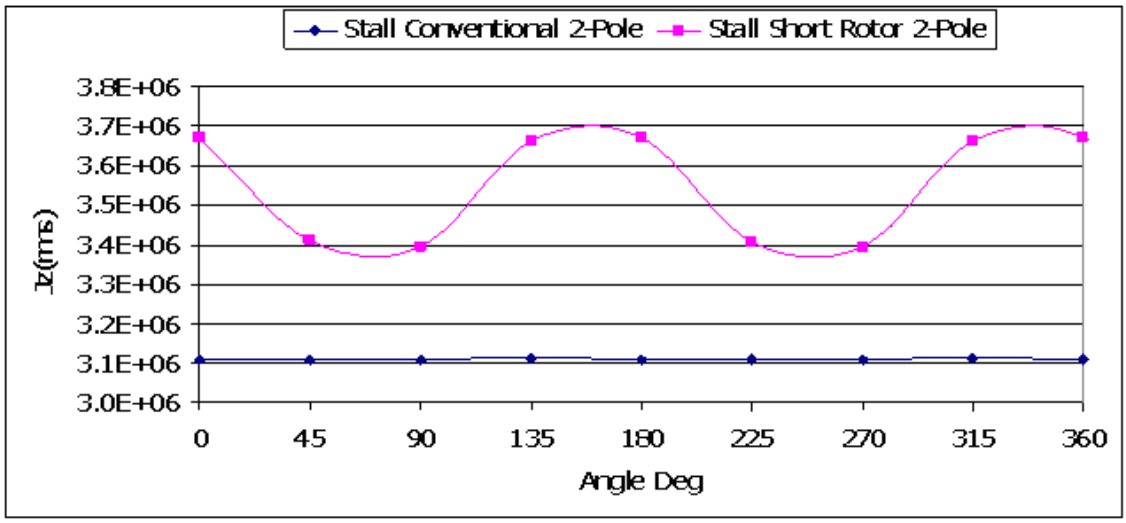

Fig. 89. Variation of plate current density by phase for conventional & short rotor machines at stall

It can be seen that at all points throughout the cycle at stall, Jz in the short rotor case is higher than in the continuous rotor case for equal lengths of rotor. This implies that more current will be flowing in the short rotor plate. As has been argued previously, X_2 in sheet rotors is small, and so the increased current

flow in the rotor is likely to produce more power in the rotor and hence more force at stall. This is confirmed in later results and in [35].

The same process was repeated for 2 pole short rotor and conventional machines at peak Force (18m/s). The Jz(rms) results of this can be seen below Fig. 90.

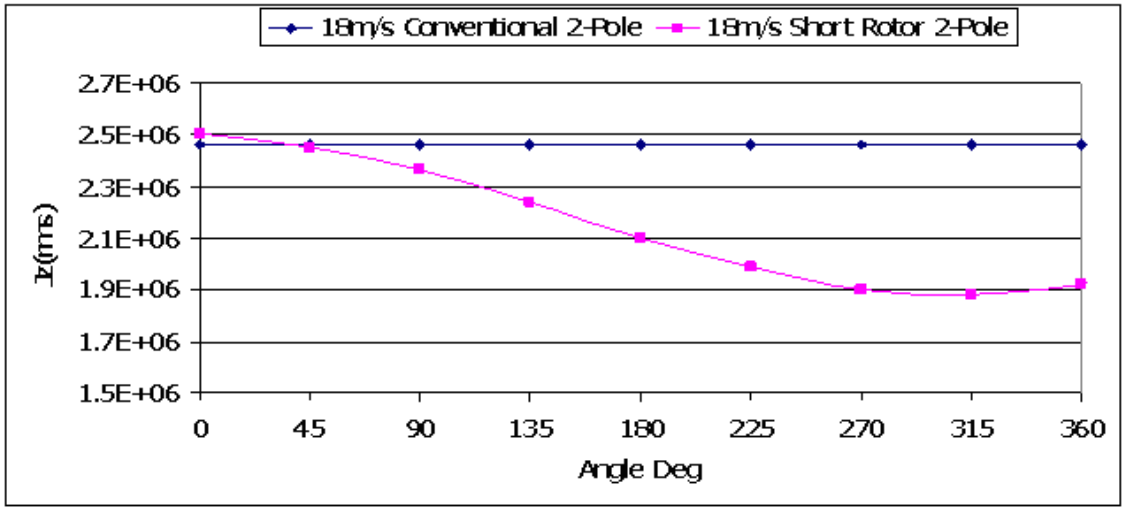

Fig. 90. Plate current density variation by phase for conventional & short rotor machines at 18m/s

As can be seen, the rms short rotor currents are now less throughout the majority of the cycle, so overall force will be less near peak thrust, as will be shown in the force results.

6.6. Results

Sample force per metre plate length results were calculated using time stepped FE with typical dimensions for an electromagnetic launcher machine. Plate rotors of length equal to ½, 1, 2, 4, 6 and 8 stator-winding pole pitches were considered. They were compared with a 'conventional' machine modelled again with FEA as a continuous stator, continuous rotor linear machine of the same length as the plate and which used the same geometry. Fig. 91 illustrates these results.

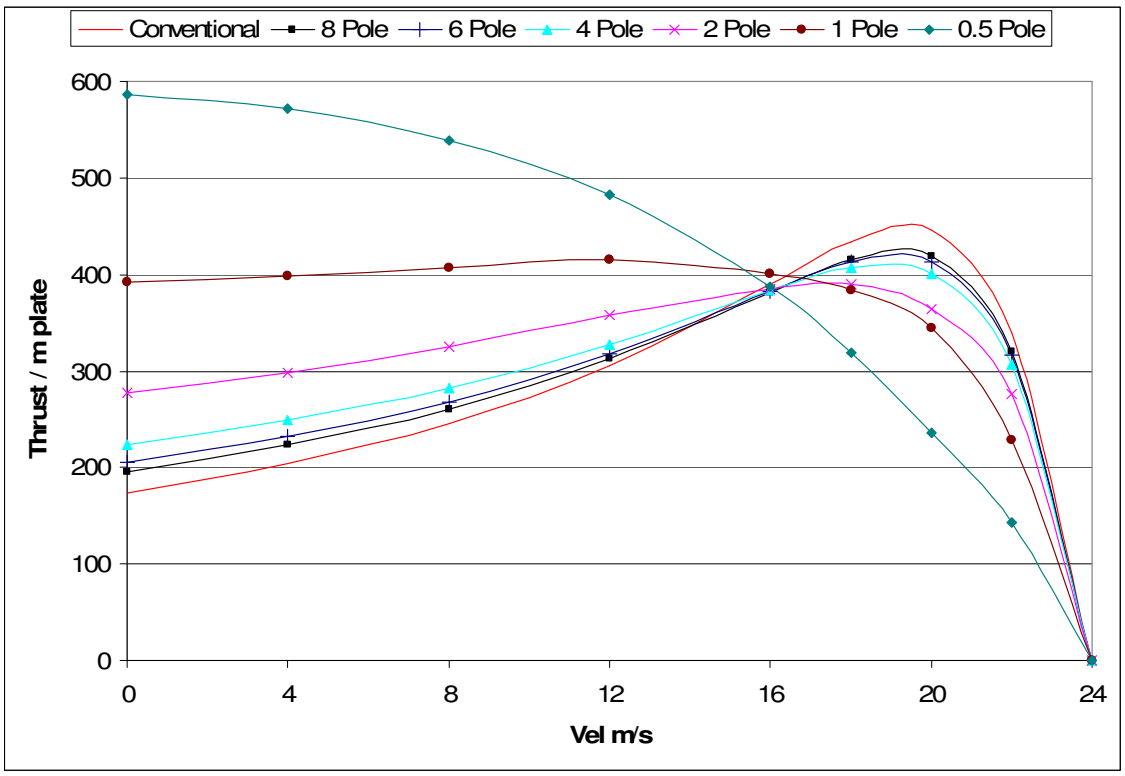

Fig. 91. Force per metre plate against speed results using FE for different short rotor lengths

The short rotor results differ from the conventional machine results because of edge effects that occur both at the leading and trailing edges of the plate. One significant difference occurs in stall thrust, with the stall thrust actually higher from the short rotor machines than that of the conventional machines. This finding correlates with [35].

It is evident from the results Fig. 91 that the short rotor effects are much reduced for plate lengths equal to or greater than 4 poles as far as the peak torque is concerned. This implies that if under inverter control the machine is run at constant slip velocity conditions near to the force peak the effect of the short rotor effects is minimal.

Fig. 92 details the short rotor Finite Element prediction results compared with short rotor thrust predictions using equation (60). This figure shows that the analytical method can predict short rotor performance to within 18% of peak

thrust, for short rotors 4 poles and above. The prediction method becomes less accurate for rotors shorter than 4 poles Fig. 93.

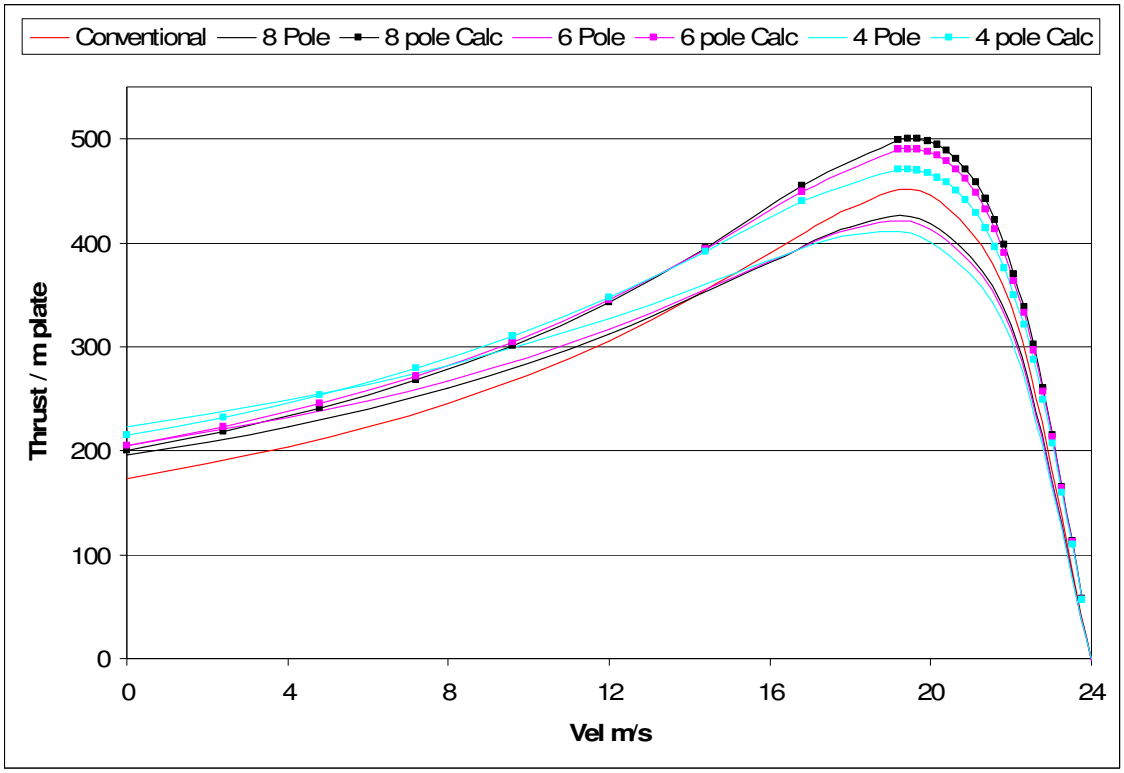

Fig. 92. Calculated and FE model thrusts for 4 6 & 8 pole short rotors & conventional machine

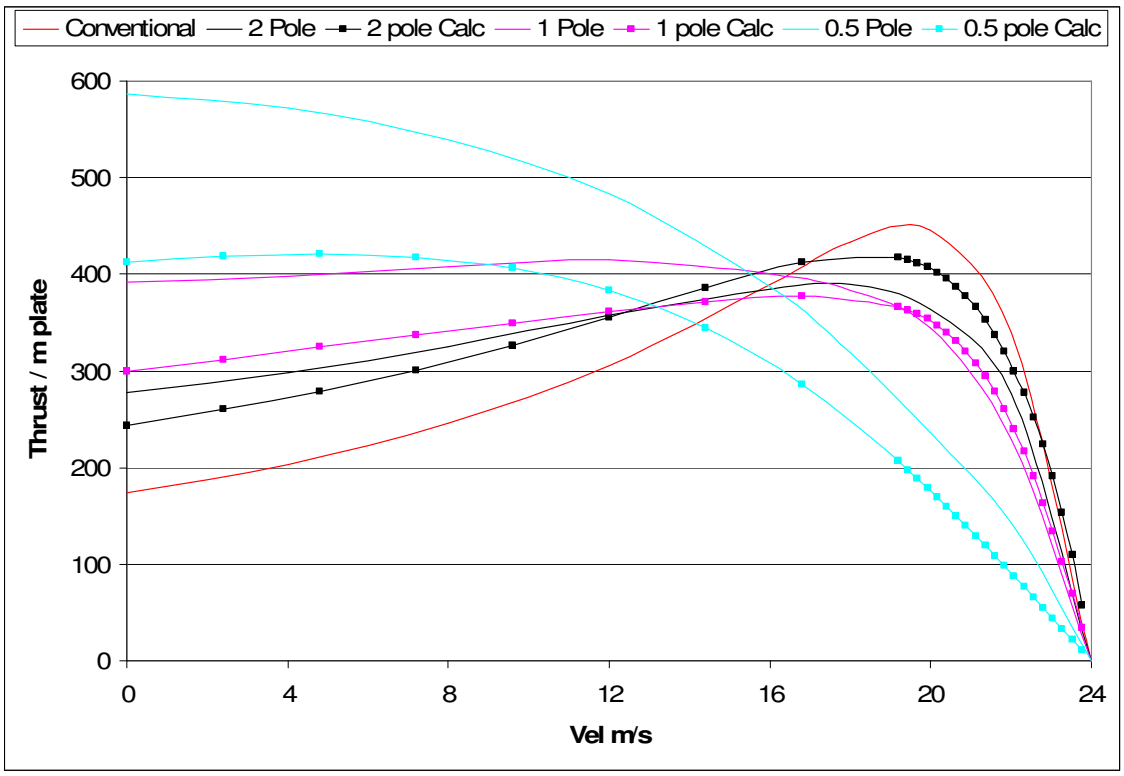

Fig. 93. Calculated and FE model thrusts for 1/2, 1 & 2 pole short rotors & conventional machine

For machines of four poles and above, it can be seen from Fig. 92 that their performance in terms of force per metre of reaction plate is within 10% of that of a conventional continuous rotor induction machine. This indicates that prediction of short rotor machine performance for a rotor of 4 poles or greater length may be achieved simply by treating the case as a conventional machine.

6.7. Examples Using Layer Theory

In the previous section simple conventional machine theory is suggested as a method of predicting short rotor machines of four poles and greater in length. One simple method used in this way was layer theory, modelling a continuous smooth rotor type machine such as a drag cup rotor.

This was tested against three various machines in order to check that the conventional machine curves did come close to modelling the curves from the

short rotor equation. The first machine Fig. 94 is an 8 pole launcher type high speed machine.

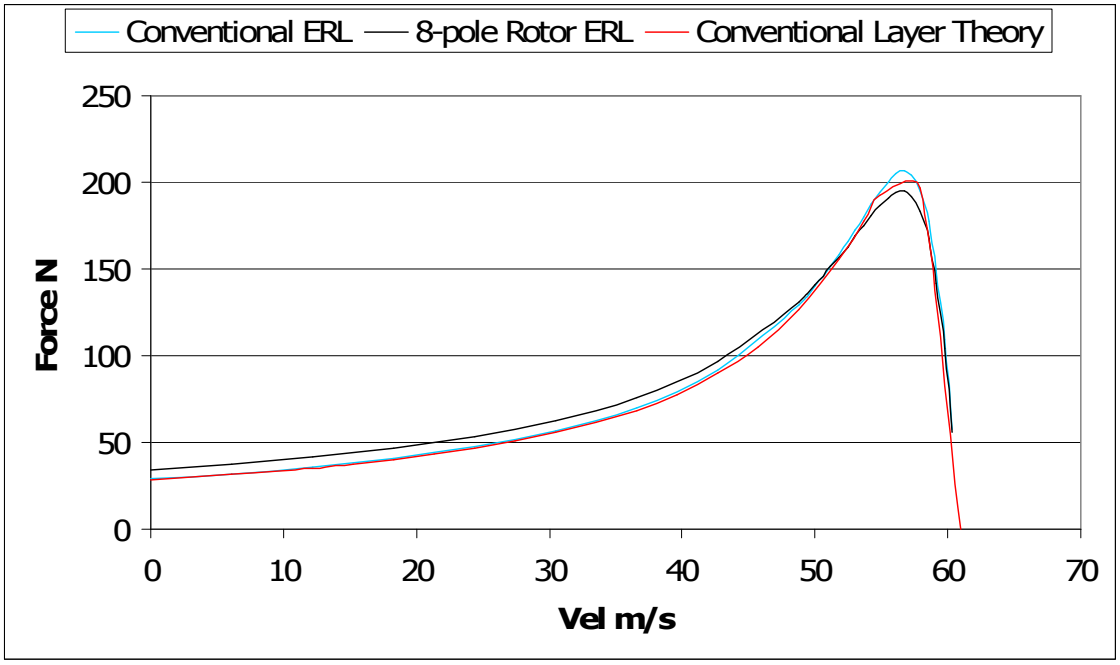

Fig. 94. 8 pole high speed launcher short rotor & conventional machine modelling

The next machine Fig. 95 is a low-medium speed single-sided baggage handling machine.

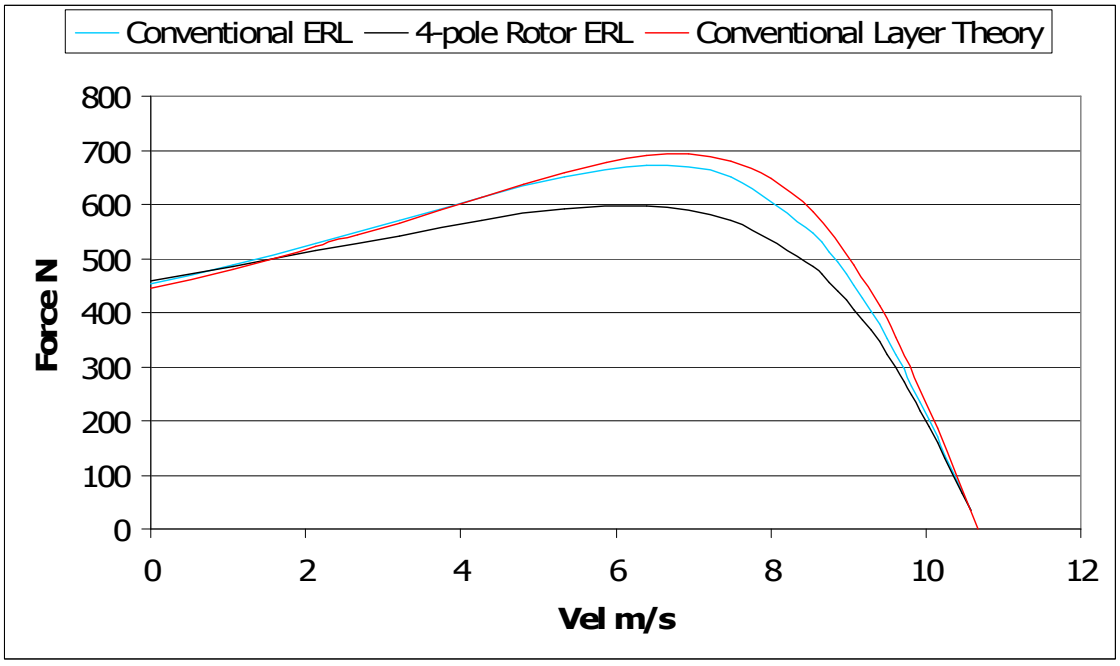

Fig. 95. 4 pole low-medium speed short rotor & conventional machine modelling

The final machine Fig. 96 is a low speed 4 pole double-sided baggage handling machine.

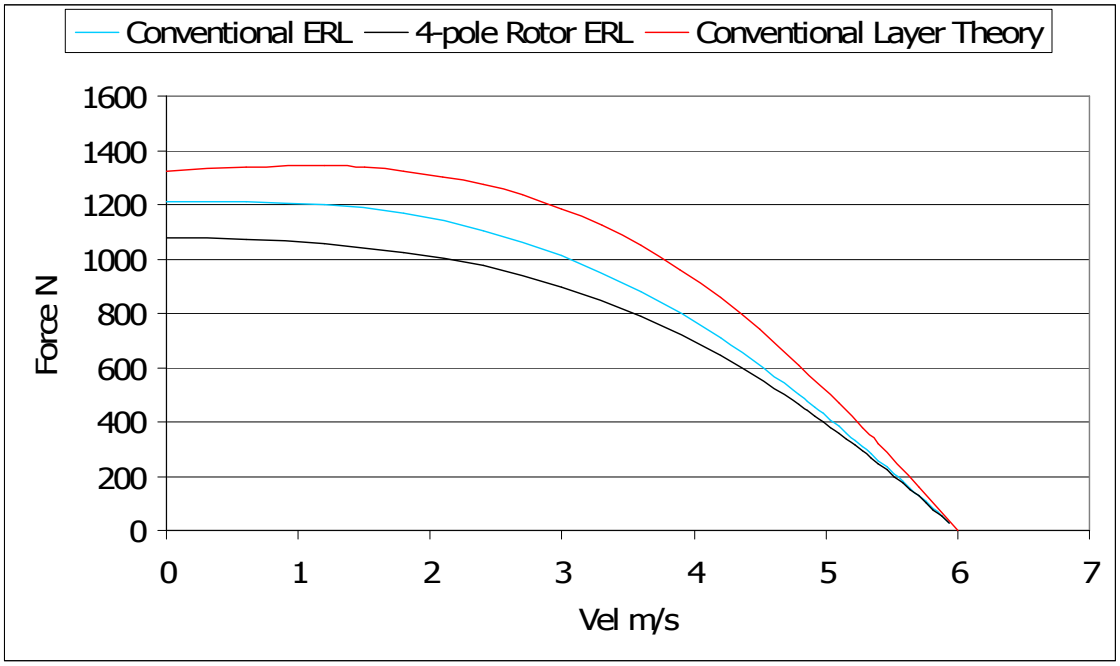

Fig. 96. 4 pole low speed short rotor & conventional machine modelling

As can be seen from these figures, reasonable agreement is reached between the two theories, supporting the view that either may be used to predict short rotor machines over 4 pole pitches in length. The shape of the force speed curves is correct in all 3 cases, however the 4 pole machines are starting to show significant inaccuracies in magnitude of force.

6.8. Conclusions

Finite element modelling has shown that the peak force per metre length of plate produced by short rotor induction machines of rotor length greater than 4 stator pole-pitches is closely the same in magnitude and slip as that from a conventional machine of the same air-gap geometry [36].

Extremely short rotors of 1 pole or less in length have a significantly increased starting torque, which may be of benefit in certain applications. This is believed

to be due to increased current density at the ends of the rotor. However, this behaviour requires further investigation, as similar effects on the torque speed curve also occur when the end regions or plate thickness are reduced, or where the plate resistivity is otherwise increased.

The 2 pole and less short rotor is currently only predictable using FEA, as simple modelling methods do not account for the effects of irregular rotor current density. Further, the secondary end ring compensation method of Russell & Norsworthy may not perform accurately with extremely short rotors. Future plans include a study of short rotor behaviour using 3D FE methods.

7. Offset Stator Harmonic Cancellation

7.1. Principle of Harmonic Cancellation

As has been detailed, a concentrated winding produces both forwards and backwards going fields which act to severely decrease the stators performance with a plate rotor. A method to suppress the effect of the unwanted harmonic has been outlined (wound rotors).

A further method has been developed which uses a double-sided machine to cancel out the negative harmonics in the mmf waveform leaving only the positive and hence allowing the successful use of plate rotors.

The concept of cancellation is relatively simple. If the simplest case of a double-sided 3 coil section of a concentrated machine is considered, the 2 and 4 pole flux waveform components can be drawn Fig. 97.

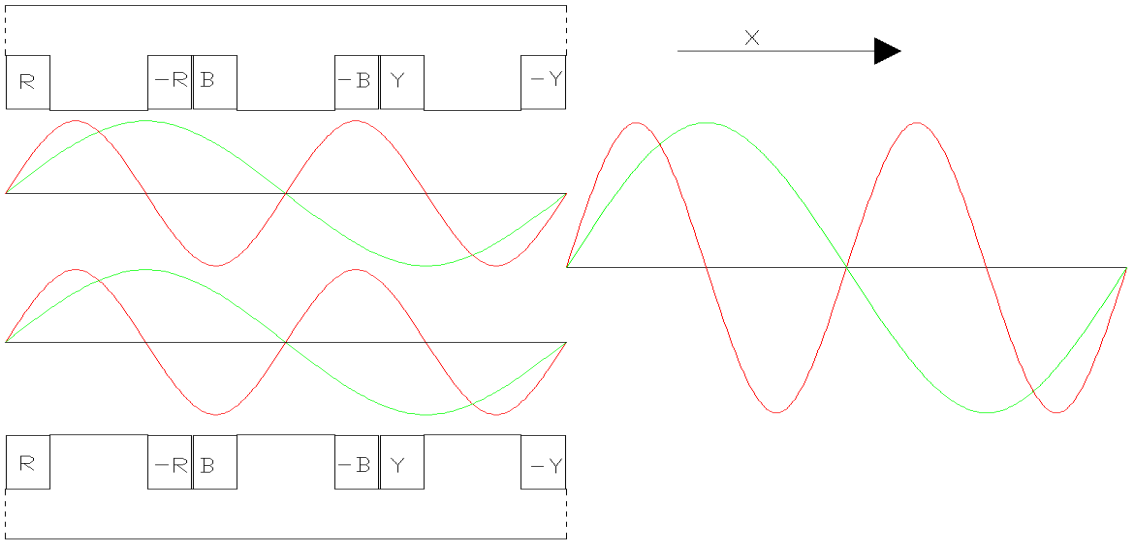

Fig. 97. 2 & 4 pole flux components from double-sided concentrated winding

As would be expected, both the 2 pole forwards going and 4 pole backwards going waveforms reinforce. The overall mmf still contains both 2 and 4 pole components at double the magnitude of a single stator's components.

To improve this situation, a mechanical offset is introduced, displacing one stator in the direction of field travel relative to the other. An offset of 180 degrees or one pole pitch of the 2 pole wave produces the following flux pattern Fig. 98.

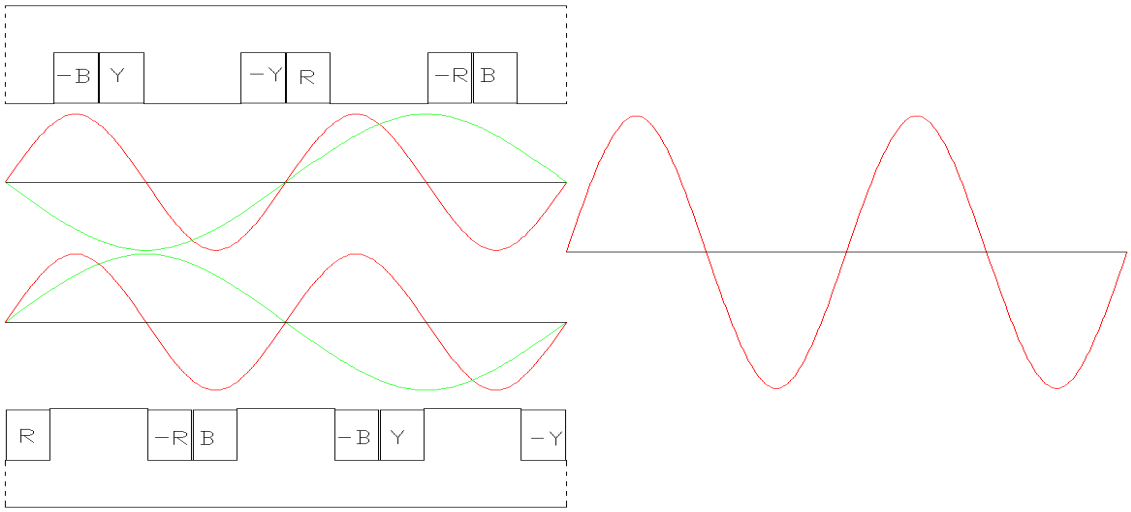

Fig. 98. Flux components from offset double-sided concentrated winding, 2 pole cancellation

It can be observed that total cancellation of the 2 pole wave has occurred, leaving only the fully reinforced 4 pole wave. A further modification is to reverse the polarity of the coils in one stator Fig. 99.

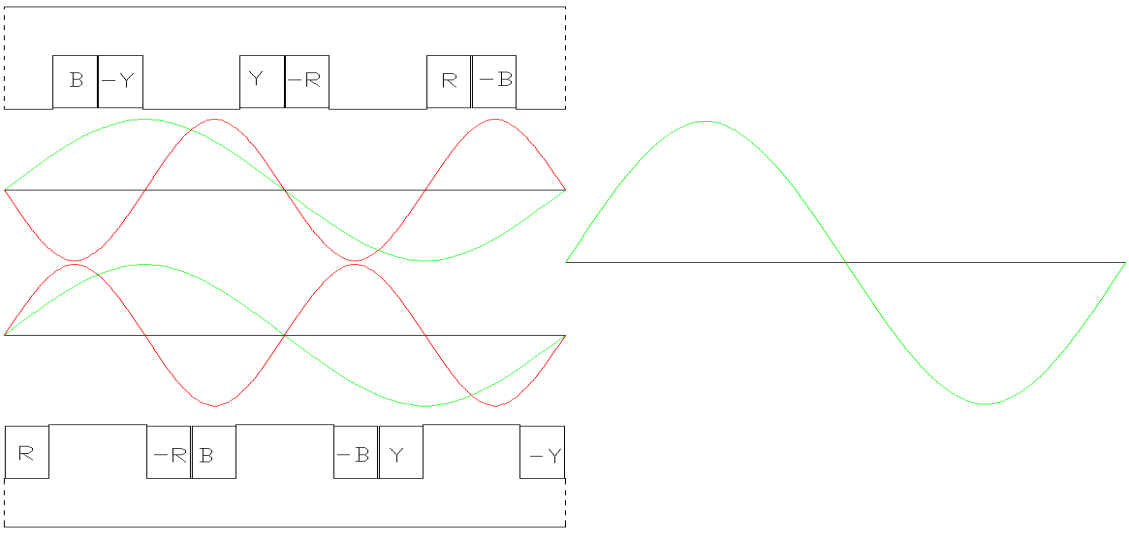

Fig. 99. Flux components from offset double-sided concentrated winding, 4 pole cancellation

As can be seen, reversing the polarity of one stator causes the 4 pole wave to be fully cancelled, and the 2 pole wave to be fully reinforced. This is an important result as it shows that the offset system can be used to produce either of the harmonics present, and totally suppress the other [37]. Machines using this configuration of one reversed stator will be referred to as reversed e.g. 6 coil 4-8 pole reversed.

Further, identical pairs of offset machines could be connected to produce either a 2 or 4 pole machine. For instance, a launch track often uses shorter pole pitch machines for the low speed starting region and longer pole pitch machines for the later regions when the vehicle is moving faster. Identical machines could be placed all along a track, but connected as 4 pole near the beginning to aid low speed starting and as 2 pole (double the pole pitch) near the end to aid high speed performance.

In a rotating machine, or a machine where speed and acceleration requirements may vary, connections could be altered from 4 to 2 pole during operation to improve efficiency and performance at different running speeds, similar to a pole change machine. It should be noted that the two harmonics travel in opposite directions and so care must be taken to also switch two phases, if motion in the same direction is required, rather than braking force.

This work was expanded to look at all three concentrated windings at various offsets, with and without one reversed stator. To aid this, a spreadsheet program has been developed that uses simple sine wave addition representations of the primary positive and negative harmonics and the steel-steel coverage.

An example of this can be seen overleaf in Fig. 100. The program inputs are primary positive and negative harmonic number, number of teeth, whether one stator is reversed and the number of degrees of the positive waveform to offset

the stators by. The positive and negative harmonics for each stator are modelled, and the resultant calculated. This is outputted as a percentage, with 0% meaning fully cancelled and 100% meaning a fully reinforced waveform. Steel to steel gap is also represented by working out the tooth coverage, where tooth opposite tooth would be 100% and tooth opposite slot would be 0%.

Degrees Offset 50		Reversed? (Y or N) N	1
Positive Poles 4	Negative Poles 8	Teeth 6	

Peak % of Max	Positive	Negative	Cover
	91	64	16

Password: Edit

	Bottom Stator		Top Stator		Resultant		Tooth offset	
Angle	Positive	Negative	Positive	Negative	Positive	Negative	Bottom	Top
0	0.00	0.00	0.77	0.98	38.3	49.2	-1.00	0.87
2	0.03	0.07	0.79	0.97	41.1	52.0	-0.99	0.91
4	0.07	0.14	0.81	0.95	43.9	54.5	-0.98	0.95
6	0.10	0.21	0.83	0.93	46.7	56.8	-0.95	0.98
8	0.14	0.28	0.85	0.90	49.4	58.7	-0.91	0.99
10	0.17	0.34	0.87	0.87	52.0	60.4	-0.87	1.00
12	0.21	0.41	0.88	0.83	54.5	61.8	-0.81	0.99
14	0.24	0.47	0.90	0.79	57.0	62.9	-0.74	0.98
16	0.28	0.53	0.91	0.74	59.5	63.7	-0.67	0.95
18	0.31	0.59	0.93	0.69	61.8	64.1	-0.59	0.91
20	0.34	0.64	0.94	0.64	64.1	64.3	-0.50	0.87
22	0.37	0.69	0.95	0.59	66.3	64.1	-0.41	0.81

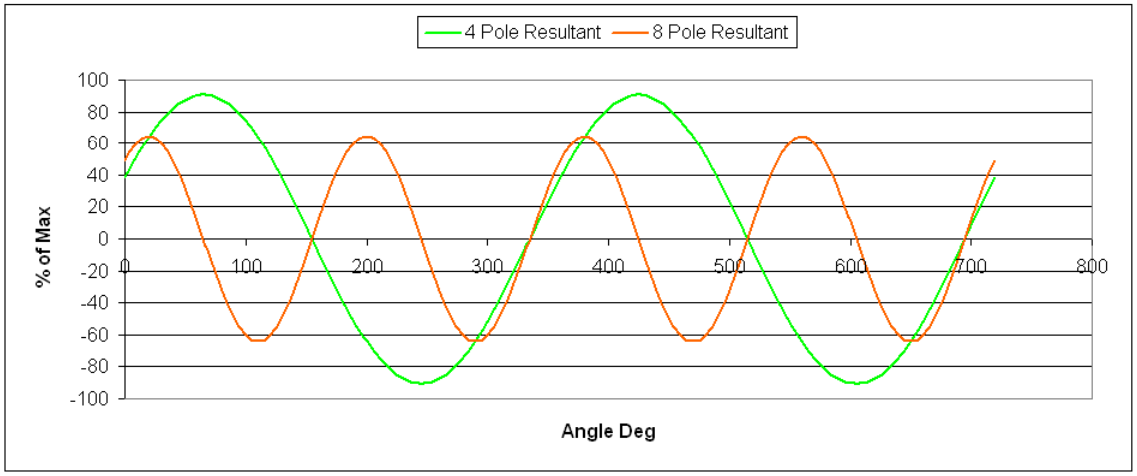

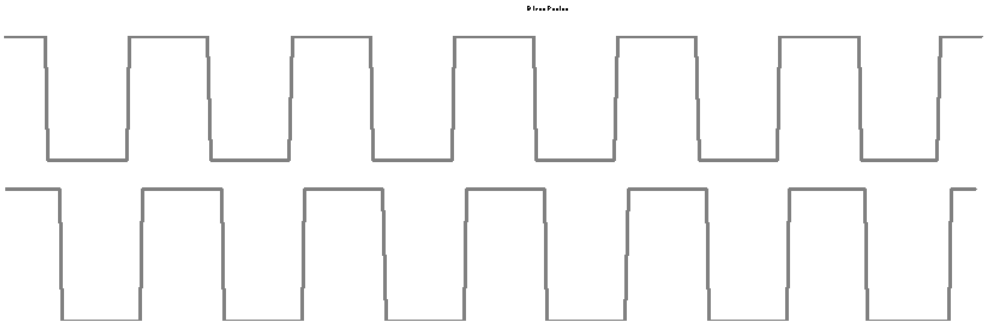

Fig. 100. Spreadsheet to find % positive and negative harmonic present in an offset configuration

The top plot represents the harmonic patterns, green being Positive primary harmonic and red being Negative primary harmonic. The lower plot represents the relative positions of the top and bottom stator teeth.

For each winding, a full range of offsets was studied. This is shown below for 6 coil 4-8 pole double-sided pair Fig. 101 and with one reversed stator Fig. 102.

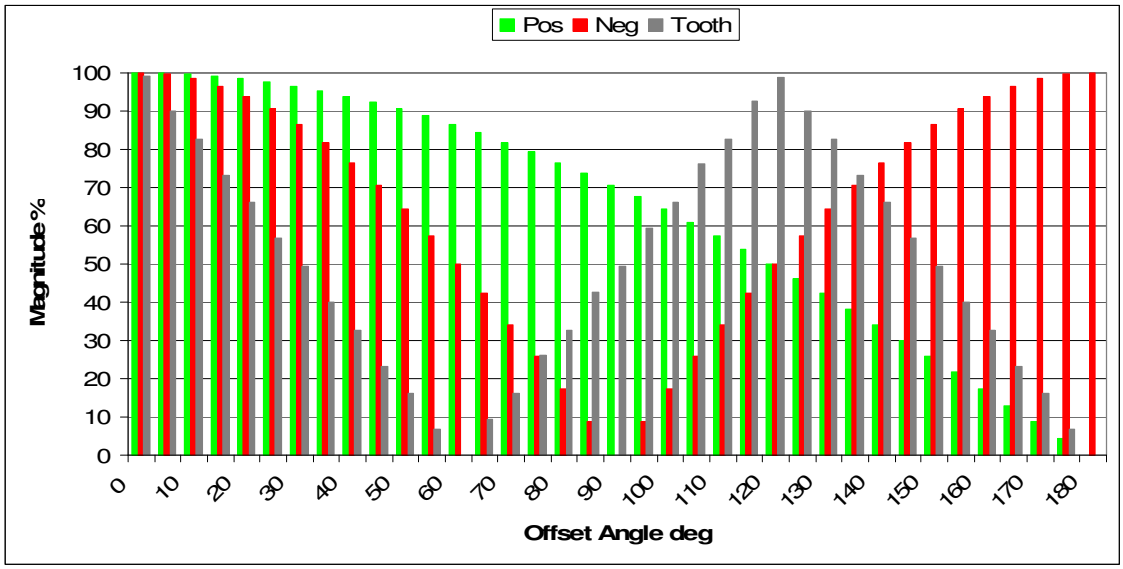

Fig. 101. 6 coil positive 4 pole & negative 8 pole % of harmonic for various offset angles

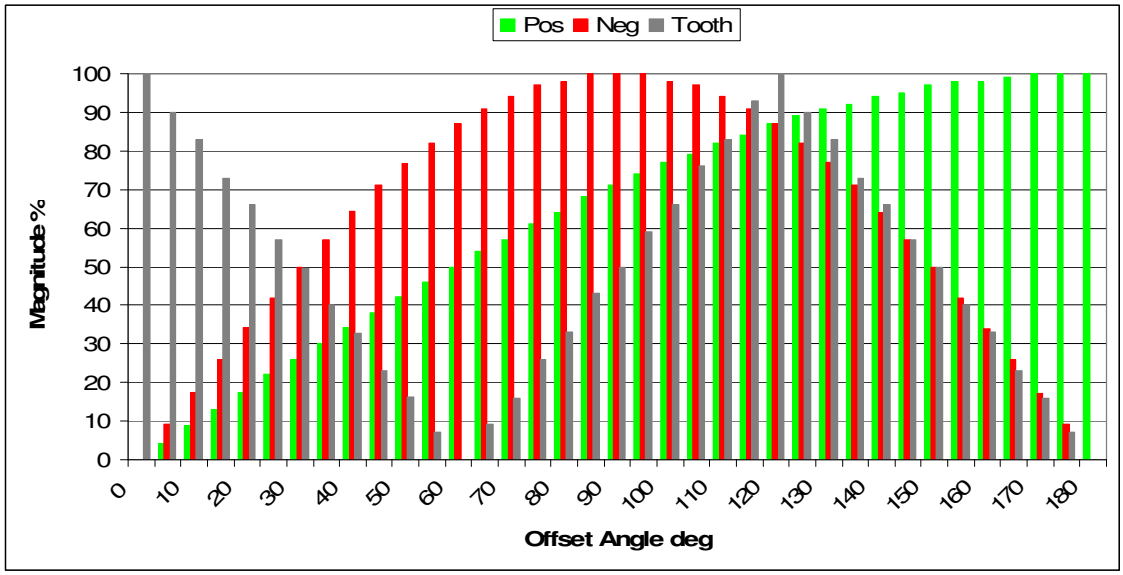

Fig. 102. 6 coil reversed positive 4 pole & negative 8 pole % of harmonic for various offset angles

As was found previously, the best offset occurs at 180 degrees, 1½ coils or 1 pole of the 4 pole wave, and this also corresponds to a tooth opposite slot type situation.

The next winding studied is the 9 coil 8-10 pole type Fig. 103. This is also shown with a reversed stator Fig. 104.

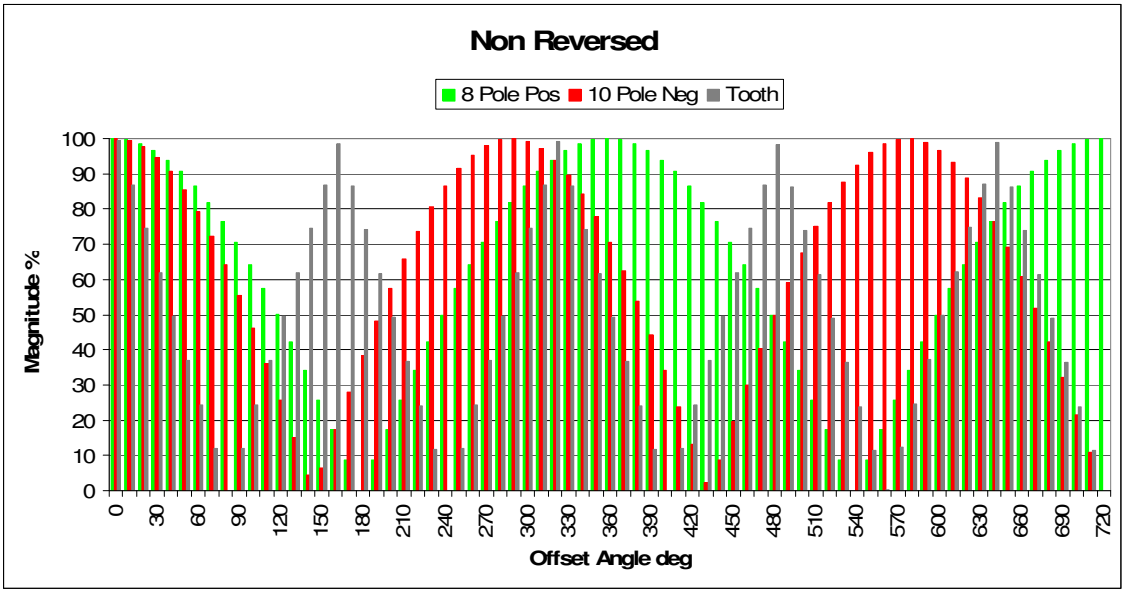

Fig. 103. 9 coil positive 8 pole & negative 10 pole % of harmonic for various offset angles

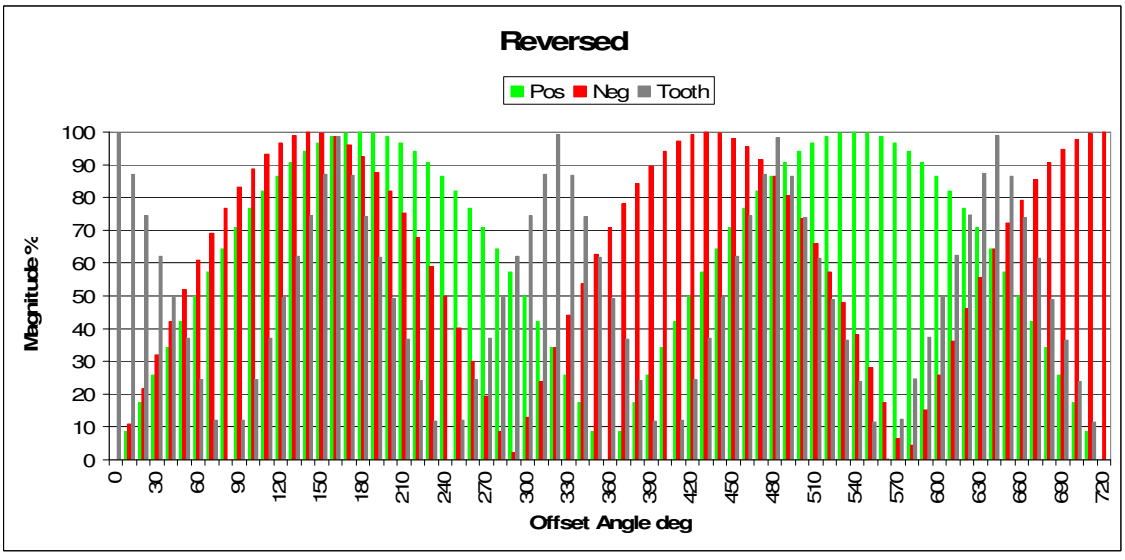

Fig. 104. 9 coil reversed positive 8 pole & negative 10 pole % of harmonic for various offset angles

It can be seen that the optimum point occurs at 720 degrees, 4½ coils or 4 poles of the 8 pole wave.

Finally, the 12 coil 10-14 pole is studied in Fig. 105 and when reversed Fig. 106.

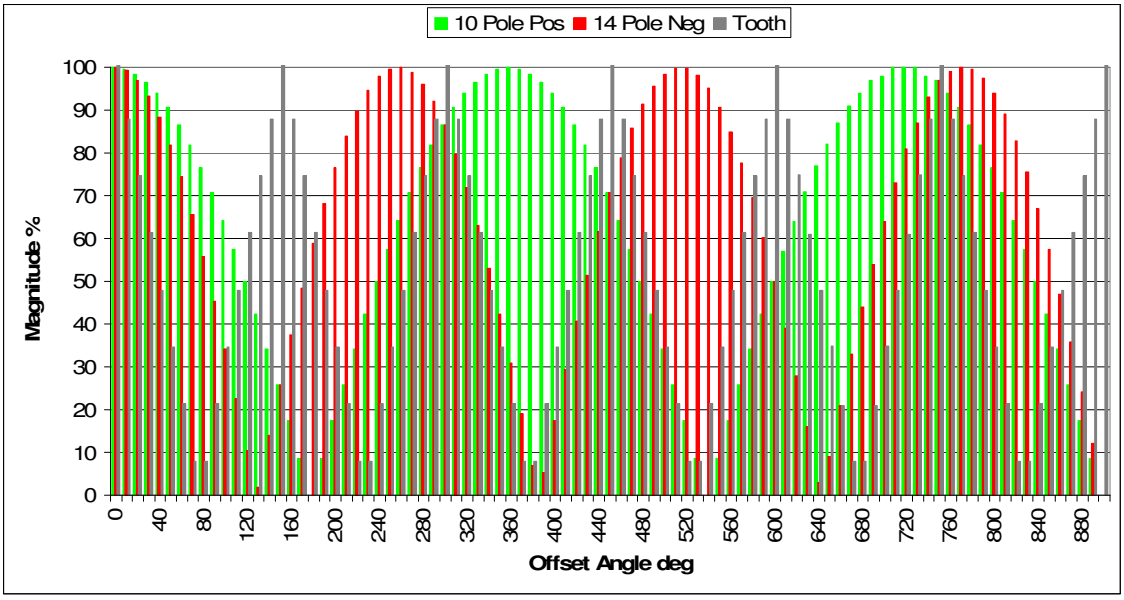

Fig. 105. 12 coil positive 10 pole & negative 14 pole % of harmonic for various offset angles

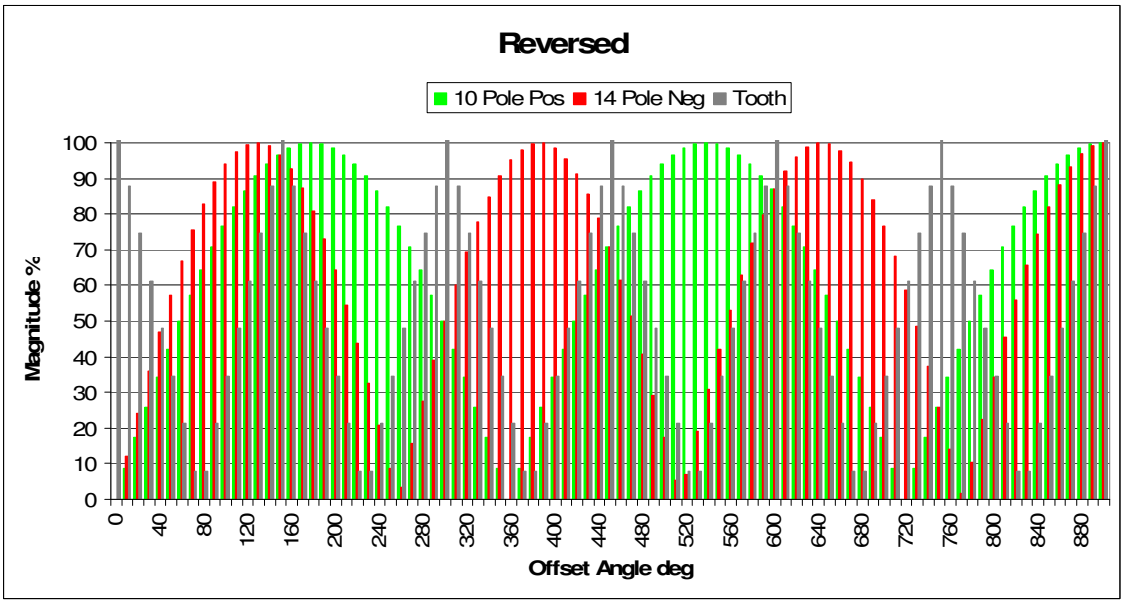

Fig. 106. 12 coil reversed positive 10 pole & negative 14 pole % harmonic for various offset angles

In the case of the 12 coil 10-14 pole machine, the optimum point is less obvious. Firstly, it can be seen from the two figures above that reversing the machine does not have an effect beyond reversing the x axis, so that when reversed, full cancellation occurs at 0 degrees, and full reinforcement of all harmonics at 900 degrees. The optimum point is 385 degrees non reversed, giving 98% of desired harmonic, 1% of non desired and a slight iron coverage of 13%.

7.1.1. Harmonic Analysis

To confirm the cancellation effects predicted above 2D FE models have been made and the airgap flux plotted. Fourier analysis was then used to look at the harmonic components present. Firstly, the 3 coil 2-4 pole will be studied Fig. 107.

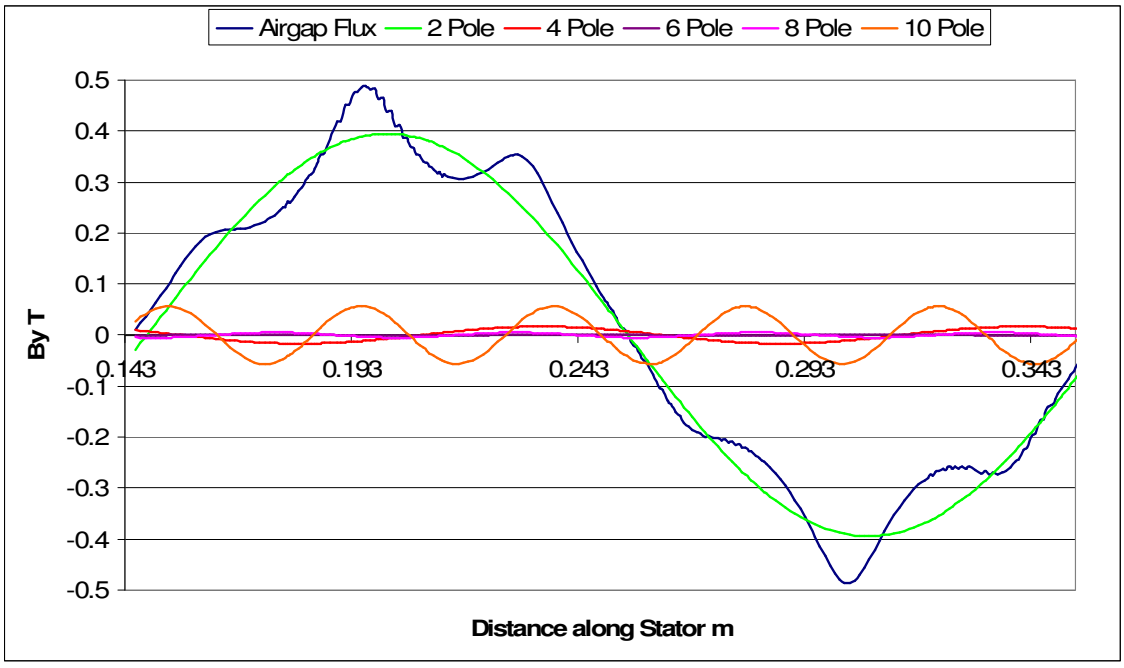

Fig. 107. 3 coil 2-4 pole reversed airgap flux analysis

As was expected the airgap flux waveform is a good approximation to a 2 pole sinusoid. The 4 pole component has been almost completely cancelled, and the only source of interference is a minor 10 pole wave. When compared to the

harmonic spectrum Fig. 60, it can be seen that there are some differences in the modelled flux due to slot harmonics.

The next machine is a 9 coil 8-10 pole type Fig. 108. As in Fig. 61, the 9 coil machine shows a strong sinusoidal 8 pole component, a near zero amplitude 10 pole component and a small 4 pole component. This shows that the cancellation process has once again worked effectively.

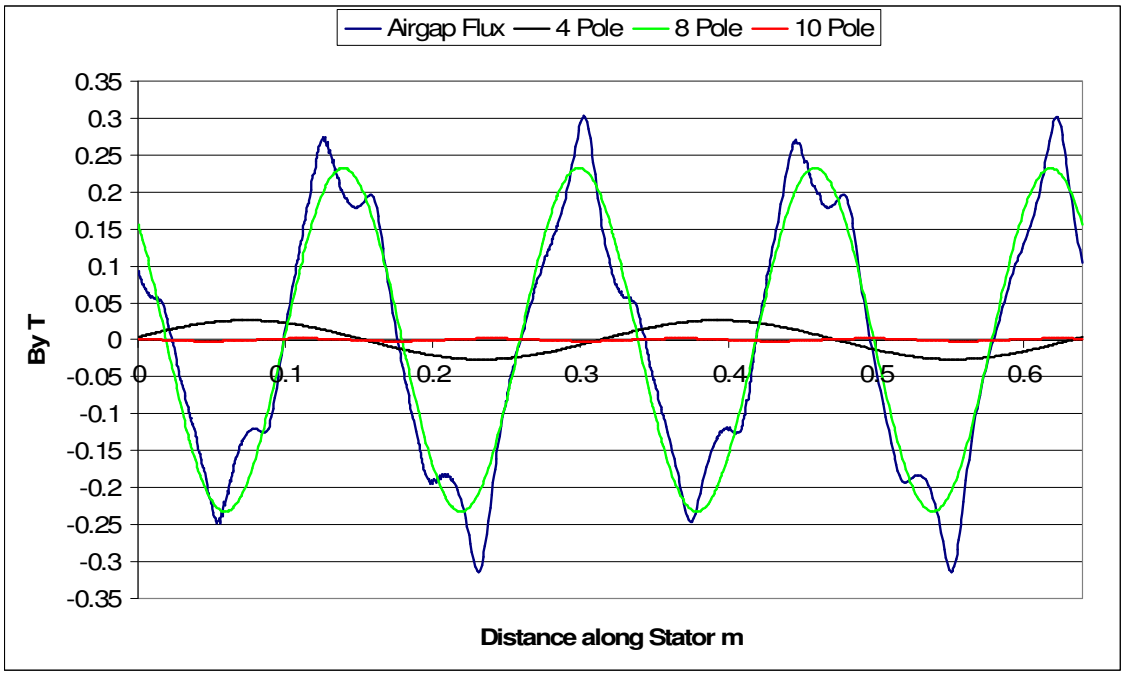

Fig. 108. 9 coil 8-10 pole airgap flux analysis

Finally, the 12 coil 10-14 pole machine is studied Fig. 109. Once again, the 14 pole waveform has been successfully cancelled to a low value, and the 10 coil is still present. The negative 2 pole waveform predicted by the earlier winding analysis is also present, and significant enough that it must be accounted for if this winding is to be used successfully. Again, the presence of slot harmonics causes some differences from the harmonic spectrum of Fig. 62.

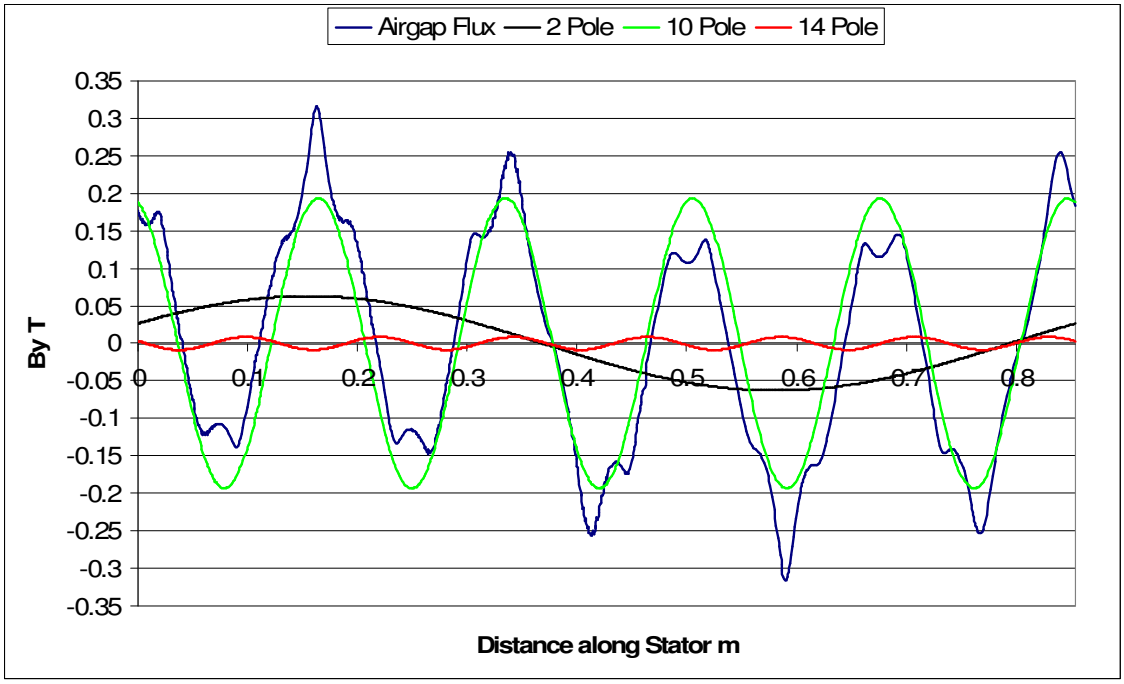

Fig. 109. 12 coil 10-14 pole airgap flux analysis

7.2. Concentrated Offset Machine Slot to Tooth Ratio

An important point to take from the above work is that in two out of three cases the optimum offset occurs when the centres of the teeth on one stator are aligned with the centres of the slots on the other stator. An important factor in concentrated offset machines is the slot to tooth ratio. Too narrow slots will reduce copper area, whilst too wide slots will lengthen the magnetic air path and reduce performance. An example of this is shown in Fig. 110 where the hatched regions can be slot or tooth material. If these regions are all slot, the flux paths are vastly different to if they are all tooth.

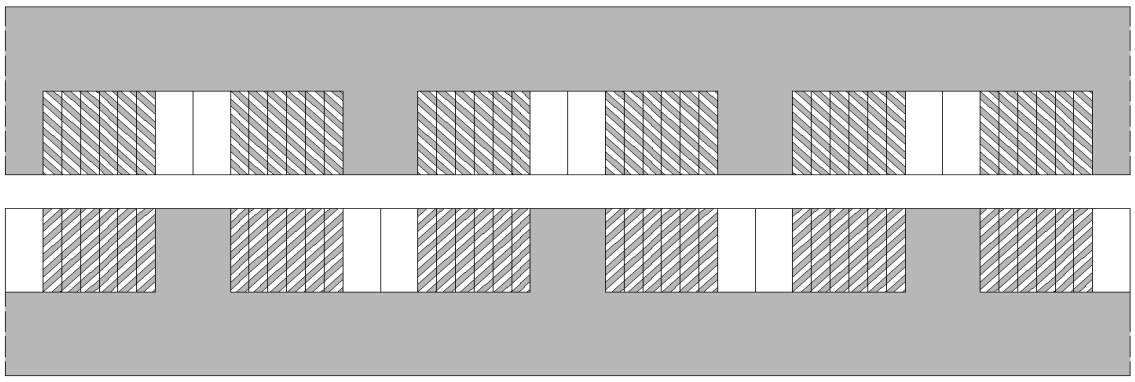

Fig. 110. Offset machines showing various slot to tooth ratios

To test this ratio and find the optimum value, 2D FE modelling was used. FE models were made with slot openings varying from 20% to 80% of total slot pitch Fig. 111. The models were supplied a constant voltage with R1 and Xe added in order to include the full effects of the narrowing slots on the machine.

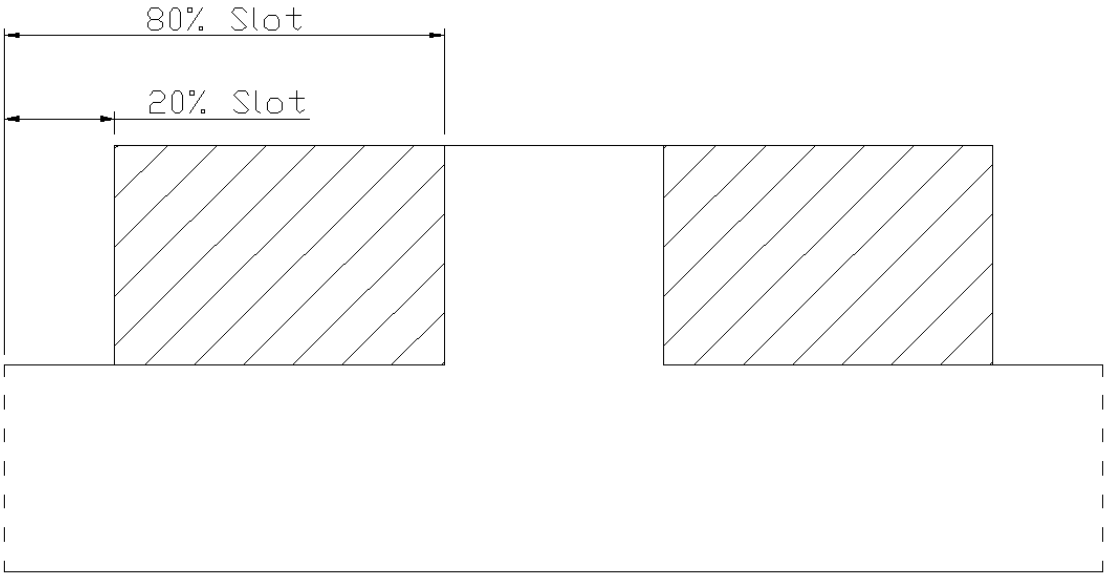

Fig. 111. Single tooth FE model showing various slot openings used

The overall machine was set up as a 3 coil 2 pole reversed offset, cancelling out the 4 pole wave. Force Fig. 112, current Fig. 113, VA/N Fig. 114 and Force per Amp Fig. 115 have all been plotted for various % values of slot width compared to total slot pitch to determine the effects of the slot opening on performance.

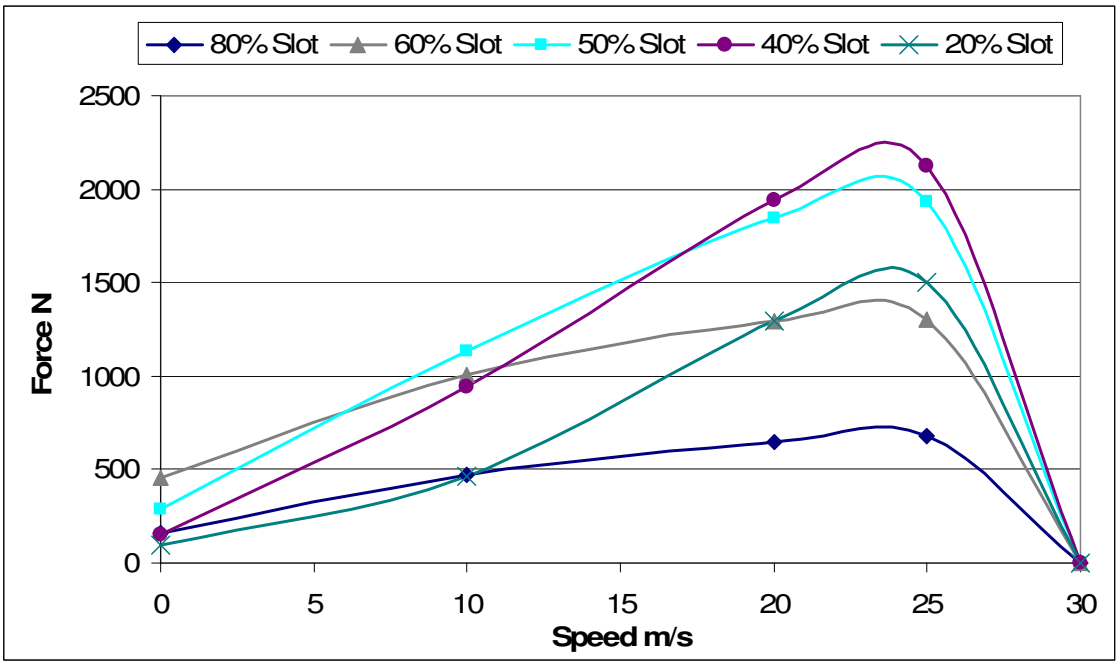

Fig. 112. Force for various % slot widths

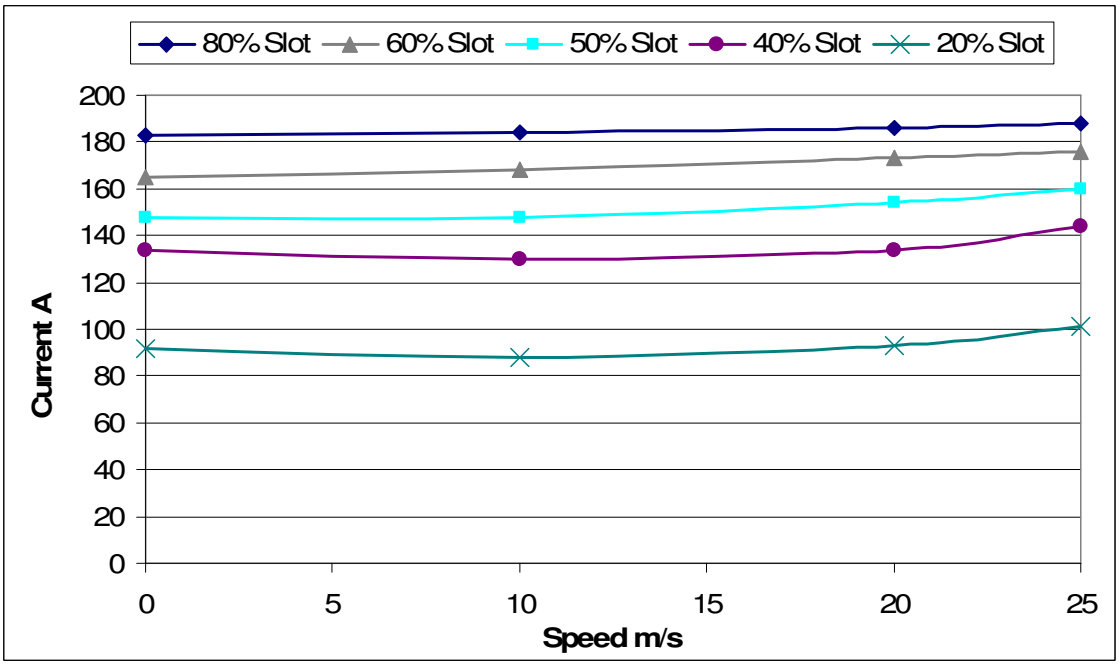

Fig. 113. Current for various % slot widths

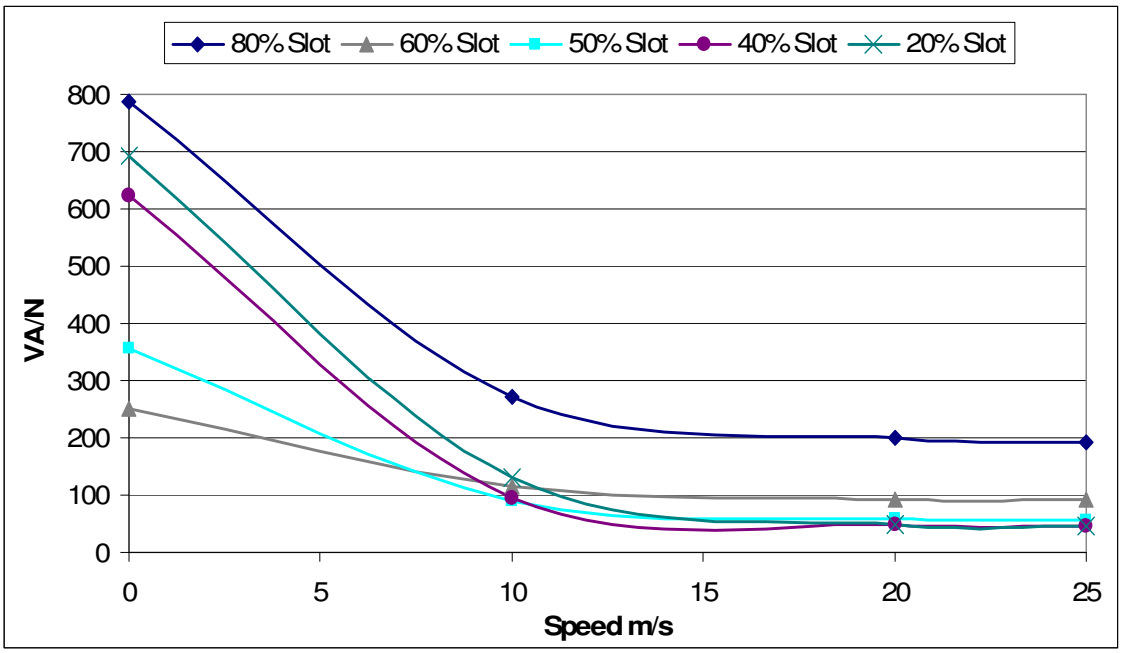

Fig. 114. VA/N for various % slot widths

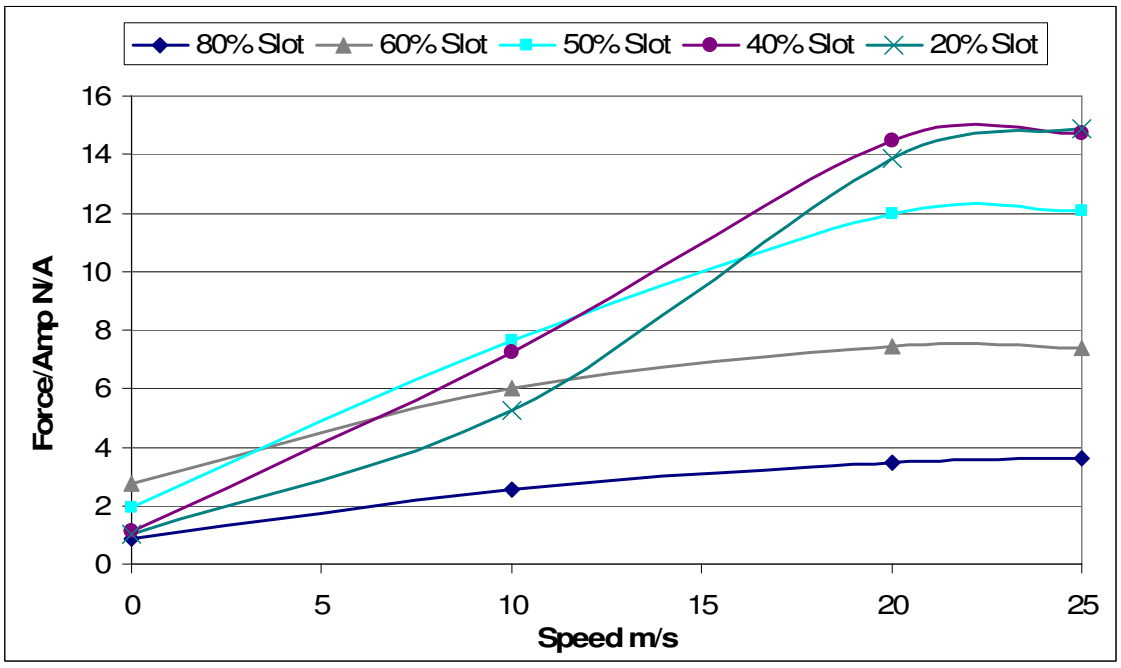

Fig. 115. Force per Amp for various % slot widths

The first conclusion from the above plots is that slot width must be equal to or less than tooth width to avoid excessive currents and low forces due to the

larger magnetic gap. Cases where the slot width is 60% or 80% of the overall slot pitch perform poorly in all of the above comparisons.

With reference to Fig. 111 the 50% slot width case performs reasonably well, however the 40% slot width case gives an excellent performance in terms of both increased force and reduced current consumption, giving a good force/amp. This is due to having overlapping iron sections between the two sides, providing a good flux path across the gap.

Slot widths less than 40% of overall slot pitch seem of limited use, as the slot area is being severely reduced and R1 & X1 consequently increased, while providing no real improvement in Force per Amp or VA/N. Therefore offset machines should be designed with the aim of less than 50% slot to tooth ratio.

A further improvement to the machine is the use of semi closed slots as shown in Fig. 116.

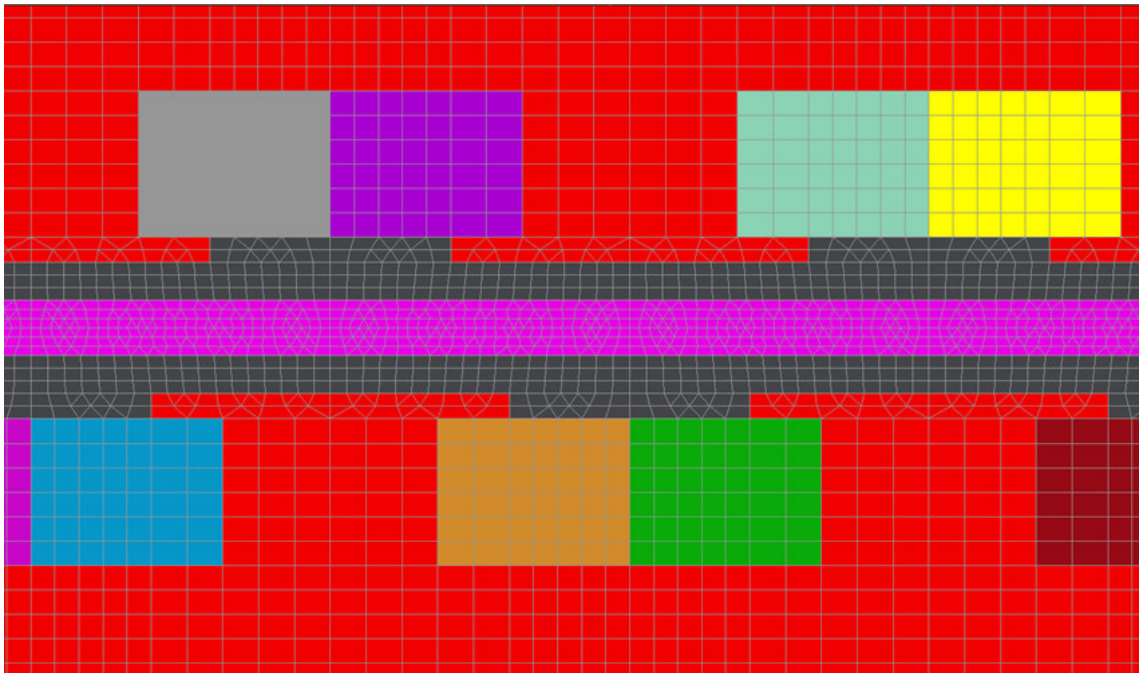

Fig. 116. FE model with semi closed slots

This way, the slot to tooth ratio at the surface of the stator can provide a good flux path, while the slot to tooth ratio for the body of the coil can be larger in order to allow more coil area.

This semi closing can add problems to the machine, as the coils can no longer be simply dropped around the teeth. Possible solutions to this include adhesive attachment of the semi closing tooth tip after coil insertion. Alternatively, ferrous slot wedges could be used with a profile designed to saturate out the centre of the wedge. A third possible solution would be the use of c clip ferrous sections Fig. 117 that could be added to the tooth tip after coil insertion.

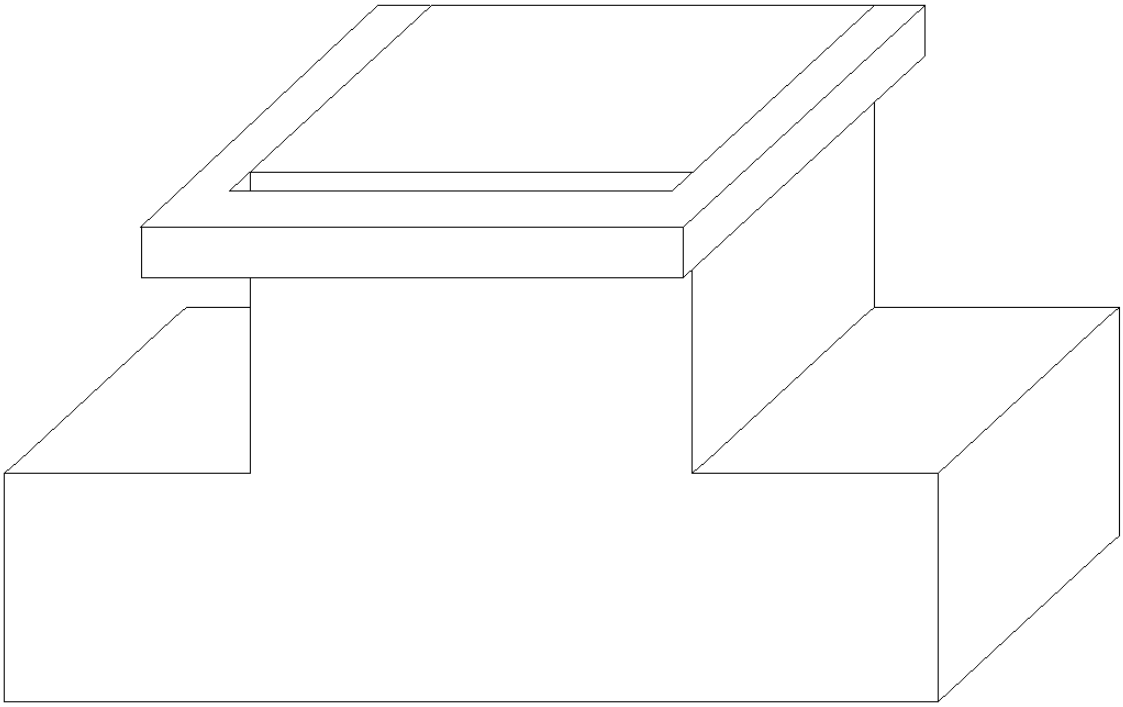

Fig. 117. C clip type tooth tip

The effect of semi closed slots is dependant on airgap length. The increase in flux path length will be much smaller as a percentage of total gap length when larger airgaps are considered. This means that the use of semi closed slots or a greater tooth to slot ratio become much less important when working with large airgaps.

7.3. Four Pole Machine Finite Element Analysis

Finite element analysis of the offset machines was undertaken. A first attempt has been made to develop an offset concentrated winding equivalent to a pair of typical linear motors used for low speed applications Fig. 118.

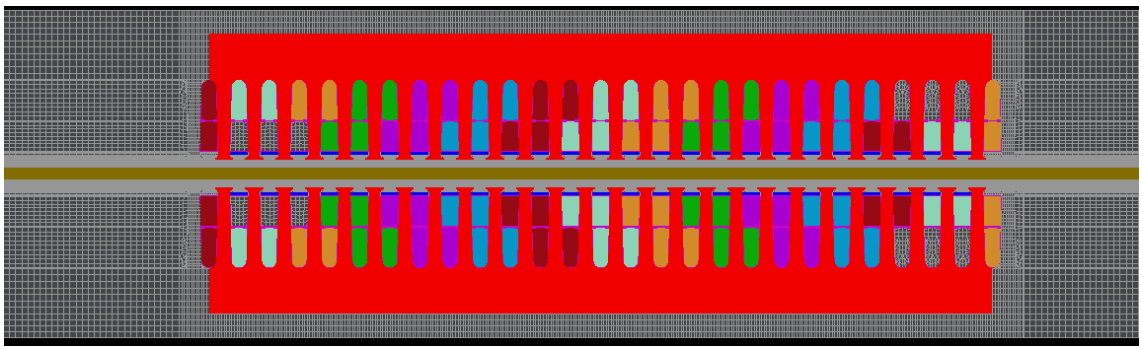

Fig. 118. 2D FE model of double-sided conventional machine

The parameters of the conventional linear motors are:

Winding: 3 phase, 4 pole, 2 Slots per pole and phase, 5/6 corded, 40 turns per coil, pole pitch 0.1068m, R1=1.024Ω per phase, Le=6.019x10^{-3}H per phase

Core: Length 0.4272m, Width 0.1m, Height .0748m, 24 slots, slot pitch .0178m, slot width 0.0104m, slot depth 0.037m

The concentrated winding type motor was originally designed as closely as possible to be equivalent to the standard linear motor Fig. 119.

Winding: 3 phase, 4 pole, ½ a slot per pole and phase, 160 turns per coil, pole pitch 0.1068m, R1=0.848Ω per phase, Le=7.009x10^{-3}H per phase

Core: Length 0.4272m, Width 0.1m, Height .067m, 6 teeth, 6 slots, slot pitch 0.0712m, slot width 0.0416m, slot depth 0.037m

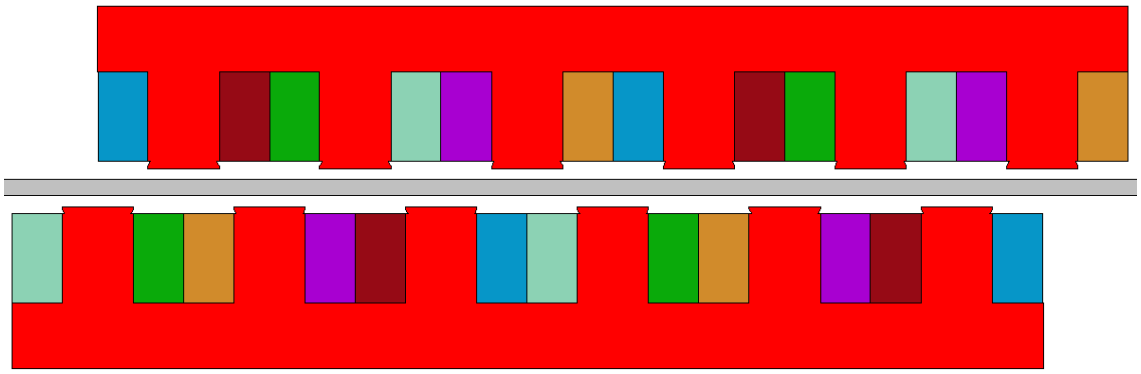

Fig. 119. 2D FE model of double-sided concentrated offset machine

The stators were connected in star, and voltage sourced at 400Vrms line, 50Hz. The motors were modelled as double-sided short stator pairs. The plate rotor used by the double-sided machine would be 0.0066m thick aluminium and rotor resistivity was $6x10^{-8}$ Ohm m, Russell & Norsworthy factor was 1.511.

Standstill performance of the machines was:

	Conventional	Concentrated
Output Thrust:	1378N	1140N
Input Current:	47.9A	59.7A
VA/N:	24.1	36.3
Force/Amp:	28.8	19.1

Several causes of this poor performance from the concentrated offset machine have been identified. Firstly, the winding factor of the offset machine is 0.866, compared to 0.933 for the conventional machine. This gives a difference in force of $(0.866/0.933)^2=0.862$. Also, the ends of the machine have a partly uncancelled negative harmonic due to the short stator topology used. The magnetic gap is also poor, as is shown from the work on slot to tooth ratio.

For the next case, slot to tooth ratio has been modified to improve the machine magnetic gap. The packing factor was also modified to represent the use of a strip wound coil, packing factor 0.76 as compared to a standard mush wound coil, packing factor 0.43. This increase in packing factor allows the production

of a shallower slot containing a smaller coil with the same number of turns and resistance as before, so that coil area and potentially inductance can be decreased.

Currently, we have a new machine with around 0.8 times conventional machine resistance, 0.93 times winding factor, approximately equal Xs and Xe and greater Xm.

If slot to tooth ratio is changed from 60% to 40%, Xm should be close to that of the conventional machine. Resistance and slot leakage reactance will increase by 60/40, 1.5 times. Xe will increase by approximately $\sqrt{1.5} = 1.22$ times.

Next, coil depth will be reduced by 1/3 to compensate for the reduction in width. Slot leakage reactance is again approximately equal. End turn reactance is around 1.1 times conventional. R1 is around 1.8 times original. We can take advantage of the improved packing factor to reduce R1. An increase in packing factor from .433 to 0.76 gives R1 approximately equal to the conventional machine.

In practice, the slot depth reduction is more complex. The aim was to match R1 and X1 of the conventional machine. For the concentrated machine with a slot depth of 0.029m, R1 is 1.035Ω, 101% of the conventional machine. X1 is 4.593Ω, 101% of that of the conventional machine.

The new machine now has R1=1.035Ω per phase, Le=8.096×10^{-3}H per phase.
Core: Length 0.4272m, Width 0.1m, Height .059m, 6 teeth, 6 slots, slot pitch 0.0712m, slot width 0.0286m, slot depth 0.029m

So R1, X1 and Xm are approximately equal to the conventional lim. This should give a concentrated offset machine much closer to the original 2 layer conventional machine performance.

	Conventional	Concentrated
Output Thrust:	1378N	1041N
Input Current:	47.9A	50.7A
VA/N:	24.1	33.7
Force/Amp:	28.8	20.5

The overall width of the conventionally wound machine is much greater than that of the concentrated machine. Therefore, the machine uses the narrower end turn protrusion of the concentrated winding in order to increase the stack width of the machine. The new stack width of the concentrated machine is now 0.15m. This obviously affects slot and magnetizing reactance, primary resistance and secondary end ring (and hence secondary resistance).

Further, tooth tips can be used to keep the same narrow slot openings while increasing coil width, reducing depth and hence reducing reactances. The turns will also be altered in the model to give a current closer to that of the original machine.

Half width end teeth were also added in order to improve the flux path at the ends of the short stator.

The new machine now has R1=1.093Ω per phase, Le=4.647×10^{-3}H per phase. Core: Length 0.4272m, Width 0.15m, Height .053m, 6 teeth, 6 slots, slot pitch 0.0712m, slot width 0.0456m, slot opening 0.0286m, slot depth 0.02m, tooth tip depth 3mm, turns per coil 153. The results of this model are shown in Table 15.

Table 15: Performance of short stator double-sided offset machines

Model Description	Vel m/s	Thrust N	Current Arms	VA/N	W/N	Cos Phi	Efficiency %
Conventional	0.0	1378	47.9	24.1	13.6	0.56	0
Concentrated offset	0.0	1263	49.8	27.3	14.3	0.52	0
Conventional	5.0	948	37.4	27.3	13.9	0.51	36
Concentrated offset	5.0	823	40.3	33.9	15.6	0.46	32

The offset machine is now close to the original in performance. Thrust and current are within 8% of stall values, while VA/N and Force/Amp are within 13%.

It should also be noted that this machine also offers significant design flexibility. When widening the core, the designer may reduce slot depth to reduce Xs and Xe and so X1, this will improve VA/N and power factor. Alternatively, the designer may increase the stack width and leave the slot depth the same to reduce R1 and improve W/N, CuW/N and so efficiency.
Further comparisons must be drawn on other aspects of the two machines.

The length of the standard conventional machine is 0.470m (0.460m stack plus 0.01m for overhanging end windings). This equals total double-sided machine length. The machine length for the offset pair for the new case is 0.463m, slightly less than the standard machine.

The width of the conventional LIM including end windings is 0.21m measured. The concentrated machine width is 0.15m core width, 0.007m end turn offset per side and 0.023m coil width per side, totalling 0.21m wide, the same as the original machine width.

The depth of the conventional LIM is 0.071m. The depth of the concentrated winding machine is 0.053m, 75% of the standard machine depth.

The volume of the conventional machine is 0.470 * 0.205 * 0.071 = $7.008 \times 10^{-3} m^3$. The volume of the concentrated winding machine is 0.463 * 0.21 * 0.053 = $5.153 \times 10^{-3} m^3$, 74% of the original LIM.

The calculated weight of a single LIM is 26.7Kg. The weight of a single new concentrated machine is 29.1Kg, 9% more than the original machine weight.

A single conventional LIM uses Iron 16.6Kg, Copper 9.2Kg. A single new concentrated machine uses Iron 20.4Kg 23% more, Copper 8.7Kg 5% less.
As can be seen, there is a small but potentially significant saving in amount of copper used.

The cost of the two machines must also be compared. The cost of the LIMs can be roughly broken down into the following percentages:

	Conventional	Concentrated
Labour	45%	25%
Copper	26%	24.5%
Steel	8%	9.5%
Other	21%	21%
Total	100%	80%

The use of the new concentrated machines will give a cost saving of up to 20%, mainly through labour savings.

As can be seen, the use of a concentrated machine would produce not only cost, size and weight improvements, but also some performance drawbacks. These factors must all be taken into consideration when looking at the offset concentrated machine for practical use.

An important point is that short stator application is not the natural field of application for concentrated machines, as they are purposefully designed to be able to form a continuous stator track.

7.3.1. Four Pole Machine Experimental Results

An experimental offset double-sided concentrated winding machine has been made and tested using the variable frequency technique described previously. The force produced is compared with first a non-offset double-sided machine using conventional double layer windings and secondly with the calculated output from the time-stepped finite element analysis of the concentrated offset machine Fig. 120.

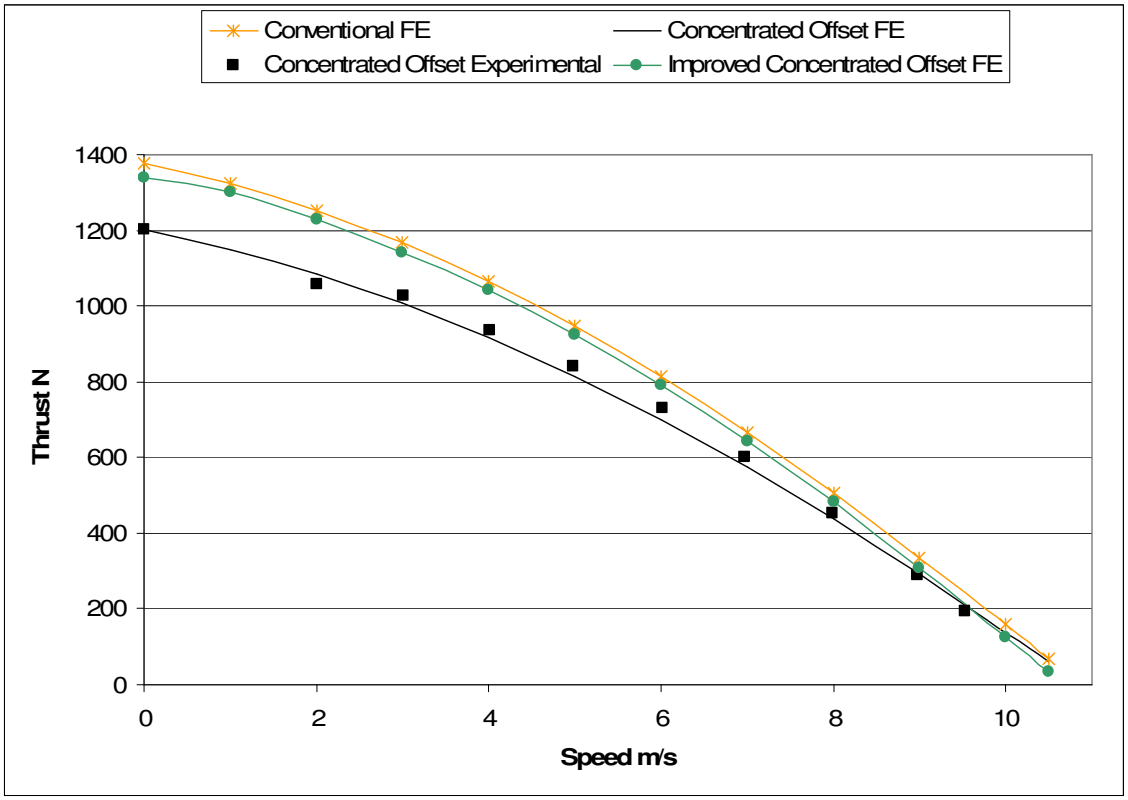

Fig. 120. Offset pair experimental thrust speed comparisons

It will be observed that the force of the offset machine using concentrated windings compares well with the behaviour of the non-offset conventional machine using double layer windings.

In an improved version more conductors can be packed in the slots due to the simple non-overlapping winding, and the slot turns and slot profile can be modified to improve machine performance. An improved machine has been

designed with similar force to the conventional but reduced assembly costs. The improved machine has also been finite Element modelled in Fig. 120.

7.4. 8 Pole Launcher Finite Element Analysis

This study concerns the design and modelling of an offset concentrated machine in the form of a 8 pole 240mm pole pitch UAV launcher, as compared to a typical 2 layer design. The original design had a core width of 0.2m and an airgap clearance per side of 11mm.

The offset machine was designed using the dual concentric coil method detailed previously, in order to reduce end turn leakage reactance. This used the 9 coil 8-10 pole winding with the 10 pole harmonic cancelled out through offsetting.

The concentrated machine used the concentric method, with two separate coils of equal width and turns. These were then separated by an iron tooth 6.67mm wide on each side. The main tooth width was reduced by this amount. The details of this layout are shown in Table 16.

Table 16: Basic parameters of offset concentrated concentric launcher

Attempted F765EQ	Concentric CC3D 2 coil				
Core width	0.23	m	Concentric Coil outer		
coil pairs per phase	3		Coil pitch	0.213333	m
Slot packing factor	0.8		Coil width	0.026667	m
Winding Factor	0.945		Coil depth	0.011	m
Frequency	127	Hz	turns per coil	9	
Volts	350				
R1 per phase	0.0302	Ω	Concentric Coil inner		
csa/turn	2.6074×10^{-5}	Sq m	Coil pitch	0.1467	m
			Coil width	0.026667	m
			Coil depth	0.011	m
			turns per coil	9	

The 3 core width method was used to find the end turn inductance of the concentric coils. The results of the 3D modelling are shown in Table 17.

Table 17: 3D modelling results for offset concentrated concentric launcher reactances

Core width	Amps	Impedance	Resistance	Reactance
230	9.3187	1.073	0.03	1.073
115	17.4489	0.573	0.03	0.572
23	57.9947	0.172	0.03	0.170

End turn leakage reactance was then plotted against core width to give a value of Xe, as seen in Fig. 121.

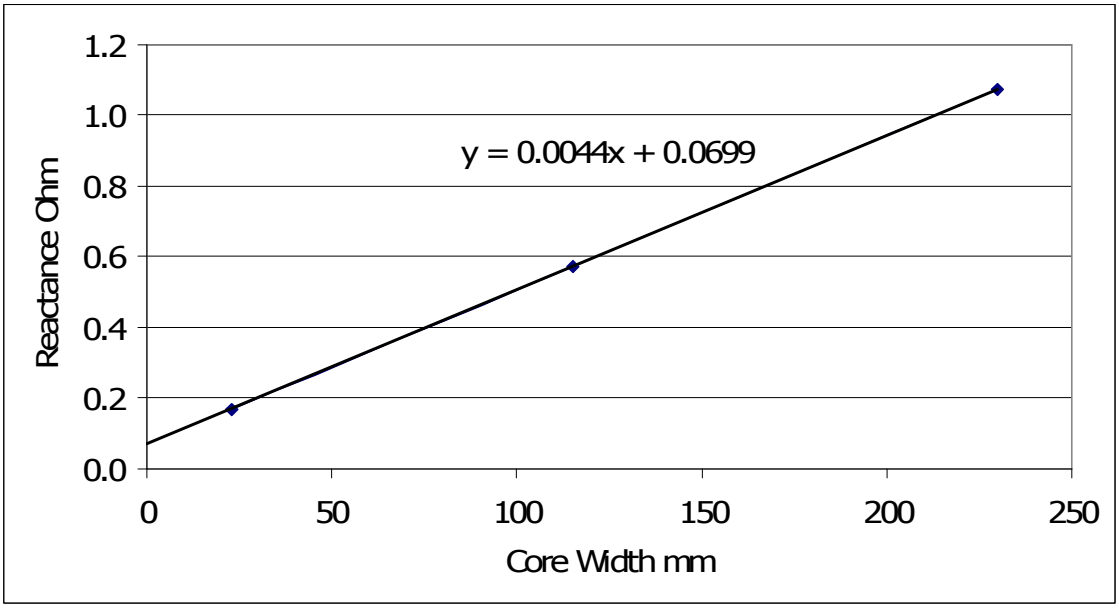

Fig. 121. 3 core width end turn reactances for 2 coil concentric offset launcher

The value of reactance .0699 Ohms per phase at 127Hz was now used for modelling the full performance of the offset launcher.

This model was now run as a full dynamic launch system, as was the 2 layer machine. This should give a good offset performance as the negative harmonics will be fully cancelled, there will be no gaps between stators and the machine will operate as a true short rotor. The conventional machine is modelled as a short stator short rotor system, necessary due to the discontinuous ends of 2 layer LIM windings.

The system was modelled with a track of four stator pairs connected in parallel and a plate rotor less than three stators (4.3m) in length, with a periodic boundary at each end. This meant that at any one time, one stator pair had no rotor secondary. This ensured that the model correctly represented a continuous track of stator pairs. This was also a reasonable assumption as at least one motor in front of the rotor is likely to be active. This may also improve the concentric machine, as the active, empty stator pair has a larger magnetic gap and so will draw less current.

Both conventional and 2 coil concentric versions were run under the same variable voltage and frequency conditions. The models were run with non linear iron conditions. Full dynamic conditions were modelled, including vehicle mass and friction forces. The results for the two systems, the 2 layer wound launcher and 2 coil concentrated winding concentric are shown below.

Both the offset and the conventional machine launcher results used the same form of 2D FE modelling and so can be directly compared.

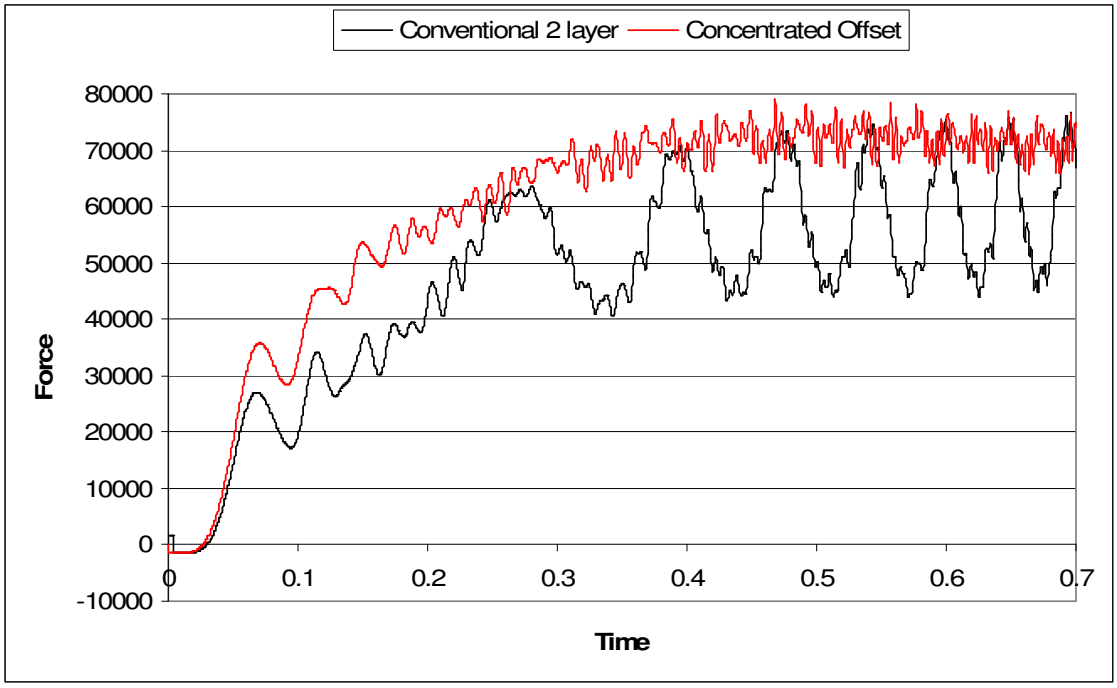

Fig. 122. Force developed on the vehicle by time

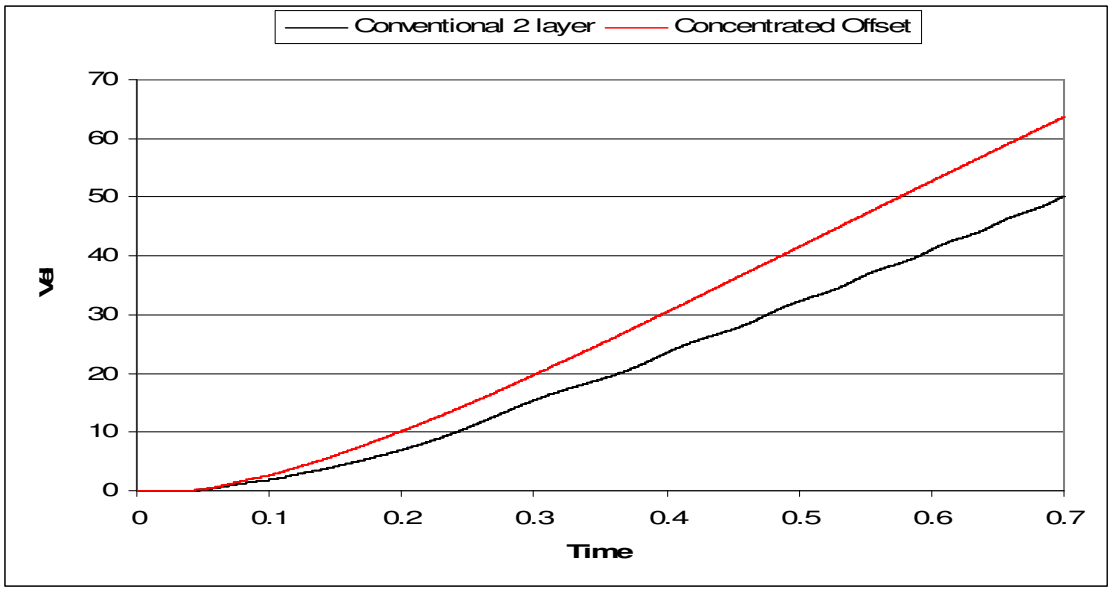

Fig. 123. Velocity developed on the vehicle by time

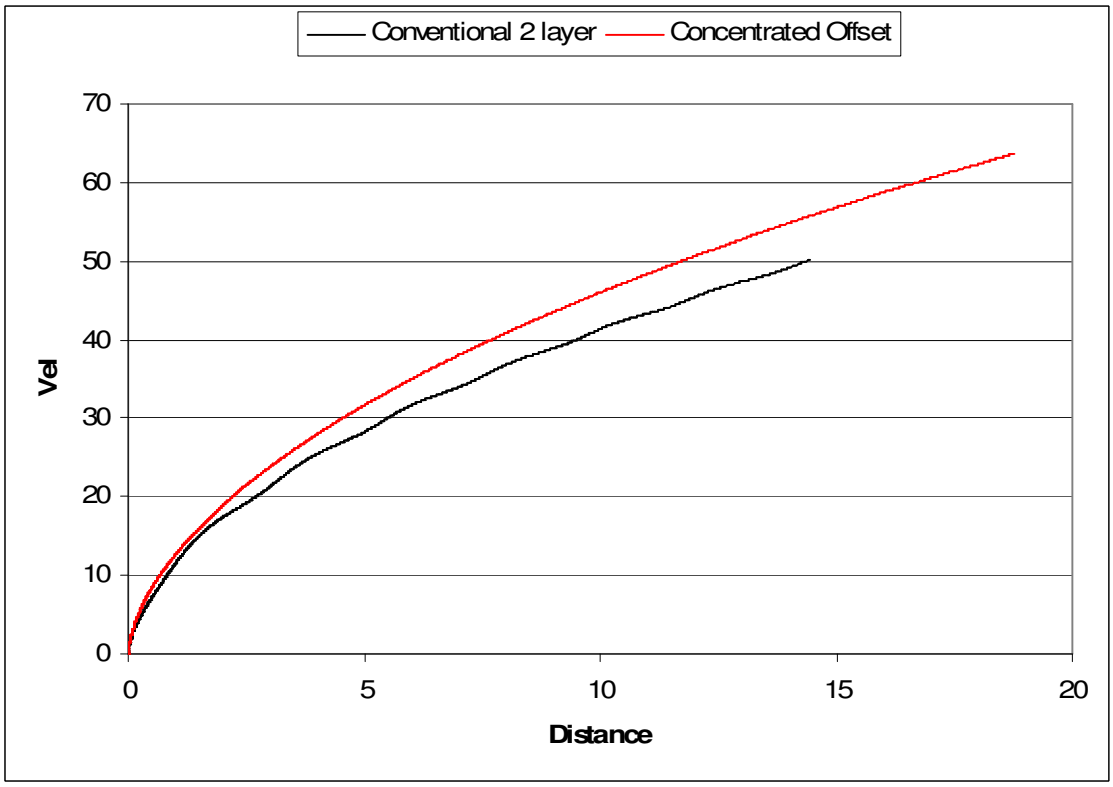

Fig. 124. Velocity of the vehicle by distance travelled

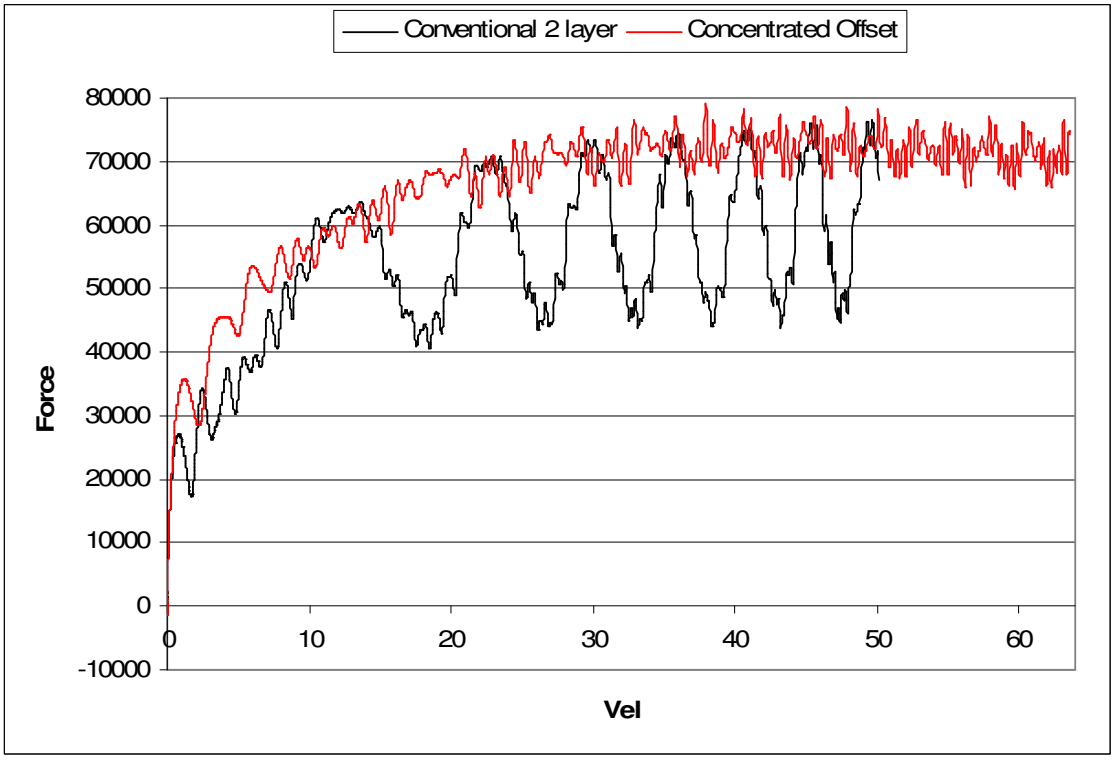

Fig. 125. Force developed on the vehicle by velocity

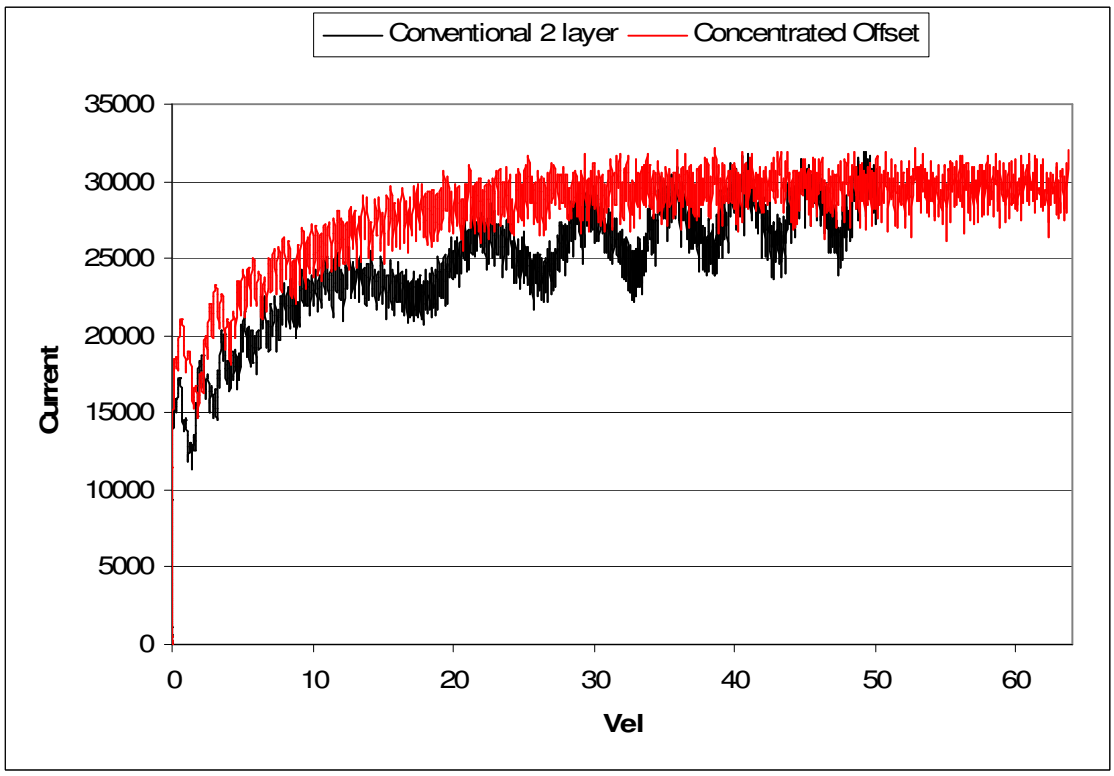

Fig. 126. Total current draw by vehicle velocity (Sum of magnitudes of current per phase)

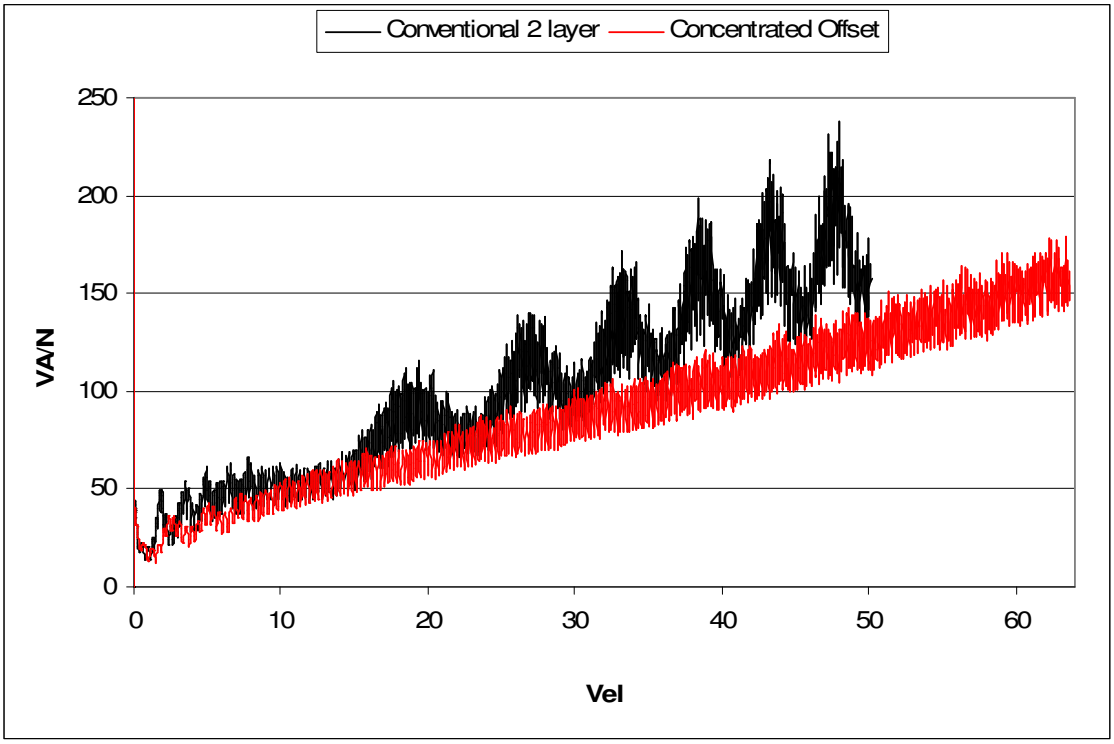

Fig. 127. VA/N by velocity (sum of magnitudes of volts times amps per phase over force

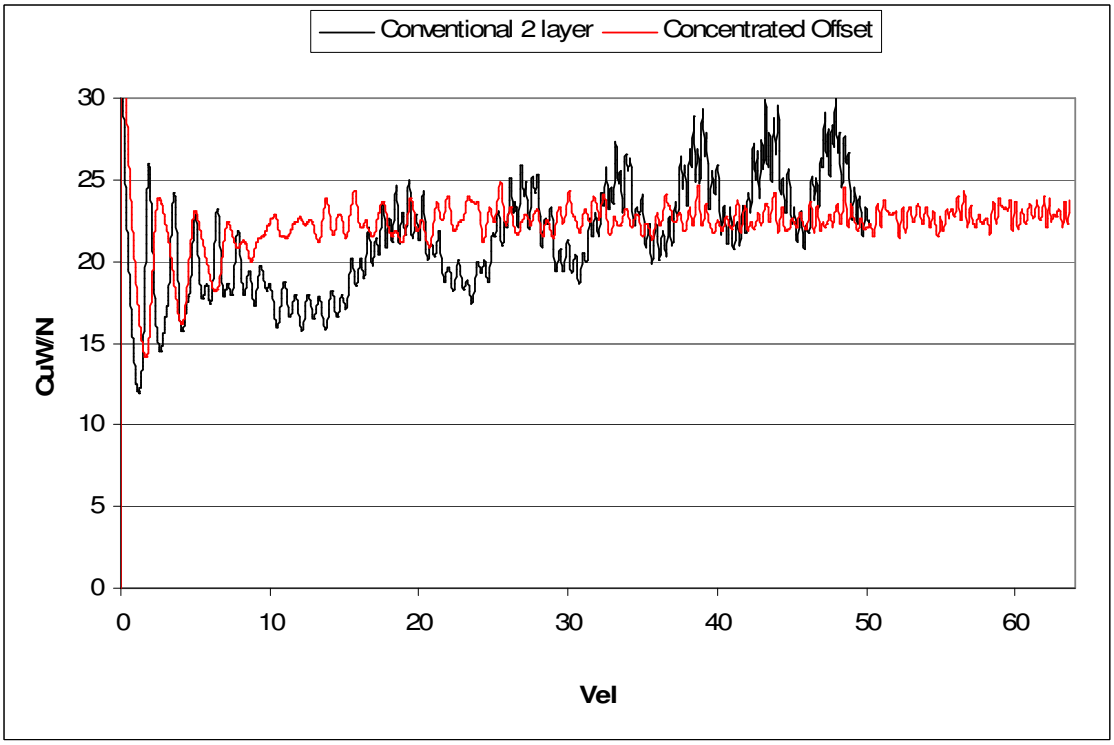

Fig. 128. Copper Watts per Newton of the system by Velocity (8 * I2R loss per stator / Force)

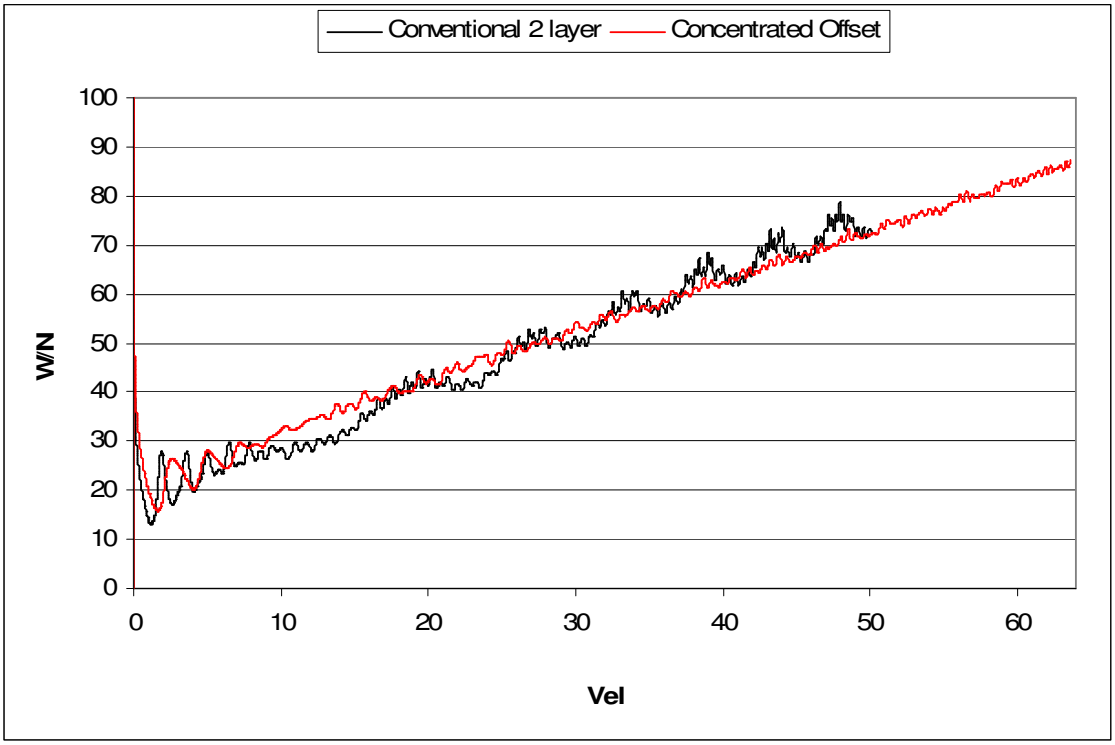

Fig. 129. Watts per Newton of the system by Velocity (CuW/N + Vel*Force/Force)

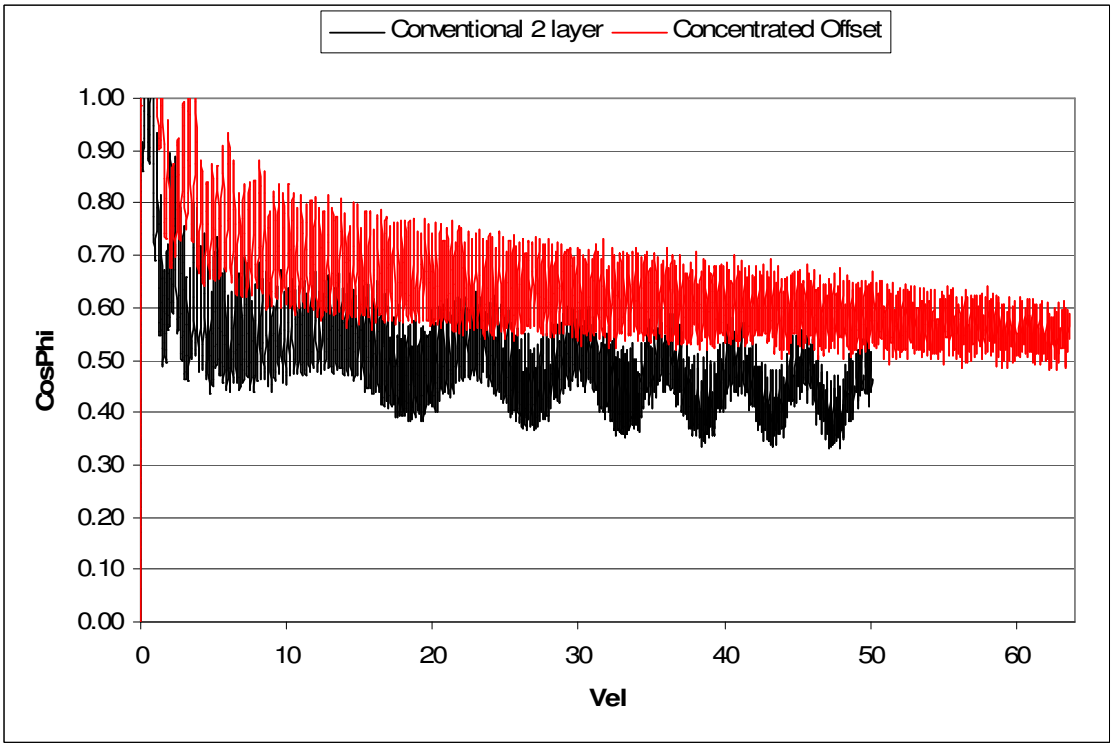

Fig. 130. Cos Phi of the system (W/VA)

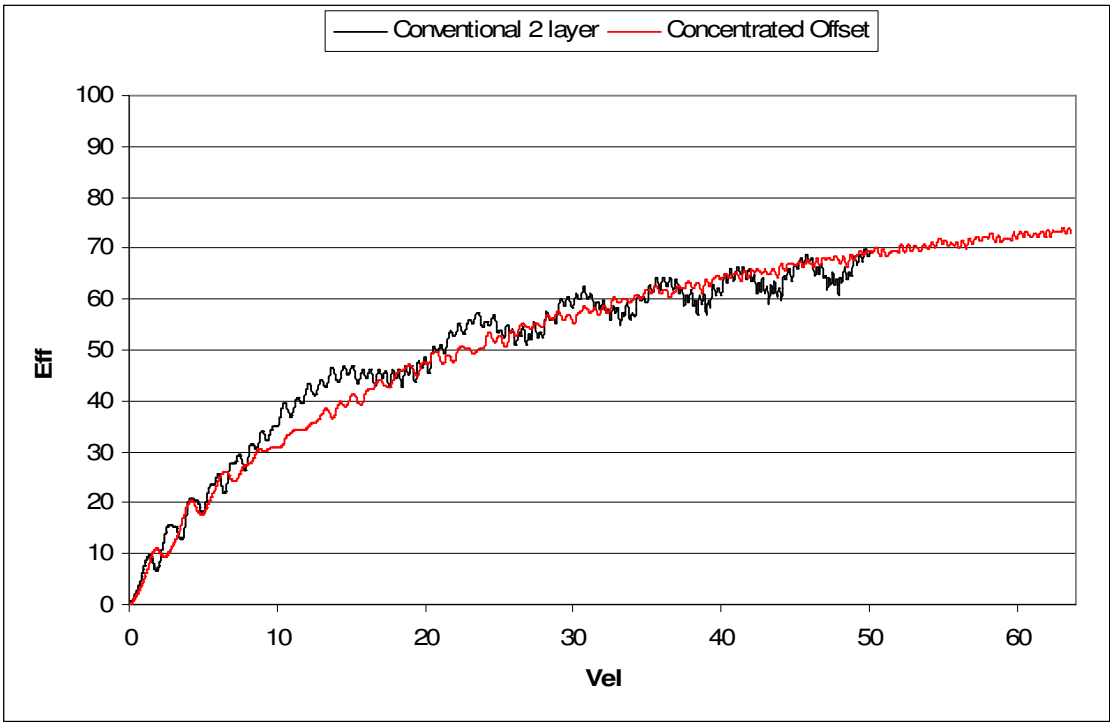

Fig. 131. Efficiency of the system (100 * Vel / W/N)

In all aspects, the 2 coil concentrated offset machine compares favourably with the conventional 2 layer LIM design. The characteristics of the conventional machine are matched or slightly exceeded in all cases by the offset machine [38].

It can also be seen that the force perturbations due to the short stator short rotor condition in the 2 layer LIM winding are not present in the offset concentrated system, producing more force on average and so a much higher final velocity.

7.5. 2D & 3D FE Comparisons

In order to give greater confidence in the 2D results, 3D FE modelling has also been undertaken in order to show that the 3D and 2D finite element results are close to one another.

A 3D model has been built with fully modelled end turns and a full plate. Stall force comparisons at a constant current were undertaken in 2D and 3D to compare the methods.

The force output from the 3D FE model at 2000A was 2073N. The force output from the 2D FE model at 2000A was 2110N. The difference between 3D and 2D methods of modelling is only 2%, which verifies that 2D modelling can be successfully undertaken to give a true representation of the output of 3D machines.

7.6. Dynamic Test Rig Design for Offset Machines

From the previous work, 2D & 3D finite element modelling and some limited experimental work have been used to model the performance of concentrated offset machines. In order to confirm the excellent results achieved from the launcher work a full dynamic test rig has been developed. A schematic of the rig is shown below in Fig. 132 & Fig. 133.

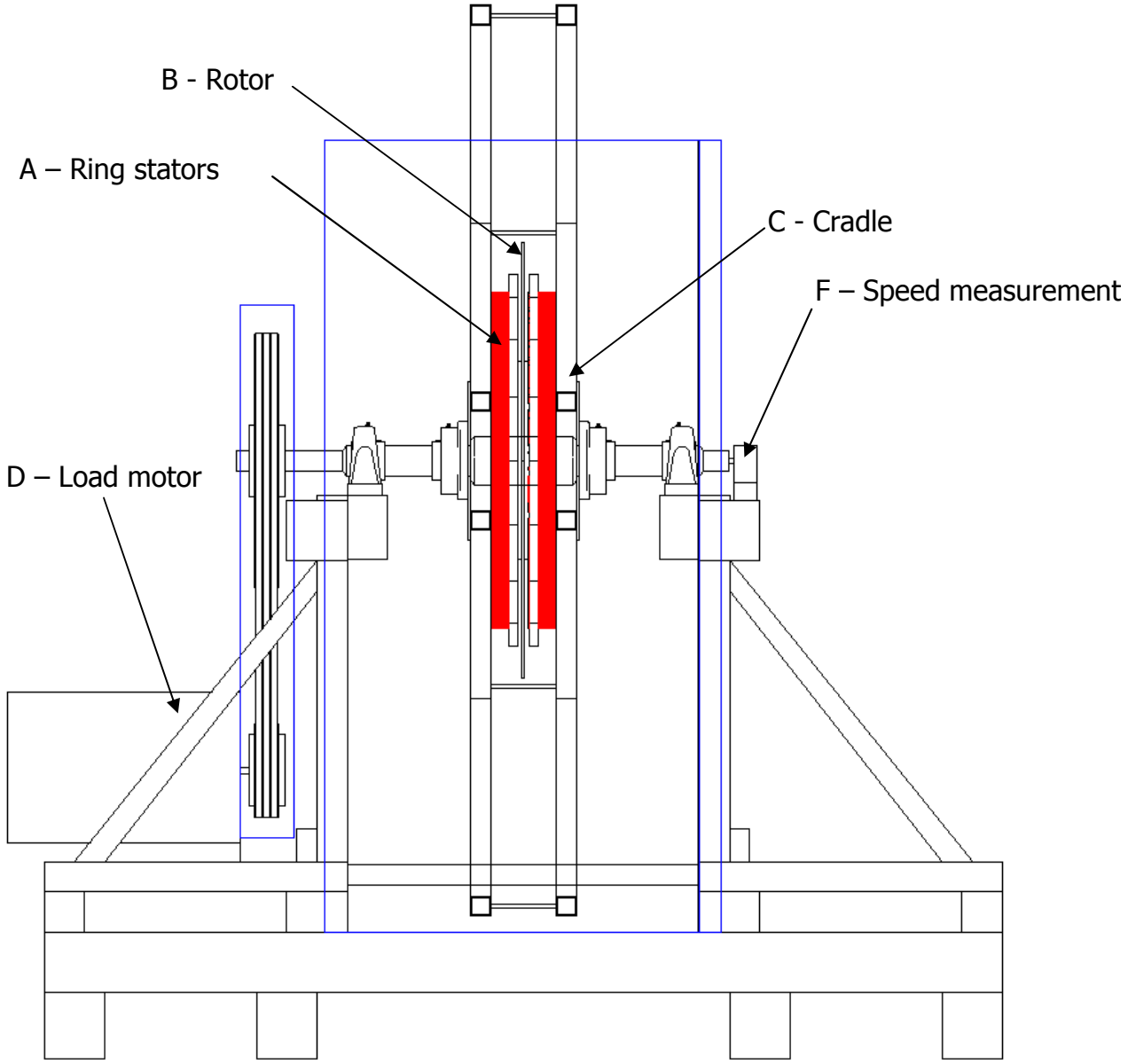

Fig. 132. A schematic of the dynamic test Rig (front view)

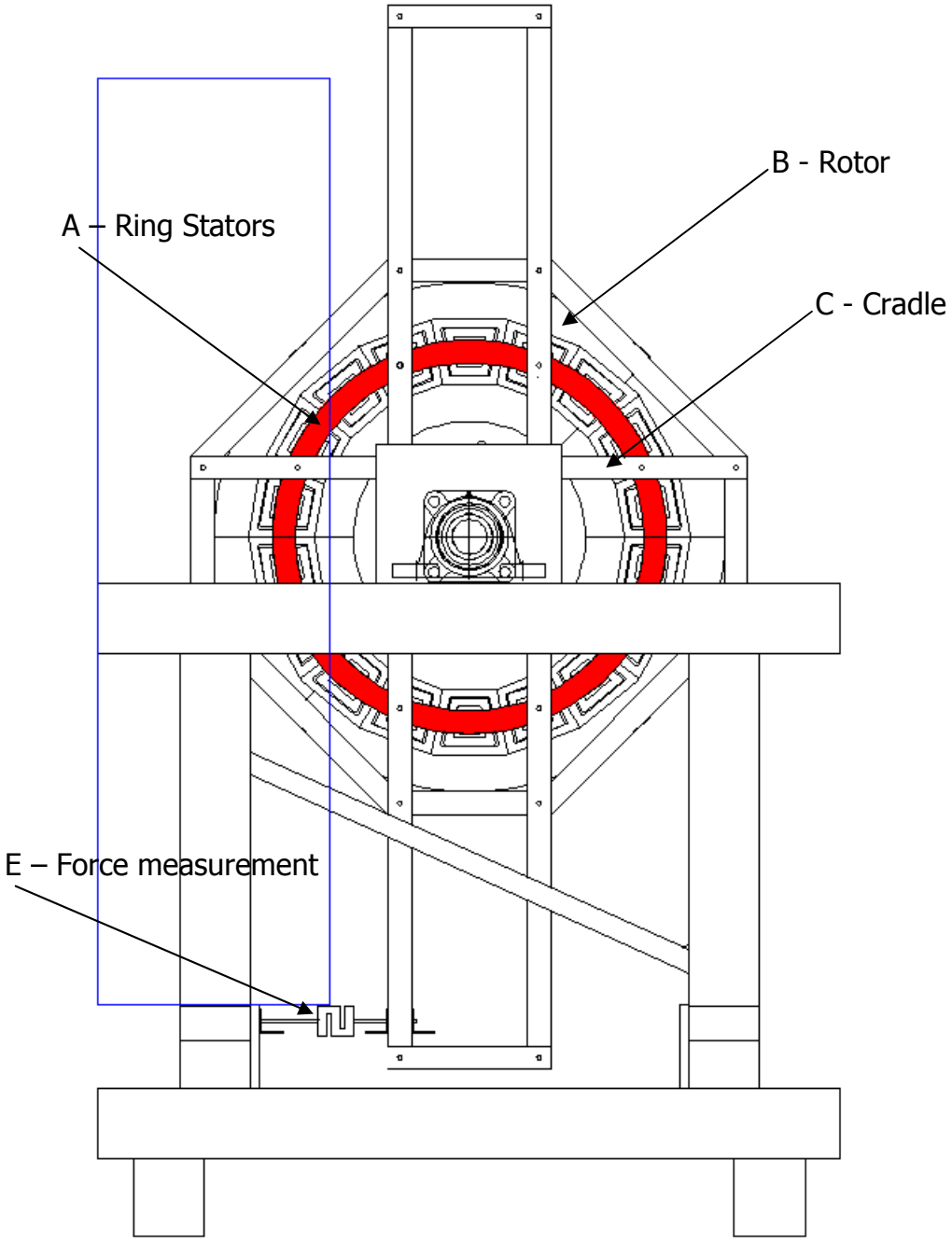

Fig. 133. A schematic of the dynamic test Rig (side view)

For this rig an offset pair of full ring concentrated stators were manufactured and used to test the behaviour of a plate rotor. The stators were mounted on a cradle, attached to the rotor shaft via bearings. The cradle was constrained via a load cell in order to measure the force developed by the stators. The rotor is adaptable, and may be either a full ring, or may be made up of pairs of short rotor sections. The rotor shaft is constrained in speed by a load motor during

testing. The stators and load motor are supplied via inverters, instrumented to measure the current, voltage, power factor and frequency.

7.6.1. Stators

There were many requirements for the stators, some of which were:

- To get non transient short rotor results, a full ring of double-sided offset stators must be used.
- The core width should be limited as much as possible to limit variation in rotor speed across the active face.
- The total current draw of the machine must be limited to a level that may be continuously drawn from the industrial unit supply, 100A per unit, preferably 70A to give a good margin of error.
- The rating of these machines must be such that they can run continuously for long enough to provide results.
- The weight of these machines must be limited to what can be handled with relative ease.
- The motors must be mounted so that the force developed between stator and rotor can be measured.
- The size of the stator should be kept as small as possible to reduce construction costs, as these will be a significant part of the overall project costs.
- The force output from the motors must be sufficient to produce a measurable force for all required conditions.
- The stator must be far enough away from the steel hub so that this does not affect results.

The Stator was designed as two circumferentially offset continuous rings, with a radius of 400mm and an average length (circumference) of 2500mm. The core width was chosen as 50mm. The full stator contains 16 poles, using the 9 coil 8 pole winding configuration, (A on Fig. 132 & Fig. 133). The concentrated stator uses 2 coil concentric windings. The stators are based on the launcher stators

modelled previously, scaled down to approximately 2/3 pole pitch and ¼ core width due to force and current constraints on the rig.

FE modelling via the methods described above was used to develop the optimum design for the rig, bearing in mind measurable force and current constraints. The inter coil tooth width was chosen to be as narrow as possible, without saturating. Core back depth and slot depth were optimised through FE. In order to keep a constant slot width and account for the varying radius of the ring stator, each lamination was designed with a different tooth width. The dimensions of the various laminations can be seen below Fig. 134.

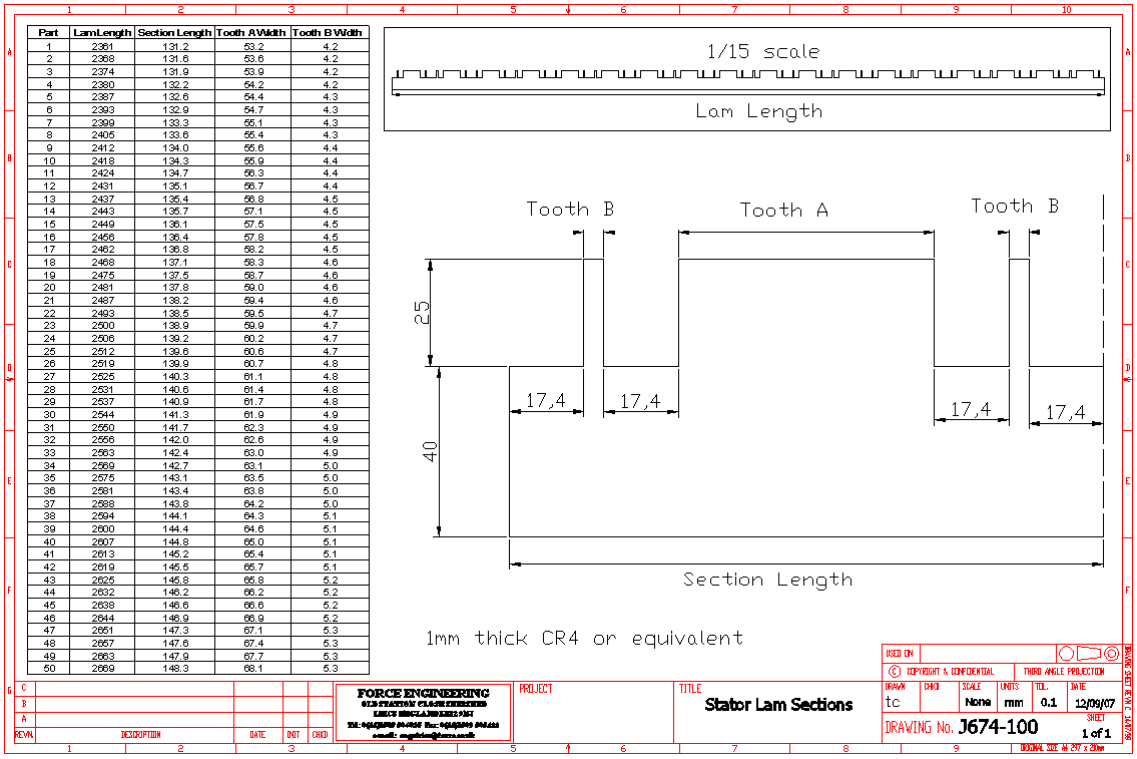

Part	Lam Length	Section Length	Tooth A Width	Tooth B Width
1	2361	131.2	53.2	4.2
2	2368	131.6	53.6	4.2
3	2374	131.9	53.9	4.2
4	2380	132.2	54.2	4.2
5	2387	132.6	54.4	4.3
6	2393	132.9	54.7	4.3
7	2399	133.3	55.1	4.3
8	2405	133.6	55.4	4.3
9	2412	134.0	55.6	4.4
10	2418	134.3	55.9	4.4
11	2424	134.7	56.3	4.4
12	2431	135.1	56.7	4.4
13	2437	135.4	56.8	4.5
14	2443	135.7	57.1	4.5
15	2449	136.1	57.5	4.5
16	2456	136.4	57.8	4.5
17	2462	136.8	58.2	4.5
18	2468	137.1	58.3	4.6
19	2475	137.5	58.7	4.6
20	2481	137.8	59.0	4.6
21	2487	138.2	59.4	4.6
22	2493	138.5	59.5	4.7
23	2500	138.9	59.9	4.7
24	2506	139.2	60.2	4.7
25	2512	139.6	60.6	4.7
26	2519	139.9	60.7	4.8
27	2525	140.3	61.1	4.8
28	2531	140.6	61.4	4.8
29	2537	140.9	61.7	4.8
30	2544	141.3	61.9	4.9
31	2550	141.7	62.3	4.9
32	2556	142.0	62.6	4.9
33	2563	142.4	63.0	4.9
34	2569	142.7	63.1	5.0
35	2575	143.1	63.5	5.0
36	2581	143.4	63.8	5.0
37	2588	143.8	64.2	5.0
38	2594	144.1	64.3	5.1
39	2600	144.4	64.6	5.1
40	2607	144.8	65.0	5.1
41	2613	145.2	65.4	5.1
42	2619	145.5	65.7	5.1
43	2625	145.8	65.8	5.2
44	2632	146.2	66.2	5.2
45	2638	146.6	66.6	5.2
46	2644	146.9	66.9	5.2
47	2651	147.3	67.1	5.3
48	2657	147.6	67.4	5.3
49	2663	147.9	67.7	5.3
50	2669	148.3	68.1	5.3

Fig. 134. Lamination details for dynamic test rig stators

The peak power output of the test motor was developed in order to allow the specification of a load motor of sufficient power. For the final design the peak power output is predicted by FE as 6.1kW. Total weight of each stator was calculated as 81Kg. Rating was calculated as just over 9 minutes, which is sufficient time to produce results.

The stack was designed to have enough clearance from the steel hub that the results would not be unduly affected. 3D FE modelling indicated that with over 100mm separation, the presence of the steel hub should make little difference to the overall results. A finished stator is shown below in Fig. 135.

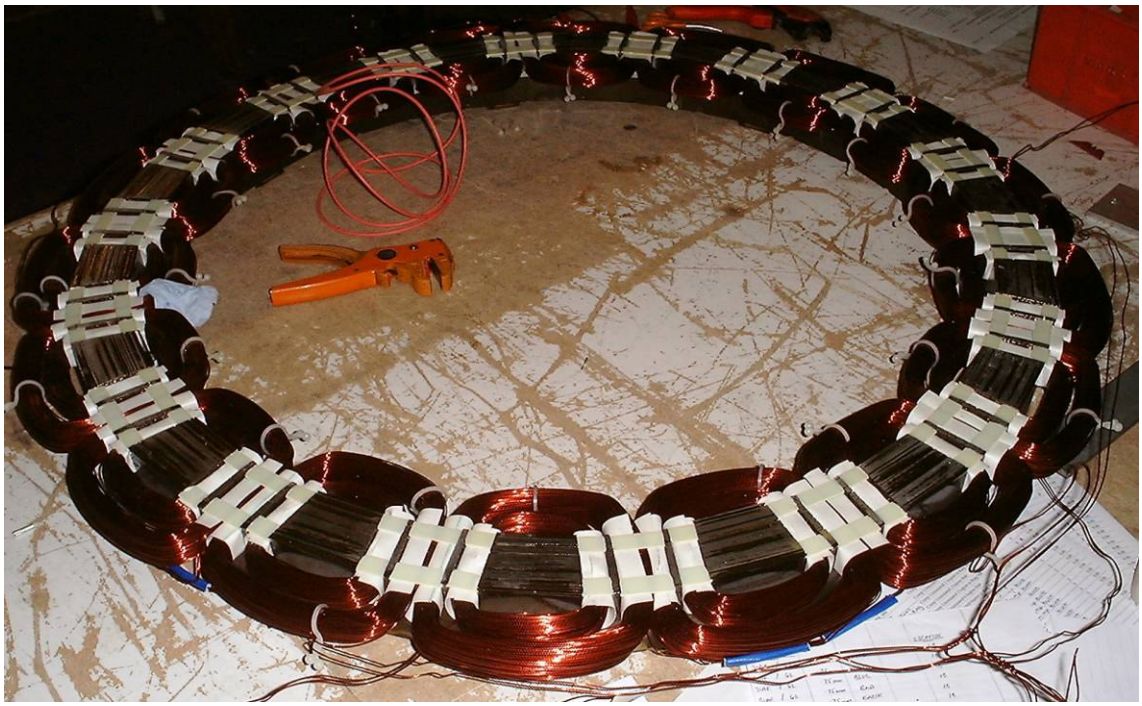

Fig. 135. Dynamic test rig stator

7.6.2. Rotors

Several rotors were made for the test rig (B on Fig. 132 & Fig. 133). Firstly, a continuous rotor was made in order to study the behaviour of the offset machine. Further rotors were made, consisting of pairs of short rotors (for balance) of various pole numbers in length, to test short rotor behaviour. These were designed as below Fig. 136.

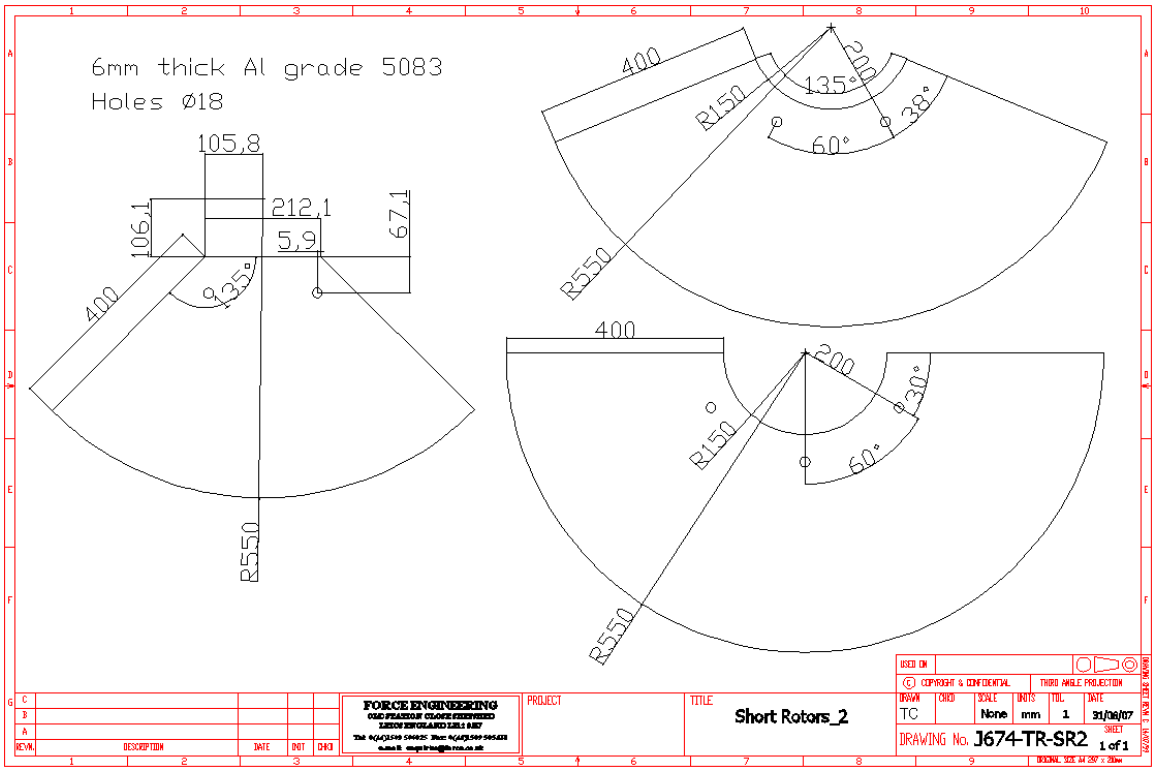

Fig. 136. Test rig short rotor sections

The rotor plates were designed to be much wider than the stack. (300mm rotor width, 50mm stack width). This was to give as much space as possible for the end ring currents, as end ring current patterns in a disk machine will be affected by the difference in radii between outer and inner end rings.

The material for the disk and rotors was chosen as 6mm thick 5083 grade Aluminium, as this is a high strength material with a relatively high resistivity ($6x10^{-8}$ Ohm m). 6mm was chosen to make the plate sufficiently thick to maintain mechanical strength, without giving an excessively wide airgap. This is also a material commonly used in high speed launcher rotors, and was used in the FE track modelling. The short rotor aluminium sections are shown below Fig. 137.

Fig. 137. Dynamic test rig short rotor sections

7.6.3. Stator Cradle Structure

The stator is attached to a cradle, which in turn is mounted on the rotor shaft via a set of bearings (C on Fig. 132 & Fig. 133). This allows the stator cradle to move freely independently of the motion of the rotor. The cradle is constrained with a load cell in order to measure the force produced by the stators. The cradle is also designed to allow the airgap to be set and adjusted as required. Further, the cradle was designed to be and is strong enough to resist the forces developed by the stators, including the normal force. The cradle is shown in Fig. 138.

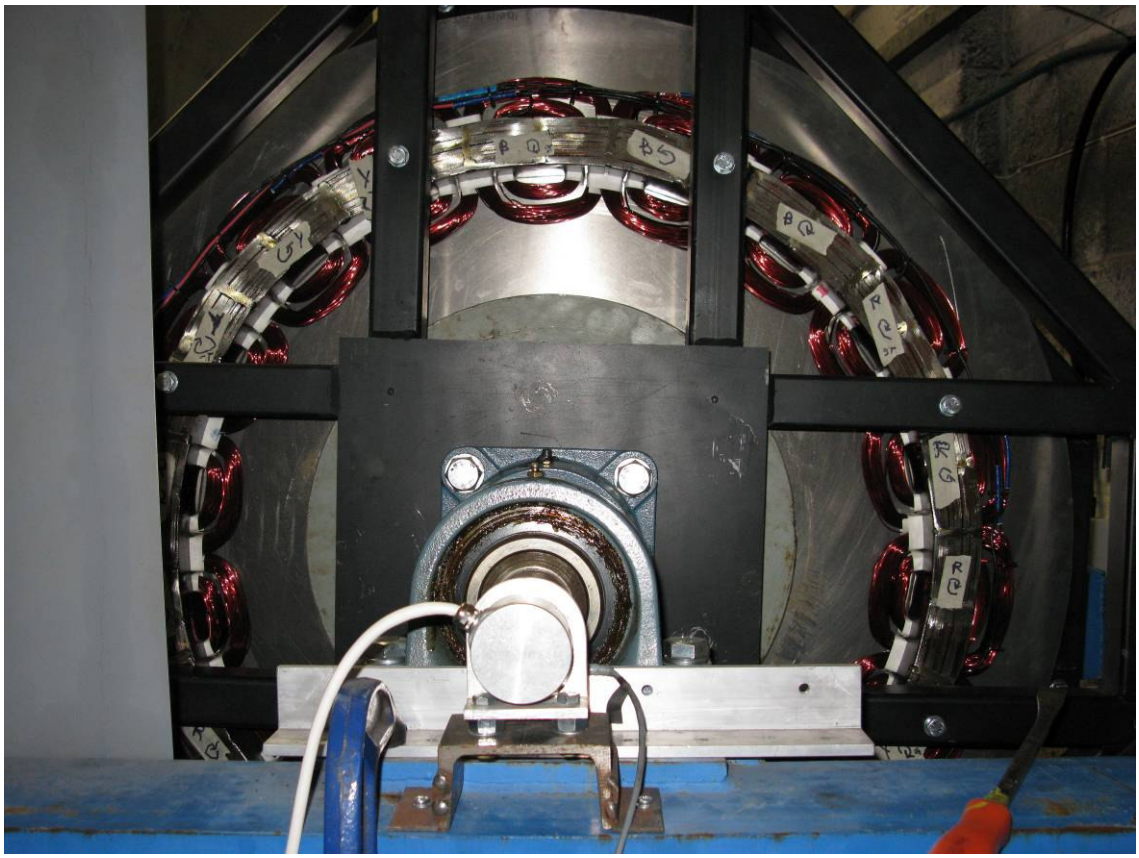

Fig. 138. Dynamic test rig cradle

7.6.4. Load Motor and Drive

In order to take measurements at set speeds, a load motor is included (D on Fig. 132). A squirrel cage induction motor is used, supplied from an inverter to give frequency based speed control. The drive was connected to the shaft via a belt and pulley system to control the speed of the linear motor rotor.

In order to maintain the speed when the test motor is active, the load motor must have a greater output power than the test motor. The maximum power output from the test motor is 6.1kW. A 15kW drive was chosen in order to provide a good margin and to give the rig flexibility for future applications. The load motor is shown in Fig. 139.

Fig. 139. Dynamic rig load motor and pulley

7.6.5. Motor Power and Control

The ring stators for testing were powered through an inverter rated at 74A. This allowed the significant flexibility of the setup due to the ability to alter frequency, and also reduced the supply current draw through power factor correction.

The load motor was supplied through a 15KW inverter which allowed control over the full speed range required. The inverter was connected to a resistor bank in order to remove the excess power developed from maintaining the speed of the rotor when the test motor is active.

7.6.6. Instrumentation

Power analysers were fitted to the inputs of both load and test motors. These are capable of recording 3 phase currents, voltages, power factors and frequency.

An S beam type tension-compression load cell was used to anchor the bottom of the cradle to the frame (E on Fig. 133). This will give force readings for either tension or compression, which allows the study of braking and acceleration forces and adds flexibility to the rig.

A rotary encoder was mounted onto the shaft to measure the rotor velocity via a flexible coupling to the end of the rotor shaft (F on Fig. 132). The range of disk speeds will be 24 to 500 rpm, and so a high resolution 5000 pulse per revolution encoder was used in order to give good performance over the required speed range (2k-30k Ppr).

The overall rig is shown below Fig. 140.

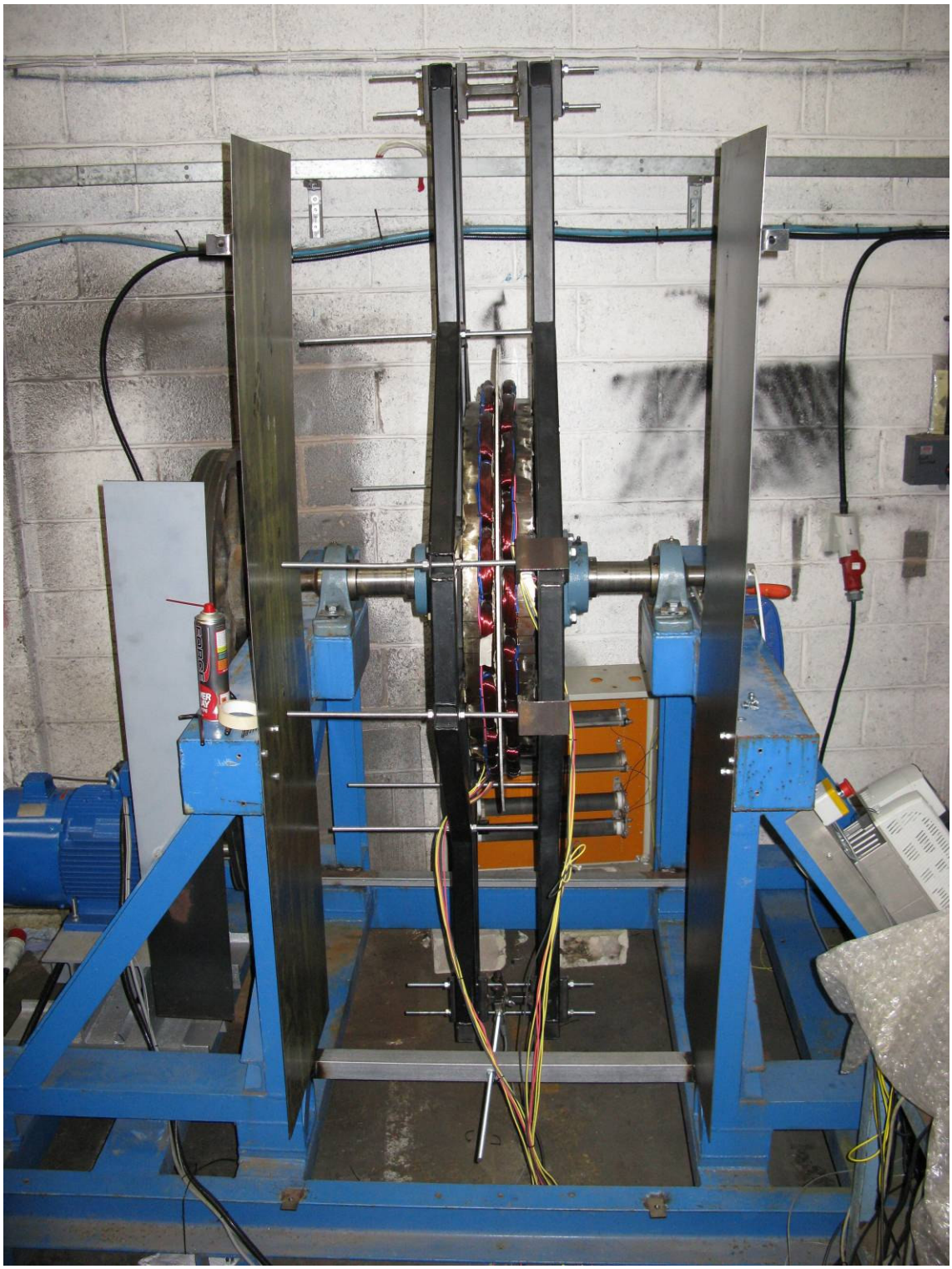

Fig. 140. Dynamic test rig for offset machines

7.7. Dynamic Test Rig FE Modelling for Offset Machines

The dynamic test rig was initially modelled in 2D FE in order to find the basic parameters required for design. In order to give a full set of results, full 3D FE modelling was undertaken. 3D FE will include the effect of curvature, uneven radius and the constrained end ring conditions that are present in the rig but ignored by the simple 2D model. The 3D test rig without a rotor is shown below Fig. 141.

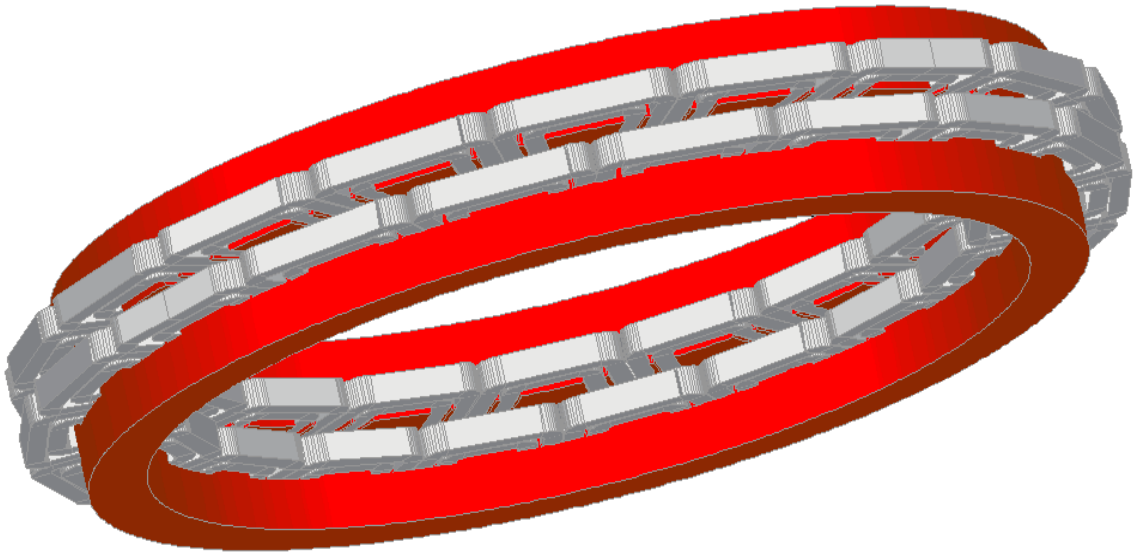

Fig. 141. 3D FE of the dynamic test rig

7.8. Dynamic Test Rig Results for Offset Machines

The results of the dynamic test rig can be seen in Table 18 & Table 19.

Table 18: 3D FE modelling results

Vel m/s	Thrust N	Current Arms	Voltage Vrms	Impedance Ohm	VA/N	W/N	Cos Phi	Efficiency
0	1133	59.44	230.9	-2.680-2.810i	36.3	25.1	0.69	0.0
1	1119	57.84	230.9	-2.630-2.720i	35.8	24.9	0.70	4.0
2	1102	56.18	230.9	-2.580-2.630i	35.3	24.7	0.70	8.1
3	1078	54.42	230.9	-2.520-2.540i	35.0	24.6	0.70	12.2
4	1048	52.58	230.9	-2.450-2.450i	34.7	24.6	0.71	16.3
5	1012	50.67	230.9	-2.370-2.360i	34.7	24.6	0.71	20.4
6	970	48.73	230.9	-2.280-2.260i	34.8	24.7	0.71	24.3
7	917	46.72	230.9	-2.170-2.170i	35.3	24.9	0.71	28.1
8	855	44.69	230.9	-2.040-2.060i	36.2	25.5	0.70	31.4
9	782	42.68	230.9	-1.890-1.940i	37.8	26.4	0.70	34.1
10	698	40.76	230.9	-1.720-1.790i	40.5	28.0	0.69	35.7
11	600	38.92	230.9	-1.530-1.610i	44.9	31.0	0.69	35.5
12	487	37.23	230.9	-1.320-1.380i	52.9	36.6	0.69	32.8
13	364	35.87	230.9	-1.130-1.090i	68.2	49.1	0.72	26.5
14	229	34.47	230.9	-0.960-0.730i	104.2	82.9	0.80	16.9
15	14	15.18	230.9	-1.370-0.607i	739.0	675.7	0.91	2.2

Table 19: Test Rig experimental results

Calculated Results									
Speed m/s	Force at load cell N	Force at stator N	Voltage /phase V	Current /phase A	Impedance Ohms	Force per Amp	VA/N	W/N	Eff %
0.98	352.2	970.7	226.5	53.6	4.228	18.1	37.5	25.7	3.8
1.99	337.5	930.1	227.3	51.2	4.436	18.2	37.6	25.7	7.8
3.00	312.9	862.5	227.1	47.8	4.752	18.0	37.8	25.6	11.7
4.01	323.7	892.3	229.4	42.2	5.441	21.2	32.5	20.3	19.8
5.01	311.0	857.1	230.8	37.3	6.193	23.0	30.1	15.7	31.9
6.03	294.3	811.2	227.0	47.4	4.793	17.1	39.7	26.7	22.6
7.31	271.7	749.0	228.1	45.4	5.023	16.5	41.5	27.4	26.7
8.00	258.0	711.1	228.9	40.3	5.673	17.6	38.9	23.3	34.4
8.98	233.5	643.5	228.2	43.2	5.282	14.9	46.0	-29.5	-30.4
9.97	208.0	573.2	229.6	38.9	5.897	14.7	46.8	-26.5	-37.6
10.99	173.6	478.6	230.8	37.3	6.193	12.8	53.9	-28.1	-39.0
12.01	138.3	381.2	230.7	35.6	6.472	10.7	64.7	-30.2	-39.8
12.99	100.1	275.8	231.7	34.6	6.690	8.0	87.3	-35.2	-36.9
14.03	55.9	154.1	231.6	33.8	6.861	4.6	152.1	-49.3	-28.5
15.00	8.8	24.3	234.1	33.7	6.945	0.7	972.9	-222.8	-6.7

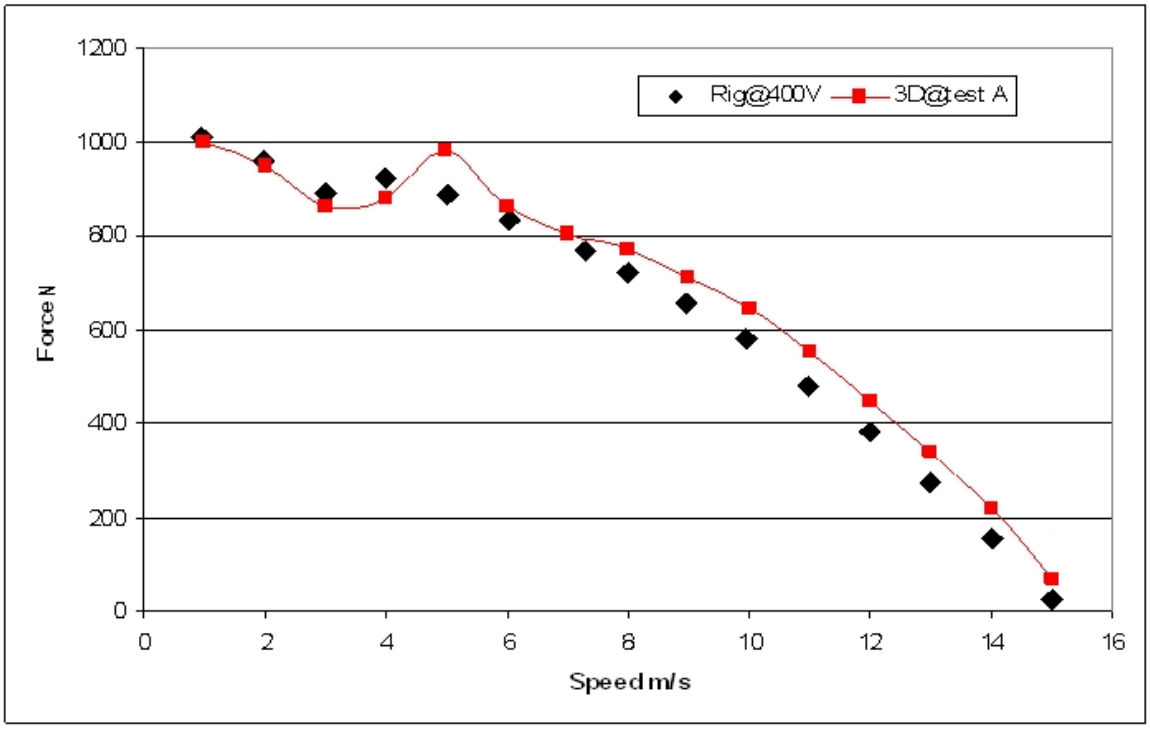

Fig. 142. Test rig output force compared with 3D FE

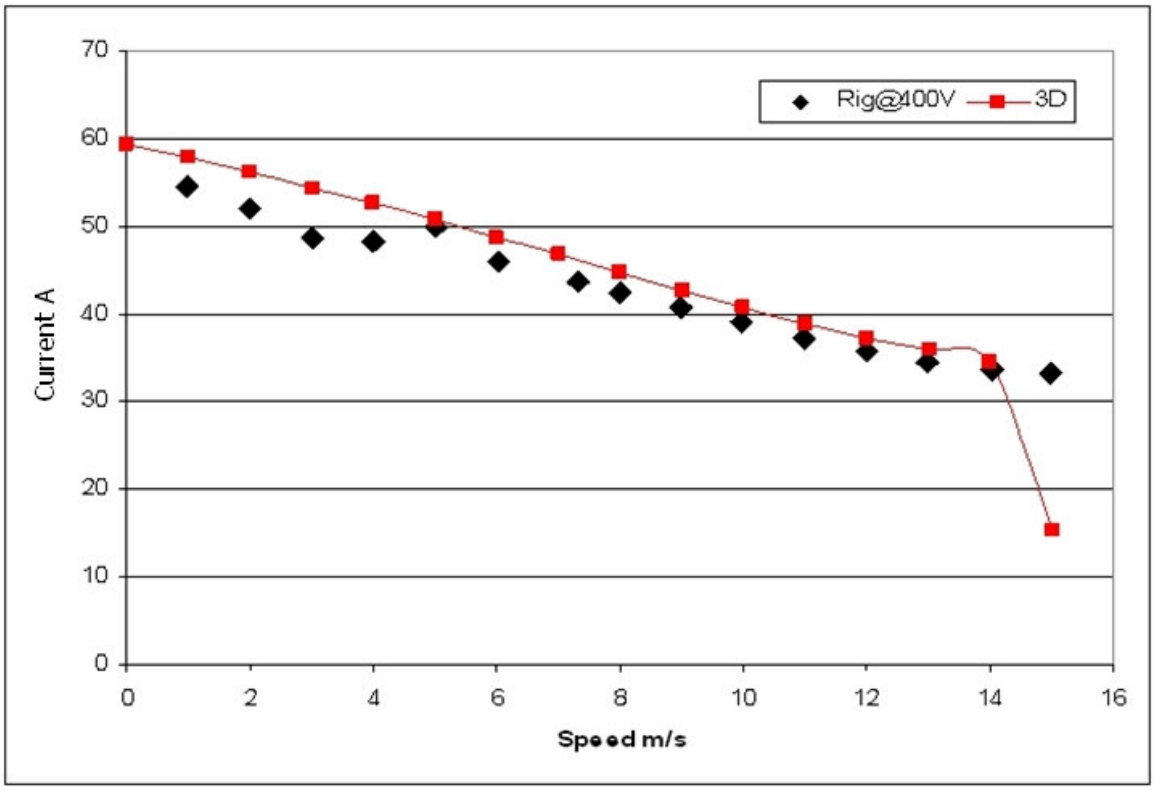

Fig. 143. . Test rig current draw compared with 3D FE

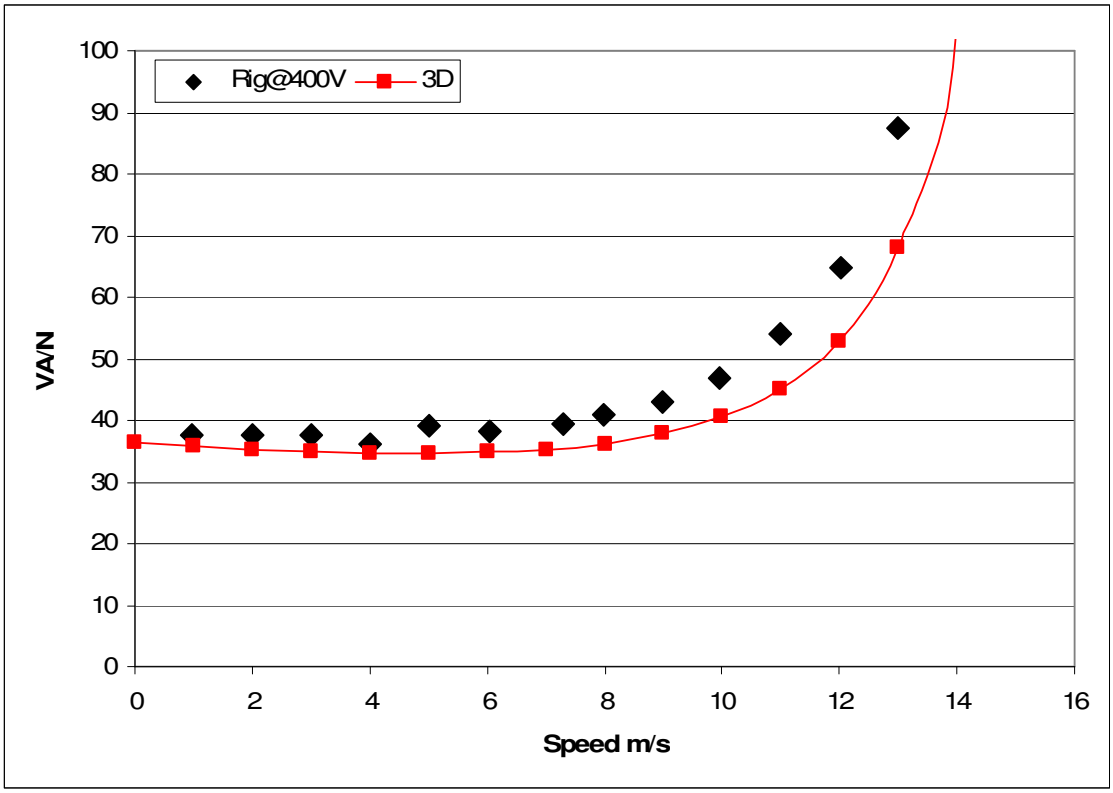

Fig. 144. Test rig VA/N compared with 3D FE

It can be seen from the above results that the performance of the test rig is close to that predicted by 3D FE. This indicates that the machines indeed behave as has been predicted. The earlier work on launch machines showed a close agreement between 2D and 3D model performance. As the 3D FE results are close to test rig performance, this indicates that the results from 2D FE will also conform to reality.

7.9. Offset Machine Conclusions

The offset machine has been shown to be a novel and effective method of using single layer concentrated windings for induction machines. [37][38] The arrangement eliminates the backward going harmonic produced by the concentrated windings so that a plate secondary can be used.

Comparisons have been drawn between the thrust produced by the arrangement and a similar double–sided machine made from stators using

conventional double layer windings and it is shown that comparable results may be obtained. A full dynamic test rig has been developed, which confirms the good performance of the offset machines when compared to 3D FE modelling. This in turn validates the excellent results from 2D FE launcher modelling, as this has been shown to agree with 3D FE.

In other cases, performance of the system using offset concentrated windings is slightly reduced, but the offset concentrated machine is significantly cheaper and easier to construct.

An important potential area of application is in high voltage machines. Producing a 2 layer wound high voltage machine adds significant cost and complexity, and simple winding techniques cannot be applied. The concentrated winding setup is very capable for high voltage use due to the physical isolation of the phase coils from one another in most positions.

The work performed has been concerned with the study of linear machines. However, these techniques may be applied to rotary induction machines using a disk rotor Fig. 145 or a cage/drag cup type rotor Fig. 146.

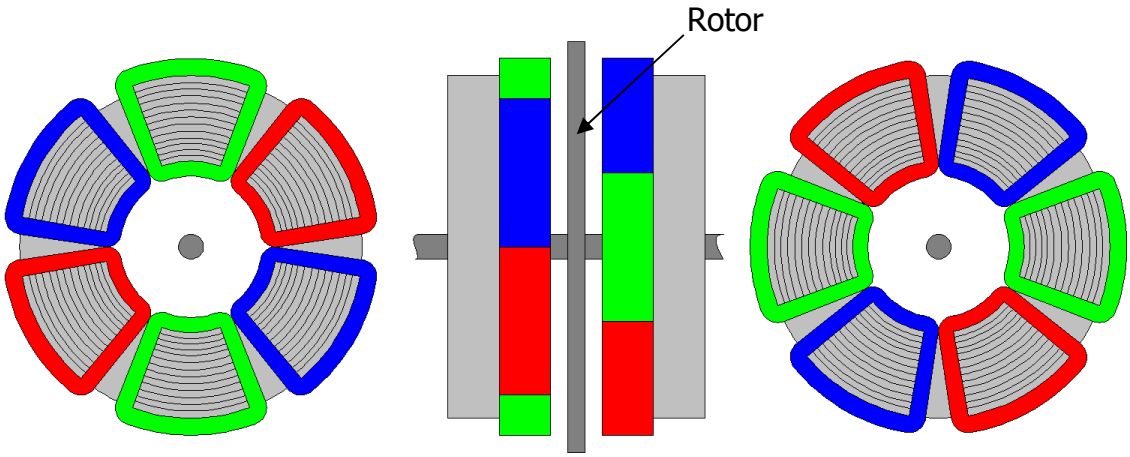

Fig. 145. Disk type rotary concentrated offset induction motor

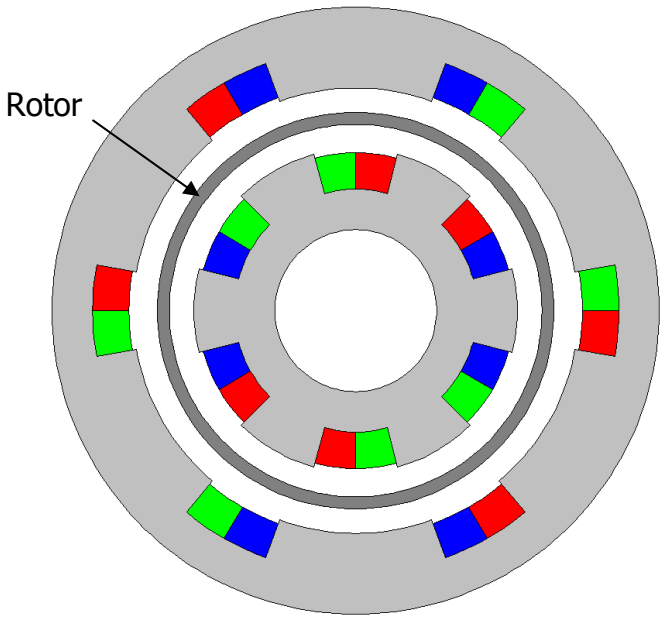

Fig. 146. Cage or drag cup type rotary concentrated offset induction motor

The technology may also be applied to synchronous machines. For example, in permanent magnet rotor synchronous machines benefits may be gained from cancellation of the backwards going field using configurations similar to those shown above, but using permanent magnet rotors.

8. Overall Conclusions

Simple analytical methods of end turn leakage inductance modelling have been found to be inexact when modelling planar concentrated iron cored coils. An improved method based on 2D & 3D Finite Elements has been developed. This has also resulted in a fast and accurate equation for calculating end turn inductance that can be solved extremely quickly with modern computer systems. A method of using concentric coils has also been developed that can significantly reduce the end turn inductance of a concentrated winding stator. The correlation between experimental results and 2D finite element results using the new methods of calculating end turn inductance is excellent.

It has been established that concentrated winding induction machines perform poorly with plate rotors due to the presence of several flux harmonics travelling in opposite directions. Two methods were developed to improve the performance of concentrated winding induction machines.

The wound rotor used with a planar concentrated stator winding provides an excellent novel arrangement and can be applied to both low speed and high speed applications.

The wound rotor gives several performance benefits including high forces and efficiencies, the ability to generate high thrusts at lower slips, a reduction in power conditioning and control requirements, a reduction in the working airgap and the freedom to more easily modify the various characteristics of the rotor. Further, the edge effects in a wound rotor linear motor are negligible, giving significant improvements for high speed applications.

Further advantages include the ability to alter rotor resistance dynamically to give simple, cheap control. Alternatively, the thrust speed characteristic of a wound rotor system can be designed to closely resemble that of a conventional (rotating) machine indicating that simple control methods such as flux vector

control can be used. Another potential benefit is power pickup, using the wound rotor to supply power to onboard systems.

Important conclusions have been reached from the short rotor work. Firstly, short rotors of 4 poles and over length tend to behave in a manner very similar to the behaviour of conventional (continuous rotor) machines of the same air-gap geometry.

The use of extremely short rotors (less than 2 poles) gives increased starting and low speed torque, which may be due to the unusual current behaviour at the ends of the rotor. This area is the subject of future investigation.

The offset machine has been shown to be a novel and effective method of using single layer concentrated windings in a double-sided configuration for induction machines. The arrangement eliminates the backward going harmonic produced by the concentrated windings so that a plate secondary can be successfully used.

Both 2D and 3D Finite Element modelling has been tied with high speed dynamic test rig experimental results, to confirm the accuracy of the FE performance predictions.

Offset machines allow many of the advantages of the concentrated winding to be employed, and also provide other benefits such as simple methods to dynamically change operating harmonic. The windings are also naturally apt for high voltage operation. Finally, the ability to cancel negative harmonics may prove extremely useful in applications such as permanent magnet machines.

9. Further Work

There are several areas where further work would be desirable in the future. Firstly, the end turn leakage inductance equation could be developed for the case of two coil concentric machines.

For the wound rotor work, static testing has been performed and gives a reasonable degree of confidence in the wound rotor FE results. With more time and resources, a dynamic test rig could be developed in order to prove the performance of wound rotor machines at various speeds.

The short rotor FE modelling exposed several points of interest for short rotors. It is hoped in the future that dynamic test results can be developed in order to more closely study the performance of short rotors over a wide range of pole number lengths.

Finally, the short stator offset machine could be further developed in order to improve its performance relative to the 2 layer conventional machines it has been developed to replace, without sacrificing the positive characteristics of the concentrated winding.

References

[1] T.C. Martin, *The inventions, researchers and writings of Nikolai Tesla,* Barnes & Noble Books, pp. 5, 1992.

[2] B. Bowers, *Sir Charles Wheatstone*, Science Museum, pp. 82, 1975.

[3] "A wound rotor motor 1400 ft. long" *Westinghouse Engineer*, vol. 6, pp. 160, 1946.

[4] E.R. Laithwaite, S.A. Nasar, "Linear-Motion Electrical Machines", *Proc. IEE*, Vol. 58, No. 4, pp. 531-542, 1970

[5] Graham Bellamy, Lt Mick Thomson, "EMKIT - Commissioning and performance testing of a technical demonstrator for the electromagnetic catapult launch of UAV's", *IMarEST Engine as a Weapon*, London, Dec. 2006

[6] A. Consoli, G. Scarcella, A. Testa, "Sensorless control of PM synchronous motors at zero speed", *IEE IAS 34,* Vol. 2, pp. 1033 – 1040 1999

[7] J. Grieg, E.M. Freeman, "Travelling-Wave Problem in Electrical Machines", *Proc. IEE*, Vol. 114, No. 11, pp. 1681-1683, 1967.

[8] D. Roger, H. C. Lai, P. J. Leonard, "Coupled Elements for Problems Involving Movement", *IEEE Transactions On Magnetics*, Vol. 26, No. 2, pp.548-550, March 1990

[9] P.J. Leonard, D. Rodger, H.C. Lai, M. Norton, R.J. Hill-Cottingham, "Coupling FE with power electronics and rotor dynamics of motors", *IEE Seminar on Current Trends in the Use of Finite Elements (FE) in Electromechanical Design and Analysis,* Ref. 2000/013, pp. 6/1-6/6, 14 Jan. 2000

[10] R.L. Russell, K.H. Norsworthy, "Eddy current and wall losses in screened rotor induction motors," *Proc. IEE*, Vol. 105A, pp. 163, Apr. 1958.

[11] D. Rodger, T. Karaguler, and P.J. Leonard, "An optimal formulation for 3D moving eddy current problems with smooth

rotors", *IEEE Transactions on Magnetics,* Vol. 26, pp. 2359–2363, Sept. 1990.

[12] J. F. Eastham, P. C. Coles, M. Benarous, J. Proverbs, A. Foster, "Linear induction motor variable frequency standstill tests to predict operational velocity performance," *Linear Drives for Industrial Applications*, Birmingham, pp. 81-84, 2003

[13] Magnussen, C Sadarangani, "Winding factors and Joule losses of permanent magnet machines with concentrated windings" *IEMDC*, Vol. 1, pp. 333- 339, 2003

[14] Libert F., Soulard J., "Investigation on Pole-Slot Combinations for Permanent-Magnet Machines with Concentrated Windings", *ICEM*, Sep. 2004

[15] J. Wang, Z. P. Xia, D. Howe, S. A. Long, "Comparative study of 3-phase permanent magnet brushless machines with concentrated, distributed and modular windings," *IET Power Electronics, Machines and Drives,* pp. 489 – 493, Mar. 2006.

[16] J. R. Hendershot Jr., T. J. E. Miller, *Design of brushless permanent-magnet motors*, Magna Physics Publishing & Clarendon Press, Oxford, pp. 98-99, 1994.

[17] F. W. Grover, *Inductance calculations*, Dover Publications, New York, pp. 94-113, 1946

[18] M. Liwschitz-Garik, C. C. Whipple, *Electric machinery: fundamental and DC machines (Vol 1)*, Van Nostrand Company, Toronto, pp. 510-511, 1946

[19] P. J. Lawrenson, "Calculation of machine end-winding inductances with special reference to turbogenerators," *Proc. IEE*, Vol. 117, No.6, pp. 1129-1134, June 1970.

[20] M.G. Say, *The performance and design of Alternating current machines*, Third Edition, CBS publishers and distributors, India, pp. 189, 1983

[21] E. C. Barnes, "An experimental study of induction machine end-turn leakage reactance," *AIEE Trans.*, Vol 70, pp. 671-679, 1951

[22] A. Taieb Brahimi, A. Foggia, G. Meunier, "End winding reactance computation using a 3D finite element program", *IEEE Transactions On Magnetics*, Vol. 29, No. 2, March 1993

[23] S. Smith, S. Williamson, "End-winding leakage reactance of concentrically-wound machines", *ICEM*, Bruges, 2002

[24] T. Cox, Prof. J.F. Eastham, J. Proverbs, "End Turn Leakage Reactance of Concentrated Modular Winding Stators", *IEEE Transactions on Magnetics*, Vol. 44, No. 11, pp. 4057-4061, Nov. 2008

[25] M. N. Hamlaoui, M. A. Mueller, J. R. Bumby, E. Spooner, "Polynomial modelling of electromechanical devices: An efficient alternative to look up tables," *Proc. IEE*, Electrical Power Applications, Vol. 151, No. 6, Nov. 2004

[26] M. Liwschitz-Garik, C. C. Whipple, *Electric machinery: fundamental and DC machines (Vol 1)*, Van Nostrand Company, Toronto, pp. 101, 1946

[27] S. Yamamura, H. Ito, "End Effect of a Linear Induction Motor of the Wound Secondary Type" *Report 434 of the General Meeting, IEEJ Japan,* 1971

[28] S. Yamamura, H. Ito, Y. Ishikawa, "Theories of the Linear Induction Motor and compensated linear induction motor" *IEE Trans. On Power Apparatus and Systems*, pp. 1700, 1972

[29] T. Onuki, Y. Kamiya, "Improvement of short primary member linear induction motor performance by partial adoption of the wound secondary" *IEE IAS 33,* Vol. 1, pp. 179 – 186 1998

[30] J F Eastham, Force Engineering Patent "Improvements in and relating to Electromotive Machines", International Patent Application No PCT/GB2007/003849

[31] Prof. J F Eastham, T Cox, Dr H C Lai, J Proverbs, A Foster, S Colyer, "Electromagnetic launch using novel linear induction machines", *IMarEST Engine as a Weapon*, London, Dec. 2006

[32] T Cox, Prof. J F Eastham, J Proverbs, "Linear Induction Motors with Modular Winding Primaries and Wound Rotor Secondaries", *IEEE Transactions on Magnetics*, Vol. 44, No. 11, pp. 4033-4036, Nov. 2008

[33] Prof. J F Eastham, T Cox, J Proverbs, "Comparison Between Plate and Wound Secondaries for Linear Induction Motors with Concentrated Winding Primaries" *SPEEDAM*, Ischia, Jun. 2008

[34] E. R. Laithwaite, *Induction Machines for special purposes*, George Newnes Ltd., London, pp. 32-33, 1966

[35] E.R. Laithwaite, D. Tipping, and D.E. Hesmondhalgh, "The application of Linear Induction Motors to Conveyors" *Proc. IEE,* Vol. 107(A), pp. 290, 1960

[36] T. Cox, J.F. Eastham, H.C. Lai, J. Proverbs, "Investigation of short-rotor linear induction motors using finite element modelling", *Linear Drives for Industrial Applications*, Lille, Sep. 2007

[37] J F Eastham, Force Engineering Patent "Improvements in and relating to Electromotive Machines", International Patent Application No PCT/GB2007/003851

[38] J. F. Eastham, T. Cox, H. C. Lai, J. Proverbs, "The use of concentrated windings for offset double stator linear induction motors," *Electromotion,* Vol. 15, No. 2, pp. 51-56, Apr. 2008

Appendix 1 - A Spreadsheet Winding Factor Calculation Method

A program has been designed to use a stator's slot conductor content to work out the winding factors for each harmonic component present in the stator mmf pattern. This uses the method given in section "Winding analysis of a general 3 phase winding". The sheet allows the modelling of single layer concentrated and multi layer distributed winding factors, but works only with regularly spaced slots e.g. when slot pitch remains constant.

The number of slots and the contents of each slot are specified, as well as the total number of motor regions to be present in the model, both excited and unexcited.

Firstly, the program works out the slot angle of each slot, relative to the entire model. This is calculated using:
Angle/rad = current slot # * π * 360 *current Harmonic pole pairs / (total coils in winding * 180)

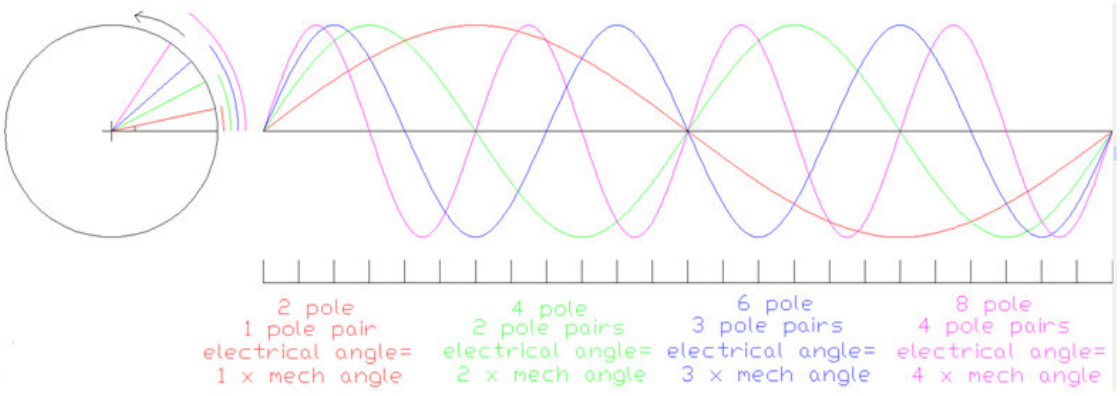

Fig. 147. Harmonics equal to multiples of the fundamental pole pairs

This is demonstrated in Fig. 147. The electrical angle is equal to mechanical or slot angle multiplied by the number of the harmonic being considered. This gives waves with frequency equal to multiples of the fundamental, harmonics.

The spreadsheet gives the electrical angle of the waveform for each slot, and allows the unit magnitude emf waveform to be modelled for each harmonic.

For each harmonic, sine and cosine terms are taken of the slot angle, to give real and imaginary vector components of the electrical angle for unit magnitude as in Fig. 148.

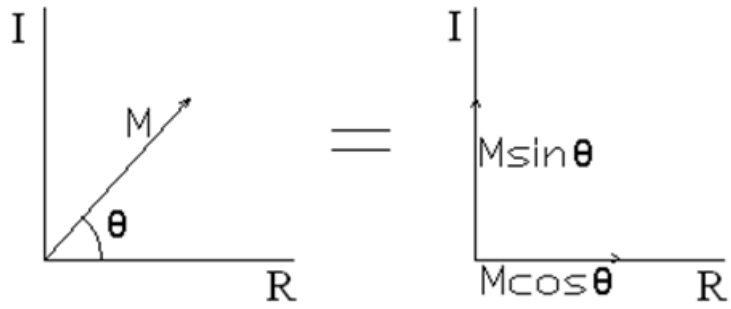

Fig. 148. Component vectors of slot angle θ with Content M for one phase

For each phase, both sin and cosine unit vectors are multiplied by the slot content for that phase, which can be expressed in terms of either coils or conductors Fig. 149. This will give the overall emf pattern in the stator.

	Pole pairs		2							Harmonic offset		0		
	Slot Angle	sine	cos	Red Cond	RC sine	RC cos	Blue Cond	BC sine	BC cos	Yell Cond	YC sine	YC cos	Angle deg	
1	0.524	0.500	0.866	0	0.000	0.000	1	0.500	0.866	-1	-0.500	-0.866	30	Top Stator
2	1.047	0.866	0.500	0	0.000	0.000	2	1.732	1.000	0	0.000	0.000	60	
3	1.571	1.000	0.000	-1	-1.000	0.000	1	1.000	0.000	0	0.000	0.000	90	
4	2.094	0.866	-0.500	-2	-1.732	1.000	0	0.000	0.000	0	0.000	0.000	120	
5	2.618	0.500	-0.866	-1	-0.500	0.866	0	0.000	0.000	1	0.500	-0.866	150	
6	3.142	0.000	-1.000	0	0.000	0.000	0	0.000	0.000	2	0.000	-2.000	180	
7	3.665	-0.500	-0.866	0	0.000	0.000	-1	0.500	0.866	1	-0.500	-0.866	210	
8	4.189	-0.866	-0.500	0	0.000	0.000	-2	1.732	1.000	0	0.000	0.000	240	
9	4.712	-1.000	0.000	1	-1.000	0.000	-1	1.000	0.000	0	0.000	0.000	270	
10	5.236	-0.866	0.500	2	-1.732	1.000	0	0.000	0.000	0	0.000	0.000	300	

Fig. 149. Spreadsheet top stator slot angles per phase including number of conductors

If two stators are modelled, the slot angle of the original stator is modified by the mechanical angle between the two stators to give the slot angles of the new stator. These are again broken up into sin and cosine components for each phase and multiplied by conductor distribution Fig. 150.

90	47.124	0.000	-1.000	0	0.000	0.000	0	0.000	0.000	0	0.000	0.000	2700				
91	47.647	-0.500	-0.866	0	0.000	0.000	0	0.000	0.000	0	0.000	0.000	2730				
92	48.171	-0.866	-0.500	0	0.000	0.000	0	0.000	0.000	0	0.000	0.000	2760				
93	48.695	-1.000	0.000	0	0.000	0.000	0	0.000	0.000	0	0.000	0.000	2790				
94	49.218	-0.866	0.500	0	0.000	0.000	0	0.000	0.000	0	0.000	0.000	2820				
95	49.742	-0.500	0.866	0	0.000	0.000	0	0.000	0.000	0	0.000	0.000	2850				
96	50.265	0.000	1.000	0	0.000	0.000	0	0.000	0.000	0	0.000	0.000	2880				
97	50.789	0.500	0.866	0	0.000	0.000	0	0.000	0.000	0	0.000	0.000	2910				
98	51.313	0.866	0.500	0	0.000	0.000	0	0.000	0.000	0	0.000	0.000	2940				
99	51.836	1.000	0.000	0	0.000	0.000	0	0.000	0.000	0	0.000	0.000	2970				
100	52.360	0.866	-0.500	0	0.000	0.000	0	0.000	0.000	0	0.000	0.000	3000				
1	0.524	0.500	0.866	0	0.000	0.000	0	0.000	0.000	0	0.000	0.000	30	Bottom Stator			
2	1.047	0.866	0.500	0	0.000	0.000	0	0.000	0.000	0	0.000	0.000	60				
3	1.571	1.000	0.000	0	0.000	0.000	0	0.000	0.000	0	0.000	0.000	90				
4	2.094	0.866	-0.500	0	0.000	0.000	0	0.000	0.000	0	0.000	0.000	120				
5	2.618	0.500	-0.866	0	0.000	0.000	0	0.000	0.000	0	0.000	0.000	150				
6	3.142	0.000	-1.000	0	0.000	0.000	0	0.000	0.000	0	0.000	0.000	180				
7	3.665	-0.500	-0.866	0	0.000	0.000	0	0.000	0.000	0	0.000	0.000	210				
8	4.189	-0.866	-0.500	0	0.000	0.000	0	0.000	0.000	0	0.000	0.000	240				
9	4.712	-1.000	0.000	0	0.000	0.000	0	0.000	0.000	0	0.000	0.000	270				
10	5.236	-0.866	0.500	0	0.000	0.000	0	0.000	0.000	0	0.000	0.000	300				

Fig. 150. Bottom stator slot angles per phase including number of conductors

Now that the content of each slot has been refined into phasor components, these components can be summed for each phase to give the overall components of magnitude for each phase, outlined in blue in Fig. 151. Using a double-sided stator sums both stators together to give the overall pattern.

90	47.1239	-1.7E-15	-1	0	0	0	0	0	0	0	0	2700	
91	47.6475	-0.5	-0.86603	0	0	0	0	0	0	0	0	2730	
92	48.1711	-0.86603	-0.5	0	0	0	0	0	0	0	0	2760	
93	48.6947	-1	-3.7E-15	0	0	0	0	0	0	0	0	2790	
94	49.2183	-0.86603	0.5	0	0	0	0	0	0	0	0	2820	
95	49.7419	-0.5	0.86603	0	0	0	0	0	0	0	0	2850	
96	50.2655	-2E-15	1	0	0	0	0	0	0	0	0	2880	
97	50.7891	0.5	0.86603	0	0	0	0	0	0	0	0	2910	
98	51.3127	0.86603	0.5	0	0	0	0	0	0	0	0	2940	
99	51.8363	1	2.5E-16	0	0	0	0	0	0	0	0	2970	
100	52.3599	0.86603	-0.5	0	0	0	0	0	0	0	0	3000	
			Sums		-12.928	7.464		12.928	7.464		0.000	-14.928	
			Sum sqs		222.851			222.851			222.851		
			Mod		14.928			14.928			14.928		
					turn by -120 Re part			-14.928		turn by -240 Re part			7.464
					turn by -120 Im part			0.000		turn by -240 Im part			12.928
			NPS	Jpart NPS	-0.000189616		Rpart NPS	0.000109475		Mod NPS	0.00021895	wdg fact	0.000
					turn by -240 Re part		7.464			turn by -120 Re part			7.464
					turn by -240 Im part		-12.928			turn by -120 Im part			-12.928
			PPS	Jpart PPS	-12.928		Rpart PPS	7.464		Mod PPS	14.928	wdg fact	0.933
				Jpart ZPS	0.000		Rpart ZPS	0.000		Mod ZPS	0.000	wdg fact	0.000

Fig. 151. Overall components of magnitude per phase

The phase sequences are now calculated (outlined in red above). The first step of this is to adjust two of the phases to account for the 3 phases being 120° apart. The blue phase is adjusted 120° relative to red.

The x and y components are multiplied by the x and y components of a unit vector 120° away from the current position, giving the equivalent vectors the blue component in the forward going sequence.

Similarly, the x and y components of the yellow phase are multiplied by the x and y components of a unit vector 240° away from the current position.

Now that the forward going vector components of all three phases have been found, the average sum of these x and y vector components is taken. The modulus of these two figures gives the resultant positive phase sequence magnitude for the harmonic in question.

The same process is now repeated, but with the yellow and red phases reversed. This reverses the field direction, and gives the reverse going field. The average sum of the x and y components is taken, and the modulus of this gives the magnitude of the negative phase sequence for the harmonic in question.

Note that the positive and negative going fields are interchangeable, depending on which way the motor is run e.g. the fundamental is generally taken as positive going.

Lastly the unmodified summed x and y components of all three phases are taken and averaged in order to get the zero phase sequence.

The values of phase sequence are then divided by the number of coils or conductors in a phase of the stator, giving a value of winding factor for the harmonic in question. Each harmonic is worked out in sequence and the winding factors for each pole number are plotted.

If a double-sided layout is being considered, this can also be accommodated. Both windings are specified to give the full harmonic spectrum for the pair.

Appendix 2 - Two Coil Concentric Concentrated Winding Factor Calculator

The above program only works with regularly spaced slots, however this is not always the case. The 2 coil concentrated concentric winding has been investigated and shown to be good at reducing end turn leakage reactance. The use of 2 concentric coils generally requires irregularly spaced slots and introduces a distribution factor to the overall concentric stator winding factor which must be accounted for.

The inputs to the concentric winding factor calculator are number of coils, number of poles, 2 coil concentric y or n, outer coil pitch, inter coil tooth width and concentric coil width as seen in Fig. 152. Current limits of the model are that it will only model 3 coil 2-4 pole, 9 coil 8-10 pole and 12 coil 10-14 pole type concentrated windings. These are the only types currently identified as useful for the company's requirements, but this may be revised in the future. From Fig. 152 it can be seen that the sheet draws one phase of the winding with the slots labelled.

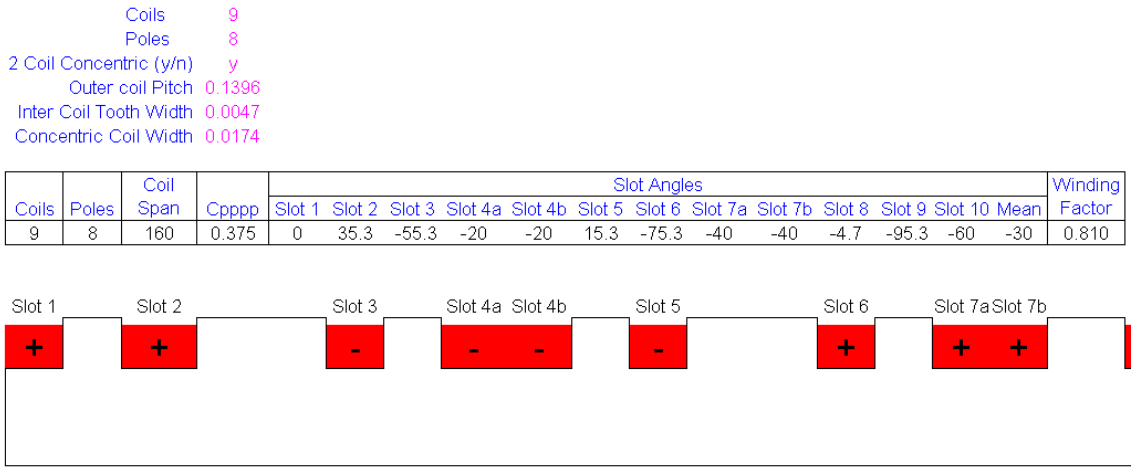

Fig. 152. Concentrated winding factor calculator inputs and outputs

From the inputs, the sheet works out the coil span in degrees using 180 * No of poles / No of coils. The number of coils per pole per phase is also calculated by the obvious method. A separation factor is also calculated to work out the

separation between outer and inner slot centres of a 2 coil concentric. This uses If statements to determine the status of the 2 coil concentric switch. If the winding is a 2 coil concentric, the following formula is used

Separation factor = (1.5*Concentric coil width + Inter coil tooth width)/outer coil pitch

This works out the physical distance from the centre of the outer slot to the centre of the inner slot and divides it by the outer coil pitch. The sheet works by summing the slot angles of one phase across the various slots.

If type statements are used to determine the slot content for each slot, based on the coils per pole per phase and hence the winding type. The slot angle is worked out using the coil span angle for outer slots and the coil span angle modified by the separation factor for the inner slots. The content of the slot is equal to the following.

Slot 1 = 0 (Starting Point)
Slot 2 = Slot 1 + Coil span angle * separation factor
Slot 3 = Slot 4a - Coil span angle * separation factor
Slot 4a = Coil span angle * 1 – 180
Slot 4b = Slot 4a (if 9cl 8pl or 12cl 10pl)
Slot 5 = Slot 4b + Coil span angle * separation factor (if 9cl 8pl or 12cl 10pl)
Slot 6 = Slot 7a - Coil span angle * separation factor (if 9cl 8pl or 12cl 10pl)
Slot 7a = Coil span angle * 2 – 360 (if 9cl 8pl or 12cl 10pl)
Slot 7b = Slot 7a (if 9cl 8pl)
Slot 8 = Slot 7b + Coil span angle * separation factor (if 9cl 8pl)
Slot 9 = Slot 10 - Coil span angle * separation factor (if 9cl 8pl)
Slot 10 = Coil span angle * 3 – 360 (if 9cl 8pl)

The mean angle of the phase is also calculated. For each active slot, the cosine of the angle between slot and mean angle is found. The average of these

cosine angles is then the winding factor including the effect of the concentric coil.

Appendix 3 - Four-layer fractional-slot windings

If a conventionally designed linear stator and wound rotor are used together, a high level of locking force may occur due to variation in the overall steel to steel gap as the rotor moves over the stator. Locking forces are undesirable as they can oppose rotor motion and will cause thrust oscillation as the stator and rotor move relatively to each other.

In order to prevent this, non-locking wound rotors can be designed. These must avoid the rotor iron teeth locking with the stator iron teeth, whilst having an equal pole pitch to the stator in order to couple effectively.

This means that the wound rotor must be created with a different number of slots to the stator, whilst at the same time ensuring that the MMF phase angle of stator and rotor match. Practically, the simplest method of achieving this is to design the rotor with only one slot less than the stator.
Both the stator and the rotor would produce the same value of instantaneous mmf at any given point along their length Fig. 153.

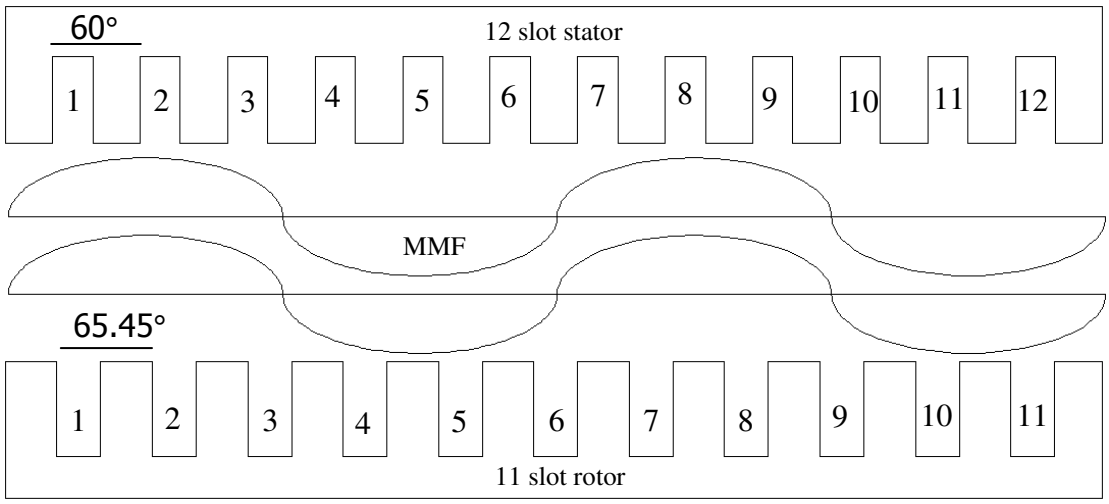

Fig. 153. Stator and rotor with a common phase pattern

As can be seen in Fig. 153, each pole of the mmf phase pattern covers a whole number of stator slots. This allows the phase pattern to be produced by a two layer winding, with a maximum of two phases per slot. The stator produces 4 poles from 12 slots or 3 slots per pole.

It can also be seen that to get the same phase pattern for the 11 slot wound rotor, each pole corresponds to a non-whole number of slots. The rotor has 4 poles from 11 slots or 11/4 slots per pole.

For example, a 12-slot stator with 4 poles has an electrical angle of 720° over the entire motor. This corresponds to 60° per slot. 60° is also the electrical angle between phases, therefore each phase occupies a single slot, giving a conventional winding.

For an 11-slot rotor with four poles, the electrical angle over the motor is still 720°. However, the electrical angle per slot is 720/11 = 65.45°.

In order to give the same phase pattern over a fractional number of slots, a four-layer winding is used. This type of winding allows the number of conductors in each layer to be varied, in order to give the required mmf/electrical angle for each slot. Fig. 154 shows an mmf angle represented as a vector.

It can be seen that by varying the number of phase conductors in a slot, any desired mmf phase angle can be produced from a slot. In Fig. 154 for instance, equal numbers of red and -blue conductors will give an mmf phase angle of 30° from zero.

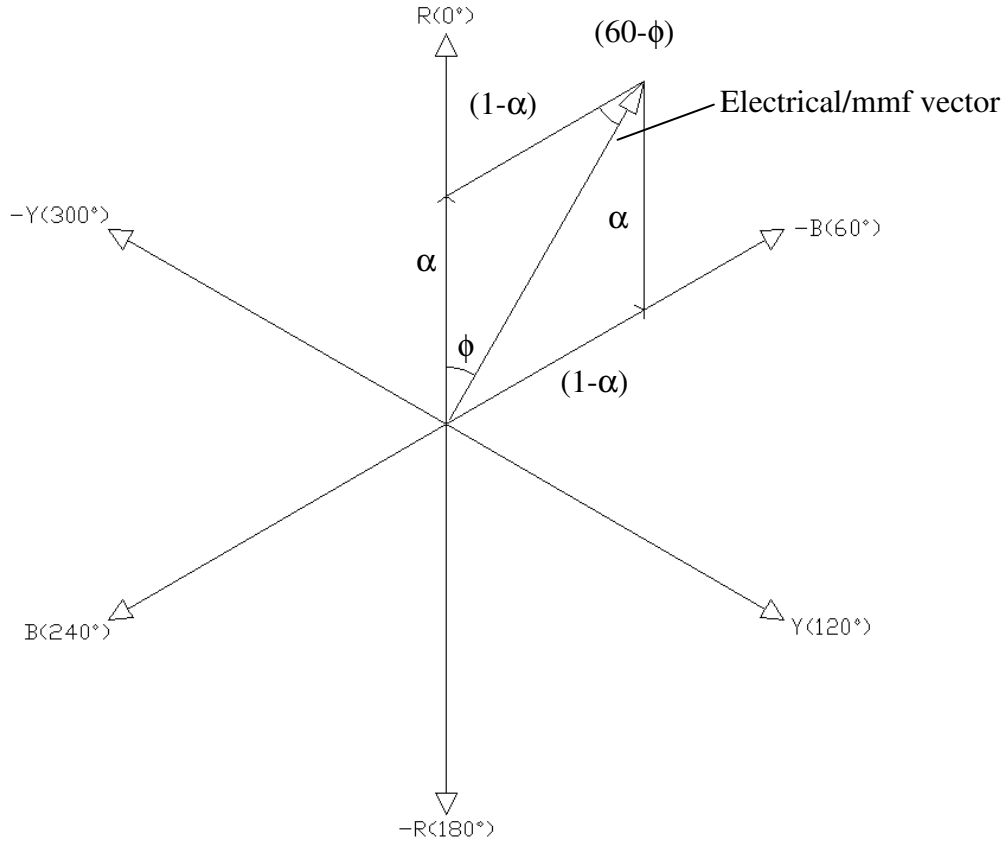

Fig. 154. Electrical/MMF angles

This method can be used to produce any electrical angle desired in a slot. As a general rule, the magnitude α of the R and -B phases to give the required angle ϕ can be found using the method below.

$$\alpha \sin\phi = (1-\alpha)\sin(60-\phi)$$
$$k = \sin\phi / \sin(60-\phi) = (1-\alpha)/\alpha$$
$$\alpha = 1/(1+\kappa)$$

Multiplying α by half of the number of conductors in the slot will give the number of Red phase conductors required in the slot. The same process with (1-α) conductors will give the number of Negative blue phase conductors.

For instance, using all red or all negative blue conductors will give phase angles of 0° and 60° respectively. If Fig. 154 is examined with reference to the stator winding, it will be seen that in a stator, the electrical angle progresses by 60°

per slot (for 1 slot per pole per phase). This means that in a stator, the bottom layer of a double layer winding consists of only one type of phase conductor as in Fig. 155.

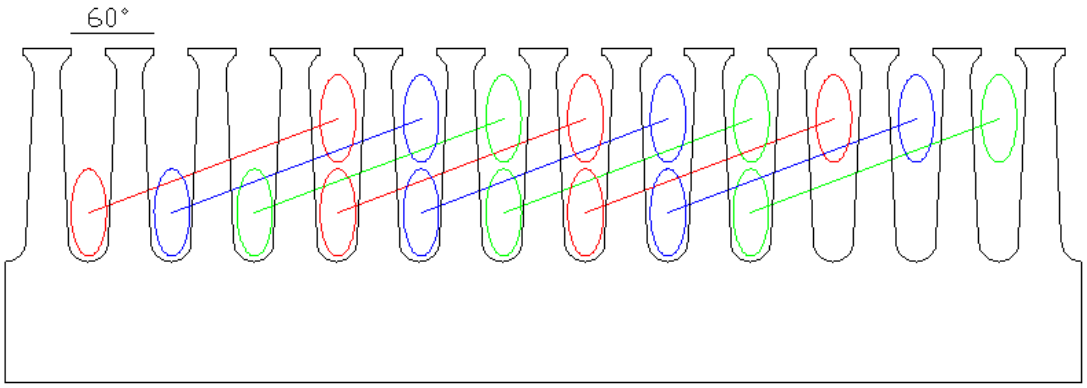

Fig. 155. Illustration of a two-layer winding

If the same process is followed with the rotor angle, it will be seen that this progresses by 720/11 = 65.45° per slot. This means that up to 4 layers of windings are used in each slot to give the correct overall phase angle. For instance, if the first slot were at angle 0, this would be purely red conductors in the bottom 2 layers. In the next slot however, the electrical angle has advanced by 65.45°. Referring to Fig. 154, the slot vector would fall between negative blue and yellow. Therefore, an unequal balance of negative blue and yellow conductors in the bottom two slots is required to give the correct overall slot phase angle. This is illustrated in Fig. 156.

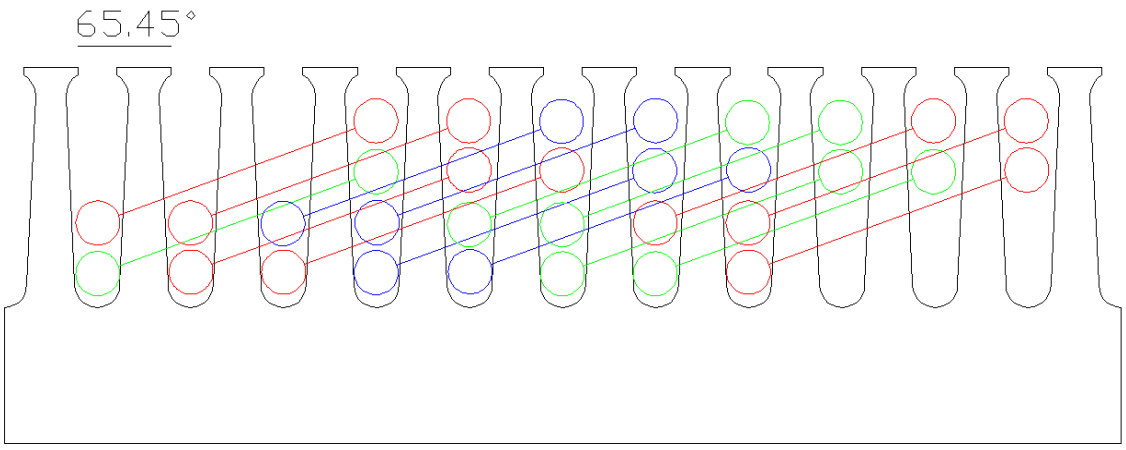

Fig. 156. An illustration of a four-layer winding